RECLAMATION

Managing Water in the West

Technical Report No. SRH-2010-22

SRH Model Applications and Progress Report on Bank Erosion and Turbidity Current Models

Conducted under Appendix No. 8 to the Agreement between American Institute in Taiwan (AIT) and Taipei Economic and Cultural Representative Office (TECRO) for Technical Assistance and Cooperation for Water Resources

U.S. Department of the Interior
Bureau of Reclamation
Technical Service Center
Denver, Colorado

February 2011

Mission Statements

The mission of the Department of the Interior is to protect and provide access to our Nation's natural and cultural heritage and honor our trust responsibilities to Indian Tribes and our commitments to island communities.

The mission of the Bureau of Reclamation is to manage, develop, and protect water and related resources in an environmentally and economically sound manner in the interest of the American public.

Cover Figure: Looking upstream at the Chi-Chi Weir (photo taken in November, 2009)

SRH Model Applications and Progress Report on Bank Erosion and Turbidity Current Models

Conducted under Appendix No. 8 to the Agreement between American Institute in Taiwan (AIT) and Taipei Economic and Cultural Representative Office (TECRO) for Technical Assistance and Cooperation for Water Resources

Report Prepared by:

Yong G. Lai, Ph.D., Hydraulic Engineer
Sedimentation and River Hydraulics Group, Technical Service Center

Blair P. Greimann, P.E., Ph.D., Hydraulic Engineer
Sedimentation and River Hydraulics Group, Technical Service Center

U.S. Department of the Interior
Bureau of Reclamation
Technical Service Center
Denver, Colorado

Peer Review Certification: This document has been peer reviewed per guidelines established by the Technical Service Center and is believed to be in accordance with the service agreement and standards of the profession. Questions concerning this report should be addressed to Timothy Randle, Group Manager of the Sedimentation and River Hydraulics Group (86-68240) at 303-445-2557.

PREPARED BY:

_____ DATE:_____

Yong Lai, Ph.D.
Hydraulic Engineer
Sedimentation and River Hydraulics Group (86-68240)

_____ DATE:_____

Blair Greimann, Ph.D., P.E.
Hydraulic Engineer
Sedimentation and River Hydraulics Group (86-68240)

PEER REVIEWED BY:

_____ DATE:_____

Jennifer Bountry, M.S., P.E.
Hydraulic Engineer
Sedimentation and River Hydraulics Group (86-68240)

Table of Contents

Index of Figures

Page

Index of Tables

Page

Executive Summary

This report documents the works accomplished in 2010 by Reclamation under the Appendix 8 agreement. The agreement is part of the technical assistance and cooperation for water resources program between the American Institute in Taiwan (AIT) and the Taipei Economic and Cultural Representative Office (TECRO).

A summary of major accomplishments and conclusions is provided below.

Concerning Degradation on the Tachia River

SRH-1D was applied to the Tachia River from the ocean to approximately 42 km upstream. We simulated two historical periods: 2000 to 2005 and 2005 to 2008. A 3-year future simulation was also carried out using 2008 geometry as the initial conditions and 2005 to 2008 flow values. Following conclusions can be drawn based on our study.

- For both the 2000 to 2005 and 2005 to 2008 simulations, the model reproduced the trends and magnitudes of sediment erosion and deposition downstream of Shih-Gang Dam at most cross sections. There are some discrepancies in the vicinity of XC 23 to 19. These may be attributed to the influence of tributaries downstream of XC 23. Overall agreement between the model results and the measured data demonstrates the accuracy and usefulness of SRH-1D for application to rivers in Taiwan.

- SRH-1D was able to reproduce the aggradation or degradation volumes in most other reaches, despite the neglect of tributaries. However, SRH-1D is a one-dimensional model, it cannot simulate changes in channel alignment due to migration or avulsion.

- Bedrock is currently present from Shih-Gang Dam to XC 32. However, bedrock geometry is unknown prior to 2007 and it was not possible to quantify the amount of bedrock erosion downstream of Shih-Gang Dam. Future surveys should indicate the extent of bedrock exposure and also depth to bedrock to allow further model tuning and testing.

- Both an analysis of the historical data and simulation of the future conditions indicate that the erosion downstream of Shih-Gang Dam on the Tachia River is expected to continue for the foreseeable future. A severe sediment imbalance has been caused by the Chi-Chi earthquake and the presence of Shih-Gang Dam. The Chi-Chi earthquake increased the sill of Shih-Gang Dam approximately 10 m and this created a deposition zone

upstream of the dam. The dam will prevent a head cut from progressing up through the bed rock and restoring the sediment supply. There will continue to be a lack of sediment supply to the downstream channel for some time into the future. Large floods will continue to erode sediment from the channel bed downstream of the dam. The erosion will likely continue to progress downstream. From 2000 to 2005, the erosion was primarily from the dam to XC 28, approximately 4.5 km downstream of the dam. There was only localized erosion below this location. From 2005 to 2008 the erosion occurred primarily from the dam to XC 20, or about 8 km downstream of the dam. There was also erosion for 8 more km, though the magnitude was significantly reduced. It is likely that severe erosion will occur downstream of XC 20 in the next large flow events. Infrastructure in the Tachia River from Shih-Gang Dam all the way to 5 km upstream from the ocean should be protected from potentially severe scour. Downstream of the Ho-Feng Bridge (XC 28-1), there was approximately 6 m of scour measured from 2005 to 2008. This type of scour could occur at the bridges further downstream in the future. The next typhoons may erode large volumes of sediment at the Highway 1 Bridge at XC 23. If sediment supply is not restored to the downstream reach then the erosion is expected to continue downstream and potentially begin to scour the riverbed near the high speed rail line at XC 19.

- The bedrock downstream of Shih-Gang dam does not provide any significant resistance to erosion. In fact, the presence of "bedrock" downstream of Shih-Gang dam creates more erosion than if the river bed was gravel and cobbles. The bedrock becomes basically wash load after it is eroded and does not provide any significant bed material load to the downstream reaches. Also, the bed does not become armored with larger particles, which would slow the erosion. The only method that will slow this erosion is to increase the passage of gravel, cobbles, and boulders through Shih-Gang dam.

Concerning Proposed Engineer Schemes Downstream of the Chi-Chi Weir

SRH-2D was applied to evaluate one of the proposed engineering schemes to prevent further bedrock degradation downstream of the Chi-Chi Weir. The model has been developed, calibrated and verified as documented in the report of Lai and Greimann (2009).

Engineering scheme number one (#1) was selected for simulation among the five proposed schemes by the 4th River Division of the Water Resources Agency (WRA, 2008a). The scheme relied on the use of stability control structures and bank protection measures at strategic locations. Key engineering consideration for the reach immediately downstream of the weir is to construct three cross stream

weirs so that no further degradation of the river bed is allowed. The stream section between the weirs is to be filled first with large sized cobbles and then smaller sized gravels. The purpose is to restore the protective bed layer of cobbles. Other various bank protection measures are less critical as far as the current modeling is concerned, as bank erosion modeling is not considered.

The following conclusions can be drawn based on the model results:

- The proposed engineering scheme #1 will succeed in preventing further erosion between XS 113 and XS 116. A small amount of aggradation was predicted. The protection is largely achieved by the use of cross stream weirs and fillings within this reach with large sized sediment materials.

- The toes downstream of proposed cross stream weirs were predicted to experience erosion if the same materials (75% with 374 mm diameter and 25% with 125 mm diameter) were used everywhere. So extra protection of weir toes is required.

- More erosion was predicted downstream of XS 113 and more flow was predicted to go along the right branch of the channel downstream of XS 113, in comparison to the existing condition scenario. This may have the implication that channel shift towards the right bank may be accelerated if nothing is done in that area.

- Between XS 111 and XS 112, channel incision was predicted, which is due mainly to the soft rock erosion. We suggest that some measures are needed at XS 111 and its nearby surroundings.

- Further downstream of XS 111, the difference in erosion and deposition between the proposed engineering scheme #1 and the existing condition was small.

Major Accomplishments of Bank Erosion Modeling

Based on a literature review, we proposed to develop the current state-of-the-art bank erosion capability that is coupled to the existing mobile-bed model SRH-2D. In the past year, the accomplishments may be summarized as follows:

- Two bank erosion modules were recommended for development, based on our extensive literature review: a non-cohesive bank module and a cohesive bank module with multi-layer materials.

- The non-cohesive bank erosion module was under development this fiscal year (2010). A bank retreat rate equation was derived based on the angle-

of-repose of the bank and the mass conservation principle. The retreat equation is general in that both retreat and encroachment are included.

- A moving-mesh method, based on the Arbitrary Lagrangian-Eulerian (ALE) formulation, was developed and implemented into SRH-2D. The ALE formulation was tested to ensure accuracy and volume conservation.

- The non-cohesive bank erosion module was implemented, debugged, and tested. A verification study was carried out using the experimental bank erosion case of Nagata et al. (2000). Preliminary results were obtained with encouraging results. The study also pointed to areas for further improvements.

- The cohesive bank erosion module was also under development in which a version of BSTEM was to be incorporated into SRH-2D. The coupled model intends to model bank erosion with multi-layer cohesive banks.

- The BSTEM model was originally developed as a spreadsheet tool, written in computer languages other than FORTRAN. The FORTRAN version of the BSTEM model was developed and tested. Work is currently under way to "merge" BSTEM model into SRH-2D.

Major Accomplishments of Layered-Averaged Turbidity Current Model

The layer-averaged turbidity current model was proposed in our study last year (Lai and Greimann, 2009). Governing equations have been formulated along with the supplemental auxiliary equations. Accomplishments in this task are listed below:

- A finite-volume based numerical method, similar to what was adopted by SRH-2D, was selected to solve the layer-averaged governing equations for the turbidity current. The model has completed its programming. Extensive debugging of the program has also been completed.

- Three stages of model tests were completed: test of unsteady flow modeling capability; test of a simple turbidity current to cover various numerical schemes and issues; and test of turbidity current flows and comparison with flume experiments.

- Highly unsteady dam-break flows were selected to test the unsteady capability of the selected numerical schemes, along with the ability to model the traveling hydraulic jump. Good results were obtained in comparison with the available measurement data and other numerical models.

- A simple turbidity current case was set up to test various aspects of the numerical schemes. In the process, a numerical difficulty associated with the modeling of the current head was identified. Despite extensive efforts, the numerical difficulty is still unresolved at present. It was found, however, that the numerical issue does not impact the modeling of the current front speed and the results of the overall turbidity current.

- Two turbidity current cases were simulated under laboratory settings. One was the conservative turbidity current in which there was no net erosion and deposition between the current and the bed; another was a non-conservative waning turbidity current in which deposition of suspended sediments occurred. Comparison of model results with the measurement data provided encouraging results; it also pointed to potential future research on ways to improve the model.

1 Introduction

The technical assistance and cooperation for water resources program between the American Institute in Taiwan (AIT) and Taipei Economic and Cultural Representative Office (TECRO) was established in the nineteen eighties (1980s). Various water resources projects have since been carried out, which were executed through the U.S. Bureau of Reclamation (Reclamation) and the Water Resources Agency (WRA) in Taiwan. Years of collaboration have produced fruitful results and have proved beneficial to both sides in dealing with the challenge facing the sustainable use of limited water resources.

In 2010, Reclamation was tasked under the program with five tasks. These tasks were developed according to the four-year (2009-2012) plan established in 2009. A brief description of each task is provided below, along with the chapter of this report corresponding to each task.

Task 1 is related to the riverbed degradation study, concentrating on applications of SRH models to projects in Taiwan. In previous years, both SRH-1D and SRH-2D models have been extended, calibrated, and verified for selected sites in Taiwan. SRH-1D has been applied to the Chosui River in 2008 and the Tachia River downstream of the Shih-Gang Dam in 2009. SRH-2D model has been applied to the reach on the Chosui River downstream of the Chi-Chi Weir in 2008 and 2009. Both models are ready to be applied to projects. This year (2010), more verification and application studies are carried out with SRH-1D for the Tachia River. The verification study is rerun with the new available data for the period from Oct. 2007 to Oct. 2008. Results are reported in Chapter 2. This year, SRH-2D is applied to the downstream of the Chi-Chi Weir on the Choshui River to evaluate one of the proposed engineering schemes in preventing further degradation downstream of the weir. Results of this task are reported in Chapter 3.

Task 2 is to continue the bank erosion research and model development which was started in 2009. Bank erosion has been observed on both Tachia River and Choshui River. For example, the river alignment has been shifted to the left downstream of the Tachia River Bridge near Freeway No.1; meandering river pattern has been developed and is continuing for the reach between Houfeng Bridge and Tachia River Bridge along Freeway No.1. Also, downstream of Chosui River, river alignment has moved northwards gradually in recent years and the levee of the right bank is endangered. There is a need to model bank erosion of these rivers so that future river alignment trend may be predicted and measures may be developed and evaluated. A four-year research, development and application plan was established in 2009 and work on bank erosion modeling has started since. In 2009, a review of existing bank erosion models was provided,

and specific bank erosion models were selected and proposed. Development of bank erosion models has since started. This year (2010), the research and development is continuing. The planned work includes: (1) Continued development and debug of the bank erosion module; (2) Test and verification of the bank erosion module with selected data; (3) Identification of a specific site on the Choshui River for bank erosion study; and (4) Preparation and initiation of a calibration study. The progress and status are reported in Chapter 4.

Task 3 is on the development of a layered-averaged turbidity current model. The 2010 work scope includes: (1) Continue the development of the layer-averaged turbidity current model; and (2) Perform the debug, testing, and evaluation of the model with benchmark turbidity current flows. The progress of this task is reported in Chapter 5.

Task 4 is the optional consultation service and technical training. A training class in the area of bank erosion modeling and data collection is to be planned and arranged by Reclamation, and it is scheduled to occur in November, 2010. Drs. Andrew Simon and Rob Thomas, at the National Sedimentation Lab (NSL), Agricultural Research Service (ARS), the Department of the Interior, in the US, have been invited; they will travel together with Reclamation delegation to Taiwan to provide the training class.

Task 5 involves the documentation through a final report. This report serves as the progress report for the work in Tasks 1 through 3.

2 SRH-1D Modeling Study of Tachia River

2.1 Background

Tachia River is located in Central Taiwan and is one of the major rivers in Taiwan. The Chi-Chi earthquake of 1999 had a large effect on the Tachia River basin. Shih-Gang Dam is located approximately 23 km upstream from the ocean on the Tachia River. The fault of the earthquake passed through the dam and raised the majority of the dam approximately 10 m. The earthquake also destabilized hillslopes in the watershed. The typhoon of 2004 had a peak flow of over 6,000 m^3/s at Shih-Gang Dam. It caused major deposition in the upper part of Tachia River and major erosion downstream of Shih-Gang Dam. Bedrock is now exposed in the river channel downstream of Shih-Gang Dam.

A bedrock erosion component was developed and incorporated into SRH-1D V2.1, as detailed in Greimann and Vanderburg (2008). SRH-1D has the capability to model one-dimensional hydraulics, mobile bed sediment transport, and bed rock erosion. The bedrock erosion component can simulate erosion due to sediment abrasion or direct hydraulic forces. The model will focus on the prediction of scour in rivers that have exposed bedrock that is eroding at noticeable rates in large areas. To the extent possible, the model was based upon parameters that can be directly measured.

The model will not address local scour that occurs adjacent to bridge piers, abutments or other structures located in rivers channel but other models are available to accomplish this. Annandale (1999) applied the scour methods of Annandale (2006) to estimate scour in bedrock around bridge piers. Hopkins and Beckham (1999) related rock quality designations to the rock scour found around bridge piers and abutments.

2.2 Modeling Overview

We simulated two historical periods using SRH-1D: 2000 to 2005, and then 2005 to 2008. The same set of parameters was used in both simulations. The first set is for model calibration, and the second serves as a verification study. Approximately 42 km of river upstream from the ocean was simulated. However, only the results in the lower 23 km are analyzed as the main concern of this model is the erosion downstream of Shih-Gang Dam. There was also a simulation of potential future conditions using 2008 geometry as the initial conditions. The purpose of this run was to determine if past erosion trends are likely to continue in the future.

SRH-1D Version 2.6 was used in all simulations. This model is available on the internet for free download at: www.usbr.gov/pmts/sediment.

The Tachia River corridor is relatively straight, has few pools, and has relatively consistent bed material sizes. Therefore, the physical system is perhaps closer to the approximations inherit in one-dimensional modeling than in systems characterized by large pool riffle complexes that have large variations in sediment sizes and hydraulic conditions.

2.3 Input data

There are several types of data and model parameters required in SHR-1D. They can be divided into the following categories:

1. Model Parameters
2. Upstream Boundary Conditions
3. Downstream Boundary Conditions
4. Internal Boundary Conditions
5. Lateral Inflows
6. Channel Geometry and Flow Characteristics
7. Sediment Model Parameters
8. Upstream Sediment Boundary Conditions
9. Lateral Sediment Discharge
10. Sediment Bed Material
11. Water Temperature
12. Erosion and Deposition Limits
13. Sediment Transport Parameters
14. Cohesive Sediment Transport Parameters
15. Bedrock Geometry and Parameters

The preparation of data and selection of parameters within each category is described in the following report sections.

2.3.1 Model Parameters

Because a long term simulation is performed, steady flow using a step hydrograph was simulated. The unsteady effects that occur within the relatively short reach upstream and downstream of the weir are not considered important. The metric units option was chosen to run the simulation. A sensitivity study was performed on the time step and if the time step was reduced beyond 0.05 hours, the change to

the final results was not significant. Therefore, all simulations used a time step of 0.05 hours.

2.3.2 Upstream Boundary Conditions

The upstream flow boundary condition was set to a time series of flow rates. Three different periods were simulated: January 2000 to October 2005, November 2005 to October 2008, and November 2008 to 2011. The flow gage located at Shih-Gang dam is used to determine the flows for the entire model. Flow and sediment inputs from tributaries downstream of Shih-Gang Dam are not simulated. If these are to be included both flow and sediment inputs would be required.

The simulated flows for the period January 2000 to October 2005 are shown in Figure 1. Only daily average flow data was available. The peaks may be significantly larger than the daily average flows and therefore hourly hydrographs were constructed using the peak flow data given in Figure 3. A triangular hydrograph was assumed with duration Δt, as illustrated in Figure 4. The duration of the triangular hydrograph was computed as:

$$\Delta t\,(\text{days}) = \frac{2Q_2 - (Q_1 + Q_3)}{Q_p - 0.5(Q_1 + Q_3)} \tag{2.1}$$

where Q_1, Q_2, Q_3 signify the daily average flow rates the day before, the day of, and the day after, respectively, and Q_p is the peak flow rate. Flows lower than 100 cms were ignored and not simulated.

Flow data for the period November 2005 to October 2008. The simulated flows are shown in Figure 2. The now available measured flow data in 2008 can be used in future simulations rather the estimates utilized in this study.

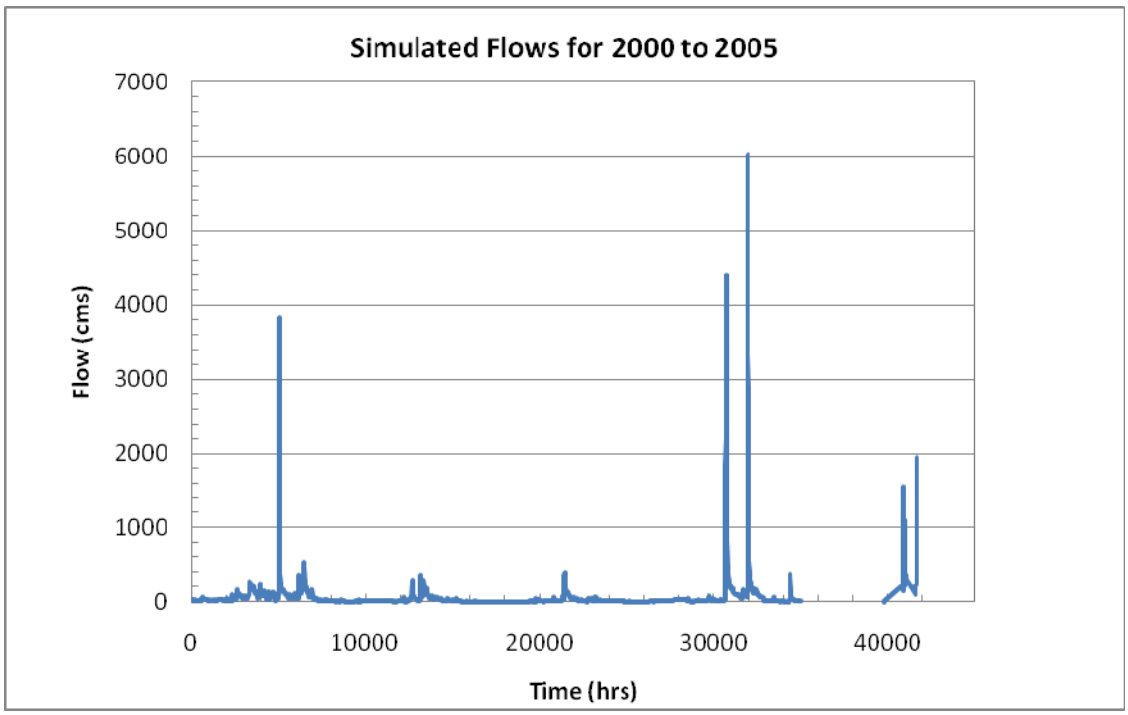

Figure 1. Flows used in simulations from January 2000 to October 2005.

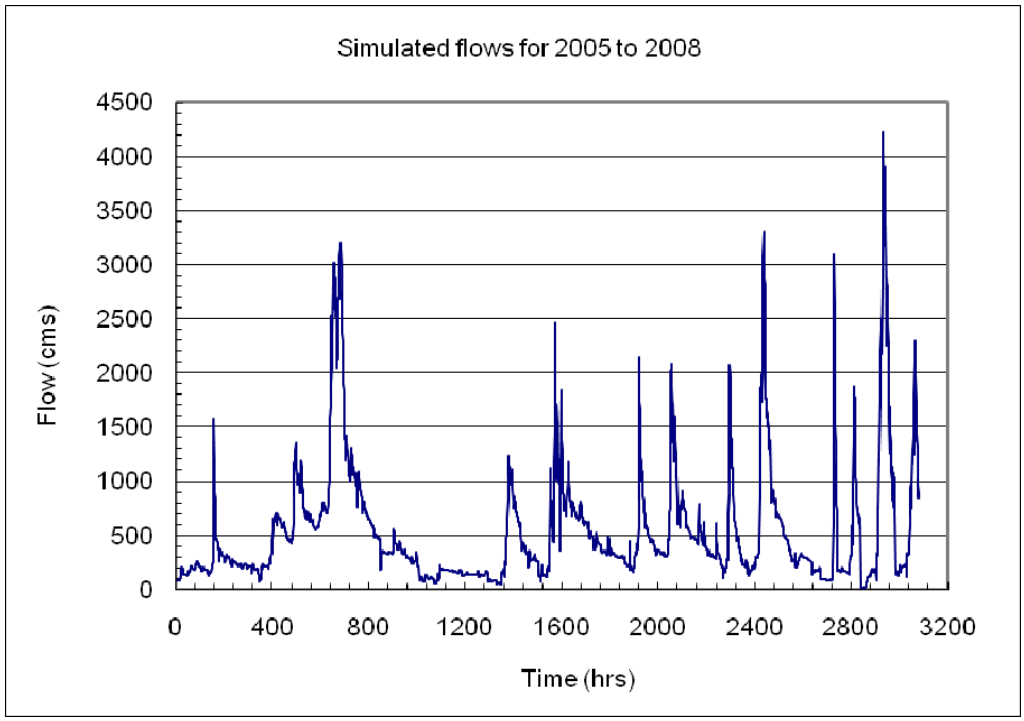

Figure 2. Simulated flows for the period November 2005 to October 2008.

表 2.3.4-2　石岡壩歷年發生最大流量統計表

年別	最大洪峰流量(cms)		年別	最大洪峰流量(cms)	
52	7,840	*	73	896	@
53	358	*	74	2,411	@
54	1,570	*	75	983	@
55	2,990	*	76	978	@
56	1,440	*	77	315	@
57	1,110	*	78	3,062	@
58	2,710	*	79	2,788	@
59	3,940	*	80	835	@
60	2,030	*	81	1,419	@
61	4,540	*	82	1,542	@
62	1,120	*	83	4,140	@
63	2,040	*	84	663	@
64	927	*	85	3,668	@
65	2,940	*	86	2,106	@
66	2,290	*	87	933	@
67	635	@	88	484	@
68	1,647	@	89	790	@
69	3,119	@	90	3,954	@
70	3,149	@	91	709	#
71	1,527	@	92	594	#
72	3,361	@	93	6,195	#

資料來源：*民國 52 年至 66 年採石岡站實測流量(大甲溪治理規劃報告，1993)；@民國 67 年至 90 年採石岡壩實測最大入流量(大甲溪流域聯合整體治理規劃，2003)；#民國 91 年至 93 年採石岡壩操作紀錄最大洩洪量(石岡壩管理中心提供資料)。

Figure 3. Peak flows at given years near Shih-Gang Dam (Water Resources Agency, 2005).

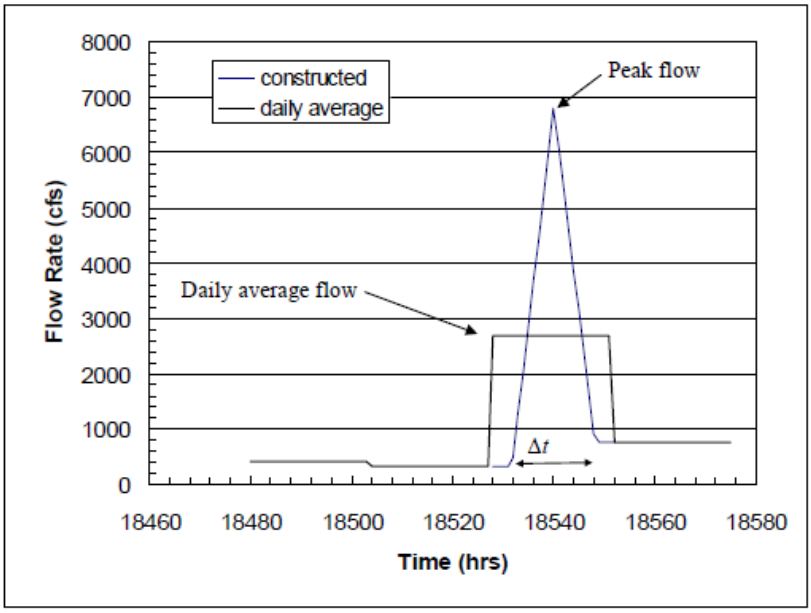

Figure 4. Example of method to reconstruct hourly hydrographs from daily average flow data.

2.3.3 Downstream Boundary Conditions

The downstream boundary condition was set to critical depth at Section -1 taken from the 2005 Tachia HEC-RAS model (see Table 1) given to Reclamation electronically in December 2007 (Water Resources Agency, 2005). This cross section is at the mouth of the river. The same downstream boundary condition was assumed to represent the entire period between 2000 and 2008.

Table 1. Downstream Boundary Conditions

Flow (m^3/s)	Water Surface Elevation at Section -1 (m)
0	0.000
100	0.248
300	0.765
500	1.017
1000	1.422
2600	2.108
3489	2.399
4500	2.663
5900	2.985
7300	3.245
7570	3.281
8900	3.509
10300	3.752
11500	3.900

2.3.4 Internal Boundary Conditions

An internal boundary condition is set at Shih-Gang Dam. The rating curve at section 36 was taken from the 2005 Tachia HEC-RAS model (Water Resources Agency, 2005), as shown in Table 2. The same rating curve condition was assumed to represent the entire period between 2000 and 2008.

Table 2. Rating Curve Used Upstream of Shih-Gang Dam (XC 36)

Flow (m^3/s)	Water Surface Elevation at Section 36 (m)
0	266.64
100	269.29
300	270.84
500	271.30
1000	272.52
2200	273.38
2946	274.02
3800	274.74
5000	275.62
6200	276.41
7430	277.14
7600	277.24
8800	277.88
9800	278.09

A boundary condition was also set at XC 20 to account for the bridge at XC 19-1 (see Table 3).

Table 3. Rating Curve Used by XC 20

Flow (cms)	Water Surface Elevation at Section 20 (m)
0	134.25
100	136.38
300	136.88
500	137.23
1000	137.67
2600	138.70
3489	139.20
4500	139.53
5900	139.94
7300	140.40
7570	140.49
8900	140.92
10300	141.35
11500	141.70

2.3.5 Lateral Inflows

No lateral inflows are considered in this study. There are perhaps significant tributaries near XC 18 and 23. No flow or sediment data was available for these tributaries, but they could be included in future efforts if data was supplied.

2.3.6 Channel Geometry and Flow Characteristics

The locations of the cross sections are given in Figure 5 and Figure 6. For the simulation from 2000 to 2005, the initial bed geometry used in the simulation was taken from a 2000 cross section survey. The cross sections were surveyed again in 2005 (Water Resources Agency, 2005). The survey of 2005 was used to compare against the simulated results.

For the simulation from 2005 to 2008, the HEC-RAS model of 2005 was used and the results were compared to the measured 2008 cross sections. For the simulation from 2008 to 2011, the HEC-RAS model from measured 2008 cross sections was used as initial conditions.

The channel Manning's roughness coefficient was set to 0.04 for all simulations for the main channel and the floodplains. No levees, ineffective flow, or blocked obstructions were used in the simulations.

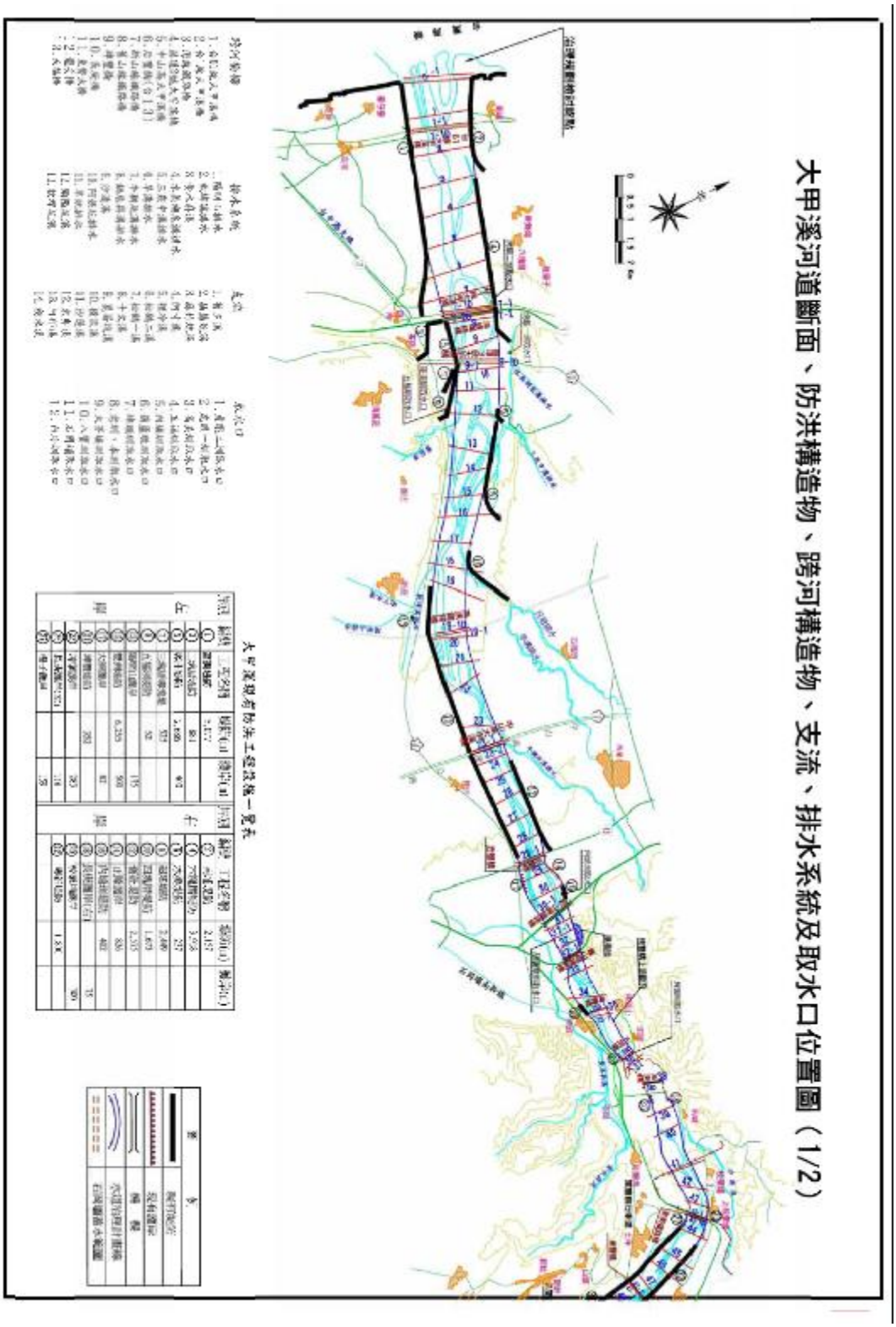

Figure 5. Cross Sections used in the Tachia Study (1 to 47).

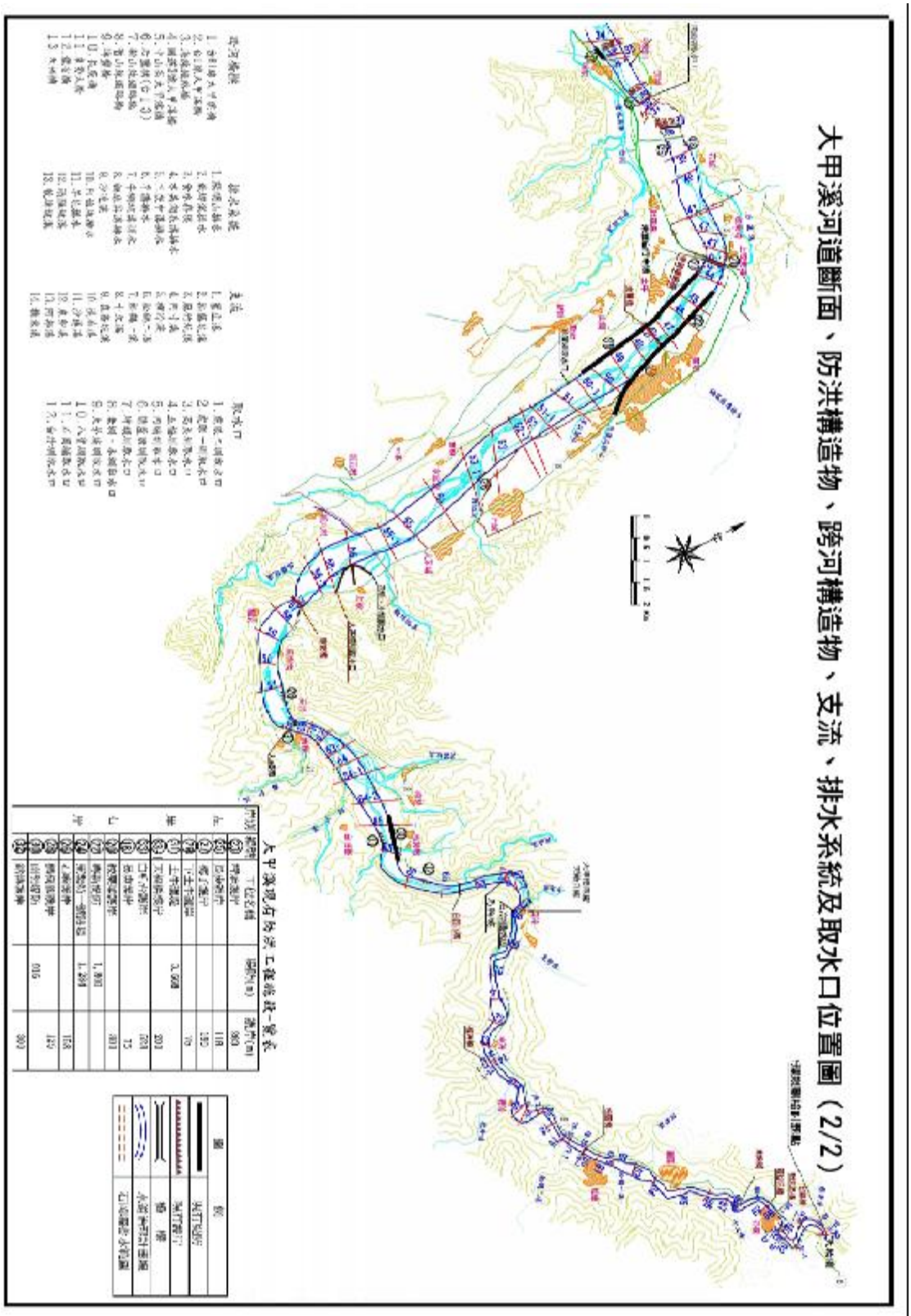

Figure 6. Cross Sections used in the Tachia Study (45 to 90).

2.3.7 Sediment Model Parameters

Sediment model parameters control the number of bed layers used to represent the river bed, the implicit factor for sediment transport computations, and the number of sediment time steps performed for each hydraulic time step. Default model values were deemed appropriate for this study. The default value for the number of river bed layers is 3. The default for the implicit factor is 1. The number of sediment time steps default value is 1. The frequency the angle of repose condition is checked is set here too. The default is that it is checked every time step. The sediment size groups are also given in this data group and thirteen sediment size classes are used ranging from 0.125 mm to 1024 mm. The assumed sediment porosity is 0.3.

2.3.8 Upstream Sediment Boundary Conditions

The upstream sediment discharge is set to a sediment capacity condition. Suspended sediment measurements are available at several locations in the study area, however, bedload measurements are not available and the bedload portion of the load will be the most important in determining the erosion of bed material in the reaches. Therefore, for the purposes of this simulation, the incoming sediment load was assumed to be equal to the sediment transport capacity as determined by the sediment transport formula.

2.3.9 Lateral Sediment Discharge

There are no lateral sediment discharge locations. As mentioned in the "Lateral Inflows" section, this may cause errors downstream of Shih-Gang Dam, downstream of XC 18 where they is a tributary that has the potential to contribute flow and sediment.

2.3.10 Sediment Bed Material

Sediment gradation data were collected in 1983 and 2007 in the Tachia River (Figure 7). The data from 2007 was used in the simulation because it was more complete and was taken nearer in time to 2000, the beginning of the simulation. Different gradations were used upstream and downstream of Shih-Gang Dam. In addition, different gradations were used for the surface and sub-surface material.

The D_{50} tended to decrease in the upstream direction, which is unusual for rivers. This trend is indicative of a large sediment release in the upper watershed, which is what happened in the 1999 earthquake. The deposition of material in the upper watershed decreased the average size of the bed material in the river. The bed

material size is expected to increase over time in the upper watershed as the river recovers from the large input of sediment.

The representative diameters upstream and downstream of the dam were computed by averaging all samples upstream and downstream of the dam, respectively (see Table 4).

Table 4. Representative diameters used in the SRH-1D simulations

	Average representative diameter (mm)								
	D10	D20	D30	D35	D40	D50	D65	D75	D90
Surface Layer									
Upstream of Dam	4.2	17.6	38.1	50.8	61.8	82.8	140.5	182.9	270.3
Downstream of Dam	1.4	23.3	50.4	64.7	77.0	107.9	163.4	207.3	284.3
Subsurface Layer									
Upstream of Dam	1.3	4.9	14.9	21.9	30.2	48.1	84.2	118.0	199.2
Downstream of Dam	0.8	6.5	25.3	33.3	48.4	75.2	132.4	184.4	261.5

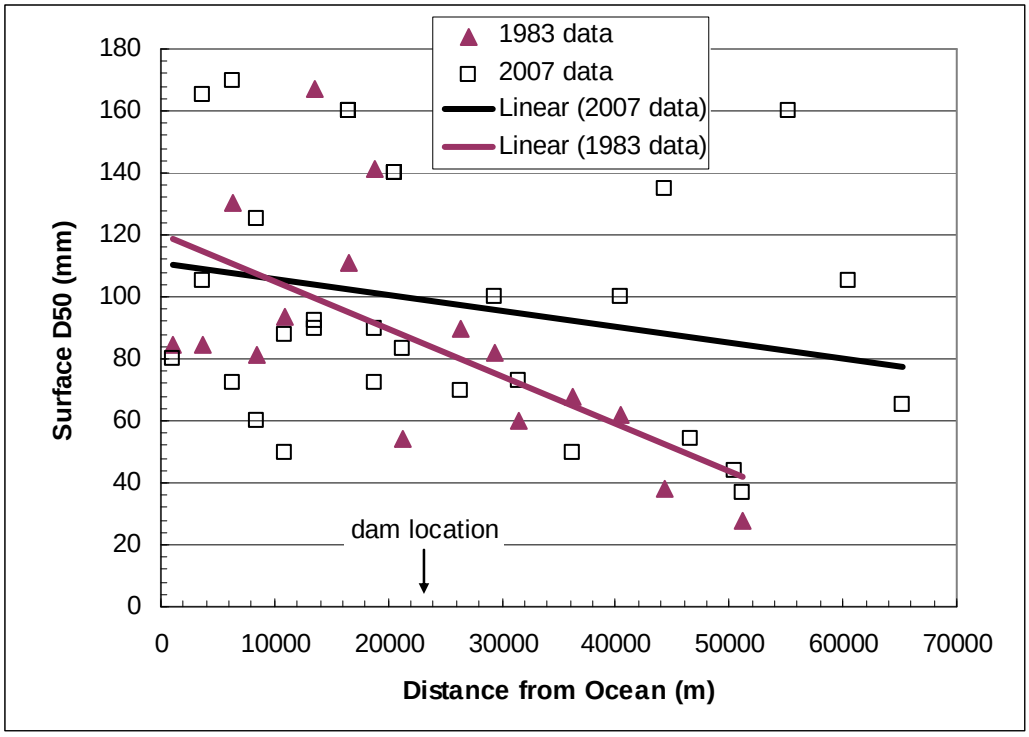

Figure 7. Measured D_{50} in Tachia River in 1983 and 2007. Linear fits to the data are shown.

2.3.11 Water Temperature

The water temperature assumed for all simulation was 20 degrees Celsius.

2.3.12 Erosion and Deposition Limits

There have been grade control structures built downstream of bridges at XC 30-1, 28-1D, 23-1D, and 19-1. There is also a water diversion at XC 32-1. These structures are represented in the model as fixed elevation locations. Some of these structures are destroyed during extreme events, but they still slow the erosion at these locations. The elevation of each structure was determined from the cross section surveys performed at the end of the simulations.

The rail bridge at XC 30-1 is shown in Figure 8. The picture was taken in 2007 and there is a noticeable drop in river bed downstream of the structure.

The Ho-Feng Bridge was destroyed by a flood in September 2008. A picture taken in November 2008 is shown in Figure 9. The cross sections measured in 2005 and 2008 just upstream and downstream of the bridge are shown in Figure 10 and Figure 11, respectively. There was approximately 3 m of erosion upstream of the bridge and 6 m of erosion downstream of the bridge. This indicates that the grade control structure downstream of the bridge was undermined by scour and then the grade control structure failed. The river then scoured around the bridge piers and caused some of them to fail.

Figure 8. Grade control downstream of bridge at XC 30-1

Figure 9. The Ho-Feng Bridge at XC 28-1, taken November 2008.

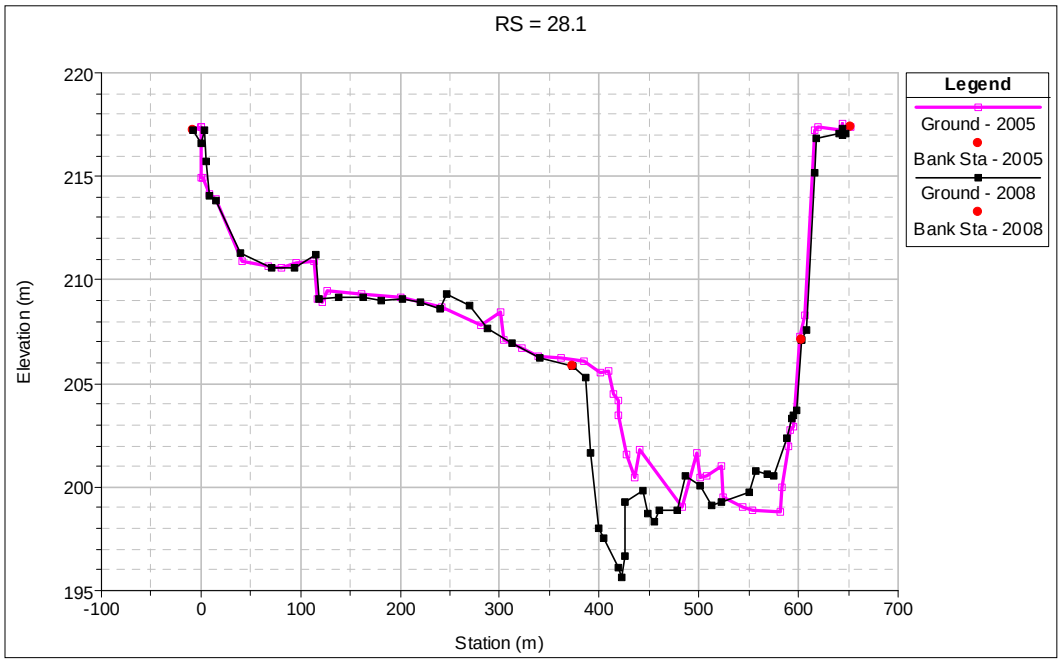

Figure 10. Cross sections measured in 2005 and 2008 just upstream of Ho-Feng Bridge at XC 28.1. Note that the minimum bed elevation decreased approximately 3 m.

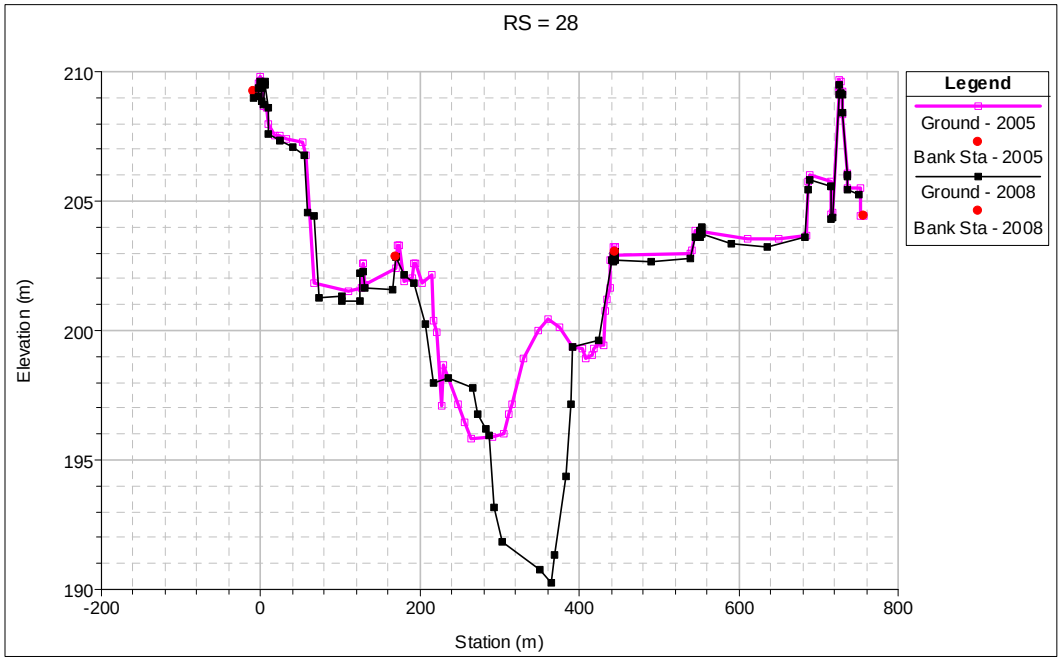

Figure 11. Cross sections measured in 2005 and 2008 just downstream of Ho-Feng Bridge at XC 28. Note that the minimum bed elevation decreased approximately 6 m.

Figure 12. Picture of Highway 1 Bridge looking downstream in December 2007 at XC 23-1.

2.3.13 Sediment Transport Parameters

Several different sediment transport formulas were used to predict the sediment transport capacities during the simulations. Wu et al. (2000) developed a non-uniform sediment transport formula for bedload and suspended load. Parker (1990) developed a transport bedload formula for mixed sized gravel sediment. Wilcock and Crowe (2003) developed a bedload formula for sand-gravel mixtures. Both Wilcock and Crowe (2003) and Parker (1990) must be combined with a suspended load formula to estimate total sediment load. Engelund-Hansen (1972) can be used to predict the suspended load in the system.

The best results from the calibration period were obtained using the bed load equation of Wu et al. (2000). Parker (1990) in combination with Engelund-Hansen also gave approximately similar results, but it was necessary to alter the reference shear stress to 0.045 from its default value of 0.0386.

The active layer thickness is set to 0.5 times the d_{max}, or approximately 0.18 m.

The bedload adaptation length was set to 20 times the local flow depth and the non-equilibrium suspended parameters were set to 0.25 for deposition and 1 for erosion. These are the default values used in SRH-1D. The value of the parameter controlling the transfer of material to the sublayer is set to 0.

Additional information on the sediment model parameters is given in the model sensitivity chapter.

2.3.14 Cohesive Sediment Transport Parameters

No cohesive sediment transport is simulated.

2.3.15 Bedrock Geometry and Parameters

There is noticeable bedrock present from Shih-Gang Dam to XC 32. Photographs of the bedrock are given in Figure 13, Figure 14 and Figure 17. The bedrock control stops between XC 32 and 31-1 (Figure 21). There is bedrock present at XC 32, but it is primarily alluvial at XC 31-1. The channel also expands at this point suggesting that horizontal bedrock control is also removed.

No survey that distinguishes the presence of bedrock from alluvial material has been conducted. Therefore, it is not possible to quantify how much erosion was due to the movement of alluvial sediment and how much was due to the erosion of bedrock. The bed rock just downstream of Shih-Gang Dam shows some evidence of bed rock erosion (Figure 13). Notice there is a low-flow channel formed through the bed rock. However, the erosion is only noticeable in a relatively small portion of the cross section. There is also evidence of bedrock erosion underneath the bridge at XC 35. A picture was taken in December 2007 and November 2008; see Figure 14 and Figure 15, respectively. The flows from the typhoon in September 2008 eroded a large portion of the right bank near the bridge.

Pictures looking downstream of the bridge are shown in Figure 17 and Figure 18. There was also significant scour between 2005 and 2008 downstream of the bridge at XC 34 to 32 (see Figure 19 and Figure 20). Most of that scour probably occurred during the typhoon of September 2008.

The data from bed geometry data form 2000, 2005 and 2008 was used to calibrate the bed rock scour parameters. The equation in SRH-1D used to compute bedrock scour is:

$$E = K_p U \left(\frac{\tau}{\tau_c} - 1 \right) \qquad (2.2)$$

where τ_c is the critical shear stress for bed-rock erosion and K_p is the non-dimensional erosion rate constant. These two parameters were calibrated based upon the observed erosion from 2000 to 2005 and from 2005 to 2008. The values of the critical shear stress for the two time periods were 200 and 150 Pa, respectively, while the values for the erosion rate constant was 1×10^{-6} and 1.25×10^{-6}. The value of the critical shear stress was decreased to reflect the weathering process of exposed bedrock that would tend to weaken the rock over time. Cycles of wetting and drying are expected to significantly weaken the rock and decrease its resistance to erosion. Field data would be necessary to verify that these are reasonable values. Also, the critical shear stress of exposed bedrock would need to be tested over a period of time to determine if the weathering process is important.

It is not possible to compare these values to other "typical" values for bedrock in Taiwan because this is one of the first applications of the bedrock component of SRH-1D and there is no case history on which to base values of the critical shear stress. It is expected that applications of the two-dimensional model may need to use different values of the critical shear stress and erosion rates. The shear stress computed in a 1D model is an average shear stress over a cross section while the shear stress in a 2D model is a shear stress averaged over a much smaller area and would be expected to be significantly different at a local scale.

Based upon measured critical shear stresses of cohesive soils (Hansen and Simon, 2001), the material would be classified as a resistant or very resistant cohesive soil. That classification seems appropriate based upon the fact that the "bedrock" downstream of Tachia is basically consolidated silt and clay material.

Figure 13. Photograph taken looking downstream from Shih-Gang Dam (XC 36) in December 2007.

Figure 14. Photograph taken looking upstream at bridge at XC 35 on December 2007.

Figure 15. Photograph taken from bridge at XC 35 looking upstream at Shih -Gang Dam on November 2008.

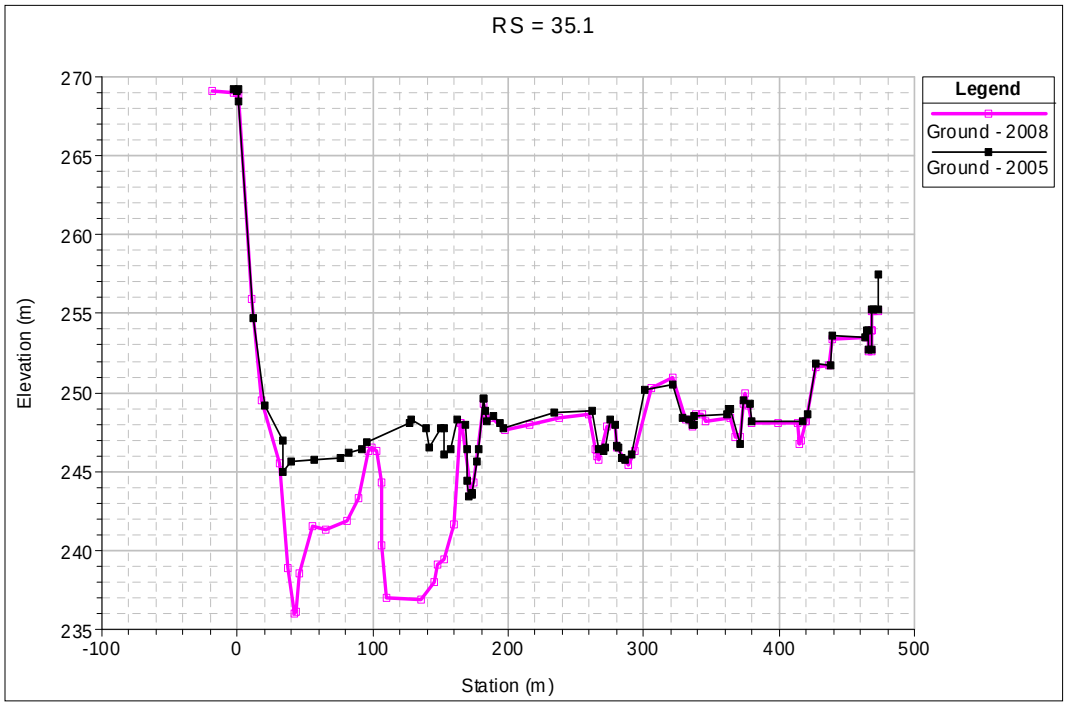

Figure 16. Cross section just upstream of bridge. There was approximately 9 m of scour along the left bank.

Figure 17. Photograph taken looking downstream from underneath the bridge at XC 35 on December 2007.

Figure 18. Picture taken from bridge at XC 35 looking downstream on November 2008.

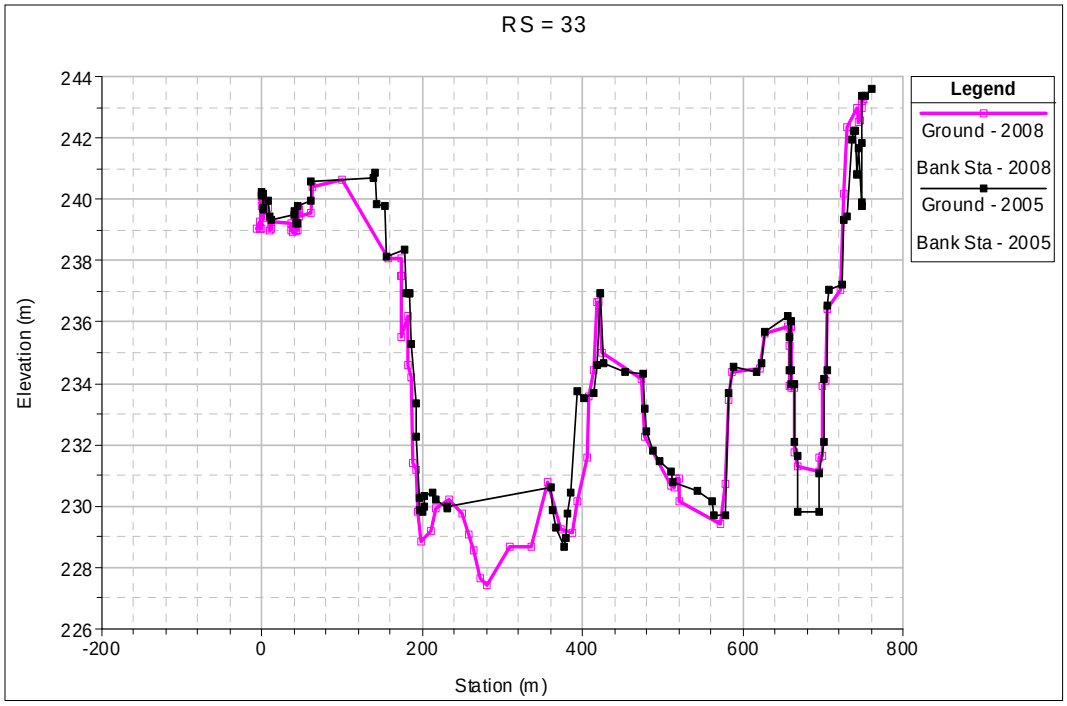

Figure 19. Cross section 33 survey data comparison where approximately 2 m of scour has occurred in the bed rock exposed reach.

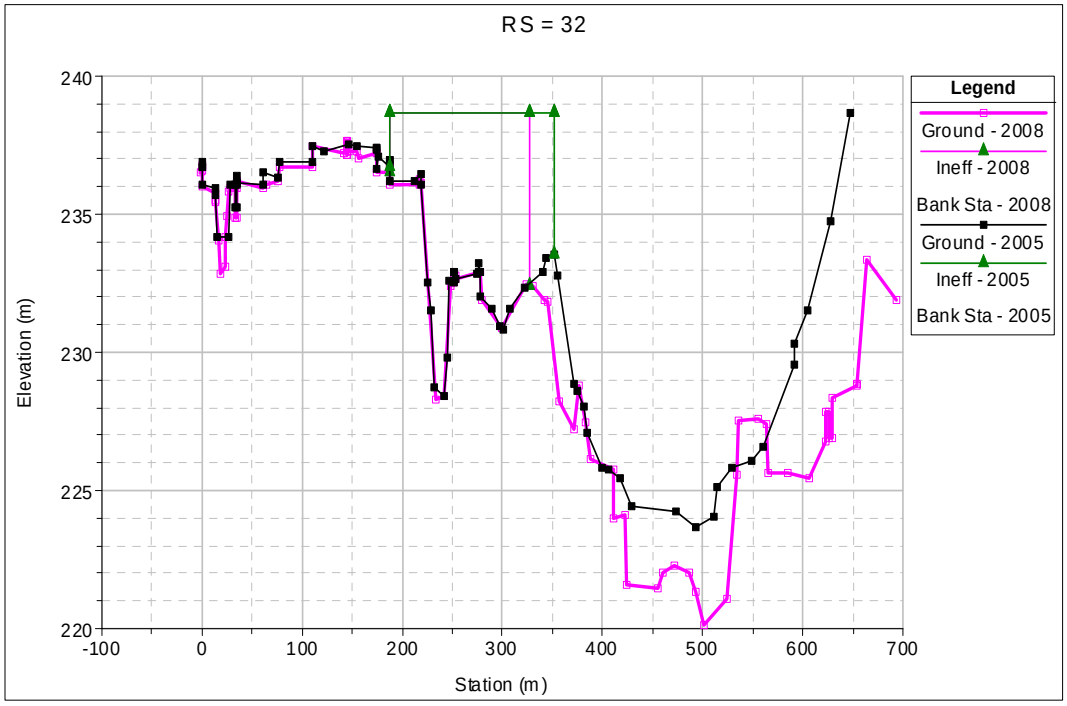

Figure 20. Cross section 32 near end of bedrock control where approximately 4 m of scour has occurred in the bed rock exposed reach.

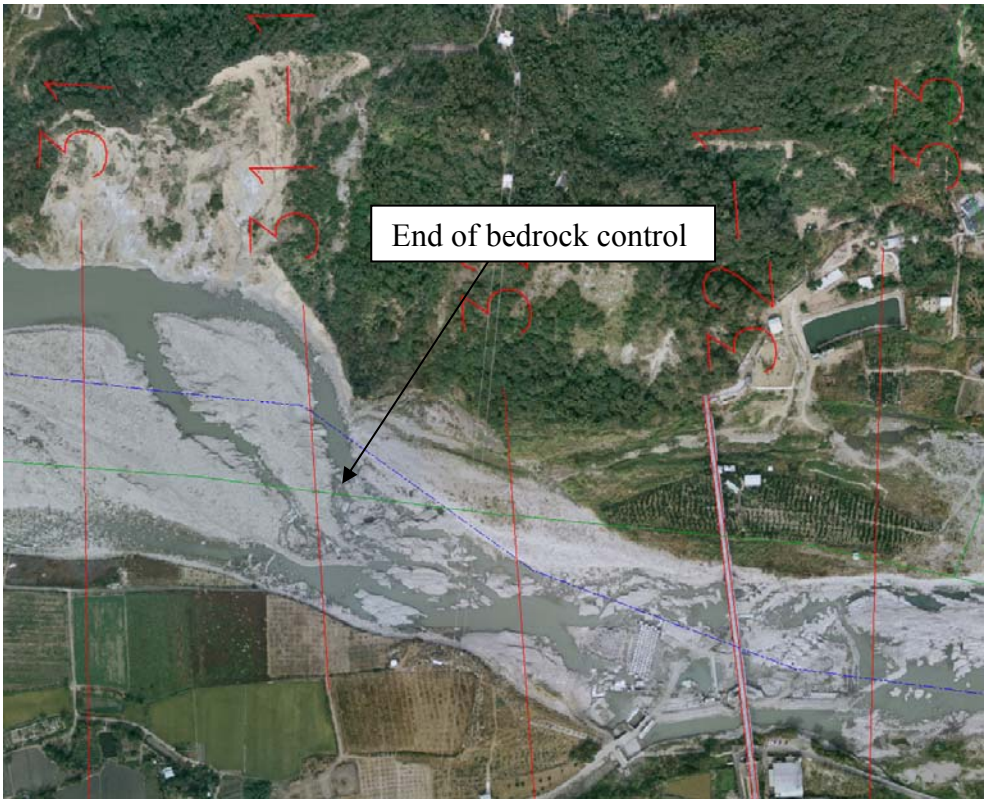

Figure 21. 2005 aerial photograph showing end of bedrock control between XC 32 and 31-1.

2.4 2000 to 2005 Simulation Results

The cross section survey data from 2005 was used to compare against the model results. Volumes of erosion and deposition were estimated by computing the average bed change from the 2000 to 2005 cross sections data then multiplying the average bed change by the width of the active cross section and the distance between cross sections. The plot of cumulative deposition downstream of Shih-Gang Dam is shown in Figure 22. The deposition in the cross section is added to the total deposition of the cross sections upstream of it to obtain the cumulative deposition. SRH-1D simulated both the location and general magnitudes of erosion and deposition in the river. The agreement between model and measured data is considered remarkable considering the relatively few cross sections that were surveyed.

The deposition at each individual cross section is shown in Figure 23. The agreement on a cross section by cross section basis is not as good. It is expected that the 1D model is most appropriately applied over a group of cross sections.

Approximately 0.3 million cubic meters of bed rock erosion was simulated from the dam to XC 34. Based upon the cross section measurements there was approximately 0.3 million cubic meters of erosion. However, it is not clear how much of this was bed rock erosion and how much was sediment.

The simulated and measured minimum bed elevations are shown in Figure 24. The general trends are modeled correctly, but a noticeable discrepancy occurs at XC 23 and 31. These XC are downstream of grade controls and had large volumes of erosion. However, the model assumed this erosion was primarily vertical, where in reality, a significant amount of erosion occurred laterally in the cross sections. The cross section comparisons are given in Figure 25. Note that in XC 23 and 31 there is a significant amount of lateral erosion. The model was able to simulate the volume of erosion correctly, but could not simulate increase in width. The model is considered more reliable in computing the erosion and deposition volumes than the magnitude of the minimum channel elevations. Said another way, SRH-1D will predict the change to the average bed elevation more accurately than the change to the minimum bed elevation.

The results from the model study are promising and the model was able to reproduce the volume of sediment erosion and deposition over the reach rather accurately. The specific changes in a given cross section geometry were modeled less accurately. The one-dimensional model is able to simulate whether a reach will erode or aggrade, but it is not able to simulate whether that change is lateral or vertical and it cannot model channel avulsions.

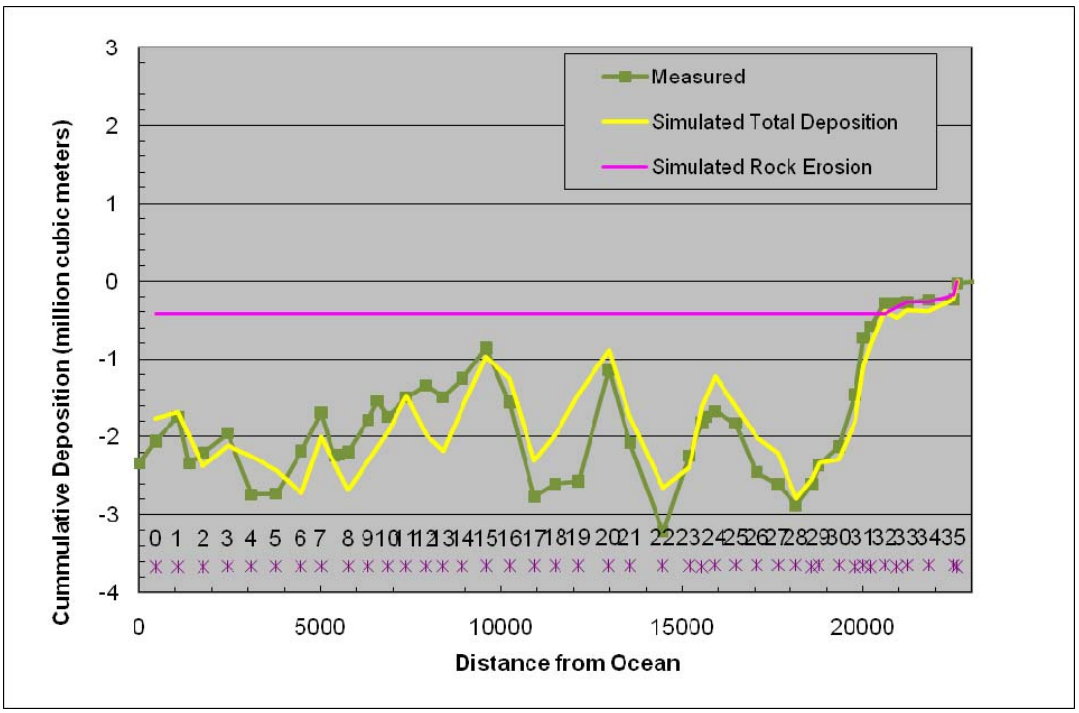

Figure 22. Comparison between measured and simulated cumulative deposition downstream of Shih-Gang Dam

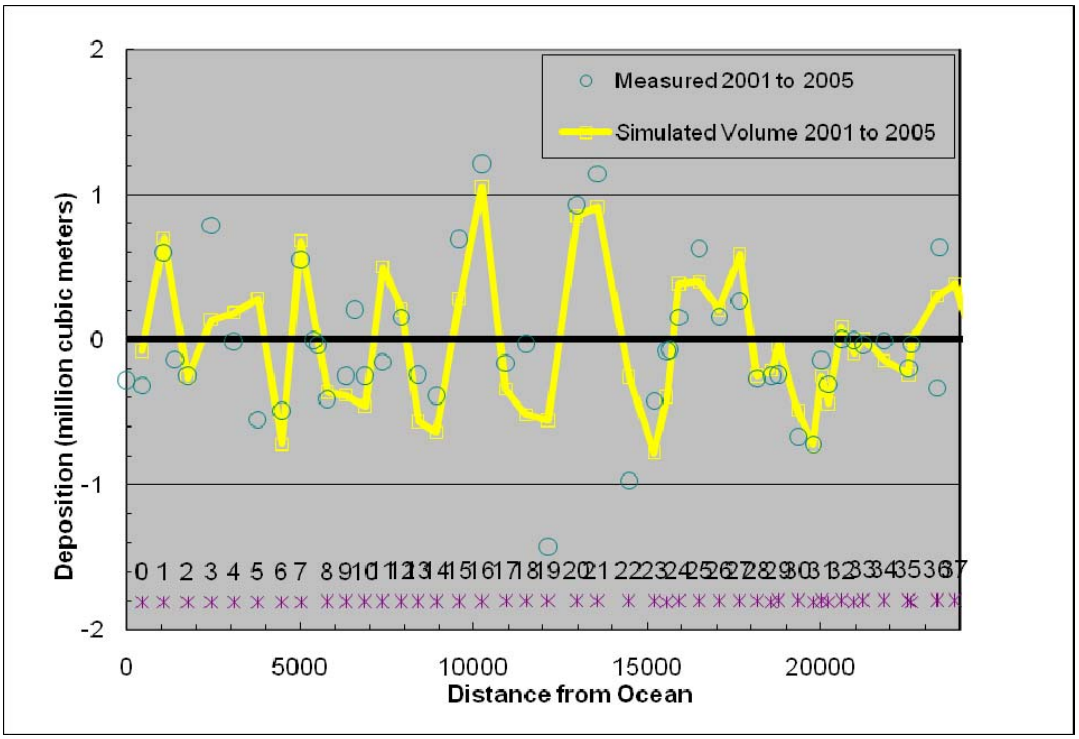

Figure 23. Comparison between measured and simulated deposition volumes downstream of Shih-Gang Dam for each individual XC (labels shown with purple x along bottom).

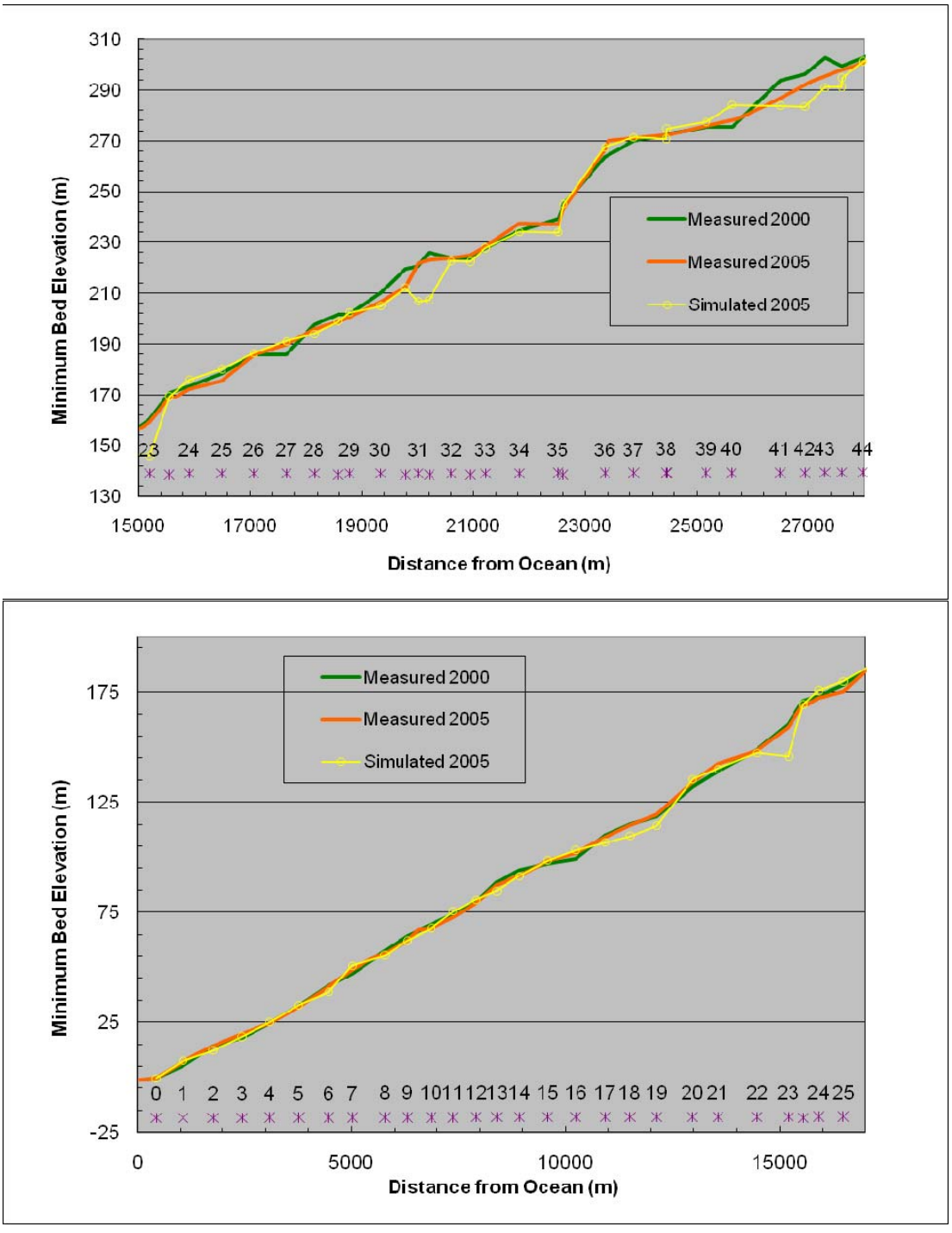

Figure 24. Comparison between measured and simulated minimum bed elevations (labels shown with purple x along bottom).

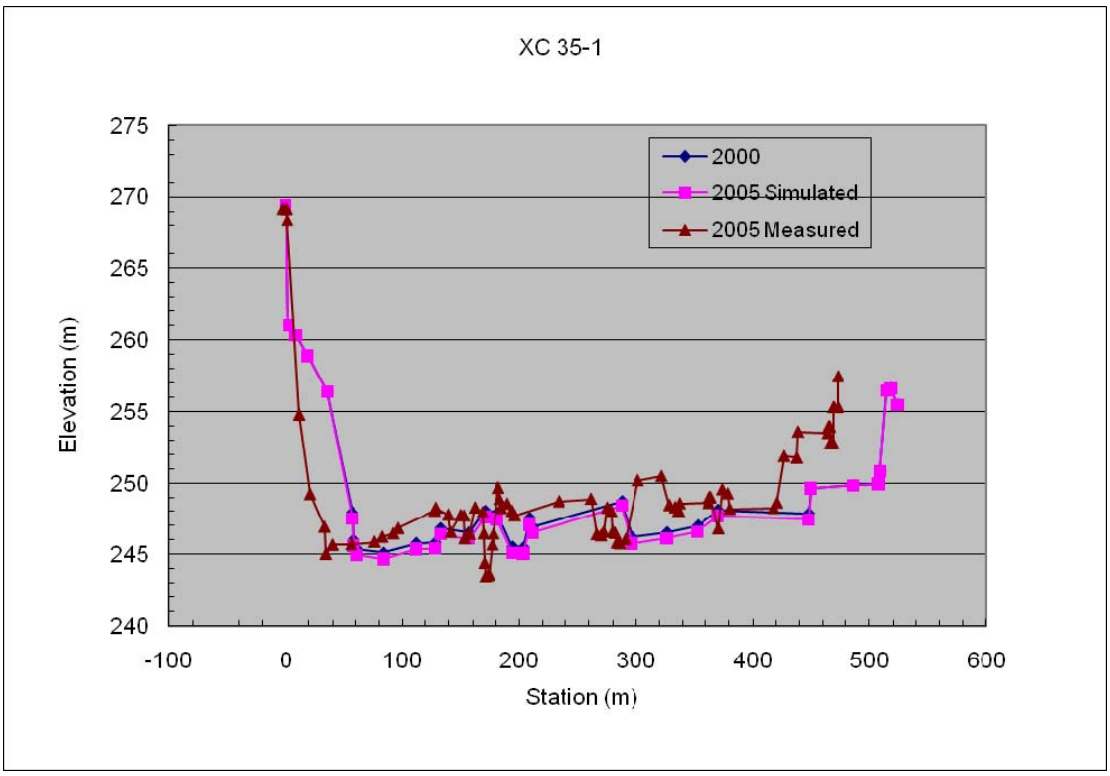
XC 35-1
2000
2005 Simulated
2005 Measured
Elevation (m)
Station (m)
275
270
265
260
255
250
245
240
-100
0
100
200
300
400
500
600

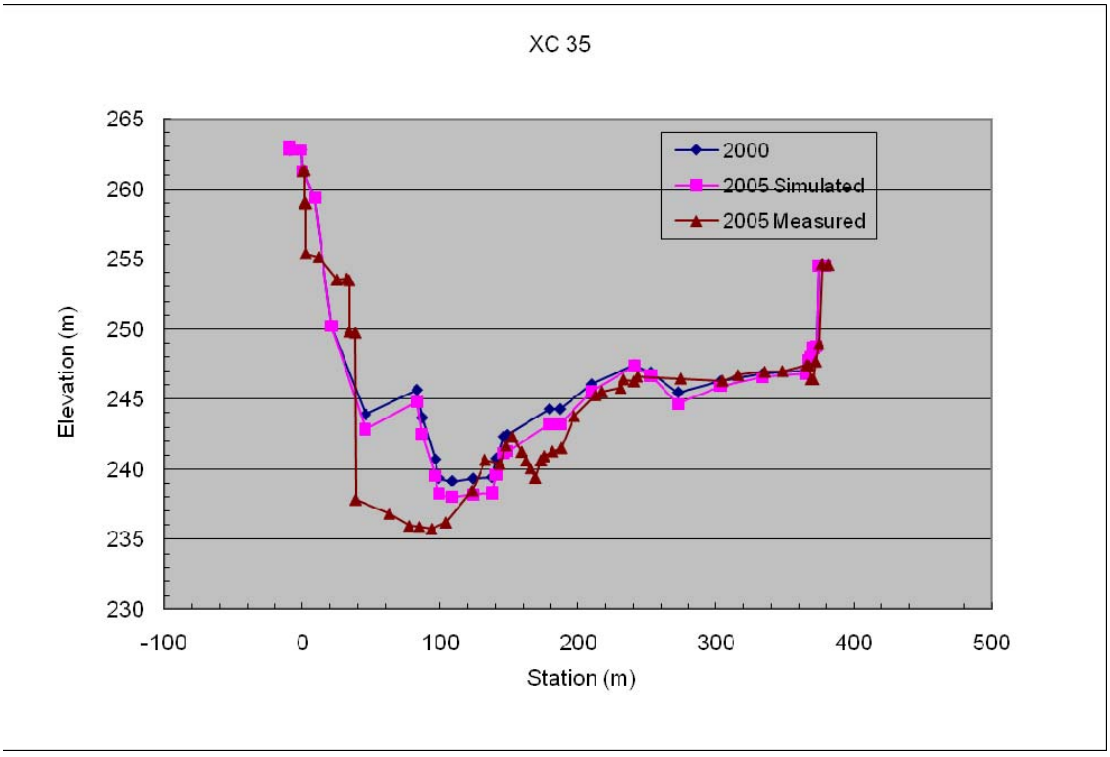
XC 35
2000
2005 Simulated
2005 Measured
Elevation (m)
Station (m)
265
260
255
250
245
240
235
230
-100
0
100
200
300
400
500

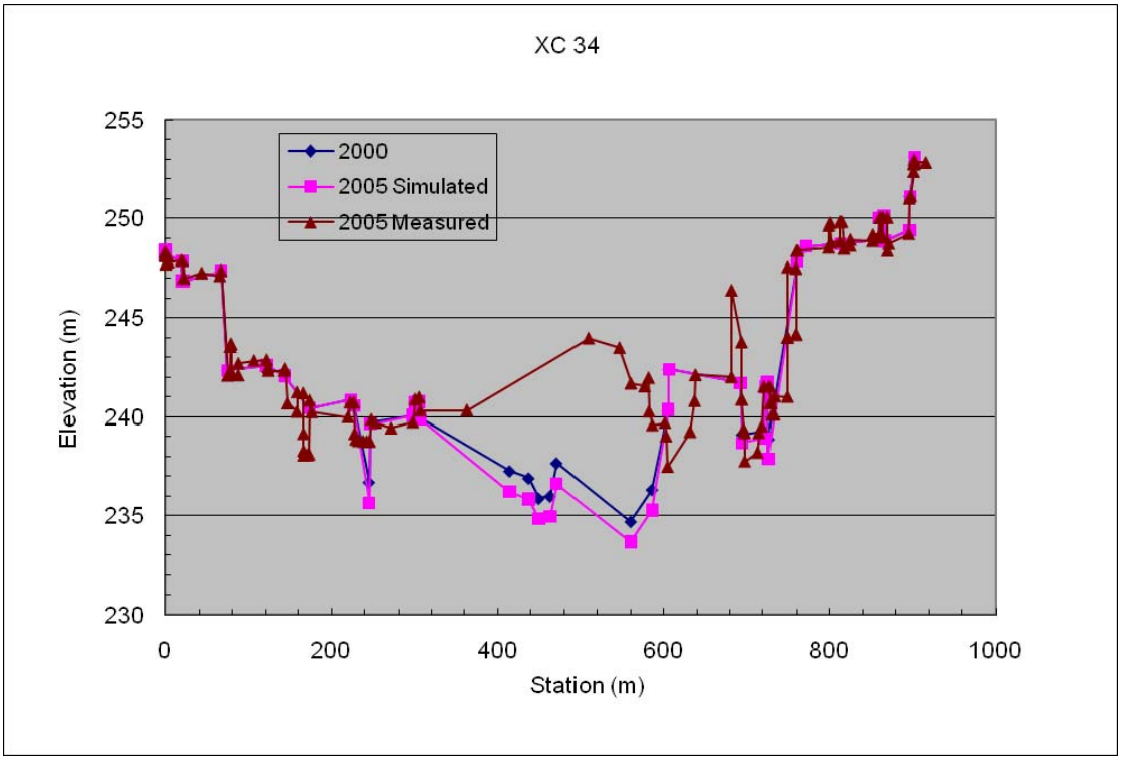
XC 34
2000
2005 Simulated
2005 Measured
Elevation (m)
255
250
245
240
235
230
0
200
400
600
800
1000
Station (m)

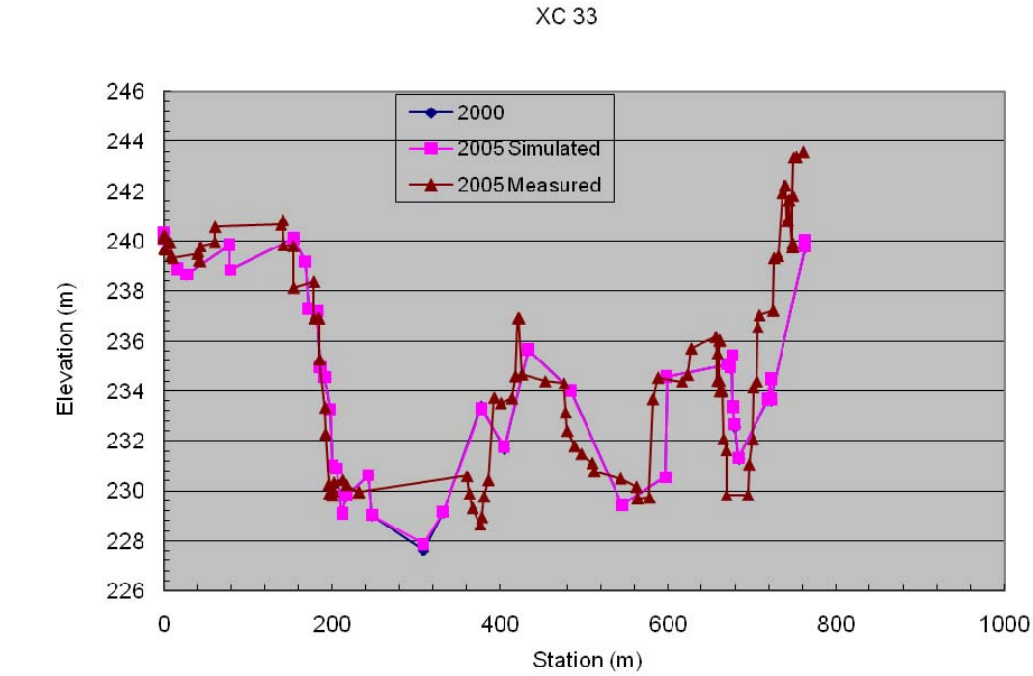
XC 33
2000
2005 Simulated
2005 Measured
Elevation (m)
246
244
242
240
238
236
234
232
230
228
226
0
200
400
600
800
1000
Station (m)

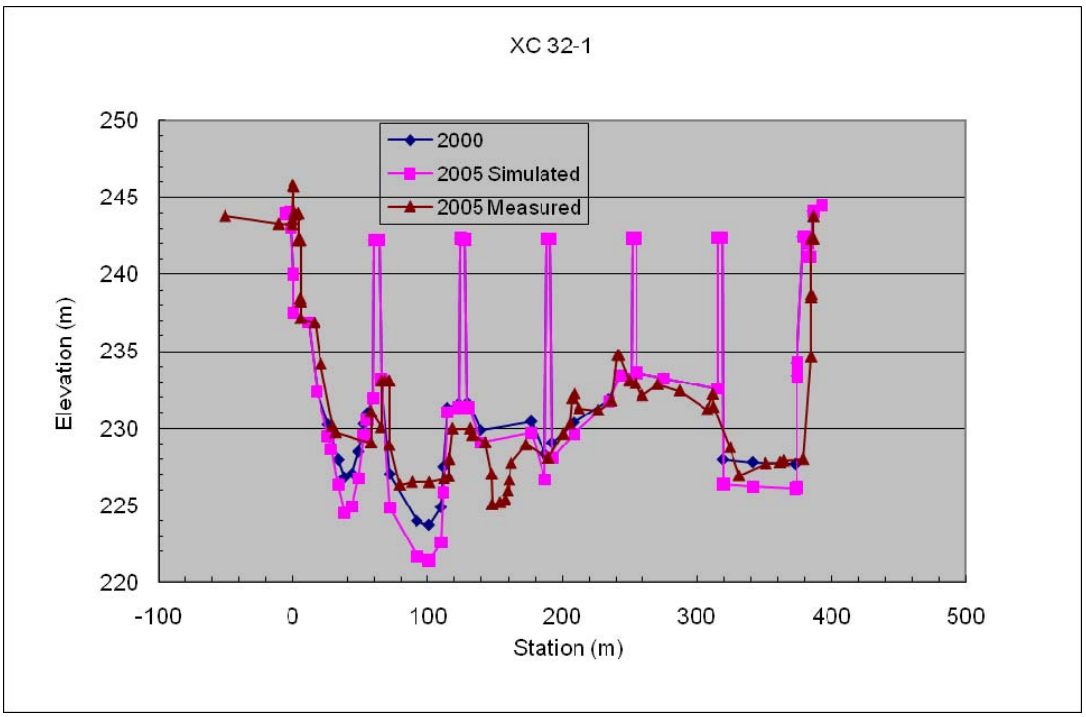
XC 32-1
2000
2005 Simulated
2005 Measured
Elevation (m)
Station (m)
250
245
240
235
230
225
220
-100
0
100
200
300
400
500

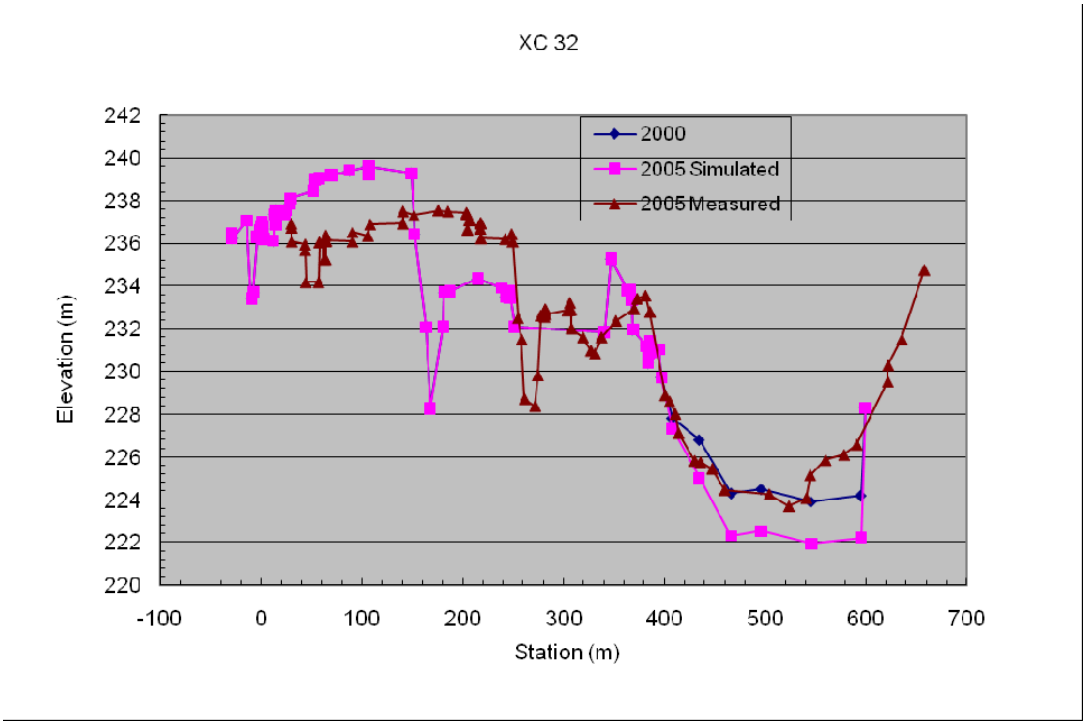
XC 32
2000
2005 Simulated
2005 Measured
Elevation (m)
Station (m)
242
240
238
236
234
232
230
228
226
224
222
220
-100
0
100
200
300
400
500
600
700

XC 31-1

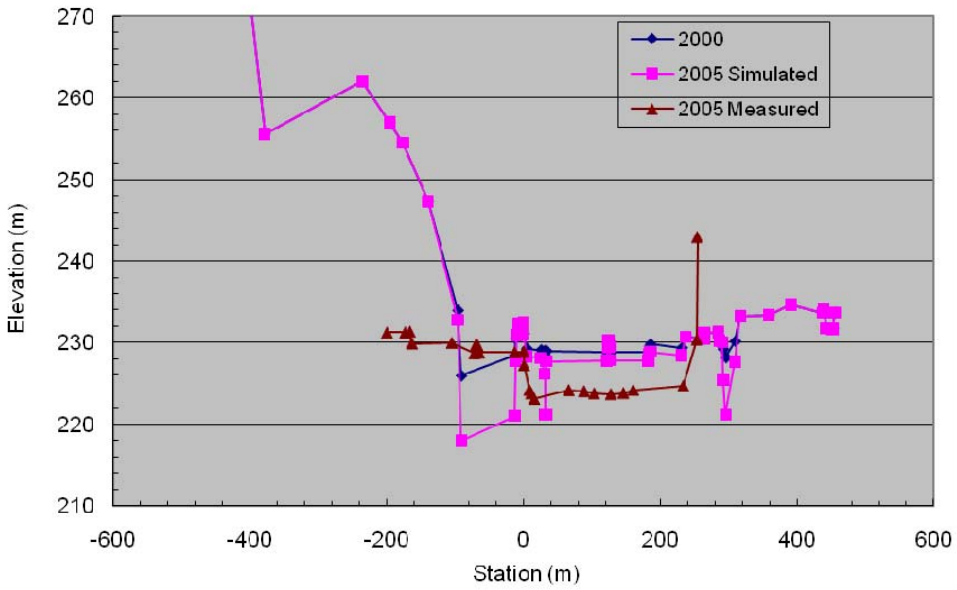
2000
2005 Simulated
2005 Measured
Elevation (m)
270
260
250
240
230
220
210
-600
-400
-200
0
200
400
600
Station (m)

XC 31

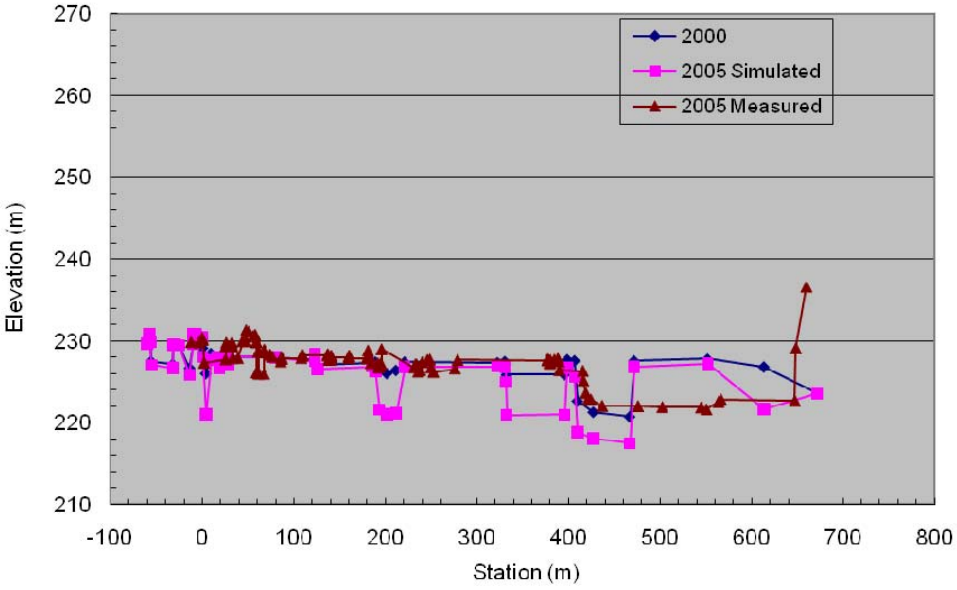
2000
2005 Simulated
2005 Measured
Elevation (m)
270
260
250
240
230
220
210
-100
0
100
200
300
400
500
600
700
800
Station (m)

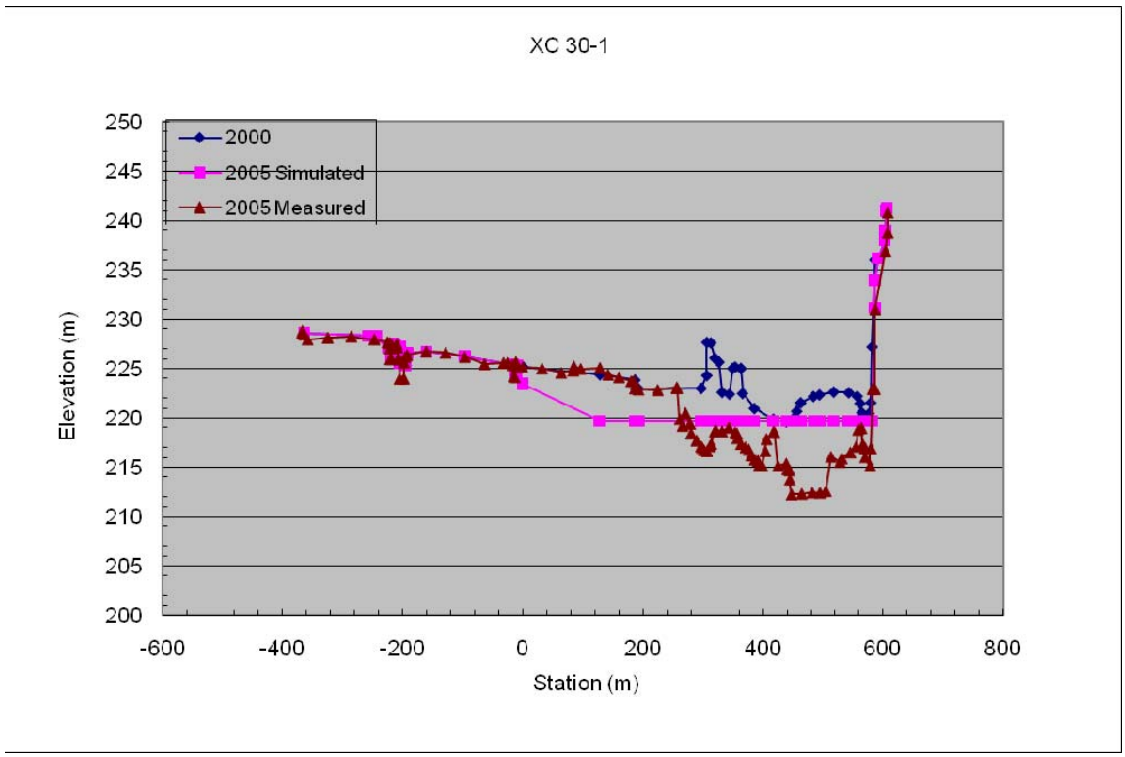
XC 30-1
2000
2005 Simulated
2005 Measured
Elevation (m)
250
245
240
235
230
225
220
215
210
205
200
-600
-400
-200
0
200
400
600
800
Station (m)

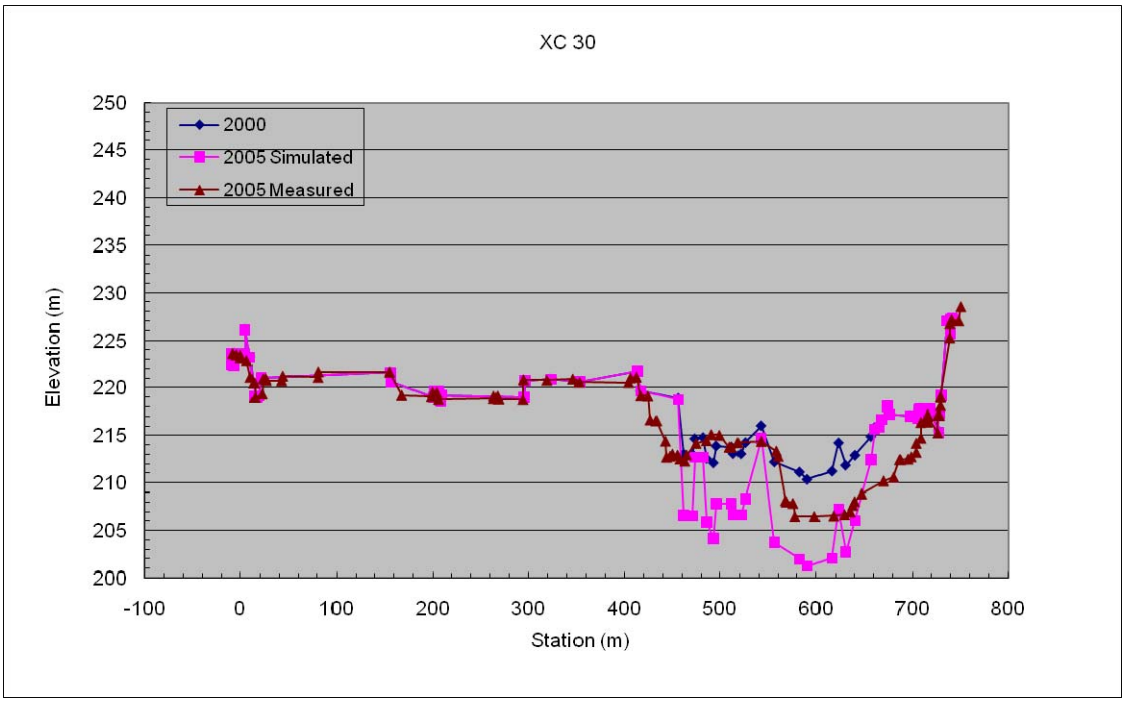
XC 30
2000
2005 Simulated
2005 Measured
Elevation (m)
250
245
240
235
230
225
220
215
210
205
200
-100
0
100
200
300
400
500
600
700
800
Station (m)

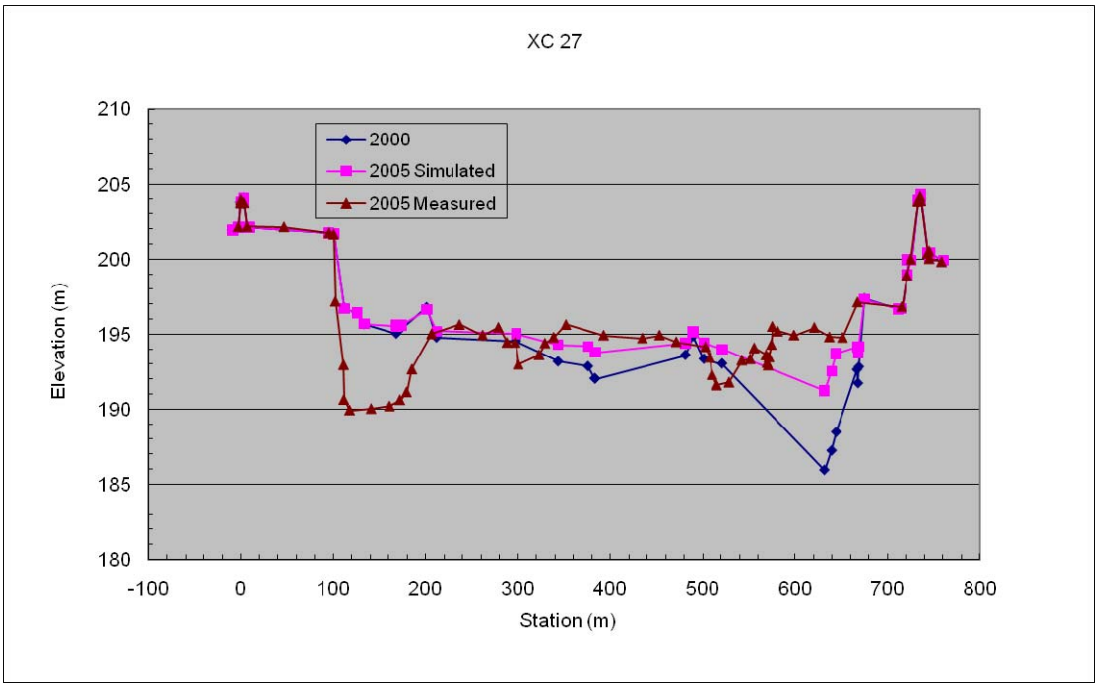
XC 27
2000
2005 Simulated
2005 Measured
Elevation (m)
Station (m)
210
205
200
195
190
185
180
-100
0
100
200
300
400
500
600
700
800

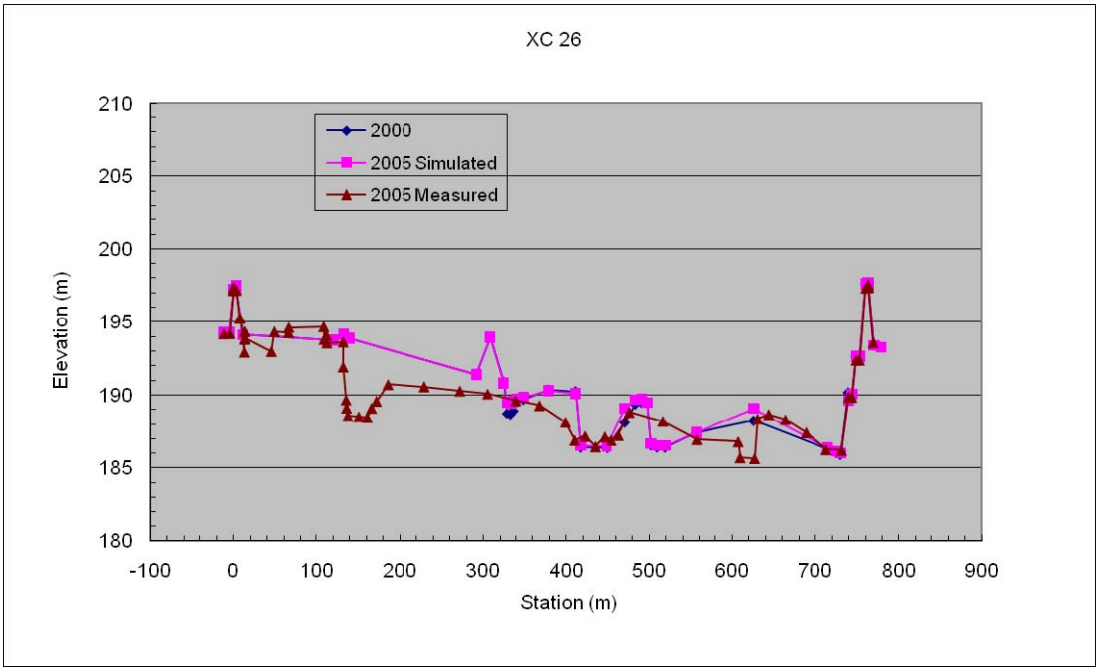
XC 26
2000
2005 Simulated
2005 Measured
Elevation (m)
Station (m)
210
205
200
195
190
185
180
-100
0
100
200
300
400
500
600
700
800
900

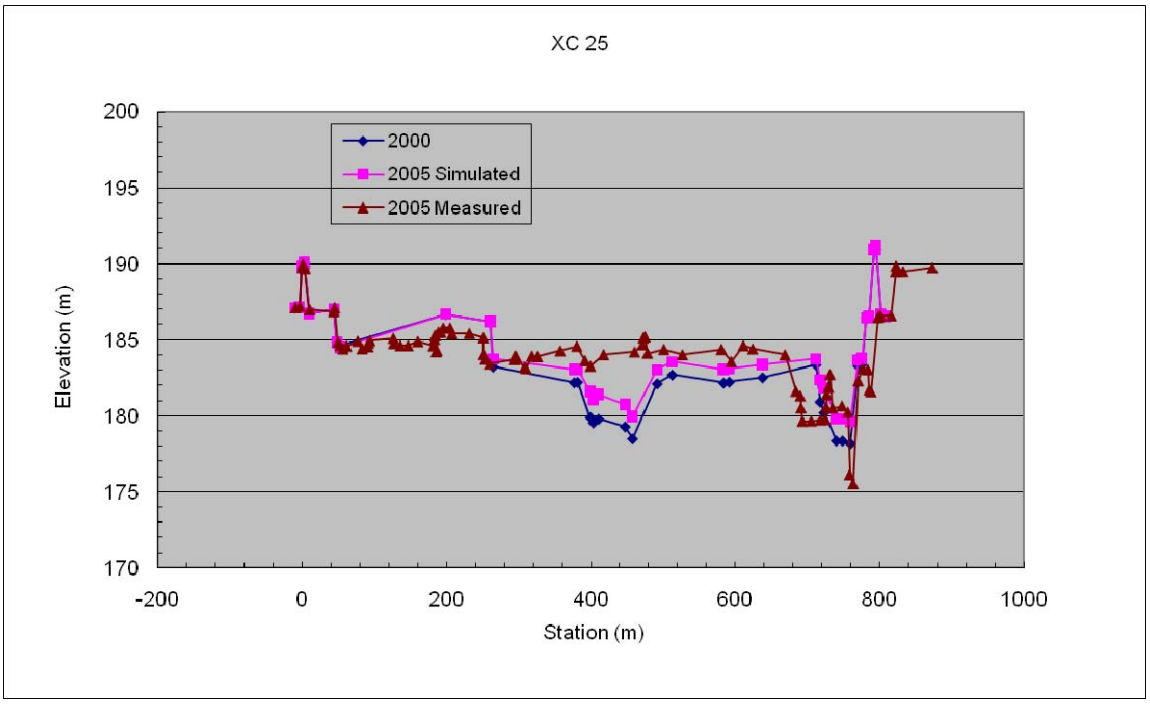
XC 25
2000
2005 Simulated
2005 Measured
Elevation (m)
Station (m)
200
195
190
185
180
175
170
-200
0
200
400
600
800
1000

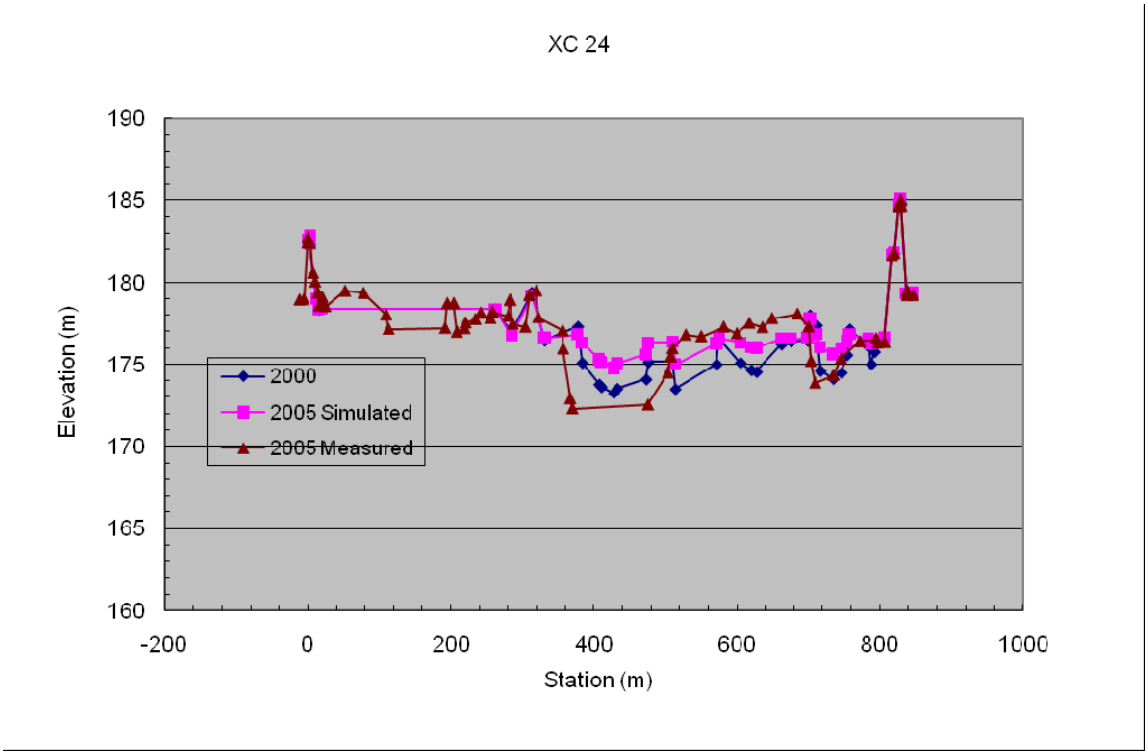
XC 24
2000
2005 Simulated
2005 Measured
Elevation (m)
Station (m)
190
185
180
175
170
165
160
-200
0
200
400
600
800
1000

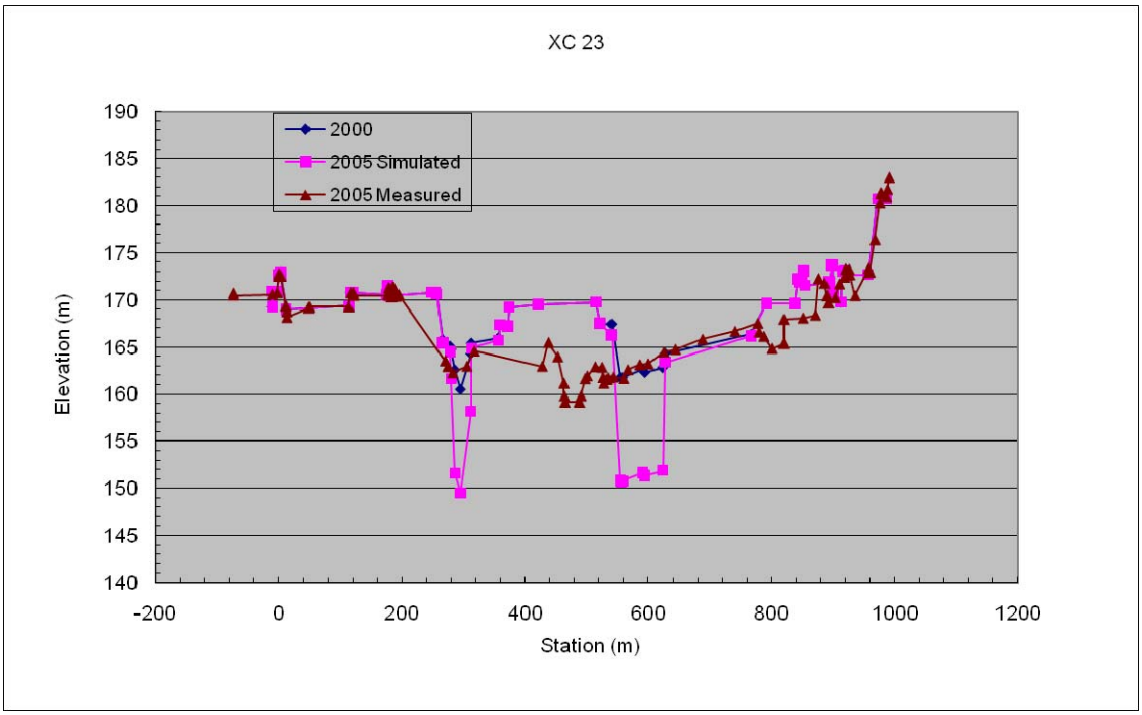
XC 23
2000
2005 Simulated
2005 Measured
Elevation (m)
190
185
180
175
170
165
160
155
150
145
140
-200
0
200
400
600
800
1000
1200
Station (m)

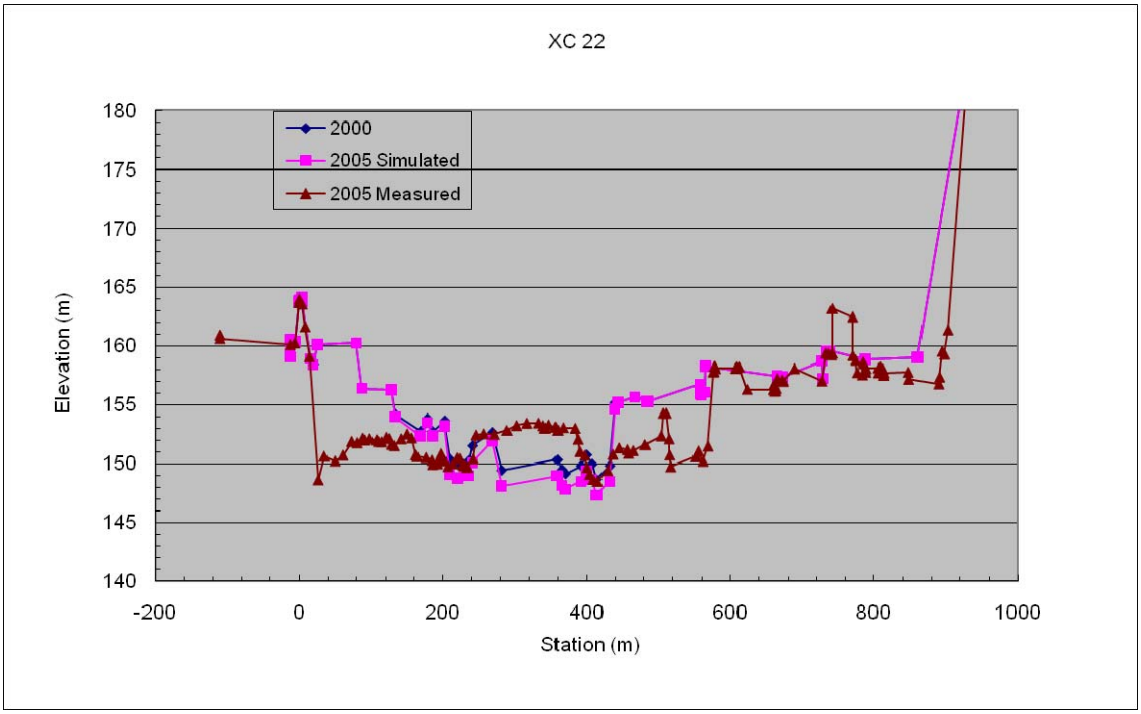
XC 22
2000
2005 Simulated
2005 Measured
Elevation (m)
180
175
170
165
160
155
150
145
140
-200
0
200
400
600
800
1000
Station (m)

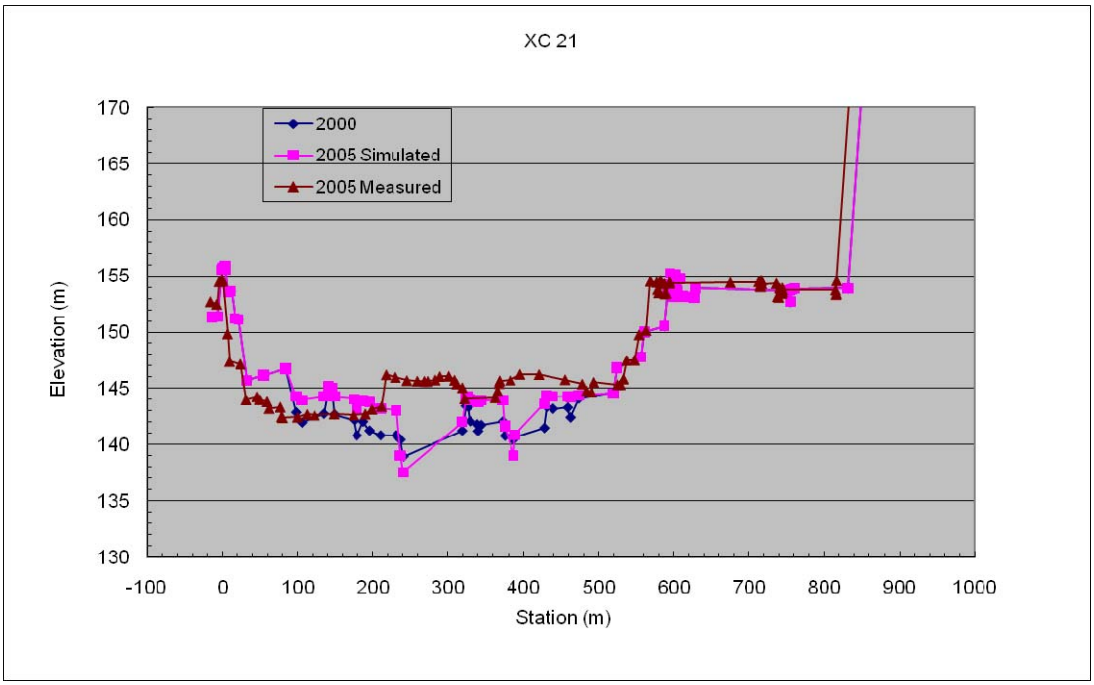
XC 21
2000
2005 Simulated
2005 Measured
Elevation (m)
170
165
160
155
150
145
140
135
130
-100
0
100
200
300
400
500
600
700
800
900
1000
Station (m)

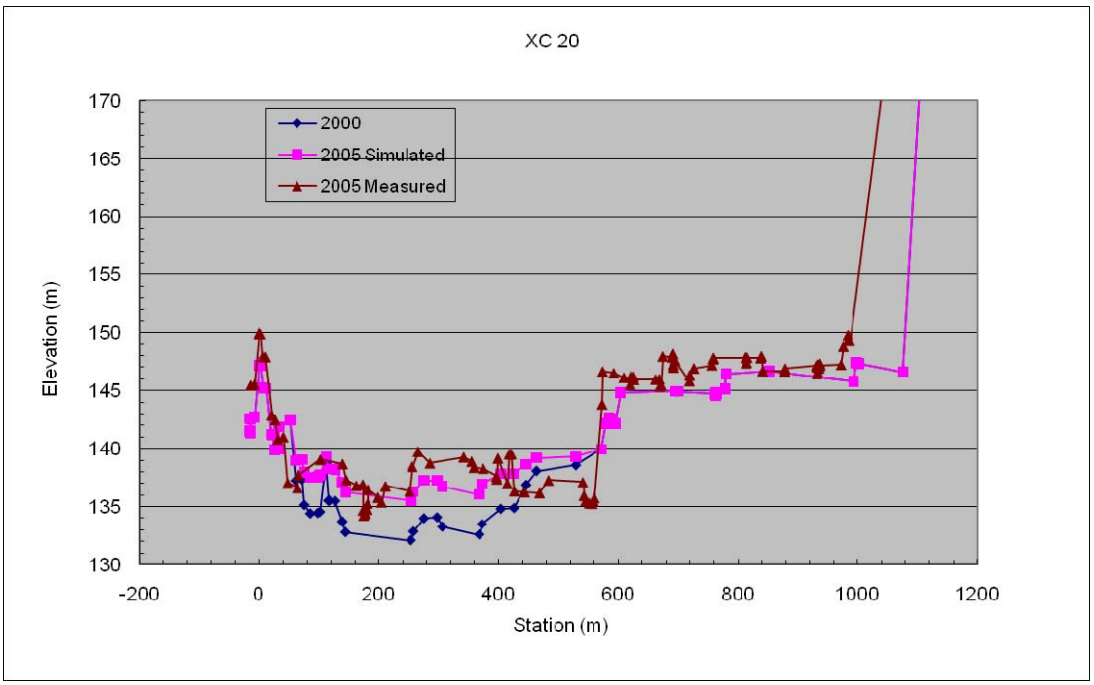
XC 20
2000
2005 Simulated
2005 Measured
Elevation (m)
170
165
160
155
150
145
140
135
130
-200
0
200
400
600
800
1000
1200
Station (m)

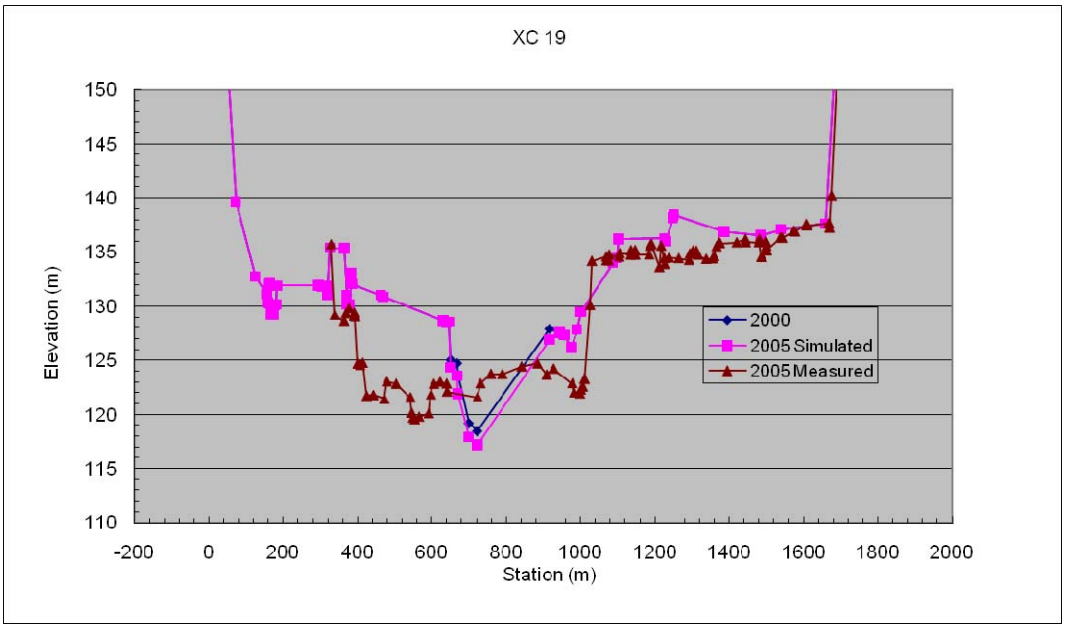
XC 19
Elevation (m)
150
145
140
135
130
125
120
115
110
-200
0
200
400
600
800
1000
1200
1400
1600
1800
2000
Station (m)
2000
2005 Simulated
2005 Measured

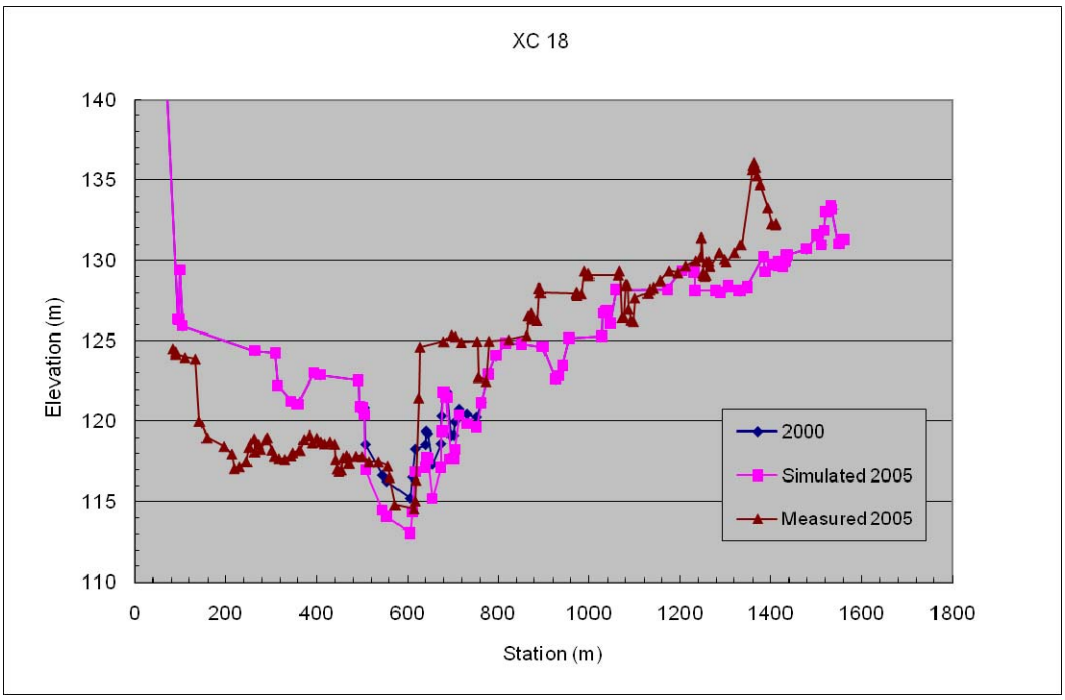
XC 18
Elevation (m)
140
135
130
125
120
115
110
0
200
400
600
800
1000
1200
1400
1600
1800
Station (m)
2000
Simulated 2005
Measured 2005

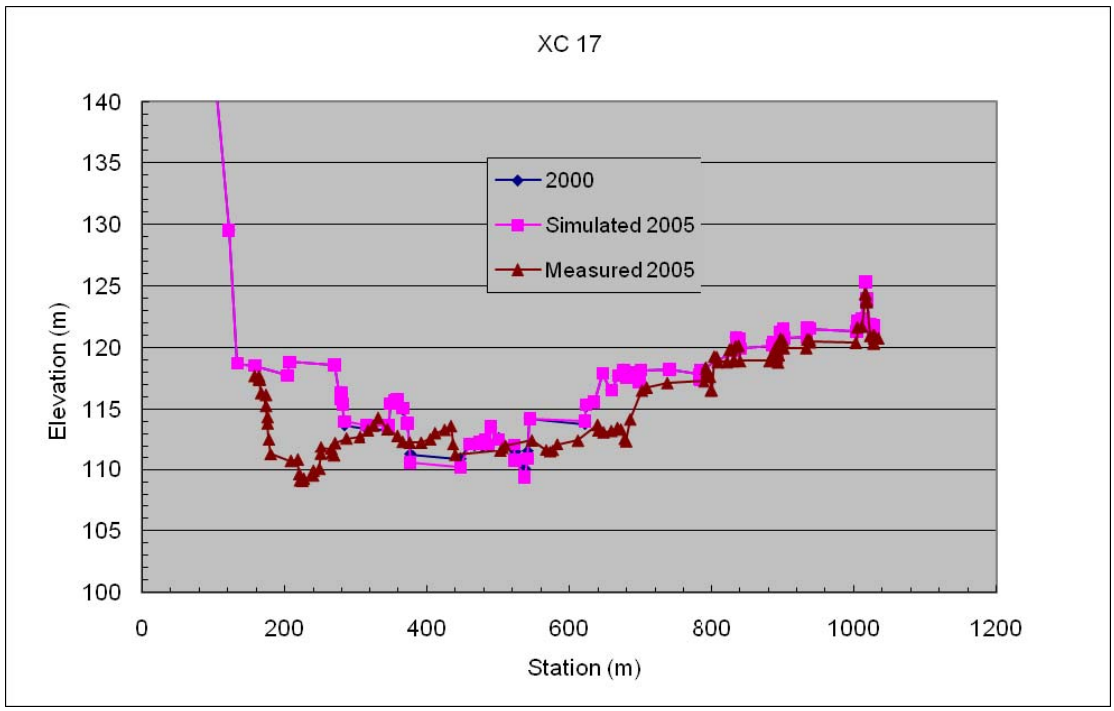
XC 17
140
135
130
125
120
115
110
105
100
Elevation (m)
0
200
400
600
800
1000
1200
Station (m)
2000
Simulated 2005
Measured 2005

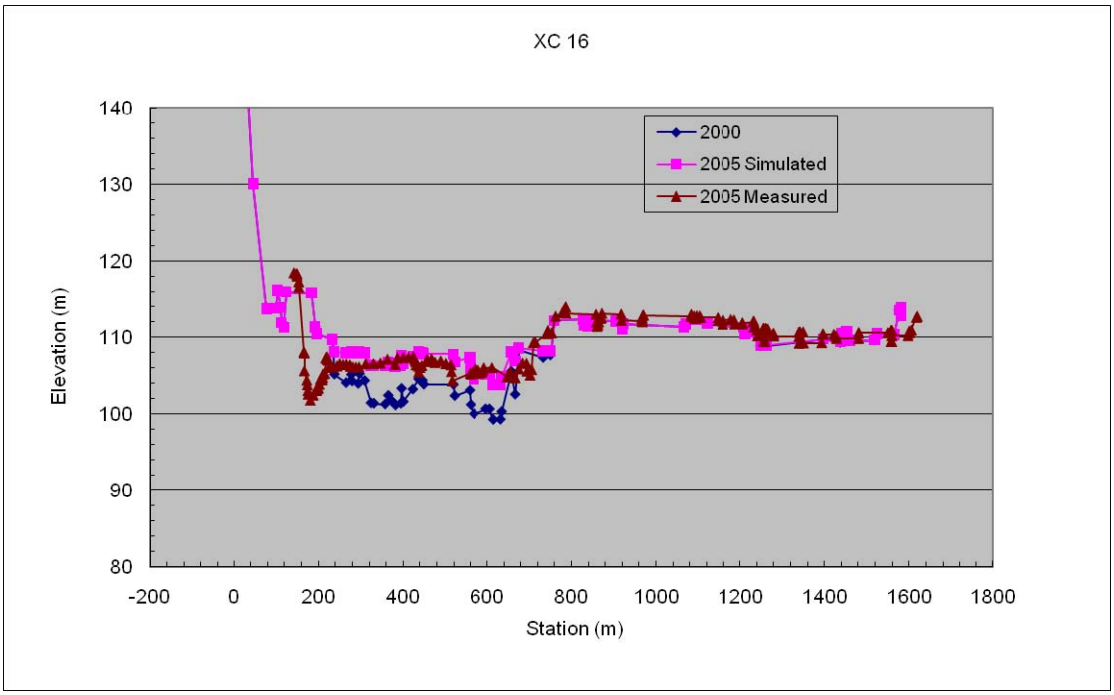
XC 16
140
130
120
110
100
90
80
Elevation (m)
-200
0
200
400
600
800
1000
1200
1400
1600
1800
Station (m)
2000
2005 Simulated
2005 Measured

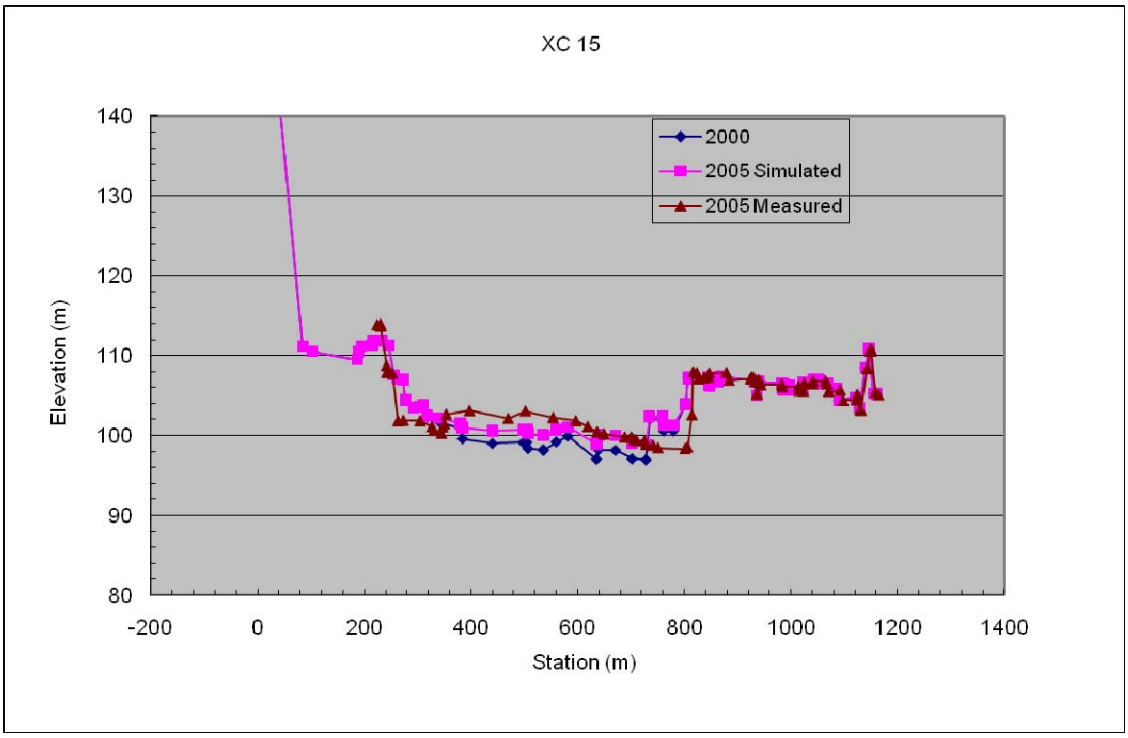

Figure 25. XC comparisons between measured and simulated bed elevations.

2.5 Sensitivity Study

Several model parameter sensitivity studies were conducted to ensure that the model is not overly sensitive to small changes in parameter values. This sensitivity study should be extended if the SRH-1D results are used to provide data for design purposes. For example, if SRH-1D results are used to design scour depth of bridge piers or levees, a more rigorous uncertainty analysis is recommended where model parameters are systematically varied over probable ranges of values to determine the uncertainty of the future predictions.

The most sensitive model parameters are discussed here. The typical range of parameter values are also discussed.

2.5.1 Reference Shear Stress

Both an increase and decrease in reference shear stress was simulated (Figure 26). The base value of the reference shear stress was 0.03, and the reference shear stress typically varies between 0.02 to 0.06 (Buffington and Montgomery, 1997)

Increasing the reference shear stress to 0.036 decreased the amount of erosion downstream of the dam. Decreasing the reference shear stress to 0.024 increased the erosion downstream of the dam. The trends of erosion and deposition remain relatively consistent regardless of the reference shear stress.

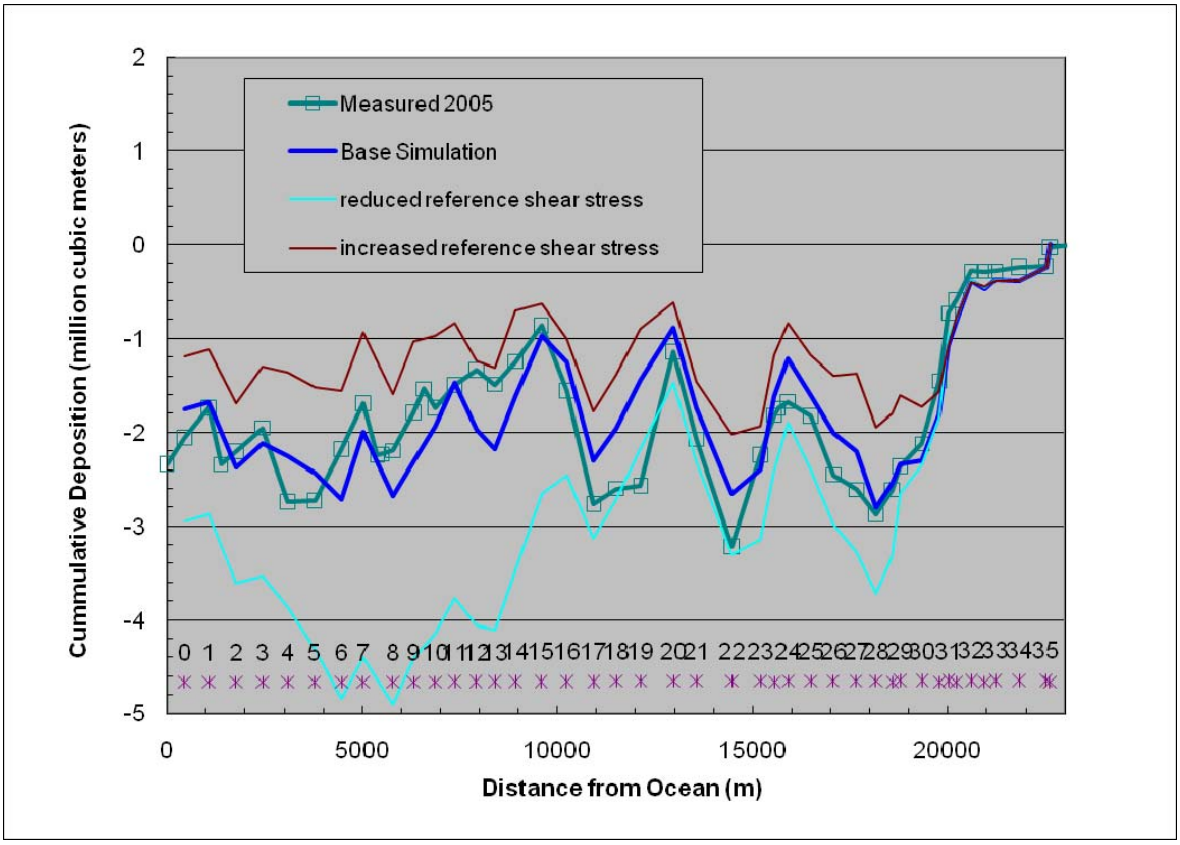

Figure 26. Sensitivity of model results to changes in reference shear stress.

2.5.2 Active Layer Thickness

The base active layer thickness for the simulations was 0.5 * the maximum size class simulated or 0.18 m. Based upon the developer's experience, typical values of the active layer in rivers where the bed material is gravel sized or larger vary between 0.5 to 2 d_{max}, where $\underline{d}_{max}$ is the diameter of the largest size class present in the bed. To study the sensitivity of the model to this parameter, the active layer thickness was reduced by half to 0.09 m and increased by a factor of two to 0.36 m. The decrease or increase in active layer had little effect on the amount of erosion downstream of the dam (Figure 27). Increasing the active layer thickness resulted in slightly more erosion downstream of the dam and reducing the active layer thickness resulted in slightly less erosion downstream of the dam.

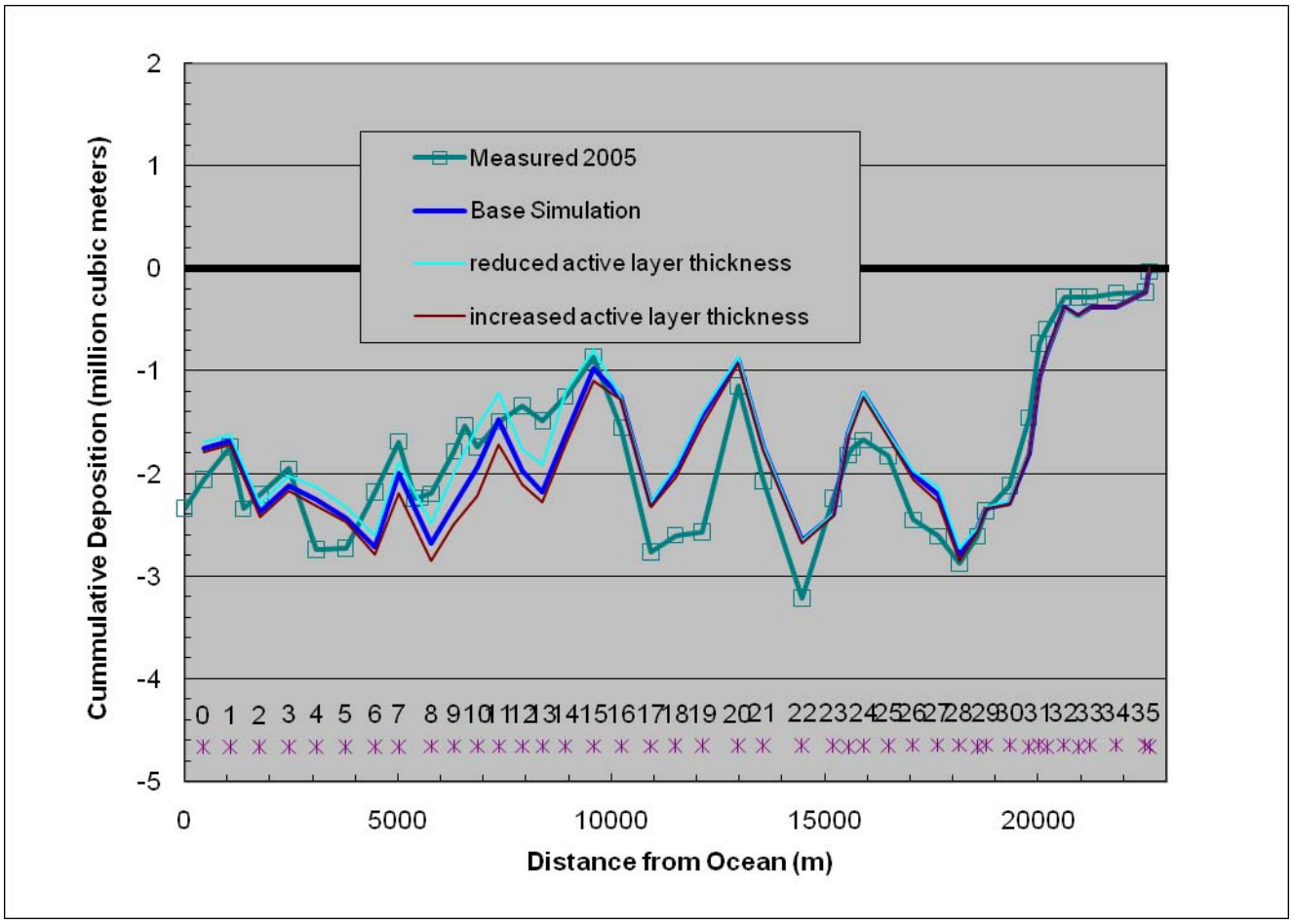

Figure 27. Sensitivity of model to reducing the active layer thickness

2.5.3 Transport Formula

The base simulation used the Wu et al. (2000) sediment transport formula. For sensitivity testing, both the Wilcock and Crowe (2003) and the Parker (1990)

(Figure 28). The trends in erosion and deposition were consistent between all the formulas. However, Parker underestimated the volume of erosion in the reach from XC 32 to XC 28. Wilcock and Crowe predicted results very similar to Wu et al. with slightly more erosion predicted in the reach between XC 15 to XC 7.

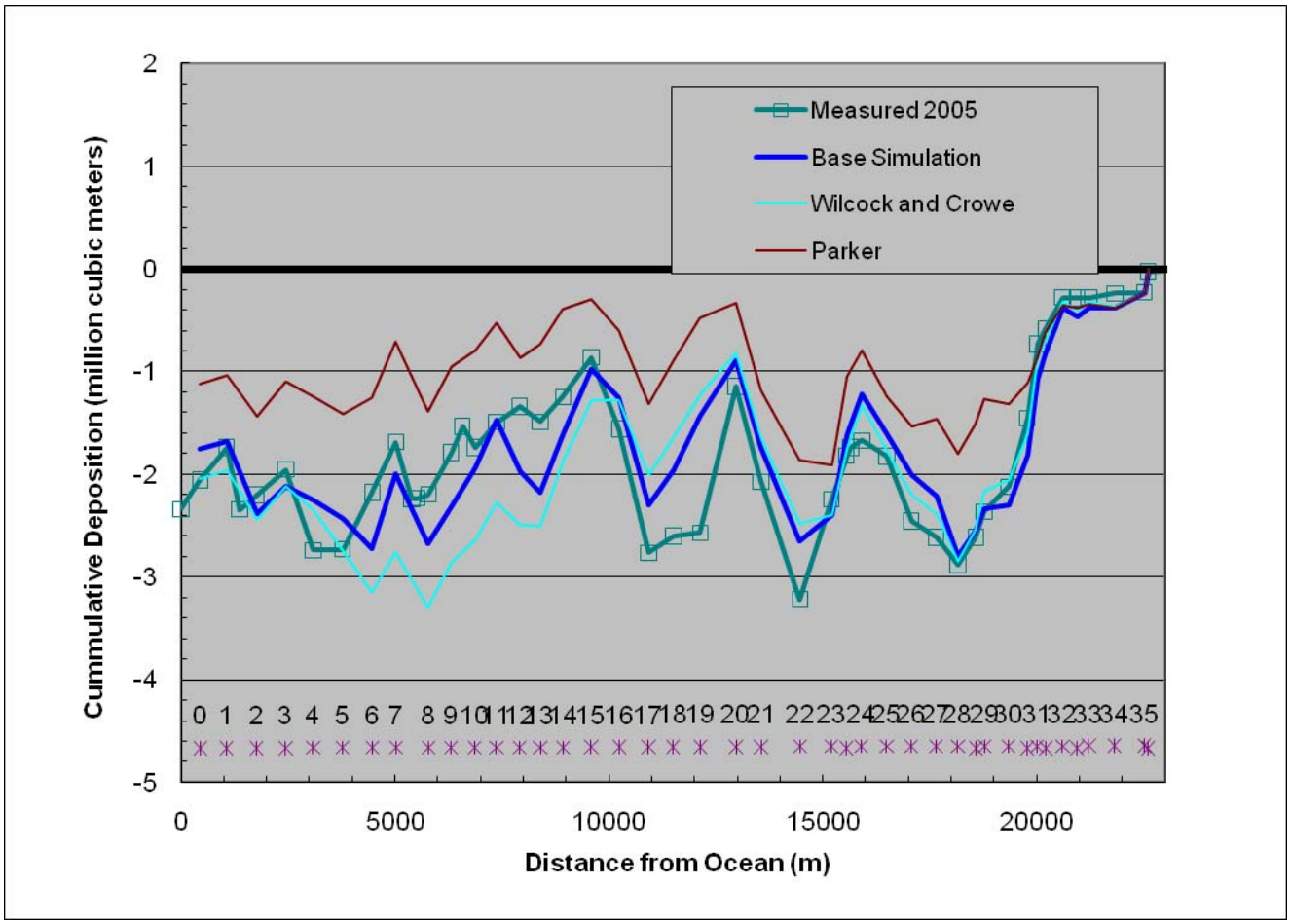

Figure 28. Sensitivity of model to transport formula selection.

2.5.4 Manning Roughness Coefficient

The base simulation assumed a Manning's roughness coefficient of 0.04. For sensitivity testing, a Manning's roughness of 0.05 and 0.03 were also simulated (Figure 29). The results for the Manning's n of 0.05 are overall, similar to the results for 0.04. However, there is significantly more erosion in the bedrock area. The results for the decreased roughness of 0.03 show significant less erosion throughout the entire model.

SRH-1D cannot simulate super-critical flow under steady flow conditions. In steep rivers such as the Tachia, using a small Manning's n will result in supercritical flow. The model will set the water surface to critical flow depth and then compute the shear stress. If the Manning's n is low and the flow depth was set to critical depth, the shear stress will be lower than that computed assuming a

higher Manning's n because both computation would have used the same velocity.

Regardless of begin able to simulate supercritical flow, a Manning's n of 0.03 is too low for a river with a d50 of over 100 mm. López, R. and Barragán (2008) suggest that the equivalent roughness is 6.1*d50 and this would equate to a Manning's n of the grain roughness of 0.037 for the Tachia River below Shih-Gang Dam. The channel roughness cannot be less than the grain roughness and therefore a total channel roughness of 0.04 is considered most appropriate for the Tachia River below Shih-Gang Dam.

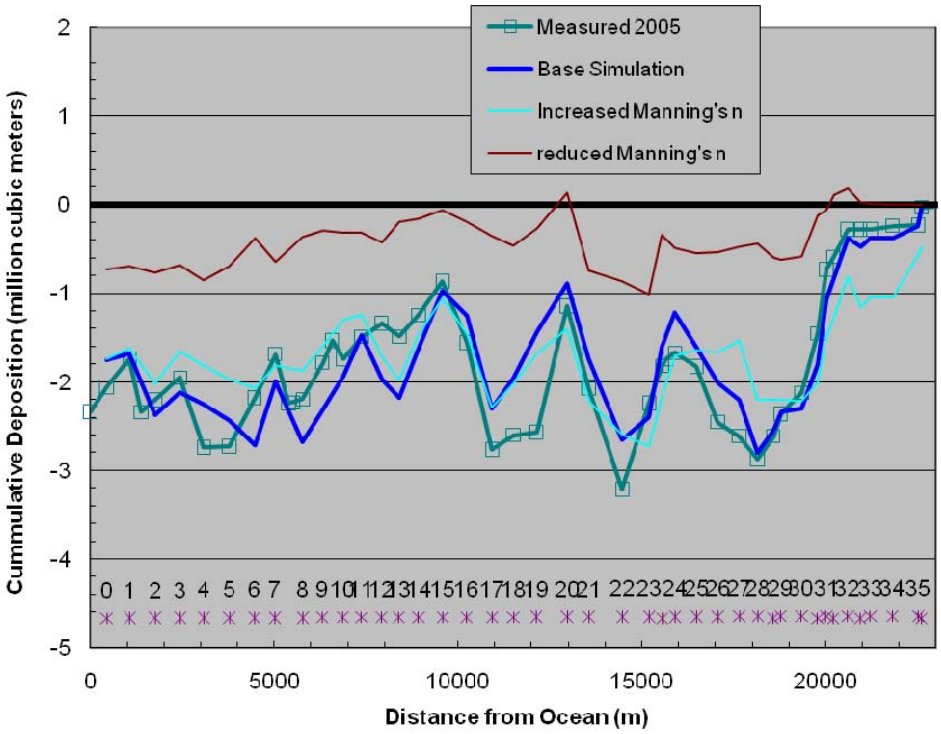

Figure 29. Sensitivity of model to Manning's roughness coefficient.

2.5.5 Minimization

SRH-1D has the capability to use the concept of stream power minimization to determine whether the erosion is lateral or horizontal (Huang and Greimann, 2008). It does this by comparing the average of the upstream and downstream friction slopes to the local friction slope similar to the method used in Chang (1988). The concept of minimization using stream tubes implemented in GSTARS 2.1 (Yang and Simoes, 2001) has been abandoned because we have found it to be unstable for most cases. The affect of turning on the minimization option is to increase the amount of bank erosion in the eroding reaches (Figure 30).

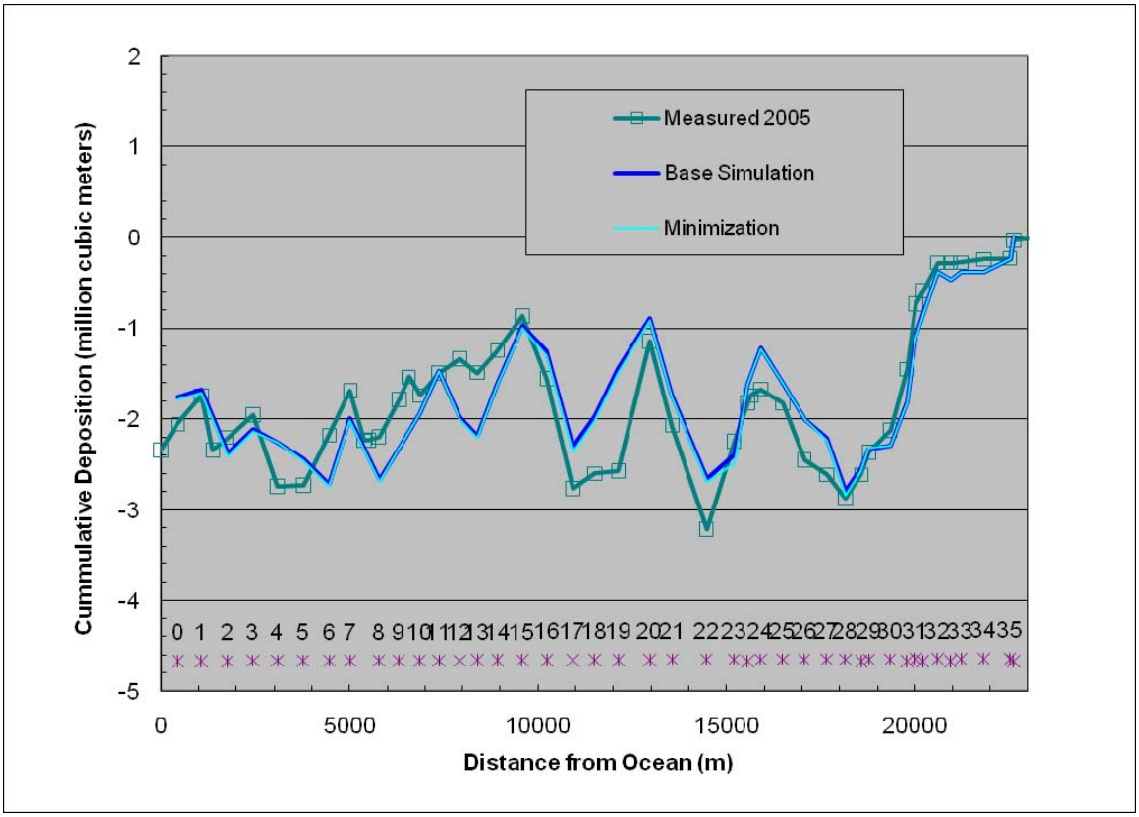

Figure 30. Sensitivity of model results to turning on minimization procedures.

2.5.6 Bed Sub-layer Transfer

The base value of the sub-layer transfer coefficient was 0.0. Toro-Escobar et al. (1996) suggest a value of 0.7. The parameter must be between 0 and 1 and most sediment models make the assumption that it is 0. Based upon the author's experience it usually has a minor affect on the simulation results.

To test the sensitivity of this parameter we simulated the case for the sub-layer transfer coefficient is equal to 0.7. The results are shown in Figure 31. The effect of setting the sub-layer transfer coefficient to 0.7 was to slightly reduce the erosion downstream of the dam and cause less deposition in the reaches where deposition occurred. However, the erosion and deposition trends remained similar.

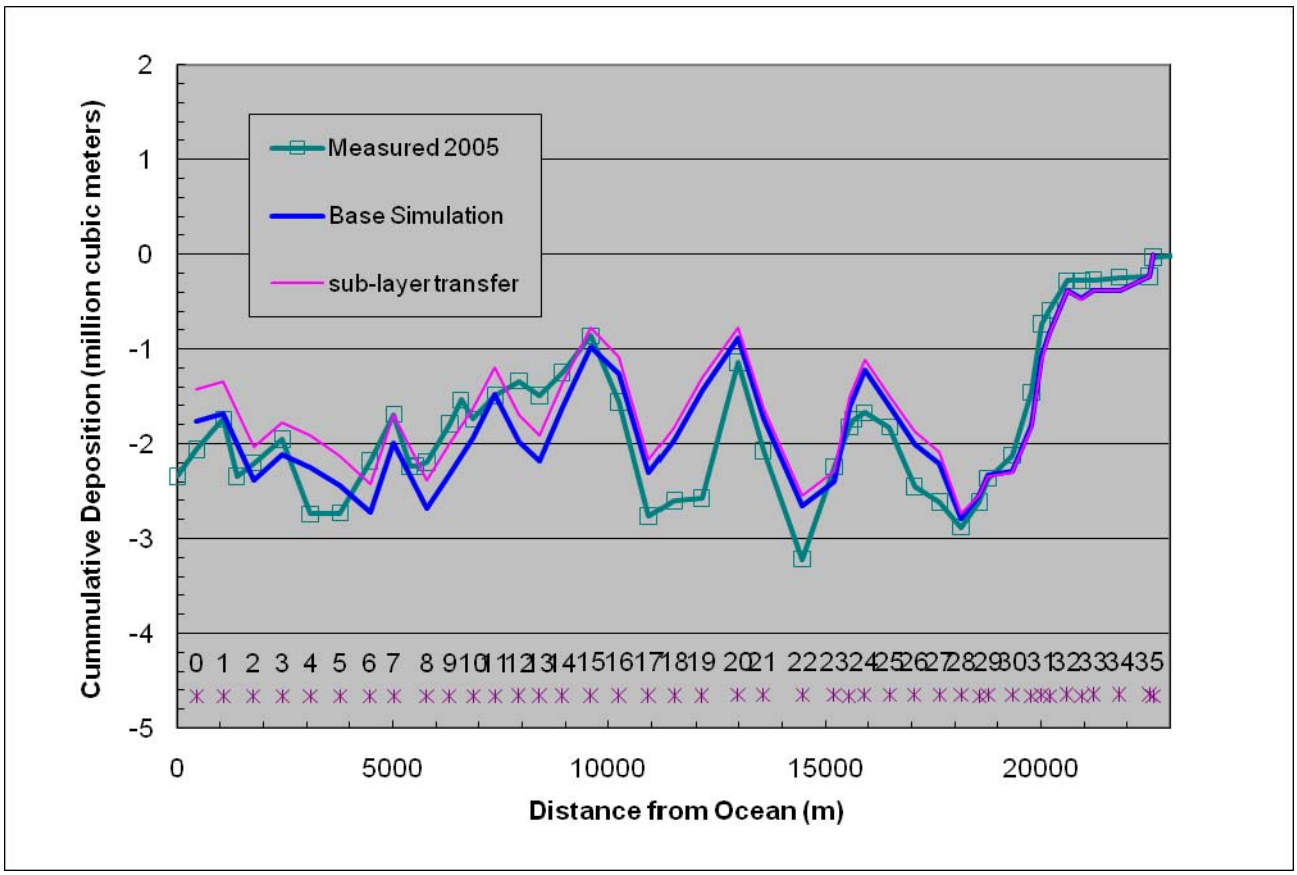

Figure 31. Sensitivity of model results to changes in sub-layer transfer coefficient. Pink line represents sub-layer transfer coefficient = 0.7.

2.5.7 Hiding/Exposure Coefficient

The base value of the hiding/exposure coefficient was 0.6. To test the sensitivity of this parameter we simulated an increase in the coefficient to 0.8 and a decrease in the coefficient to 0.45. The results are shown in Figure 32. When the hiding/exposure coefficient is reduced, the large particles become relatively less mobile and armoring may occur sooner. When the hiding/exposure coefficient is increased, the large particles become relatively more mobile and erosion is increased.

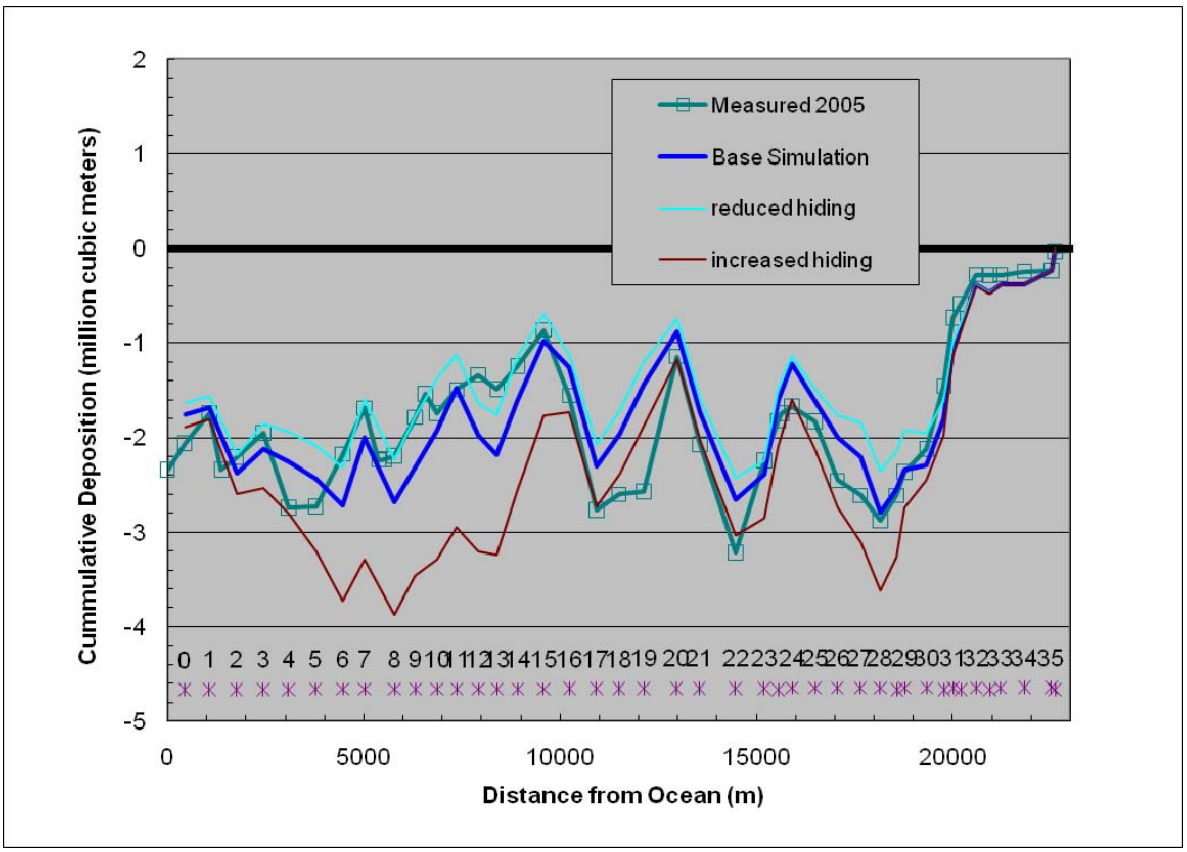

Figure 32. Sensitivity of model results to changes in hiding coefficient.

2.6 2005 to 2008 Results

The period from 2005 to 2008 was simulated using the same model parameters as the simulation from 2000 to 2005. The flow record was taken from the corresponding period.

The simulated erosion and deposition were compared against the geometry measured in 2008 (Figure 33). There was general agreement between the model and measured data for the first 7 km downstream of the dam where significant erosion occurred. The bedrock sections 35 to 32 showed almost 2 million m^3 of bedrock erosion and the model was able to reproduce this.

Downstream of XC 24, the model predicted deposition at XC 23 and 22 whereas the measured data indicated slight erosion. The reasons for the discrepancy are not clear, but it is assumed that the tributary that enters near XC 23 is important to the river behavior and should be simulated. Currently, no lateral inflow is assumed at XC 23. Both the model and the measured data show large amounts of deposition in the 5 km upstream from the ocean.

It is important to note that the measured data and model results showed significant erosion downstream of most major bridges where there is grade control. The floods of 2008 caused significant erosion downstream of Ho-Feng Bridge at XC 28-1 that caused its failure. There was also significant erosion downstream of the Highway 1 Bridge at XC 23-1 and at the high speed rail bridge at XC 19-1. The erosion downstream of these structures is expected to continue into the future. The grade control structures downstream of the bridges will have to be protected against scour similar to that which occurred at the Ho-Feng Bridge.

The results for the average bed elevation changes were similar to the volume of erosion and deposition (Figure 34). The measured results showed significant amounts of erosion from Shih-Gang Dam to XC 22, with less significant erosion from XC 22 all the way to XC 7. The model correctly predicts erosion from Shih-Gang Dam to XC 23, but did not capture the erosion from XC 23 to XC 15. It is likely that tributary influences are important in this reach.

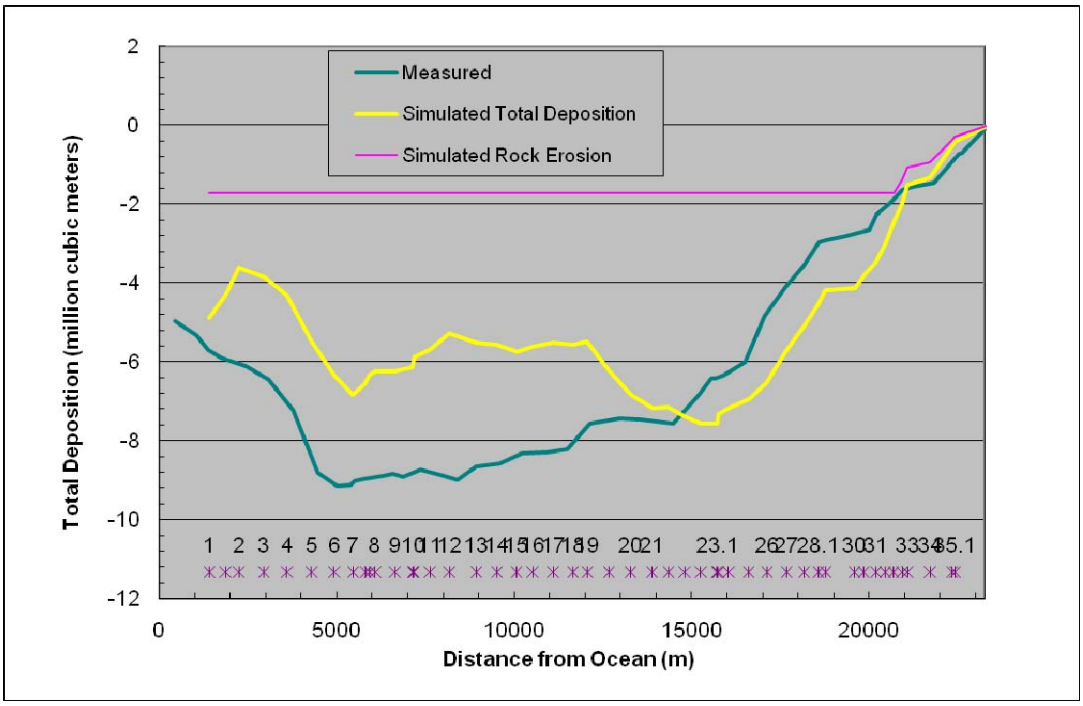

Figure 33. Simulated and measured total deposition from 2005 to 2008.

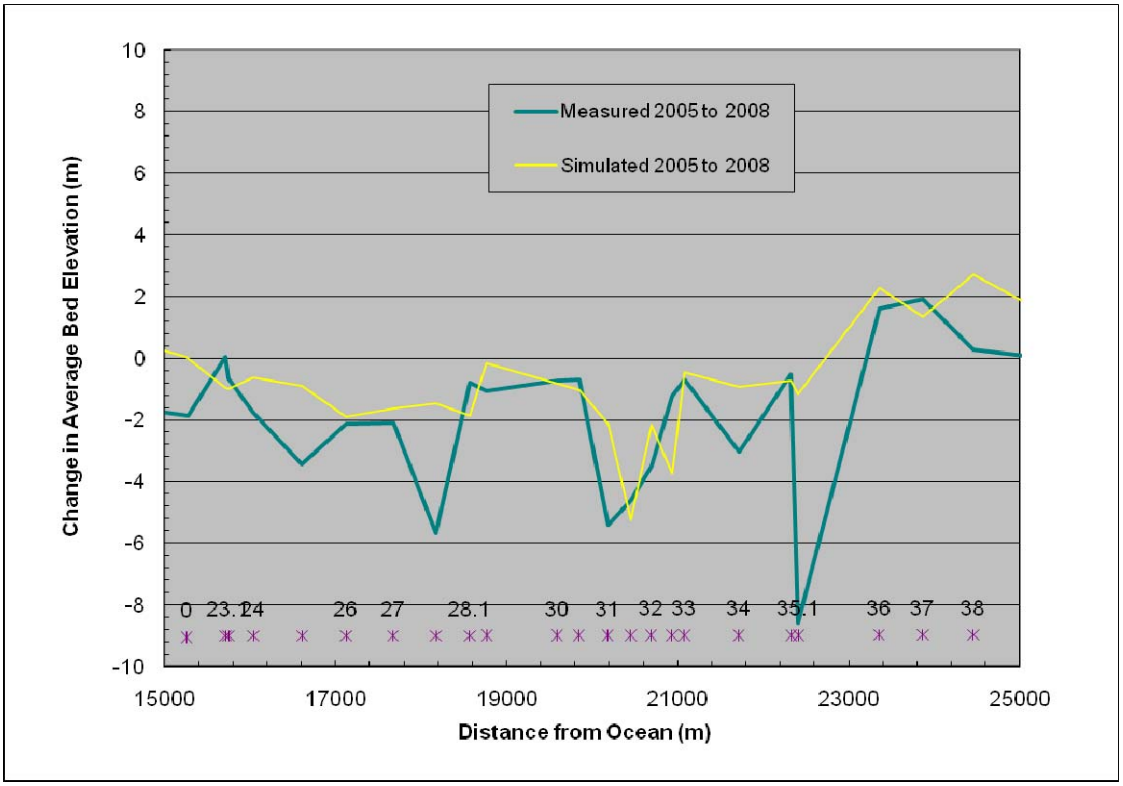

Figure 34. Measured and simulated average bed elevation change from 2005 to 2008.

2.7 Future Predictions

A simulation was performed using the measured 2008 geometry as initial conditions. The flows used in the simulations were the same as the 2005 to 2008 simulation. The cumulative deposition downstream of Shi-Gang dam is shown in Figure 35. There was continued erosion throughout the Tachia River from the dam until about 5 km upstream of the ocean. The model predicted that there would be approximately 6.5 million m^3 of erosion from the dam to XC 7 if the flows from 2005 to 2008 were to occur again.

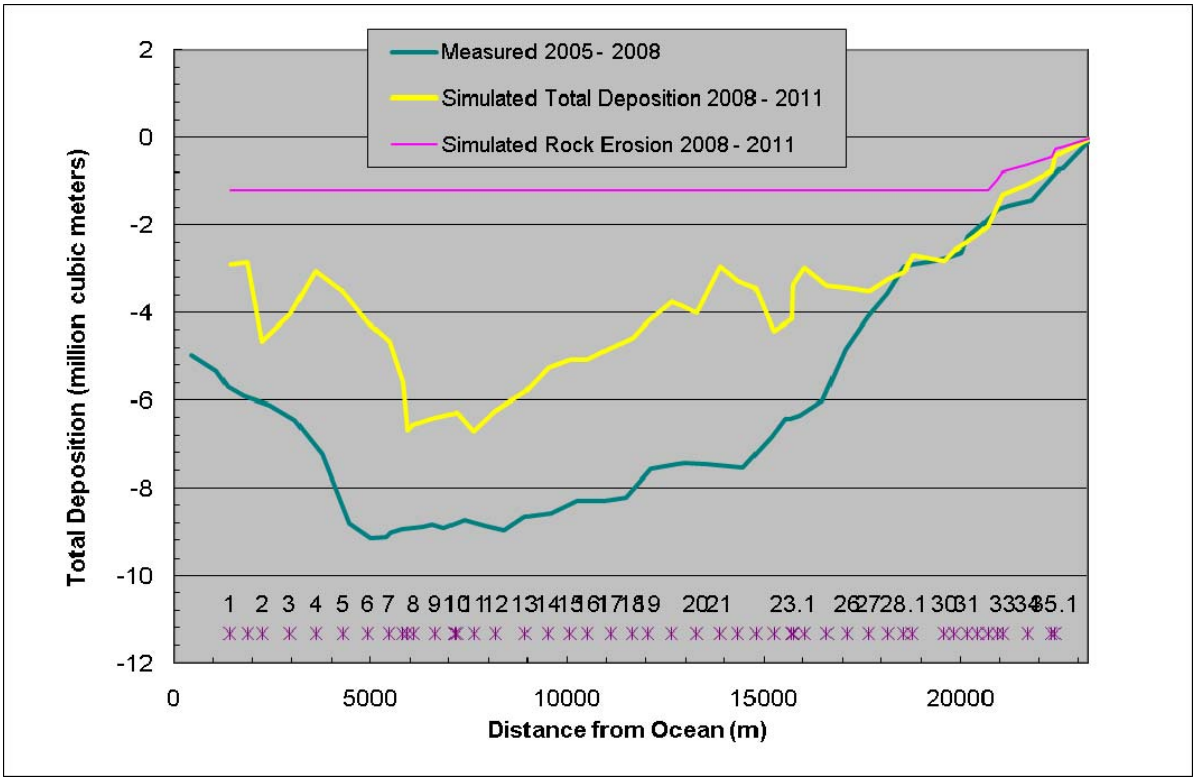

Figure 35. Prediction deposition downstream of Shih-Gang Dam based upon a repeat of the flows from 2005 to 2008.

2.8 Modeling Summary

SRH-1D was applied to the Tachia River from the ocean to approximately 42 km upstream. We simulated two historical periods: 2000 to 2005 and 2005 to 2008 using SRH-1D. There was also a 3 year future simulation performed using 2008 geometry as the initial conditions and 2005 to 2008 flow values. The same set of model parameters were used in all simulations.

For both the 2000 to 2005 and 2005 to 2008 simulations, the model reproduced the trends and magnitudes of sediment erosion and deposition downstream of Shih-Gang Dam at most cross sections. There are some discrepancies in the

vicinity of XC 23 to 19. It is suspected that the influence of tributaries is important downstream of XC 23.

Despite the neglect of tributaries, SRH-1D was still able to reproduce the aggradation or degradation volumes in most other reaches. Because SRH-1D is a one-dimensional model, it cannot simulate changes in channel location due to migration or avulsion.

Bedrock is currently present from Shih-Gang Dam to XC 32. However, bedrock geometry is unknown prior to 2007 and it was not possible to quantify the amount of bedrock erosion downstream of Shih-Gang Dam. Future surveys should indicate the extent of bedrock exposure and also depth to bedrock to allow further model testing.

Both an analysis of the historical data and simulation of the future conditions indicate that the erosion downstream of Shih-Gang Dam on the Tachia River is expected to continue for the foreseeable future. A severe sediment imbalance has been caused by the Chi-Chi earthquake and the presence of Shih-Gang Dam. The Chi-Chi earthquake increased the sill of Shih-Gang Dam approximately 10 m and this created a deposition zone upstream of the dam. The dam will prevent a head cut from progressing up through the bed rock and restoring the sediment supply. There will continue to be a lack of sediment supply to the downstream channel for some time into the future. Large floods will continue to erode sediment from the channel bed downstream of the dam. The erosion will likely continue to progress downstream. From 2000 to 2005, the erosion was primarily from the dam to XC 28, approximately 4.5 km downstream of the dam. There was only localized erosion below this location. From 2005 to 2008 the erosion occurred primarily from the dam to XC 20, or about 8 km downstream of the dam. There was also erosion for 8 more km, though the magnitude was significantly reduced. It is likely that severe erosion will occur downstream of XC 20 in the next large flow events. Infrastructure in the Tachia River from Shih-Gang Dam all the way to 5 km upstream from the ocean should be protected from potentially severe scour. Downstream of the Ho-Feng Bridge (XC 28-1), there was approximately 6 m of scour measured from 2005 to 2008. This type of scour could occur at the bridges further downstream in the future. The next typhoons may erode large volumes of sediment at the Highway 1 Bridge at XC 23. If sediment supply is not restored to the downstream reach then the erosion is expected to continue downstream and potentially begin to scour the riverbed near the high speed rail line at XC 19.

The bedrock downstream of Shih-Gang dam does not provide any significant resistance to erosion. In fact, the presence of “bedrock” downstream of Shih-Gang dam creates more erosion than if the river bed was gravel and cobbles. The bedrock becomes basically wash load after it is eroded and does not provide any significant bed material load to the downstream reaches. Also, the bed does not become armored with larger particles, which would slow the erosion. The only method that will slow this erosion is to increase the passage of gravel, cobbles, and boulders through Shih-Gang dam.

3 SRH-2D Application to Chosui River

In Taiwan, many alluvial rivers are characterized by the presence and exposure of soft rocks on the river bed. The rock consists of mainly mudstone and sandstone which is relatively weak (shear strength between 0.5 ~ 25.0 MPa) and subject to substantial erosion during high flows. Therefore, soft rock erosion is an important river process in Taiwan that needs to be understood.

In the past few years, an extensive study on the bedrock erosion modeling has been carried out by the Reclamation under the Appendix 8 agreement. The work has been documented in the final report by Lai and Greimann (2009). The completed works can be summarized as follows: (1) a literature review of available rock erosion models was provided; (2) specific bedrock erosion models were recommended and there were modified and/or adapted for use by SRH; (3) bedrock erosion models were implemented into both SRH-1D and SRH-2D numerical models and there were debugged and tested; (4) the new SRH models with the soft rock models were calibrated and verified against available measurement data for rivers in Taiwan, and (5) The SRH models were also applied to selected rivers in Taiwan. The new SRH-1D may be used to estimate the reach-averaged erosion of rock and is the first known mobile-bed model of its kind suitable for bedrock erosion prediction in rivers. The new SRH-2D may be used to estimate localized erosion and deposition issues for both granular materials and bedrock on the river beds.

In this study, the calibrated and verified SRH-2D model is applied to downstream of the Chichi Weir to evaluate one of the engineering schemes proposed for erosion control.

3.1 Description of the Engineering Scheme Simulated

Extensive studies have been carried out by Taiwan WRA in an attempt to control the continued erosion downstream of the Chichi Weir. Five alternative engineering schemes were proposed in February, 2008, which were documented in a report by the 4th River Division of the Water Resources Agency (WRA, 2008a). A detailed discussion of the five alternatives, along with additional modifications, were also provided in December, 2008, by a joint study report between the National Chiao-Tung University in Taiwan and the National Center for Computational Hydroscience and Engineering at the University of Mississippi (WRA, 2008b)

One of the engineering schemes, number one (#1), was chosen for application simulation in this study. The original scheme relied on the use of stability control structures and bank protection measures at key locations to provide the protection.

It was based on the principle of "following the nature," i.e., not to modify the channel alignment and flow direction. The overall layout of the proposed control structures under the engineering #1 is shown in Figure 36.

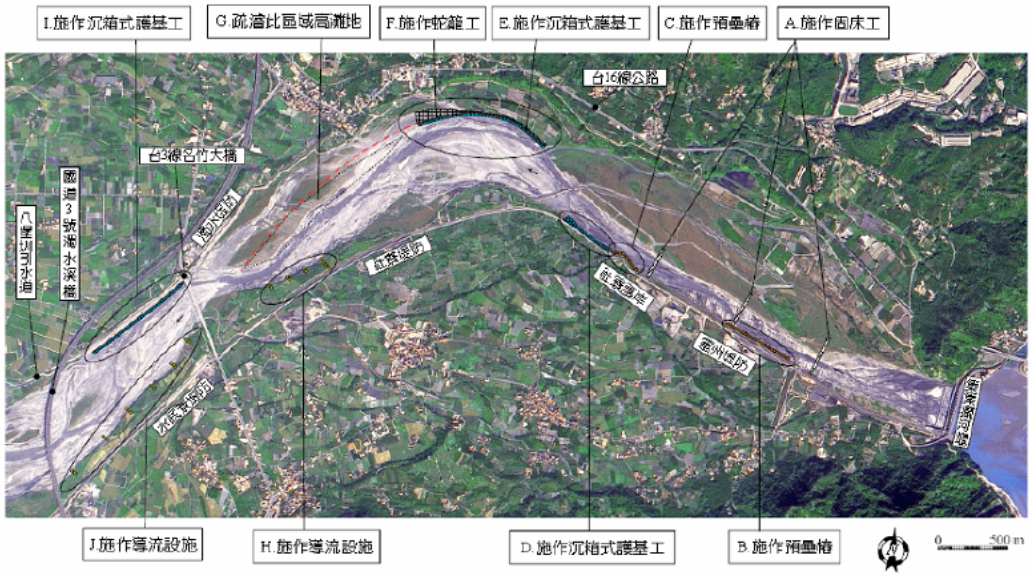

Figure 36. Schematic of key stability control structures proposed in the original engineering scheme #1 (Source: WRA Report, 2008b)

Key engineering considerations for the reach immediately downstream of the weir is to construct three cross stream weirs so that no further degradation of the river bed is allowed. The stream section between the weirs is to be filled first with large sized cobbles and then smaller sized gravels. The purpose is to restore the protective bed layer of cobbles. Other various bank protection measures are less critical as far as the current modeling is concerned, as bank erosion modeling is not considered.

Engineering scheme #1 one has been numerically simulated using the CCHE2D model. The results were reported by WRA (2008b). The numerical representation of the control structures and the related changes to the engineering scheme #1 are shown in Figure 37.

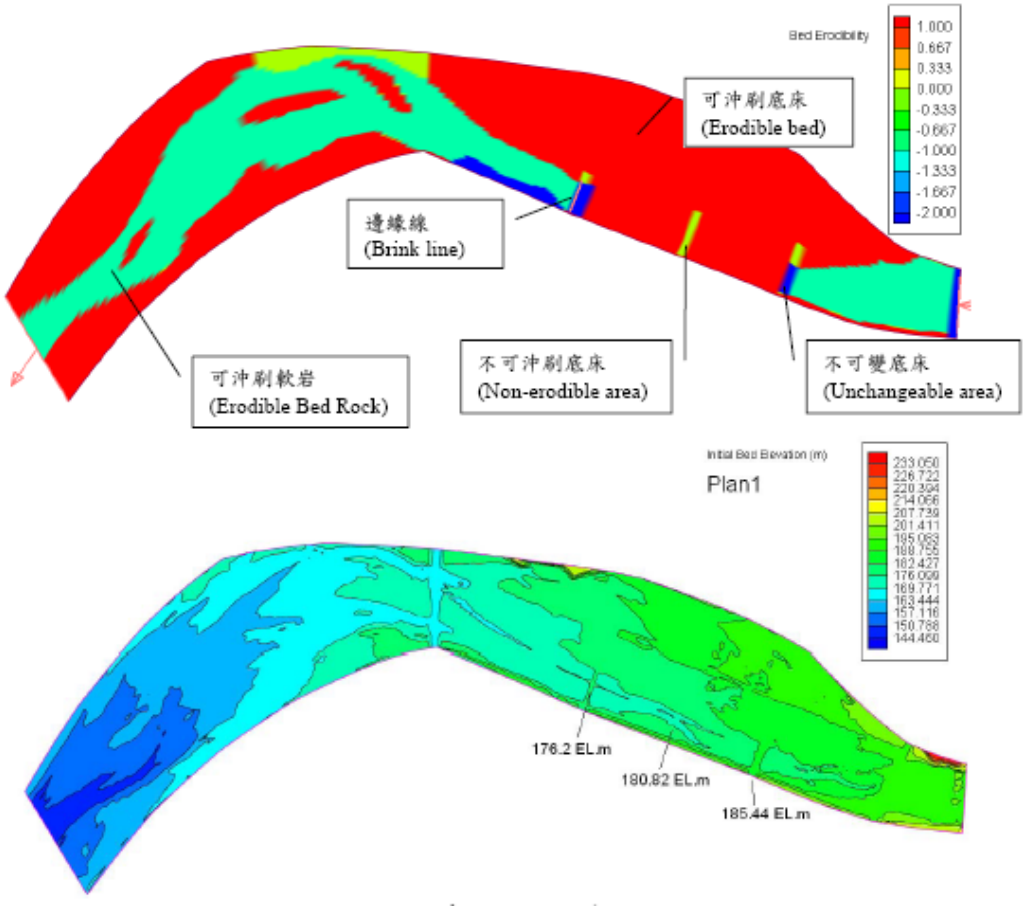

Figure 37. Layout of key stability control structures represented by the numerical model of CCHE2D for engineering scheme #1 (Source: WRA, 2008b)

3.2 Numerical Model Details

In this study, SRH-2D model is used to simulate the engineering scheme #1. In this section, the numerical model details are presented for documentation purpose.

For a typical SRH-2D modeling, following steps are generally taken:

(1) Selection of a solution domain;
(2) Mesh generation for the solution domain and topography representation;
(3) Zonal representation of bed properties including flow roughness and sediment gradation distribution;
(4) Simulation model development and calibration; and
(5) Model applications.

The first three steps are discussed in the following; calibration and verification studies were reported by Lai and Greimann (2009); and SRH-2D application study for the engineering scheme #1 is presented later.

3.2.1 Solution Domain and Mesh Generation

A 2D analysis begins by defining a solution domain and generating a mesh that covers the domain. In this application study, the solution domain is almost the same as determined during the calibration and verification study of Lai and Greimann (2009). It is briefly described as follows (Figure 38):

- Upstream boundary: It is located at the Chilu Bridge about 2.06 km upstream of the Chi-Chi Weir. The upstream boundary is between survey cross sections 121 and 122.
- Downstream boundary: It is located at the Mingchu Bridge about 6.7 km downstream of the Chi-Chi Weir. This boundary is located between survey cross sections 106 and 107.
- Lateral extent: The solution domain is wide enough laterally that the domain would fully contain the highest flow to be simulated. Average width is about 740 meters.

The total length of the river reach modeled is about 8.76 km.

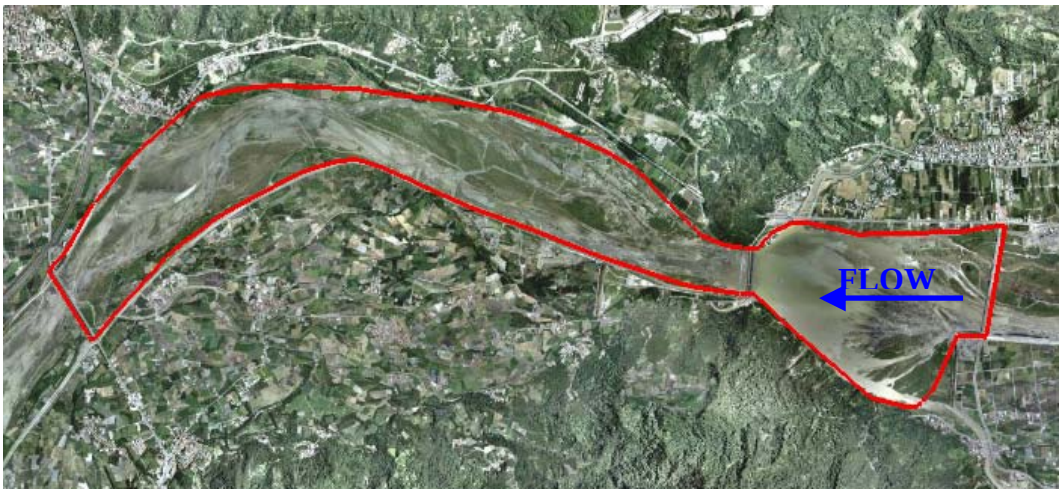

Figure 38. Solution domain is in red which is from Chilu Bridge to Mingchu Bridge (background aerial photo was taken in 2004).

A 2D mesh was generated using the Surface-water Modeling System software (SMS). The following website link provides more information on SMS: http://www.aquaveo.com. Additionally, the SRH-2D manual (Lai, 2008) may be referred to on how SRH-2D interacts with SMS.

The numerical mesh is based on the verification study, only slightly modified according to the layout of the engineering scheme #1. The final mesh is shown in Figure 39. It has a total of 12,717 hybrid quadrilateral and triangular mesh cells and 12,961 nodes. The majority of the cells are quadrilaterals; triangles are used only for mesh zone transition.

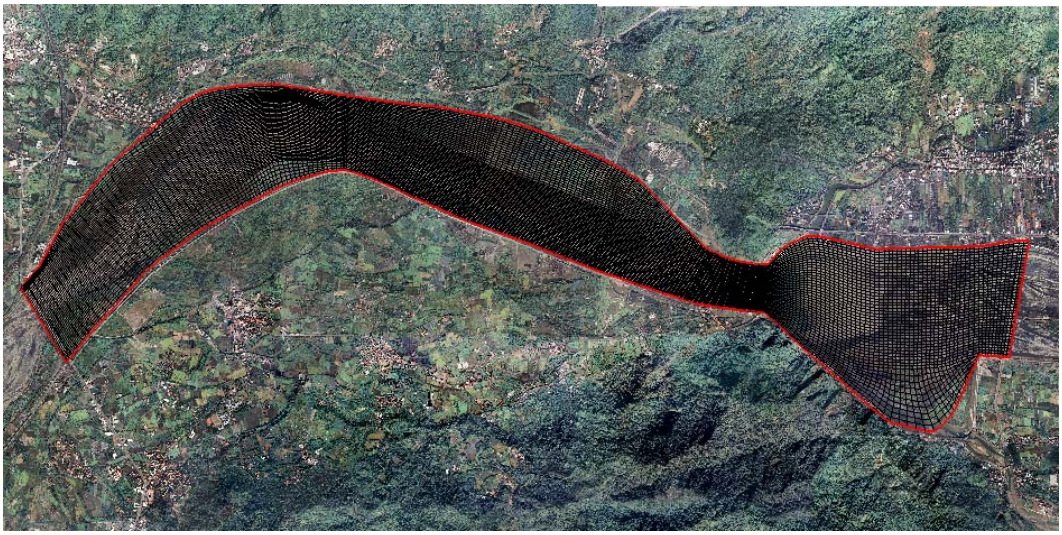

Figure 39. Hybrid mesh generated for the simulation of the engineering scheme #1 (background aerial photo was taken in January, 2007)

3.2.2 Bathymetric and Topographic Data

The bathymetric and topographical data at the beginning of the simulation (January 1, 2007) comes from two sources: the survey data of the existing river reach made in January 2007 and the geometric modifications made by WRA (2008b) as required by the engineering scheme #1.

The bed elevation, based on the survey data of the existing channel made in January 2007 is shown in Figure 40a. And the final bed elevation representing the condition after the implementation of engineering scheme #1 is shown in Figure 40b. This final bed elevation data, representing engineering scheme #1, were supplied to us by WRA, and they were originally developed by the CCHE2D work reported in WRA (2008b). The bed elevation data are imported into SMS and interpolated to the 2D mesh in Figure 39 to represent the initial bed. Figure 41 shows the river bed elevation contours represented by our 2D mesh. Figure 42 shows a 3D perspective view of the bed elevation downstream of the Chi-Chi Weir.

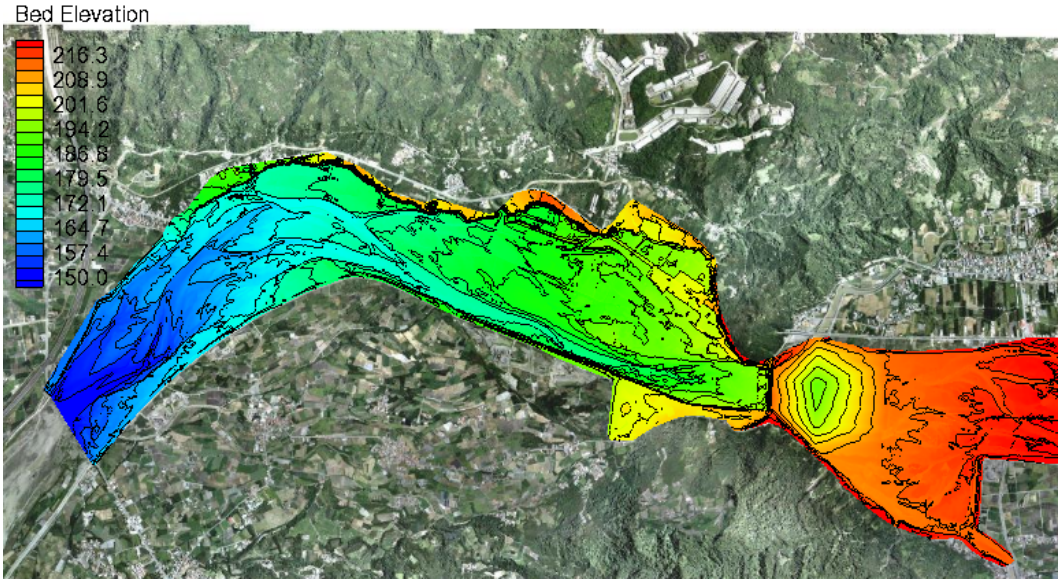

(a) Generated directly from the survey data in January, 2007

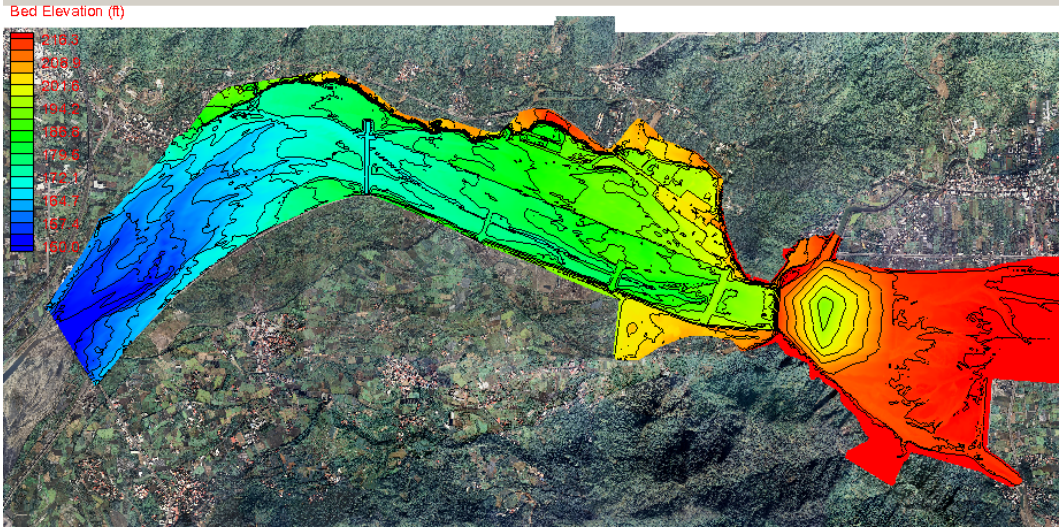

(b) Engineering scheme #1 incorporated into the January, 2007 data

Figure 40. Bed elevation contours based on the January 2007 DEM data with engineering scheme #1 incorporated.

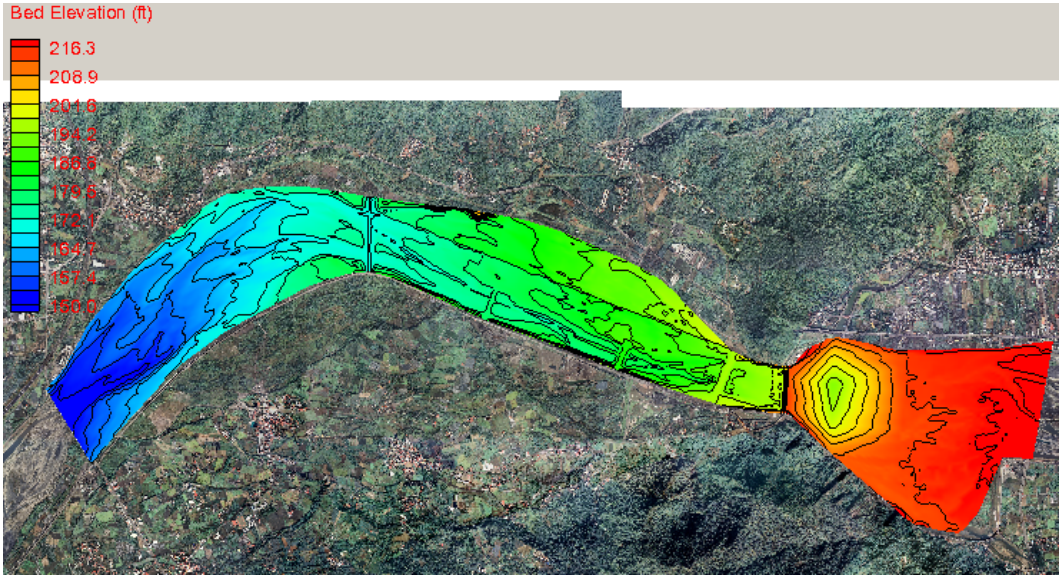

Figure 41. Bed elevation contours based on the final mesh representing the engineering scheme #1.

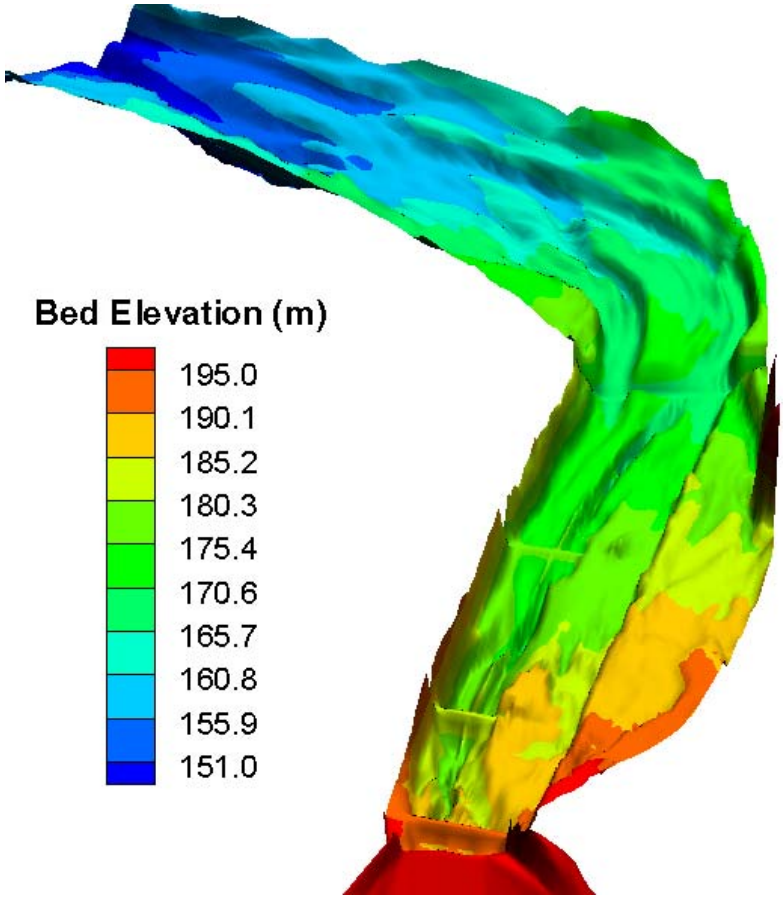

Figure 42. 3D perspective view of the bathymetry downstream of the Chi-Chi weir

3.2.3 Representation of Flow Roughness and Bed Gradation

River bed properties needed for modeling include the Manning's roughness coefficient and the bed gradation of surface and subsurface bed layers. These bed properties are usually spatially distributed over the solution domain.

Flow resistance is calculated using the Manning's roughness equation in which the Manning's coefficient (n) is used to prescribe flow resistance and is a model input. The same Manning's coefficient is used for the application study as the previous calibration and verification study. That is, a constant coefficient of 0.04 is used, based on the 2004 bed material analysis results by Taiwan WRA.

In the calibration and verification study, bed gradation was spatially distributed using multiple zones; and the survey data provided by WRA engineers were used. The same distribution is used in this study except for the areas affected by the proposed stability control structures with the engineering scheme #1. It includes primarily the reach between the three cross-stream weirs. They are described in detail below.

A total of 11 zones, as shown in Figure 43, are used to assign the bed gradation. The first four zones represent the upstream reach of the Chi-Chi Weir. Survey was conducted in July 2005 in this area and survey points are displayed in Figure 44. The cumulative size distribution of sediments at all survey points are shown in Table 5. An average gradation between point No.3 and 4 is used to represent zone 1, an average of points 5 and 6 is used for zone 2, point 7 is used for zone 3, and an average of points 8, 9, and 10 are used for zone 4.

The remaining 7 zones are downstream of the weir. The sediment cross-sectional survey data conducted in 2004 are used outside the reach where the proposed changes are to be made according to engineering scheme #1. The measured gradation data for the four cross-sections are listed in Table 6. Zone 5 takes the gradation data at Cross Section (XS) 117, zone 6 is from XS 109, zone 7 is from XS 107, and zone 8 is from XS 106.

The remaining three zones are special. Zone 9 represents the erodible soft rock whose properties are the same as those of the verification study of Lai and Greimann (2009). Zone 10 is created to represent the non-erodible bed where concrete is present immediately downstream of the weir and three cross-stream control weirs are proposed for bed grade control with engineering scheme #1. In these zones, no erosion is allowed but deposition is allowed if it occurs. Finally, zone 11 is used to represent the materials used to fill the reach between the cross-stream weirs. The materials consist of two sizes: 75% with 374 mm diameter and 25% with 125 mm diameter. Note that the materials in this zone were treated as "non-erodible" in the study of WRA (2008b). In this study, however, they are treated as regular granular materials. The model will determine whether they are erodible or not.

The sediment size distribution for the first eight zones is plotted in Figure 45 except for zone 4. Zone 4 has very fine materials and survey data showed that 99% of the sediments are less than 0.074 mm in diameter.

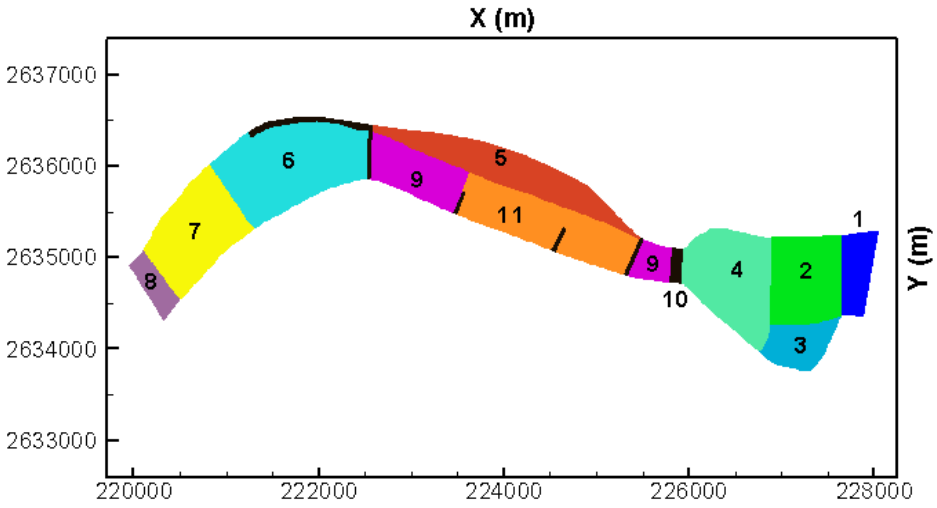

Figure 43. Bed gradation zones used by SRH-2D to specify variation of bed sediment materials

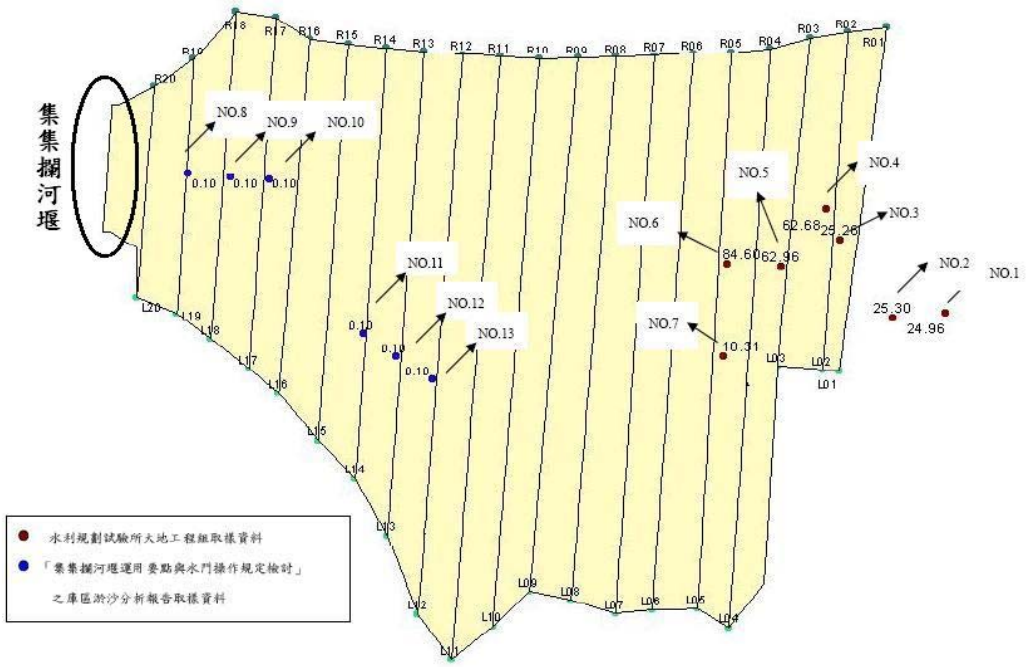

Figure 44. Locations of 13 survey points upstream of the Chi-Chi Weir where sediment gradation was measured in July, 2005

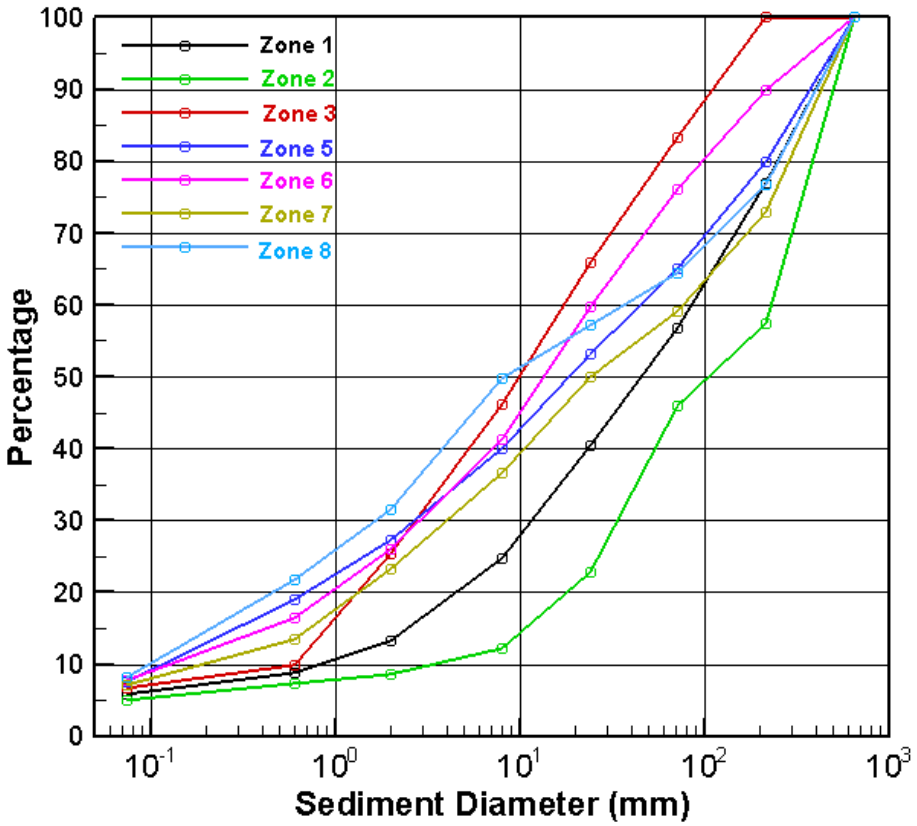

Figure 45. Cumulative sediment size distribution for seven zones shown in Figure 44

Table 5. Measured cumulative size distribution for points shown in Figure 44 (July, 2005)

Point ID	Distance to Weir (m)	d10(mm)	d25(mm)	d50(mm)	d60(mm)	D75(mm)	Note
No8	200	-	-	-	-	-	99% pass 0.074
No9	300	-	-	-	-	-	99% pass 0.074
No10	400	-	-	-	-	-	99% pass 0.074
No11	700	0.012	0.025	0.042	0.06	0.09	
No12	800	-	-	-	-	-	99% pass 0.074
No13	900	-	-	-	-	-	99% pass 0.074
No6	1600	6.25	30.38	84.6	295.66	360.41	
No7	1600	0.6	1.96	10.31	16.33	43.51	
No5	1800	2	11.13	64.96	125.9	259.31	
No3	1900	1.05	5.56	25.26	49.02	113.41	
No4	1900	1.2	9.05	62.68	108.9	262.67	
No2	2200	1.1	5.82	25.3	48.93	141.34	
No1	2300	1.012	8.89	24.96	64.6	97.23	

Table 6. Measured cumulative size distribution for bed gradation at selected cross sections (data were from 2004)

XS ID	d10	d20	d30	d40	d50	d65	d75	D90
106	0.2	0.48	1.77	3.72	8.17	77.18	196.5	445.78
107	0.39	1.37	4.2	11.25	23.87	146.7	238.95	480.08
109	0.24	1	3.13	7.3	13.95	32.3	65.72	218.42
117	0.28	0.65	3.01	7.93	17.99	72.03	157.57	413.12

3.2.4 Boundary Conditions

At the upstream inlet boundary, i.e., Chilu Bridge, flow discharge and sediment supply rate for each sediment size are needed.

A time series flow hydrograph is specified at the inlet boundary which represents the measured hourly flow data from January 1, 2007 to December 31, 2008. Only discharges above 600 cms are used for modeling. The same procedure was adopted during the calibration and verification study of Lai and Greimann (2009), as lower flows do not mobilize the bed sediments appreciably. The applied flow hydrograph is plotted in Figure 46, which consists of eight major floods due to

typhoon: June-Storm (June 8-11, 2007), Sepat (August 13-24, 2007), Wipha (September 18-19, 2007), Krosa (October 6-9, 2007), Kalmaegi (July 16-29, 2008), Nuri (August 19-21,2008), Sinlaku (September 11-16, 2008), and Jamgmi (September 26-29, 2008).

The upstream sediment supply is computed using the sediment transport equation based on the local flow at the Chilu Bridge. This same procedure was used by the calibration and verification study. This means the sediment supply is equal to the sediment transport capacity. Due to the existence of the Chi-Chi Weir, the assumption is not expected to impact the downstream erosion results significantly.

At the downstream boundary, i.e., the Mingchu Bridge, water surface elevation (stage) is specified. The same rating curve used by the calibration and verification study, as listed in Table 7, is used to compute the water surface elevation at the downstream boundary. Variation of the water surface elevation at the boundary is displayed in Figure 46.

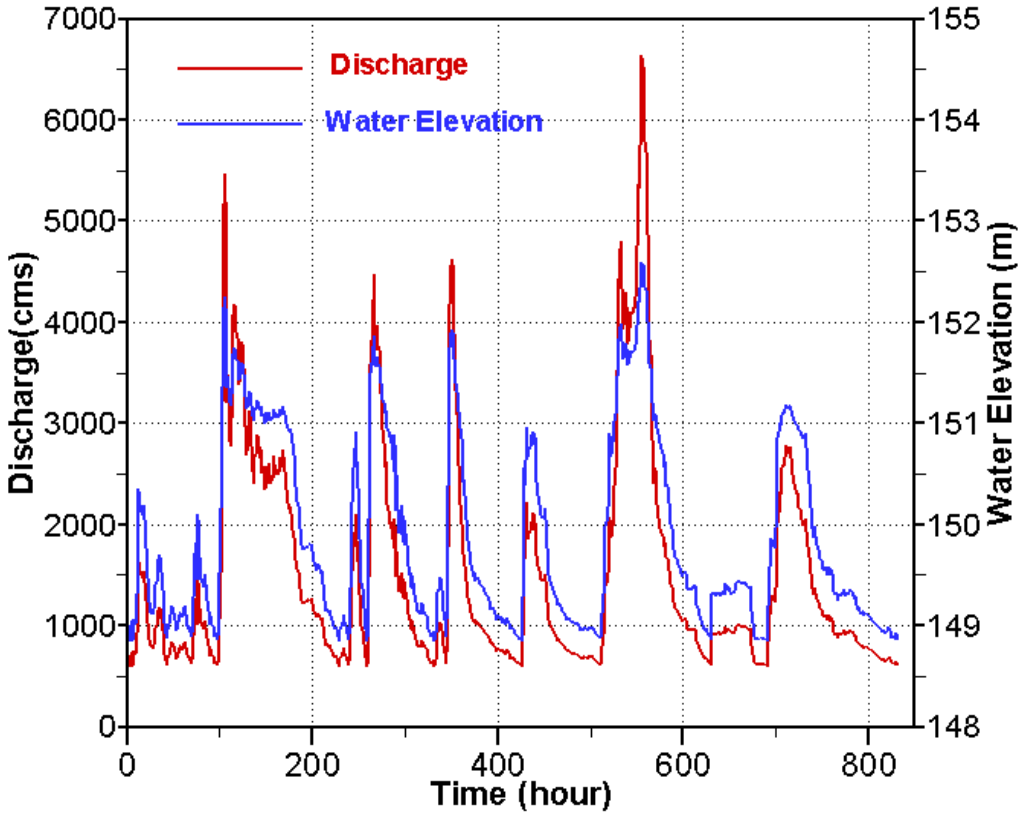

Figure 46. Flow hydrograph at the upstream boundary and water surface elevation at the downstream boundary for simulation period from January 1, 2007 to December 31, 2008 (note that discharges below 600cms are excluded)

Table 7. Discharge versus water surface elevation rating curve at the Mingchu Bridge on the Choshui River

Discharge (cms)	Water Surface Elevation (m)
10	148.0
2000	150.87
5500	152.27
9300	153.35
11900	153.97
14500	154.56
15300	154.73
17900	155.25
20500	155.76

3.2.5 Other Model Parameters

Eight sediment size classes, shown in Table 8, are used to represent the sediments on the river bed and those in transport. Each size class is transported and modeled individually.

Table 8. Size ranges of each sediment size class used for sediment transport modeling

Sediment Size Class	Size Range (mm)
1	0.001 to 0.074
2	0.074 to 0.6
3	0.6 to 2
4	2 to 8
5	8 to 24
6	24 to 72
7	72 to 216
8	216 to 648

Several sediment transport capacity equations are available with SRH-2D. Parker (1990) developed a bedload formula applicable to mixed sand and gravel sediments. Wilcock and Crowe (2003) developed a similar bedload formula for sand-gravel mixtures. Both of them are applicable to the present project. In addition, the Engelund-Hansen equation may be used to predict the suspended load in the river system. Since the SRH-1D study showed that the best results were obtained with the Parker equation, and it was also used in the previous calibration and verification studies, the same is used in this application study.

Other parameters include the non-equilibrium adaptation length of 500 m, and the active layer thickness of 0.25 m. Bedrock erosion model parameters adopt the Mixed-Scour scenario used by the calibration and verification studies. That is, the erosion model parameters are set as follows: $k_p = 5 \times 10^{-7}$, $\tau_{cri} = 200 Pa$, $k_v = 75.0$, $Y = 5.0 \times 10^4 MPa$, and $\sigma_T = 7.0 MPa$.

3.3 Model Results

First, a flow-only model run is carried out with a constant flow of 601 m/s. It is used as the initial condition for the subsequent sediment modeling. The model results are shown in Figure 47 to gain an understanding of the flow field with the engineering scheme #1 scenario.

For comparison purpose, the flow model results of the existing condition scenario, without any engineering modifications, is also plotted (see Figure 48). It is seen that the proposed engineering scheme reduced the velocity magnitude in the river section between the three cross-stream weirs, and the impact to further downstream is small. Also, higher velocity is predicted at the crest of the three weirs.

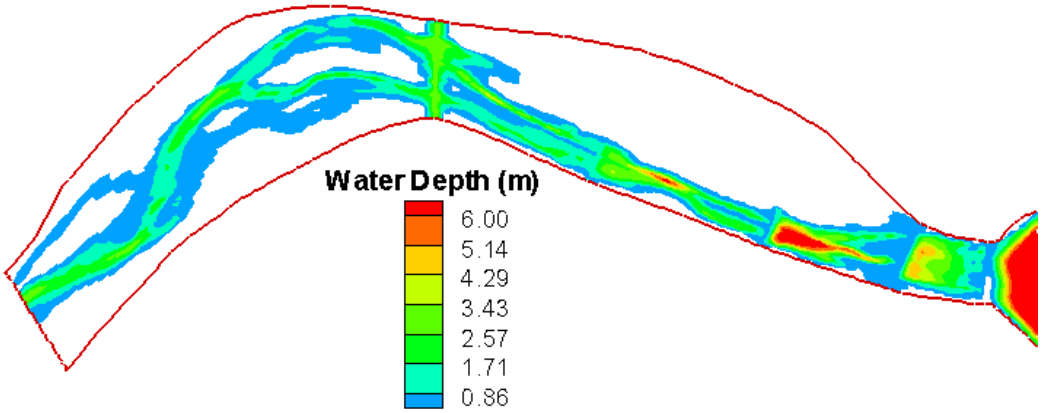

(a) Water Depth

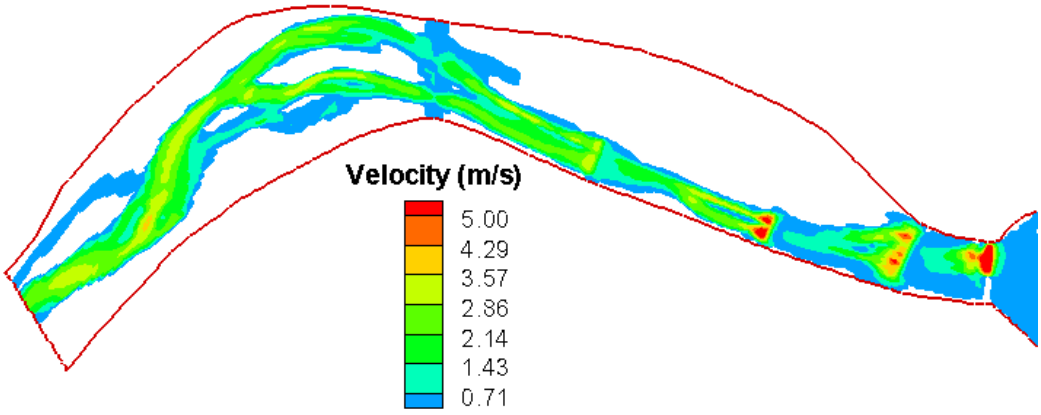

(b) Velocity Magnitude

Figure 47. Predicted water depth and velocity with a constant flow of 601 m/s and a fixed bed under the scenario of engineering scheme #1 implementation

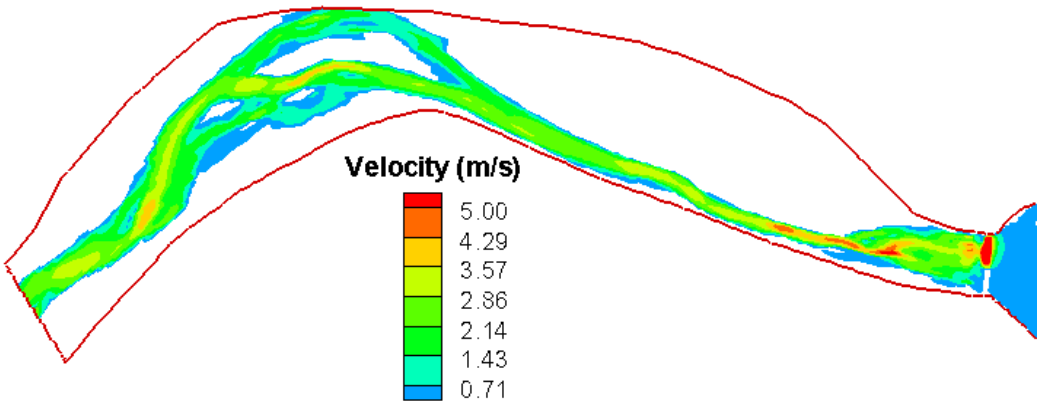

Figure 48. Predicted water velocity with a constant flow of 601 m/s and a fixed bed under the scenario of the existing condition

Next, simulation is carried out with the sediment transport and rock erosion using the two-year flow hydrograph from January 1, 2007 to December 31, 2008. The net eroded depth is shown Figure 49 in which the model results under the existing condition is also shown for comparison purpose.

The following conclusions can be drawn based on the model results:

(1) The three cross-stream weirs proposed between XS 113 and XS 116 are successful in preventing further river bed degradation for the reach protected. Instead of erosion, a small amount of deposition is predicted.
(2) The toe downstream of the weirs, however, is predicted to experience erosion if the same materials (75% with 374 mm diameter and 25% with 125 mm diameter) are used everywhere.
(3) Downstream of XS 113 (the last cross-stream weir), slightly more erosion is predicted in comparison with the existing condition scenario, particularly between XS 112 and XS 113. Between XS 111 and XS 112, channel incision is predicted, which is due to soft rock erosion. We suggest some measure needs to be done at XS 111 and its nearby surroundings.
(4) Further downstream (after XS 111), the difference in erosion and deposition between the proposed engineering scheme #1 and the existing condition is small.

Predicted magnitude of the flow velocity at time 552 hours, when discharge is at 5,367 cms, is plotted in Figure 50. The velocity at the end of the simulation on December 31, 2008 is shown in Figure 51. It is seen that velocity magnitude is reduced between XS 112 to XS 116 and width of the flow is increased. It predicts that more flow is sent towards to the right branch of the channel downstream of

XS 111 with the proposed engineering scheme #1, due possibly to the channel incision predicted. This prediction needs to be taken into consideration at XS 10 as it may accelerate the channel shift towards the right bank.

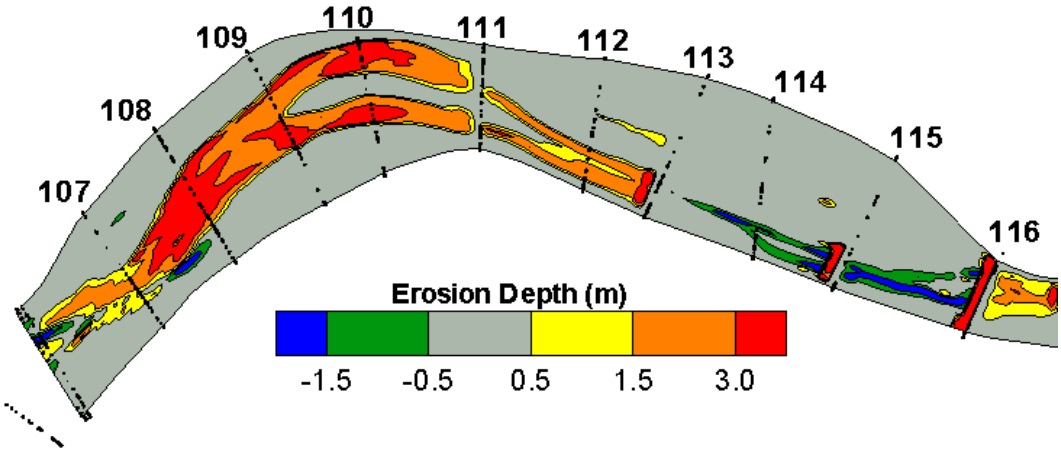

(a) With the project as proposed by engineering scheme #1

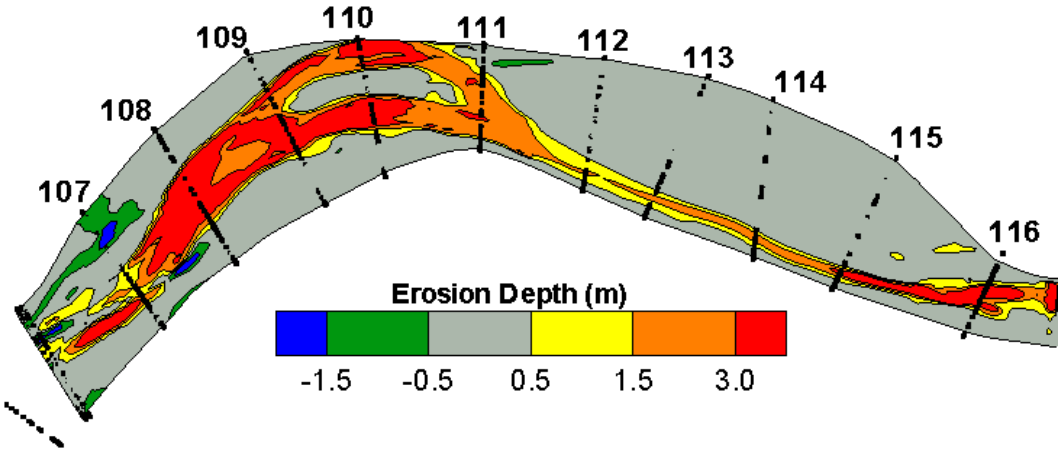

(b) Without the project (existing condition)

Figure 49. Comparison of predicted erosion depth from January 1, 2007 to December 31, 2008 between scenario of with the project of engineering scheme #1 and without the project

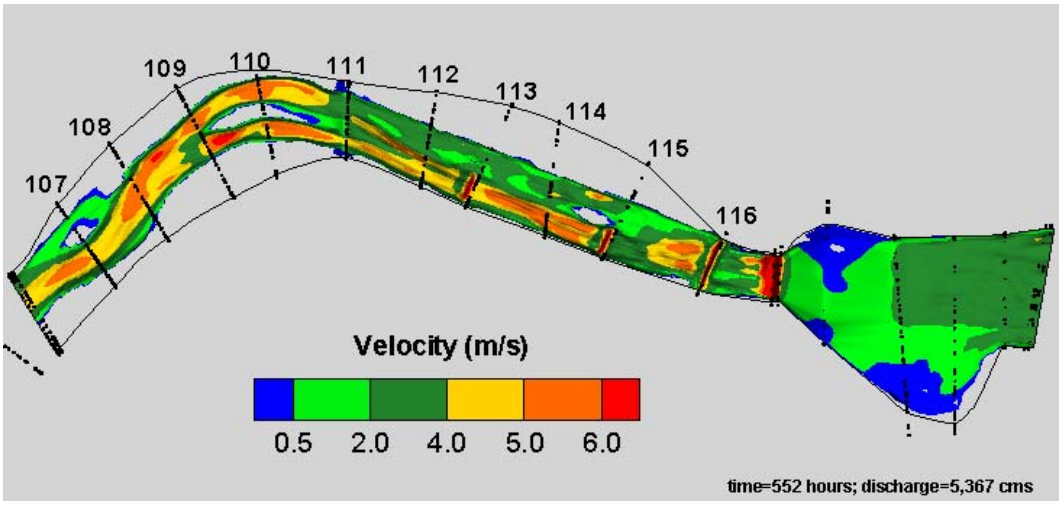

(a) With the project as proposed by engineering scheme #1

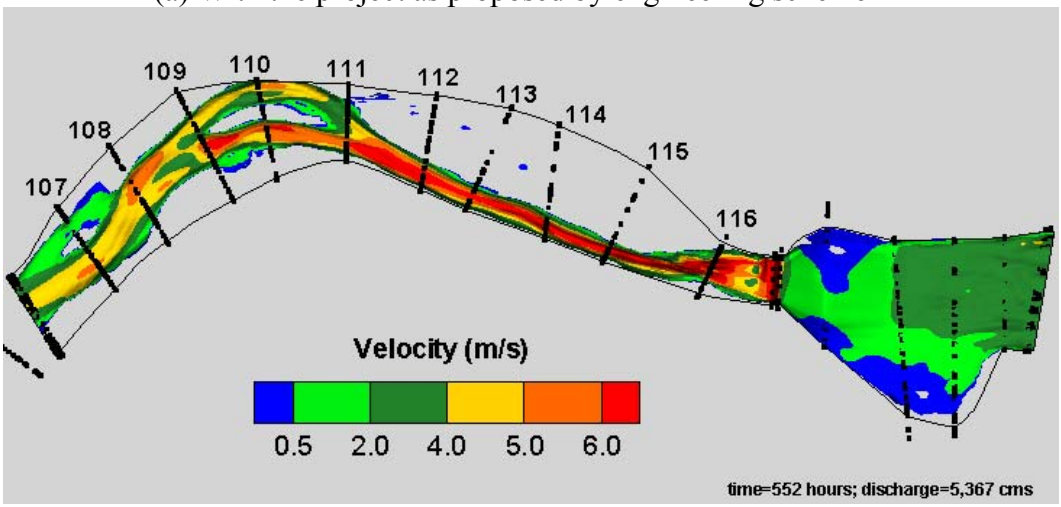

(b) Without the project (existing condition)

Figure 50. Comparison of predicted flow velocity at time 552 hours when discharge is at 5,367 cms between the scenario of the proposed engineering scheme #1 and the existing condition scenario

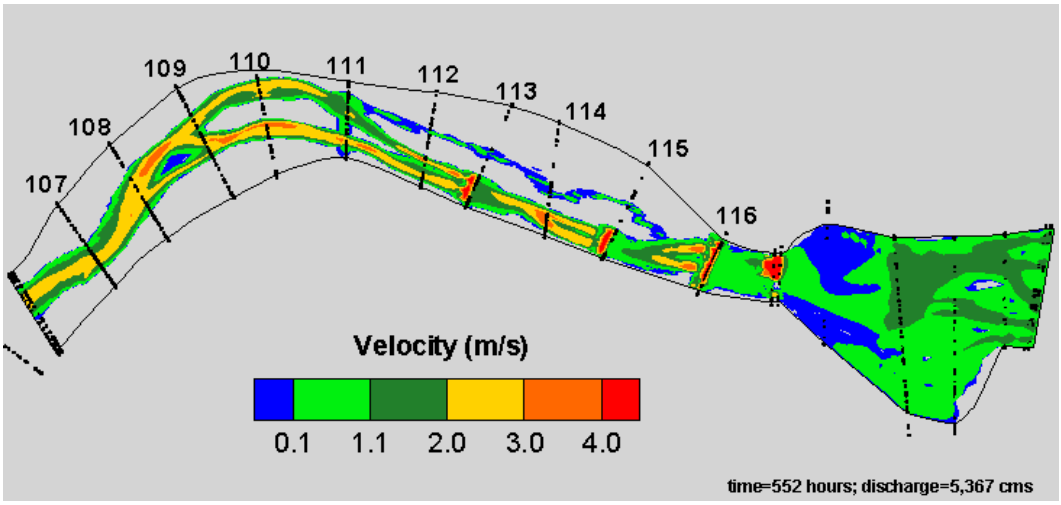

(a) With the project as proposed by engineering scheme #1

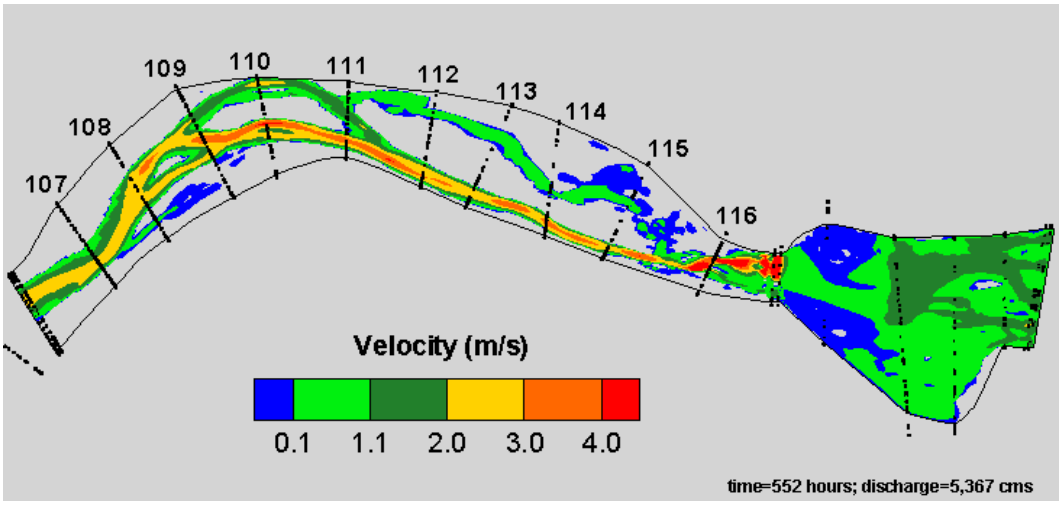

(b) Without the project (existing condition)

Figure 51. Comparison of predicted flow velocity on December 31, 2008 (the end of the model simulation) between the scenario of with the project of engineering scheme #1 and without the project

3.4 Summary

The proposed rock erosion model was implemented into the existing mobile-bed model, SRH-2D, which is under research and development at Reclamation. The new SRH-2D model was then used to conduct calibration and verification studies downstream of Chi-Chi weir, as reported by Lai and Greimann (2009). Reasonable results were achieved.

In this report, the SRH-2D model is applied to evaluate the effectiveness and impact of the proposed engineering scheme #1 in presenting further erosion for the project site. Based on the model results, it may be concluded that the proposed

engineer scheme #1 succeeds in preventing further erosion between XS 113 and XS 116. It is largely achieved by the use of cross stream weirs. More erosion is predicted downstream of XS 113; and more flow is predicted to go through the right branch of the channel downstream of XS 113. This may have the implication that channel shift towards the right bank may be accelerated if nothing is done in that area.

4 Bank Erosion Modeling – A Progress Report

The research and development of bank erosion models started last year (2009) as part of a four-year study plan. This chapter reports what have been achieved up to the current year (2010) of the study.

4.1 Introduction

Stream bank erosion is a natural geomorphic process occurring in all channels. It is one of the important mechanisms by which a channel adjusts its size, shape and slope to convey the discharge and sediment supplied to it from the upstream watershed. Most existing numerical models do not consider bank erosion explicitly and therefore, have limited use for studying the geomorphic response of a channel.

Bank erosion has both benefits and pitfalls. It may be beneficial to the ecology of waterways, since erosion and deposition create a variety of habitats for flora and fauna which contribute to ecological diversity (Environment Agency 1999). In many cases, however, bank erosion is detrimental as it causes land loss and becomes a resources management problem. Bank erosion is responsible for laterally shifting stream courses in numerous drainage basins. Rapid shift examples include 14 meter/year shift in the Cimarron River, Kansas (Schumm and Lichty, 1963), 50 meter/year in the Gila River, Arizona (Simon and Molinas, 1991), 100 meter/year in the Toutle River, Washington (Simon, 1992), and up to 824 meter/year in the lower Meghna River, Bangladesh (Banglapedia, 2005).

Stream bank erosion is also a dominant source of sediment supply in many river systems, leading to sediment management problems. It contributed about 37% in the River Ouse, Yorkshire, UK (Walling et. al., 1999), 50% in the Midwestern streams, USA (Wilkin and Hebel, 1982), 78% in the Gowrie Creek, Murray Darling Basin, Australia (Howard et. al., 1998), 80% in the loess area of Midwest United States (Simon et. al., 1996), and up to 92% (including channel scour) in Gelbaek stream, Denmark (Kronvang et. al., 1997). An increase in sediment supply due to accelerated bank erosion can be a major cause of non-point source pollution within river systems.

4.2 Bank Erosion Processes

It is important to understand different bank erosion processes first before the attempt of identifying bank erosion measurement techniques, modeling methods, or mitigation techniques.

Bank erosion occurs by a wide variety of processes. Broadly, they can be divided into two groups (Watson and Basher, 2006): (1) hydraulic fluvial processes near a bank below the water surface; and (2) mass failure processes. The two groups are related – a hydraulic-induced undercutting at a bank toe can cause a gravitationally-induced mass failure; but materials from the mass failure may protect toe erosion, at least temporarily. Processes within each group are briefly discussed.

4.2.1 Hydraulic Fluvial Processes

Hydraulic fluvial erosion is often a precursor to gravitational mass failures; it is also responsible for transport of the sediment deposits produced by mass failures. Hydraulic fluvial erosion results from an imbalance between hydraulic shear stress and bank material resistance strength. Where the shear stress exceeds bank material strength, erosion processes will be initiated. In general, shear stress increases as flow increases, while bank strength typically reduces (e.g., when the bank becomes saturated). Three types of hydraulically induced failures may be identified: bed degradation (vertical), basal cleanout, and bank undercutting. They are shown in Figure 52 and are discussed further below.

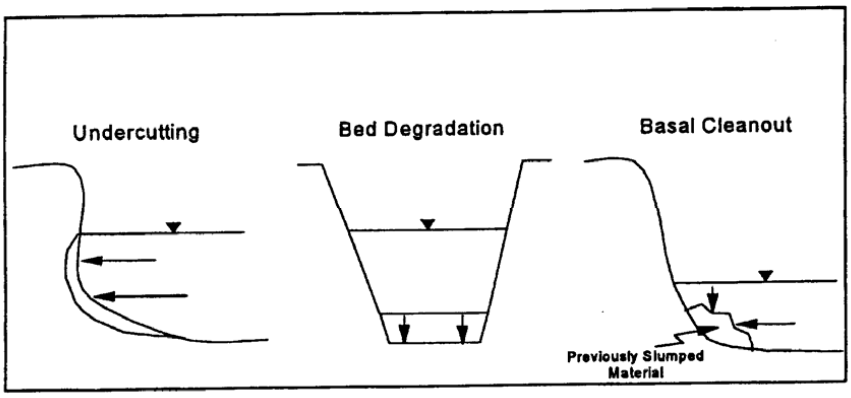

Figure 52. Schematic of hydraulic fluvial processes (Source: Watson and Basher, 2006)

Bed Degradation: It occurs when the erosive power of flowing water increases to a point that sediments on a channel bed are mobilized and eroded. The erosion process is usually in the vertical direction and it effectively increases the bank height and steepens the bank slope, making the bank more susceptible to undercutting and mass failure.

Basal Cleanout: It is a process of removing the supportive or protective materials at the bank toe. This usually occurs at high flows. The protective materials may be placed or from mass failures. Repeated cycle of basal cleanout, undercutting, mass failure, and bank toe accumulation plays an important role in controlling the retreat rate of a stream bank.

Undercutting: It is the direct removal of bank materials laterally by the flowing water. Undercutting may be due to local effects such as presence of debris and vegetation, bank soil characteristics such as poor drainage, and/or presence of layer of non-cohesive materials. It occurs often on the outside bank of a meander bend. Undercutting is an important process for the initiation of mass failures with the cohesive material banks.

4.2.2 Mass Failure Processes

Gravitation plays a key role in mass failure. Different classifications have been proposed. One classification is according to Watson and Basher (2006) who divided mass failure mechanisms into six categories, as described below.

Dry Granular Flow: It is a process in which individual sediment grains roll, slide and bounce down the bank in a layer. Eroded loose sediments usually accumulate near bank toe in the form of cones and fans. This type of failure typically occurs on non-cohesive banks at the angle of repose. When toe or wetted bank is hydraulically eroded, the angle of bank increased above the friction angle and dry granular flow occurs.

Shallow Slide: It is a process on the bank where a layer of material moves along a plane parallel to the bank surface (Figure 53). Such failure mechanism often occurs on banks whose soils have low cohesion and angles are moderately steep, and when the angle of the bank, due to hydraulic fluvial process, exceeds the angle of internal friction of the bank material. Shallow slide failure often occurs as a secondary failure following rotational and/or slab failures (Thorne, 1998).

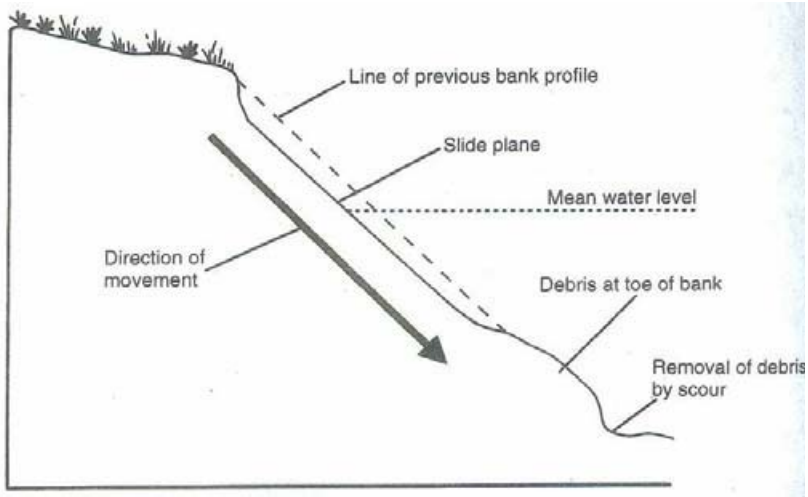

Figure 53. Schematic of shallow slide (Source: Watson and Basher, 2006)

Rotational failure: It is a deep-seated movement of material both downward and outward along a curved slip surface (Figure 54). After failure, the upper slope of the slipped block is typically tilted inward toward the bank. The failure is often

linked to the formation of vertical tension cracks within the bank structure and/or high pore pressure within the bank material. It often occurs during rapid drawdown following high flow events on the highest banks. Rotational failure commonly occurs on cohesive banks with tall bank height and shallow profile. Its occurrence is less common, however, according to Simon (see BSTEM, 2009). Rotational failure produces greater sediment volume than planar failure (Dapporto *et al.* 2003).

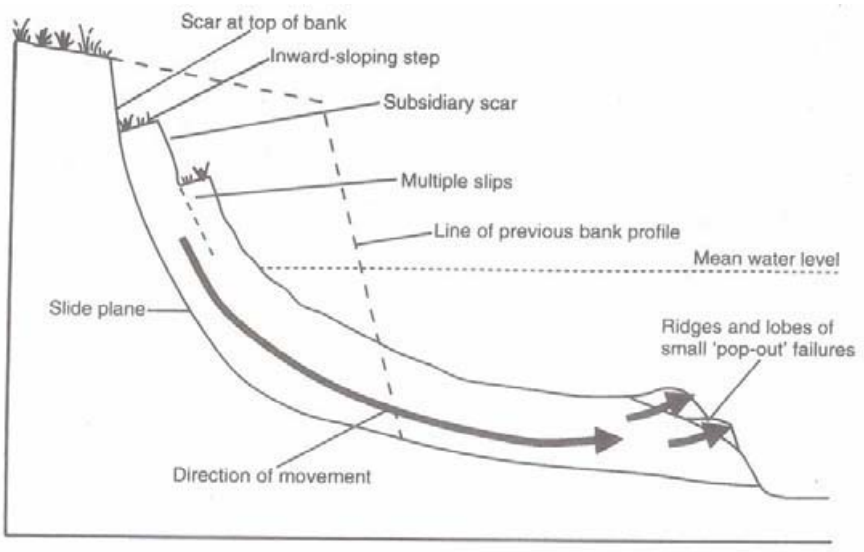

Figure 54. Schematic of rotational failure (Source: Watson and Basher, 2006)

Planar (or Slab) Failure: It is the sliding and forward toppling of a deep-seated mass into the channel (Figure 55). It results from a combination of factors: scour at the bank toe, high pore pressure in the bank material, and the development of tension cracks at the top of the bank. Failed material accumulates at the lower section of the bank and it can offer temporary protection of the bank. Vertical tension cracks, forming at a distance from the river bank, often characterize the planar failure. Desiccation and tension can develop rapidly and cracks develop due to stress release. Tension cracks reduce the effective length of the potential failure surface and hence decrease bank stability. Crack development can also allow surface and subsurface flows to drain into the bank, increasing seepage forces and reducing bank stability. Planar failure occurs often on steep, low height, fine-grained cohesive banks, and it tends to occur during lower flow conditions. Planar failure is more common according to Simon (see BSTEM, 2009).

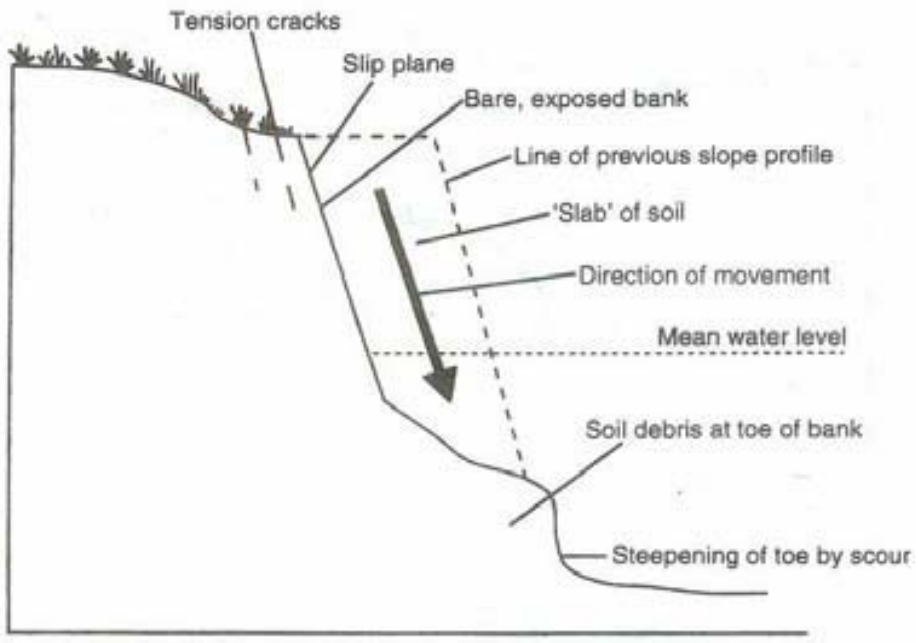

Figure 55. Schematic of planar failure (Source: Watson and Basher, 2006)

Cantilever Failure: It is the collapse of an overhanging block into the channel (Figure 56). Cantilever failure is the result of significant undercutting, and it tends to occur on banks with composite layers of fine/coarse and/or cohesive/non-cohesive materials (e.g., see a case illustrated in Figure 57). Cantilever failure is more active under low-flow conditions.

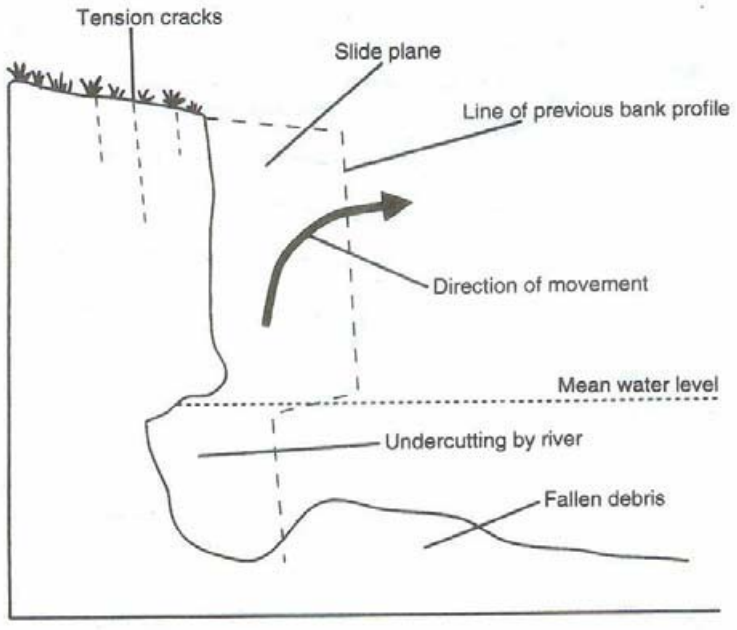

Figure 56. Schematic of cantilever failure (Source: Watson and Basher, 2006)

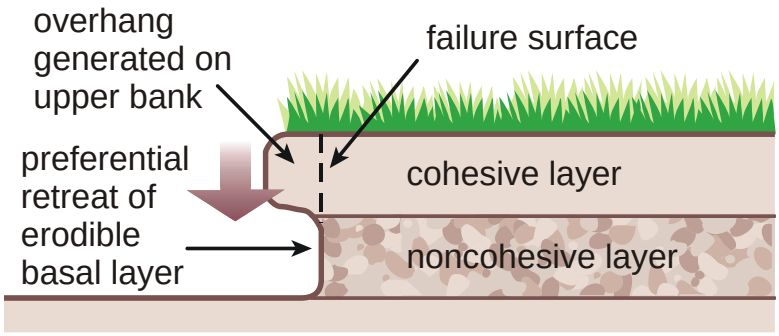

Figure 57. An illustration of a cantilever failure (Source: BSTEM, 2009)

Wet Earthflow: It is a process where the soil of a bank flows as a highly viscous liquid. The material flows down the bank to form lobes of material at the toe (Figure 58). Such material is extremely weak and is easily removed by hydraulic fluvial process, even at lower flows (Thorne, 1998). Wet earthflow is the result of significant loss of strength on a section of bank due to saturation and increased bank weight. Wet earthflow typically occurs on low-angle banks and banks subject to strong seepage and poor drainage. It is typically caused by waterlogging associated with high rainfall, snowmelt, or rapid drawdown of water in the channel.

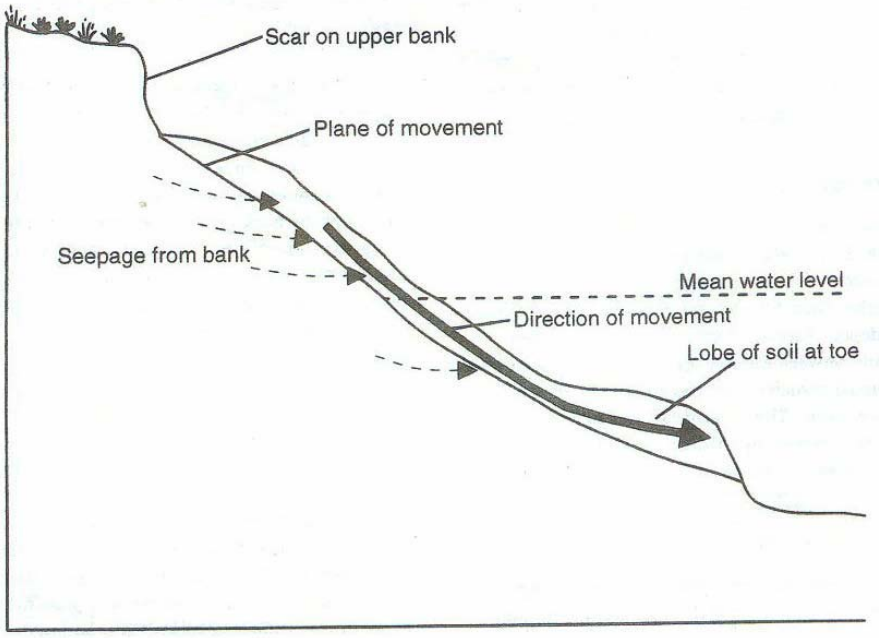

Figure 58. Schematic of wet earthflow (Source: Watson and Basher, 2006)

Simon (BSTEM, 2009) added another failure mode which needs to have a separate discussion: piping failure, as described below.

Piping Failure: It is the collapse of part of the bank due to high groundwater seepage pressures and seepage flows causing selective removal of sections of the bank. An illustrative process is shown in Figure 59. The failure is usually due to preferential ground water flow along inter-bedded saturated layers contained within stratified river banks, with lenses of sand and coarser material sandwiched between layers of finer cohesive material. Flow is induced in the more permeable layers by changes in river stage and/or ground water seepage. If the flow magnitude through the permeable lenses is capable of dislodging and transporting particles, material is slowly removed. This can lead to undermining of portions of the cohesive upper bank leading to planar or cantilever failures (Thorne, 1998).

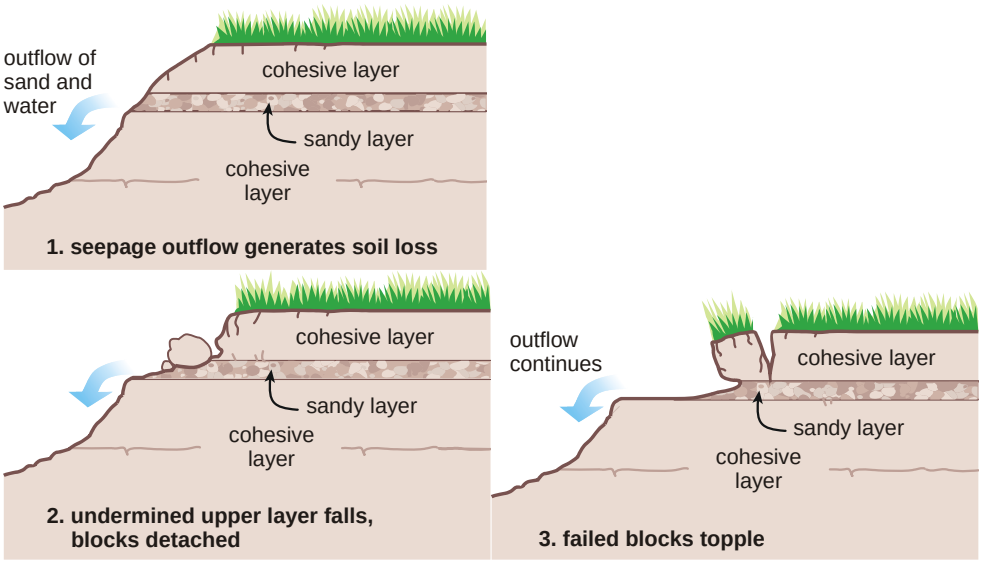

Figure 59. An illustration of piping failure (Source: BSTEM, 2009)

4.3 Important Factors Associated with Bank Erosion

Knighton (1998) provided a detailed discussion on factors influencing bank erosion processes. Some important factors are discussed below. Readers are also referred to Ott (2000) who provides an annotated bibliography related to the topic.

Flow Properties: Flow induced shear stress is the dominant factor causing hydraulic fluvial bank erosion process. A good estimate of flow and shear stress distribution on the bank is important, as the removal of bank material by hydraulic action is closely related to near-bank velocity and its gradient close to the bank. High flows not only remove material directly from the bank but also scour the base, leading to bank over steepening and subsequent mass failures. Important flow properties include magnitude, frequency and duration of flow discharge, magnitude and distribution of stream velocity and shear stress, and level of turbulence.

Channel Geometry: It is related to width, depth, slope of channel, and stream curvature (concave, convex, straight). Channel geometry affects the hydraulic forces

causing bank erosion and is important when considering the distribution of bank erosion along a channel reach. For example, high rates of erosion commonly associated with stream curvature results from the higher velocity gradients and hence higher shear stresses against the outer banks of channel bends. Different channel geomorphic units (e.g., pools, riffles, runs) are associated with different flow velocity and stream gradient, and hence shear stress on the bed and banks. The geometry of the stream cross-section is a good indicator of the potential for stream bank instability.

Bank Geometry: It is characterized by height, slope, length, profile, and shape. Bank height and slope are critical parameters when assessing stream bank erosion potential, particularly when dealing with cohesive bank material (Rosgen 1996; Dapporto et al. 2003). Failures occur when the erosion of the bank and the channel bed adjacent to the bank, have increased the bank's height and steepness to a point where it reaches a condition of limiting stability. The mechanics of failure are then dependant on the properties of the bank material and the geometry of the bank at the point of collapse.

Bank Material: Bank properties include size, gradation, cohesiveness and stratification of bank materials. A bank can be broadly classified as non-cohesive, cohesive, and stratified. Non-cohesive bank materials are relatively coarse grained and are usually well drained. As a result, pore water pressure is seldom a significant problem (Thorne and Tovey, 1981). Erosion tends to occur grain-by-grain, in the form of dry granular flow. Cohesive bank are less susceptible to erosion grain-by-grain, but can be eroded rapidly by mass movement due to gravity and positive pore water pressure. Since cohesive materials are more likely to be poorly drained, positive pore water pressure can develop, particularly during rapid drawdown in the channel (Thorne and Tovey, 1981). The stability of cohesive banks is also affected by the presence of tension cracks. These are near-vertical cracks which develop from the ground surface downwards at some distance back from the bank. They result from the tensile stress exerted on the upper part of the bank close to a steep slope. Tension cracks adjacent to river banks can extend to a considerable portion of bank height, thereby weakening the overall stability of the slope. Weakening is further enhanced because cracks form pathways for water to move downward from the surface to lubricate a potential slide plane (Environment Agency, 1999). Stratified bank is generally the product of the history of local sediment deposition by the river. It consists of layers of materials of differing size, permeability and cohesion, resulting in a mixture of cohesive and non-cohesive materials (Simons and Li, 1982; Federal Interagency Stream Restoration Working Group, 2001). The non-cohesive layers are eroded more quickly, producing a stepped bank with benches formed in the more resistant material. In general, the combination and type of erosion features will more or less be dependant upon the sequence, or order, of layering within the exposed bank, and the properties of the individual layers and how these respond to changing hydraulic forces. Piping is also common in stratified alluvial banks.

Bank Soil-Moisture Conditions: They are related to soil moisture content, seepage, pore water pressure and piping. The process of weakening and weathering related to soil moisture conditions reduces the strength of intact bank material and decreases stability. The freeze-thaw cycle associated with frost action can play a

preparatory role in bank weakening by widening pre-existing cracks and loosening surface material to leave the bank more susceptible to future erosion. Hard dry banks are very resistant to erosion, while cycles of wetting and drying can cause swelling and shrinkage of the soil leading to the growth of fissures and tension cracks which encourage failure. Seepage forces can reduce the cohesion of bank material by removing clay particles, and may promote the development of soil pipes in the lower bank (Knighton, 1998). Cohesive stream bank material is normally in a condition of partial saturation, and consequently subject to negative pore water pressures (suctions) that produce an increase in apparent strength of the bank material. Negative pore water pressures in stream banks can fluctuate frequently due to rainfall, variation in river flow and evapotranspiration of the vegetation on the bank. During rainfall and rising stages, changes in bank storage cause an increase in water content and in pore water pressure due to the rising water table. During major events the bank material can become fully saturated, so that the apparent cohesion reduces and positive pore water pressure occurs. Under these conditions stability can still be maintained due to the confining pressure of the water in the stream on the bank face. However, bank failures are likely to occur particularly during rapid drawdown, when the bank material is still at or near saturation, and as the confining pressure of the water approaches zero (Casagli et al. 1999; Simon and Collison, 2001). Piping is common in alluvial banks. In stratified banks with lenses of sand and coarser material sandwiched between layers of finer cohesive material, flow is induced in the more permeable layers by changes in river stage (Simons and Li, 1982). If the flow through the permeable lenses is capable of dislodging and transporting particles, the material is slowly removed. This can lead to undermining of portions of the cohesive upper bank leading to gravitation-induced block failures.

Vegetation: It includes type, percentage of cover, age, root depth, and exposed roots. Vegetation provides a protective cover which helps to absorb the forces exerted by flowing water. It also influences the mechanical strength of bank material, as roots increase the shear strength of the soil (Watson and Marden, 2004). Plant evapotranspiration can contribute to better drained and drier bank conditions. The height of the stream bank in relation to rooting depth can be critical. With low banks roots are likely to cross any potential slide plane and provide reinforcement. If bank height is greater than the rooting depth, any potential slide plane is likely to pass below the rooted layer and undercutting of the lower unrooted layer may promote cantilever type failures (Environment Agency, 1999). Trees and shrubs leaning over the water may lead to failure of steep banks if they fall and dislodge soil as they uproot.

Storm frequency: It is characterized by rainfall intensity and duration, and is related to the pore-water pressure, seepage flow, and piping failure. The amount of precipitation in a storm, a measure of flood duration, is not necessarily important when considering bank failure (Simons and Li, 1982). Bank retreat, notably mechanical failures under gravity, is more closely related to pre-storm soil conditions produced by antecedent rainfall. Smaller floods attacking thoroughly wetted bank material during the winter months can produce more

extensive and severe erosion than large summer storms that occur when bank material is hard and dry and not easily eroded. Multi-peaked flows, which are more characteristic of winter months, may be more effective than single flows of comparable or greater magnitude, because of increased incidence of bank wetting. The degree of preparation of the bank material can give a seasonal effect to the erosion process (Knighton, 1998).

4.4 Bank Erosion Model Review

Many watershed-based erosion models, e.g., SHESED, WEPP, CREAMS, and Mike-11, have modules for predicting in-stream sediment transport, routing, and bed erosion, but often neglect the contribution of bank erosion to sediment load (Merritt et al., 2003). Bank erosion, as discussed before, may contribute up to 80 to 90 percentage of the sediments transported for some streams. Therefore, it is imperative that it is taken into account for some rivers.

Existing bank erosion modeling may be classified into two categories (Chen and Duan, 2006): empirical models or process-based models. Empirical models are often used to predict the long-term equilibrium channel form under regime (stable) conditions; process-based models attempt to incorporate various physical processes into consideration to provide short to medium range erosion.

4.4.1 Empirical Models

Most empirical models rely on regime formulas developed from field observations. Regression analyses were used to correlate the geometry of equilibrium channels with basin characteristics, such as drainage areas (Dunne and Leopold, 1978; Montgomery and Gran, 2001), bankfull or effective discharge (Leopold and Maddock, 1953; Hey and Thorne, 1986; Kellerhals and Church, 1989; Knighton, 1998), and sediment size (Schumm, 1968; Ferguson, 1973). For example, in SEDNET (Sediment River Network model developed for Australia; Prosser *et al.* 2001), the rate of bank retreat (*BE*, m/yr) along any river segment is calculated as a function of bankfull discharge ($Q_{1.58}$) as

$$BE = 0.008 Q_{1.58}^{0.6} \tag{4.1}$$

This function was derived from an analysis of global river bank migration data. The flux of sediment is calculated from the length of each segment, bank height, and sediment bulk density, and applied to the proportion of the river bank not protected by riparian vegetation. Dickinson et al. (1989) used a similar empirical approach to predict bank erosion rates in Ontario, Canada:

$$Y_b = 2 * 10^{-10} \left(K^{2.5} A_{gf}^{7.2} \right) + 1.75^{(0.5/H_s)} \tag{4.2}$$

where Y_b is bank erosion rate (cm/yr), K is the USLE soil erodibility factor, A_{gf} is a numerical index of agricultural intensity, and H_s is the ratio between the critical flow depth for initiation of bed material transport and the bank-full flow depth.

These empirical equations have been widely applied to predict regime conditions of alluvial channels. However, these models have also been used by some to unstable channels and scenarios beyond their useful applicability range, as discussed by Simon et al. (2007). Actually, these models are not suitable to predict unsteady response of an alluvial channel to disturbances.

Some empirical models resort to extremal theories to predict the equilibrium channel form. Extremal theories assume that alluvial channels attain equilibrium when an "indicator variable" reaches the maximum or minimum (ASCE Task Committee, 1998). Various indicator variables have been proposed, including the minimum stream power (Yang, 1976; Chang, 1979), the maximum sediment transport efficiency (Kirkby, 1977), the maximum sediment transport capacity (White et al., 1982; Millar and Quick, 1993; 1998), the minimum variance (Williams, 1978), and the principle of least action (Huang and Nanson, 2000; Eaton et al., 2004). The width of the equilibrium channel was also determined using the threshold concept of sediment incipient motion (Glover and Florey, 1951; Lane, 1955), or by accounting for the lateral diffusion of downstream momentum (Parker, 1978; Ikeda et al., 1988; Ikeda and Izumi, 1990; Kovacs and Parker, 1994; Vigilar and Diplas, 1997). Despite its theoretical attractiveness and some claims of success, extremal theories in general are used infrequently to predict the width adjustment process, which often is of greater interest than the shape of the equilibrium channels (Sun et al., 1996).

Other empirical relations have also been developed by correlating the reach-averaged rate of meander migration to basin characteristics, channel geometry, and flow parameters (Hooke, 1980; Nanson and Hickin, 1983; ASCE Task Committee, 1998). The rate of meander migration, defined as the distance of bank retreat perpendicular to the bank line, was obtained by superimposing meandering courses over a sequence of maps or photographs. However, the regression coefficients in empirical formulas varied significantly from one locality to another (ASCE Task Committee, 1998). For example, Larsen (1995) analyzed nearly 200 bends in the Mississippi River and found that the bend migration rate showed no significant correlation with the local radius of curvature. In addition, Larsen (1995) also showed that empirical or statistical methods may be applicable only to the case studied and, therefore, they are not adequate in establishing a general physical law that governs the evolution of river meander.

Rosgen (1996, 2001) describes a practical method to predict bank erosion rate from two types of river systems in the United States. A bank erosion hazard index (BEHI), velocity gradient, and near-bank stress are used to predict bank erosion rate. BEHI is rated from field measurements of (a) the ratio of stream bank height to bankfull stage height; (b) bank angle; (c) the ratio of root depth to bank height; (d) root density; (e) the amount of bank surface protection given by roots and

other woody debris; (f) soil stratification (bank material stratigraphy and presence of soil lenses); and (g) particle size (the composition of stream bank materials). Each of these factors is assigned a rating based on criteria and diagrams published in Rosgen (1996, 2001), and is used to derive BEHI. Published data on velocity profiles in streams is used to obtain velocity isolevels and gradients, and the stream width is divided into thirds to apportion the near-bank shear stress. The velocity gradient and near bank shear stress are then converted into ratings. BEHI and near bank stress are integrated in graphical form to predict bank erosion rate. Despite the widespread use of the method, the limitation of the method has been extensively discussed by, e.g., Simon et al. (2007). The method is also problematic in predicting unsteady response of an alluvial channel.

In view of the complexity involved in application, plus immaturity, with the processed-based models, the empirical based models will continue to see their applications, and useful information may be obtained as long as users are aware of the limits and bounds of the method used.

4.4.2 Process-based Models

Much research has been conducted to develop process-based bank erosion models, as these models hold better promise to predict unsteady erosion processes. The process-based models are often used to estimate the local retreat rate of a bank; and frequently, they are incorporated into analytical and/or numerical models.

A simple bank erosion model was proposed by Ikeda et al. (1981) who assumed that the rate of bank erosion was linearly propositional to the magnitude of near-bank velocity perturbation. The difference between depth-averaged near-bank velocity and cross-sectional mean velocity was used. This model was employed in numerous subsequent analytical studies, mostly related to the meander migration models (e.g., Parker et al., 1982; Parker, 1983; Parker and Andrew, 1986; Johannesson and Parker, 1989; Odgaard, 1989; Larsen, 1995; StØlum, 1998; Sun et al., 1996, 2001a,b). However, this assumption is unrealistic, because bank retreat and advance depend also on many other factors, as discussed above. For example, one of the important processes impacting bank erosion is removal or accumulation of sediment at the bank toe where the near-bank excess velocity may be less or greater than zero. Also, the model does not take bank geometry, properties, and geotechnical information into account.

Other simple models were proposed. For example, Crosato (1989) and Odgaard (1989) assumed that the bank erosion rate is proportional to excess near-bank water depth; Mosselman (1992) combined both the excess shear stress and excess bank height mechanisms to compute the rate. In general, these similar simple models are restricted to artificial morphologies tied to idealized representations of the river planform, such as the most probable path or sine-generated curve (Langbein and Leopold, 1966; Thakur and Scheidegger, 1970). They are limited in scope because natural rivers often have irregular shapes.

Osman and Thorne (1988) developed a process-based model, based on the factor of safety analysis, which became widely used. The model predicts channel-width adjustment by taking the combined effects of lateral erosion and mass failure into account. A spreadsheet-based model was developed by Thorne and Abt (1993) to predict bank instability due to toe scour and lateral erosion, based on the work of Osman and Thorne (1988). The model requires inputs such as total and submerged bank height, bank slope, soil density, friction angle, cohesion and a tension crack index. In this model, the initial factor of safety of the bank with respect to planar failure is computed to assess the bank stability. The model may be used to test the sensitivity of bank stability to changes in the engineering properties of the bank material, to analyze the response of bank stability to toe erosion and/or lateral erosion, and to find the geometry of the failure surface and failure block.

The model of Osman and Thorne (1988) has been modified and advanced by a number of researchers. For example, Simon et al. (1991, 1999) and Rinaldi and Casagli (1999) took into account the pore water pressure in bank and the confining hydrostatic pressure in the channel; Dapporto et al. (2003) investigated the role of river stage and pore water pressure in triggering planar and cantilever failures and two types of stability analysis were used: (1) the limit equilibrium method was used to predict the effect of pore water pressure on bank stability; an d (2) a seepage analysis based on hydrographs of different return periods was used to assess the effect of river stage and pore water pressure on bank stability; Pollen and Simon (2005) combined the bank stability model with a model of root reinforcement from riparian vegetation to predict the effect of different tree species on bank stability. A number of limitations of the factor of safety analysis models were identified by Darby and Thorne (1996). They include: use of idealized bank geometry; inadequate representation of tension cracks; constraints on location of the failure plane (at the bank toe only); inadequate treatment of soil pore water pressures and hydrostatic confining pressure from water in the channel; and inability to simulate failure over a wide range of bank slope. Some modifications and developments were proposed by Darby and Thorne (1996), particularly for steep cohesive stream banks.

Among process-based models based on the factor of safety analysis discussed above, the BSTEM model, developed by Simon et al. (2000), represents probably the current state-of-the-art. The BSTEM model is part of the development work in this project; therefore, a detailed description will be provided later in this chapter.

Major difficulties to apply bank erosion models lie in the accurate prediction of basal erosion and incorporation of sediment transport in the streams. A major advancement to improve the bank erosion modeling is to resort to numerical models. In recent years, numerical models are emerging as alternative tools to simulate and understand the morphological process of alluvial channels. These models often link the stream fluvial processes directly to the bank erosion process, and have the capability to take many physical processes into account and

to predict unsteady migration processes. Some of the important works include: Mosselman (1998), Nagata et al. (2000), Duan et al. (2001), Darby et al. (2002), Olsen (2003), etc.

Most numerical models incorporate bank erosion models into two-dimensional (2D), depth-averaged models of flow and sediment transport. Mosselman (1998) was one of the few early attempts in which the excess bank height bank erosion model and the quasi-steady 2D model are coupled. The model was applied to a reach of the River Ohre; but poor results were obtained. He attributed the poor performance to the formulation of the bank erosion mechanism or the calibration of the bank erosion parameters. Also, the 2D flow and sediment transport model was also to "blame", leading to recommendations for further improvement of the 2D model, and even the use of 3D models.

Nagata et al. (2000) developed a coupled model of bank erosion and a 2D morphological model. The basic equations were cast in a moving boundary fitted coordinate system; and a new formulation of non-equilibrium sediment transport was introduced to reproduce the channel processes. The model was applied to examine the morphological behavior of experimental channels. The bank erosion model, however, was limited to the non-cohesive banks with the angle of repose method used. Also, the model neglected the difference between basal erosion and bed degradation.

Duan et al. (2001) solved the two-dimensional, depth-averaged equations, along with a bank erosion model based on the angle of repose for non-cohesive banks. The bank erosion model was derived from a mass conservation analysis of sediment transport near the bank. The rate of bank retreat was linked to the longitudinal gradient of sediment transport, strength of secondary flow, and erosion of sediment from the bank. Although sediment transport and basal bank erosion were considered, the geotechnical bank failure of cohesive bank material following basal erosion was not considered. As a result, the simulated meandering wavelength and amplitude did not agree with the observations for the case modeled.

Darby et al. (2002) coupled a new bank erosion module to the 2D, depth-averaged model RIPA. The bank model allowed the basal erosion of cohesive bank material and subsequent bank failure. Particularly, they considered the deposition of failed bank material at the toe of the bank and its subsequent removal. The rate of basal erosion of cohesive material was based on a simple model (ASCE Task Committee, 1998), where the rate of basal erosion was an exponential function of the excessive shear stress. The volume of bank failure was calculated from the model of Osman and Thorne (988). The eroded bank material was divided into three groups according to grain size, and transported or deposited at bank toes as bedload or suspended load.

Some authors see the need to go beyond the 2D depth-averaged modeling, at least for some applications. Darby *et al.* (2004) described attempts to use a

Computational Fluid Dynamics (CFD) approach to model the shear stress on a river bank causing bank erosion in meandering rivers. Field based data sets (topographic, hydraulic, bank erodibility and retreat) from two rivers in Italy and UK were used to parameterize and verify the model. Olsen (2003) developed a full three-dimensional (3D) CFD model that was applied successfully to simulate the formation of meandering streams in the laboratory. A 3D CFD model may compute a more accurate flow field for cases which have complex flow hydraulics that vary both laterally and vertically.

4.4.3 Summary

The above review leads to the following conclusions and observations:

- Despite the existence of a range of bank erosion models, most have limited application and scope. The process-based bank stability models are particularly in their infancy for cohesive banks.
- Among all process-based models, the BSTEM model seems to be the most general and represents the current state-of-the-art. Previous studies suggested that a good and accurate flow and sediment transport is necessary before process-based models are calibrated and verified.
- Most numerical models have certain limitations related to (1) a simplified flow and sediment transport numerical model applicable only to idealized cases; (2) simple bank erosion models which do not take into account of key physical processes; and (3) limited calibration and verification of the numerical model. In this project, we seek to overcome most of these limitations.

4.5 Proposed Bank Erosion Models

SRH-2D version 3 is a 2D depth-averaged flow and sediment transport model developed at Reclamation, well tested and verified. It has been developed for applications to natural rivers. Therefore, we believe we are in a unique position to couple the SRH-2D to bank erosion models to assess the current-state-of-the-art in bank erosion modeling.

Two inter-related physical processes are at play for bank erosion modeling: hydraulic fluvial process and mass failure process (bank collapse), as reviewed in the above. Only the fluvial processes on the bank are relevant for bank erosion modeling.

Basal erosion refers to the fluvial entrainment of bank material by flow-induced forces acting on the bank surface – drag force, resistance force, and lift force. Particularly, erosion at the bank toe is the main initiator for bank collapse. Therefore, it is critical to determine how to compute the basal erosion which is discussed next.

Two bank erosion models are proposed to be implemented into SRH-2D: A non-cohesive bank model and a cohesive multi-layered bank model.

The non-cohesive bank erosion model will model the dry granular flow process, intended for non-cohesive banks. The model may also be applied to the shallow slide process which occurs often on banks with low cohesion (the friction angle replaces the angle of repose). The angle of repose method is used to compute the bank retreat rate.

The more general cohesive multi-layered bank model adopts the BSTEM model as the bank erosion module (BSTEM, 2009). Collaboration between the Bureau of Reclamation and National Sedimentation Lab (NSL), Agricultural Research Service (ARS), U.S. Department of Agriculture (USDA) has been established to develop a joint bank erosion model, which would take advantage of both SRH-2D and BSTEM. The cohesive bank model is capable of modeling planar failure and cantilever failure. The ability of the model for the rotational failure is yet to be investigated. At present, however, the wet earthflow and piping failures are not modeled, due to limited knowledge and understanding of these failure mechanisms. However, piping failure is under research currently at NSL/ARS by incorporating the ground water model into BSTEM.

4.5.1 A General Discussion of Basal Erosion

Among the three hydraulic fluvial processes, bed degradation has been simulated by the SRH-2D model, and so it needs no special treatment. Undercutting is a process that cannot be modeled within the 2D depth-averaged modeling framework. However, undercutting can be modeled with the BSTEM module where a simplified approach used. Therefore, the non-cohesive bank erosion model will be able to handle undercutting through BSTEM module. The basal erosion discussed below then is limited to the basal cleanout, which may be modeled more accurately with SRH-2D than other 1D or simplified methods.

One of the approaches is to compute basal erosion directly with the 2D sediment transport model such as SRH-2D. That is, “vertical” erosion is computed over all wetted areas of a channel, including the bank. This approach is similar, if not equivalent, to the control volume approach proposed by Hasegawa (1981), and subsequently adopted by Nagata et al. (2000), Duan et al. (2001), and Chen and Duan (2006). There are drawbacks with the approach: flat bed degradation has to be assumed from bank toe to half the channel width. The definition of “half-channel-width” is applicable only to simple geometry and it is hard to be implemented in general. Also, “vertical” erosion on a steep wetted bank may not be accurate with the depth-averaged model. Errors come from several sources: steep bank, limited mesh points on bank, and difficulty in specifying different materials on the bank with layers.

An alternative method is proposed in this study. In our approach, a bank toe point is designated. One side of the toe point represents bank and the other side is

channel bed of any slope and shape. Movement of the toe point is computed first - it consists of the vertical movement (ω_V) and the lateral movement (ω_L). The vertical component is obtained with the 2D mobile-bed model (SRH-2D in this study), while the lateral component is computed with an empirical formula. The vertical erosion rate computed by SRH-2D is relatively accurate. The lateral rate of bank toe erosion may be computed with a number of approaches discussed below.

A popular method to compute the lateral erosion rate is based on the excess shear stress (e.g., Darby et al., 2002; Darby, 2007; Simon, 2003; etc.). The lateral rate of toe movement is computed by:

$$\omega_L = k(\tau - \tau_c)^a \tag{4.3}$$

The exponent (a) is usually one. The erodibility and critical shear stress can be estimated readily for granular materials and obtained through in-situ jet tests for cohesive materials. A discussion was provided by Darby (2007). Also, a regression relation has been proposed by BSTEM (2009), which relates the erodibility to the critical shear stress. Use of the regression relation reduces the two model parameters to one. When the in situ data are not available, the critical shear stress may be selected as a calibration parameter.

Another approach was proposed by Chang and Hill (1976) and used, e.g., by Chen and Duan (2008). It may be expressed as

$$\frac{\omega_L}{\omega_V} = \frac{\tau - \tau_{cL}}{\tau - \tau_{cV}} \tag{4.4}$$

where τ, τ_{cV} and τ_{cL} are shear stress, critical shear stress for stream bed material, and critical shear stress for bank toe material, respectively. Note that critical stress may be obtained with the method of Shields' Diagram for the granular materials and it may be measured or estimated through calibration for the cohesive bank toe.

Other methods are possible, for example, Duan and Julien (2005) used an analytical expression for lateral toe erosion. However, they are less tested.

4.5.2 Non-Cohesive Bank Model

The non-cohesive bank erosion model is developed first as a separate module, which paves the way for addition and development of more advanced models. The angle of repose is used as the major parameter for bank retreat analysis. In this study, the bank material mass conservation principle is used to derive the bank retreat rate so that the total amount of bank materials removed is compatible with the amount removed by stream water on the bank under the water surface.

Derivation of Bank Retreat Rate

Refer to Figure 60. Assume the initial bank is G'ABC (G'AB is under water) and the bank is already at the angle of repose. A is bank toe, C is bank top, and G' is the mesh node adjacent to A. After a time step, toe A would be eroded vertically to A' and G' to G, as computed by SRH-2D. By applying the separate lateral erosion of the toe, A' would move to F (see discussion above). A new bank, therefore, would be GFBC assuming that erosion on AB is linear. Since the new bank angle would exceed the angle of repose, the bank material above B would "fail" to reduce the bank angle to the angle of repose. The failed materials would fill the toe area. Therefore, the "final" bank profile would be GDIE. Note that there are two possibilities for the final location of toe D, depending on the local conditions: D may be on the left or right of point A (on the channel or bank side of A). In Figure 60 and the derivation discussed below, D is assumed to be on the left; but it is "forced" to be the same as A. This would lead to the bank retreat rate equation derived to be more general than the scenario if D is on the right of A. As mentioned later, the bank retreat equation for the scenario of D being on the right is a special case of the scenario of D being on the left.

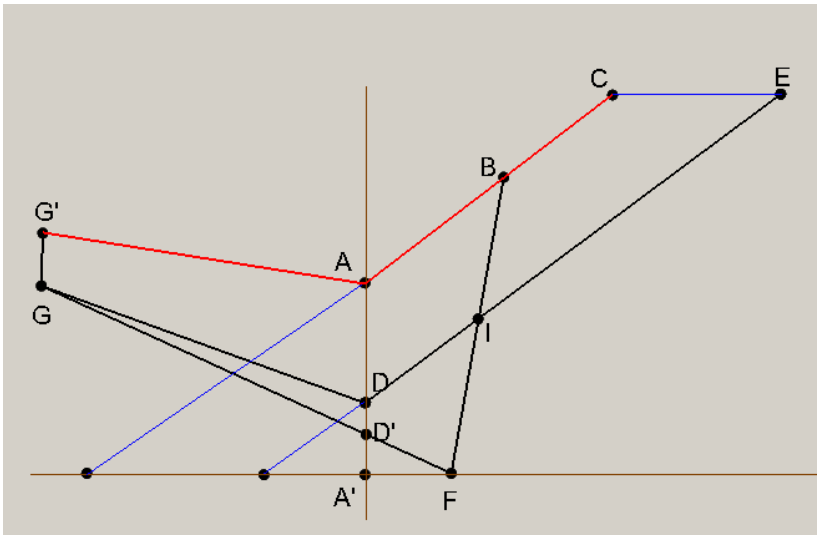

Figure 60. Illustration of bank retreat computation for non-cohesive bank model

Volume conservation requires the following (e.g., *IBCE* refers to the area contained within the polygon):

$$IBCE = GDIFD' \tag{4.5}$$

With some derivation, the bankline retreat distance r_B can be computed by the following equation:

$$r_B = 0.5\,\frac{(h_0+\omega_V)(\omega_L+\dfrac{\omega_V}{\tan\alpha})+|GD|\omega_V}{(H_0+\omega_V)+0.5|GD|\tan\alpha} \tag{5.6}$$

In the above, h_0 is initial water depth at toe, H_0 is initial bank height, α is the angle of repose, ω_V is the vertical erosion distance of toe predicted by SRH-2D, ω_L is lateral erosion distance of toe predicted by a lateral equation, $|GD|$ is the horizontal distance between G and D. The above derivation procedure is a generalization of the method of Chen and Duan (2006).

The bank retreat distance r_B for the scenario that D being on the right of A can be similarly derived and the final form is the same as equation (6) by setting $|GD|$=0. So it is not presented separately.

Further, if SRH-2D predicts that there is deposition at toe A, the bank is assumed to intrude towards the stream. The bank intrusion distance is similarly computed and is not repeated.

Moving Mesh Formulation

The numerical model has to accommodate the bank retreat. There are two methods that may be used: the fixed mesh method and the moving mesh method. With the first, a fixed mesh is used when bank retreats. It has the advantage that mesh is fixed so no additional mesh movement and the associated geometric computation and variable interpolations are needed. However, the bank line does not align with the mesh line. It leads to a series challenge: how to represent the bank retreat accurately using the nearby mesh nodes. Often, much refined mesh is required, increasing the computational cost significantly or the accuracy is seriously in question. The moving mesh approach aligns the mesh line with the bank line initially, and the "alignment" is enforced continuously throughout the bank retreat process. The advantage now is that the bank retreat may be computed and represented accurately. However, the mesh has to be "moved" every time the bank retreats, and re-mesh needs to be carried out continuously and geometric quantities, as well as some flow variables, need to be updated or interpolated. In this study, the moving mesh approach is adopted as its advantage outweighs the drawback. Also, we believe we have adopted a relatively efficient moving mesh method so that the method is more efficient and accurate than the fixed-mesh method. The method is described below.

We adopt the Arbitrary Lagrangian-Eulerian (ALE) formulation for moving mesh problem, as developed by Lai and Przekwas (1994). With this formulation, a mesh may be "moved" in an arbitrary way. When the governing equations are expressed in integral form with an arbitrarily moving mesh cell, they are expressed as:

$$\frac{d}{dt}\int_A h dA + \int_S h(\vec{V} - \vec{V}_g) \bullet d\vec{s} = 0 \tag{4.7a}$$

$$\frac{d}{dt}\int_A h\vec{V} dA + \int_S h\vec{V}(\vec{V} - \vec{V}_g) \bullet d\vec{s} = \int_S h\vec{\bar{\sigma}} \bullet d\vec{s} + \int_A \vec{S}_V dA \tag{4.7b}$$

$$\frac{d}{dt}\int_A h\phi dA + \int_S h\phi(\vec{V} - \vec{V}_g) \bullet d\vec{s} = \int_S h\vec{q} \bullet d\vec{s} + \int_A S_s dA \tag{4.7c}$$

In the above, (4.7a) is the mass conservation equation, (4.7b) is the momentum conservation, and (4.7c) is any scalar transport equation (e.g., sediment size class equations); A is an arbitrary moving mesh cell, S is the side (edge) of the cell with vector representing the unit normal, $\vec{V}$ is fluid flow velocity vector (depth-averaged), $\vec{V}_g$ is the mesh grid velocity vector, and the rest corresponds to the terms the same as the non-moving-mesh form of the governing equations. It is seen that the above equations introduce an extra unknown, namely the grid velocity $\vec{V}_g$. The grid velocity is computed using a geometric constraint called the space conservation law written as:

$$\frac{d}{dt}\int_A dA = \int_S \vec{V}_g \bullet d\vec{s} \tag{4.8}$$

Refer to the paper of Lai and Przekwas (1994) for a detailed explanation of how equation (4.8) is used to compute an accurate grid velocity. Once $\vec{V}_g$ is known, the solution of governing equations in equation (4.7) is similar to the non-moving-mesh method presented in the SRH-2D document.

An advantage of the ALE method is that all flow and sediment variables represented by the mesh cell are automatically computed and there is no need for additional interpolation. The only variable that needs to be interpolated after mesh movement is the bed topography.

4.5.3 Cohesive Bank Model

A collaborative agreement between Reclamation and NSL in Oxford, MS has been established to jointly develop a cohesive bank erosion model combining SRH-2D and BSTEM. The basic theory was described by Simon et al. (2000). For completeness, a presentation of BSTEM is provided in Section 3.5.4 below. This section was written by Rob Thomas, at the University of Tennessee, Knoxville, TN, Andrew Simon at NSL, and members of Watershed Physical Processes Research Unit at NSL.

4.5.4 BSTEM Technical Description

4.5.4.1 QUANTIFICATION OF CHANNEL PROCESSES

Conceptual models of bank retreat and the delivery of bank sediments to the flow emphasize the importance of interactions between hydraulic forces acting at the bed and bank toe and gravitational forces acting on *in situ* bank materials (Carson and Kirkby, 1972; Thorne, 1982; Simon *et al*., 1991; Langendoen and Simon, 2008). Failure occurs when erosion of the bank toe and the channel bed adjacent to the bank increase the height and angle of the bank to the point that gravitational forces exceed the shear strength of the bank material. Streambank failure can occur by several mechanisms (Figure 61), including cantilever failures of undercut banks, toppling of vertically arranged slabs, rotational slumping, and wedge failures (Thorne *et al*., 1981). The type of failure reflects the degree of undercutting (if any) by fluvial scour or other mechanisms, and the nature of the bank materials. After failure, failed bank materials may be delivered directly to the flow and deposited as bed material, dispersed as wash load, or deposited along the toe of the bank as intact blocks, or as smaller, dispersed aggregates (Simon *et al*., 1991).

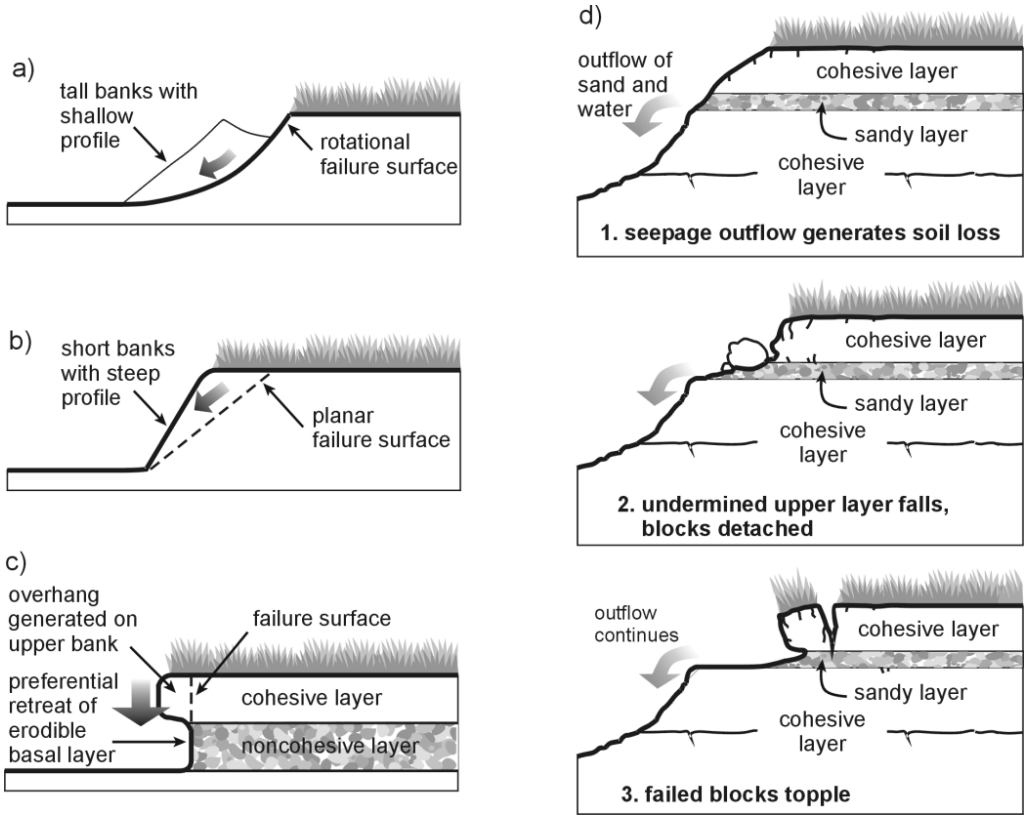

Figure 61. Selection of failure types observed in the field

4.5.4.2 QUANTIFYING GEOTECHNICAL STABILITY

The Bank Stability Model and Toe-Erosion Model (BSTEM; Simon *et al*. 2000) simulates failure types (b) and (c) and a modification of type (b) where a tension crack forms at the instant of failure. All these are shear-type failures that occur

when the driving force (stress) exceeds the resisting force (strength). BSTEM combines three limit-equilibrium methods that estimate the Factor of Safety (F_s) of multi-layer streambanks. F_s is the ratio between the resisting and driving forces acting on a potential failure block. A value of unity indicates that the driving forces are equal to the resisting forces and that failure is imminent (F_s = 1). Instability exists under any condition where the driving forces exceed the resisting forces (F_s < 1), conditional stability is indicated by F_s values between 1 and 1.3, with stable bank conditions having a F_s value of >1.3.

Quantifying the Resisting and Driving Geotechnical Forces

Soil shear strength varies with the moisture content of the bank and the elevation of the saturated zone in the bank mass. In the part of the streambank above the "normal" level of the groundwater table, bank materials are unsaturated, pores are filled with both water and air, and pore-water pressure is negative. The difference ($\mu_a - \mu_w$) between the air pressure, μ_a, and the water pressure in the pores, μ_w, represents matric suction. The increase in shear strength due to an increase in matric suction ($\mu_a - \mu_w$) is described by the angle ϕ^b. ϕ^b varies for all soils and with moisture content for a given soil (Fredlund and Rahardjo, 1993), but generally takes a value between 10º and 20º, with a maximum of the effective soil friction angle, ϕ', under saturated conditions (Fredlund and Rahardjo, 1993). The effect of matric suction on shear strength is reflected in the apparent cohesion (c_a) term, which incorporates both electro-chemical bonding within the soil matrix (described by the effective cohesion, c') and cohesion due to surface tension on the air-water interface of the unsaturated soil:

$$c_a = c' + (\mu_a - \mu_w)\tan\phi^b \qquad (4.9)$$

where c_a = apparent cohesion (kPa), c' = effective cohesion (kPa), μ_a = pore-air pressure (kPa), μ_w = pore-water pressure (negative if unsaturated), ($\mu_a - \mu_w$) = matric suction (kPa), and ϕ^b is the angle describing the increase in shear strength due to an increase in matric suction (degrees).

As can be seen from the above equation, negative pore-water pressures (positive matric suction) in the unsaturated zone provide for cohesion greater than the effective cohesion, and thus, greater shearing resistance. This is often manifest in steeper bank slopes than would be indicated by ϕ'. Conversely, the wetter the bank and the higher the water table, the weaker the bank mass becomes and the more prone it is to failure. Accounting for the effects of friction, the shear strength of a soil, τ_s, may thus be described by the Mohr-Coulomb shear strength criterion for unsaturated soils (Fredlund *et al*., 1978):

$$\tau_s = \frac{1}{F_s}\left[c' + (\mu_a - \mu_w)\tan\phi^b + (\sigma - \mu_a)\tan\phi'\right] \qquad (4.10)$$

where F_s = Factor of Safety, the ratio between the resisting and driving forces acting on a potential failure block, σ = normal stress on the shear plane (kPa) and ϕ' = effective angle of internal friction (degrees).

Whilst it is assumed that the pore-air pressure is atmospheric (i.e. $\mu_a = 0$), positive and negative pore-water pressures are calculated for the mid-point of each layer or slice based on hydrostatic pressure above and below the water table so that:

$$\mu_w = \gamma_w h \tag{4.11}$$

where μ_w = pore-water pressure (kPa), γ_w = unit weight of water (9.807 kN m^{-3}) and h = head of water above the mid-point of the layer or slice (m).

The geotechnical driving forces are controlled by bank height and slope, the unit weight of the soil and the mass of water within it, and the surcharge imposed by any objects on the bank top. The driving forces are gravitational, and may be computed by $S_d = W \sin \beta$. The force balance is illustrated in Figure 62.

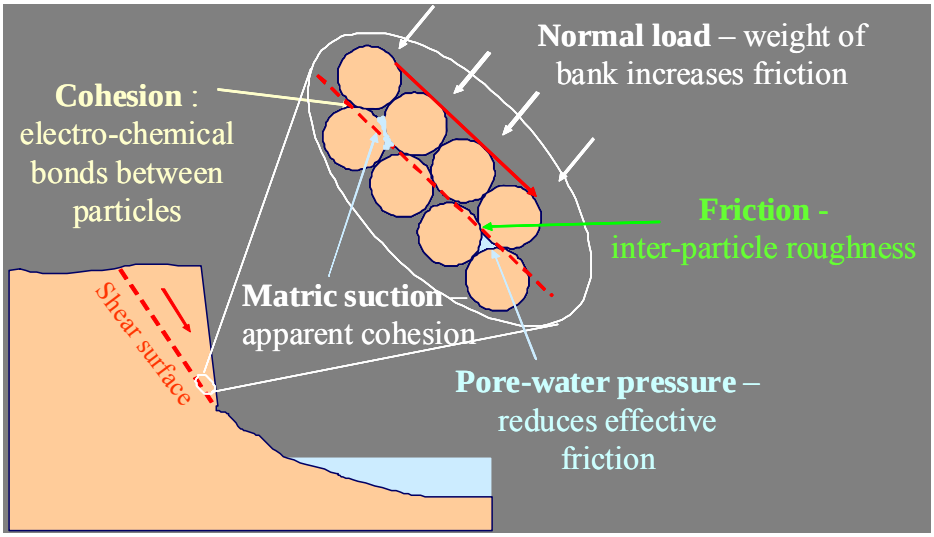

Figure 62.A graphical illustration of the factor of safety analysis for bank stability (Source: BSTEM, 2009)

A number of parameters may be field measured in the above bank stability model. The cohesion (c') and friction angle (ϕ') may be obtained using the borehole shear test (BST). The pore-water pressure may be measured with the tensionmeters and piezometers or inferred from water table height: $\mu_w = h\gamma_w$ [μ_w = pore-water pressure; h = head of water (m) relative to water table; and γ_w = unit weight of water (kN/m3)]. The matric suction may be measured directly with the digital tensionmeter. The only parameter which is hard to measure is the ϕ^b-parameter; its value ranges from 10 deg up to ϕ' at saturation. Some "ball-park" values for various soil types have been compiled by BSTEM model and they are reproduced in Figure 63.

Some "Ball Park" Figures

Soil Type	Statistic	c_a (kPa)	c' (kPa)	ϕ' (degrees)	γ_{sat} (kN/m^3)
Gravel*		-	**0.0**	**36.0**	**20.0**
Sand	75th percentile	5.8	1.0	32.3	19.1
	Median	2.9	**0.4**	**30.3**	**18.5**
	25th percentile	1.3	0.0	25.7	17.9
Loam	75th percentile	11.9	8.3	29.9	19.2
	Median	8.4	**4.3**	**26.6**	**18.0**
	25th percentile	4.6	2.2	16.7	17.4
Clay	75th percentile	18.0	12.6	26.4	18.3
	Median	11.0	**8.2**	**21.1**	**17.7**
	25th percentile	7.2	3.7	11.4	16.9

Figure 63. Some "ball park" values of the bank stability parameters used by BSTEM (Source: BSTEM, 2009)

Assessing the Potential for Geotechnical Failure

The methods employed within BSTEM are horizontal layers (Simon *et al*., 2000), vertical slices with tension crack (Morgenstern and Price, 1965; Langendoen and Simon, 2008), and cantilever failures (Thorne and Tovey, 1981). All three methods account for the strength of multiple soil layers, the effect of pore-water pressure (both positive and negative (matric suction)), and the confining pressure due to streamflow.

Horizontal Layer Method: The Horizontal Layer method is a further development of the wedge failure type developed by Simon and Curini (1998) and Simon *et al*. (2000), which in turn is a refinement of the models developed by Osman and Thorne (1988) and Simon *et al*. (1991). The Factor of Safety (F_s) is given by:

$$F_s = \frac{\sum_{i=1}^{I}\left(c_i' L_i + (\mu_a - \mu_w)_i L_i \tan\phi_i^b + \left[W_i \cos\beta - \mu_{ai} L_i + P_i \cos(\alpha - \beta)\right]\tan\phi_i'\right)}{\sum_{i=1}^{I}\left(W_i \sin\beta - P_i \sin[\alpha - \beta]\right)} \quad (4.12)$$

where c_i' = effective cohesion of i^{th} layer (kPa), L_i = length of the failure plane incorporated within the i^{th} layer (m), W_i = weight of the i^{th} layer per unit length of

stream channel (kN m^{-1}), P_i = hydrostatic-confining force due to the external water level (kN m^{-1}) acting on the i^{th} layer, β = failure-plane angle (degrees from horizontal), α = local bank angle (degrees from horizontal), and I = number of layers. The hydrostatic confining force, P_i, is calculated from the area of the confining pressure ($\gamma_w h$) by:

$$P_i = \frac{\gamma_w h^2}{2} \tag{4.13}$$

where h = head of water in the channel (m). The loss of the hydrostatic-confining force is the primary reason bank failures often occur after the peak flow and on the recessional limb of hydrographs.

Cantilever Shear Failure Algorithm: The cantilever shear failure algorithm results from inserting $\beta = 90°$ into equation (4.12) and simplifying. F_s is given by:

$$F_s = \frac{\sum_{i=1}^{I} \left(c_i' L_i + (\mu_a - \mu_w)_i L_i \tan \phi_i^b + \left[P_i \sin \alpha - \mu_{ai} L_i \right] \tan \phi_i' \right)}{\sum_{i=1}^{I} \left(W_i + P_i \cos \alpha \right)} \tag{4.14}$$

Put simply, the F_s is the ratio of the shear strength of the soil to the weight of the cantilever. The inclusion of α-terms in equation (4.14) ensures that if the bank is partially or totally submerged the weights of the layers affected by water are correctly reduced irrespective of the geometry of the basal surface of the overhang.

Vertical Slice Algorithm: The vertical slice algorithm is an adaptation of the method employed in the CONCEPTS model (Langendoen and Simon, 2008). The algorithm is a limit equilibrium analysis that satisfies force equilibrium in the vertical and horizontal directions on individual slices and horizontal force equilibrium on the complete failure block. In addition to the forces incorporated in the Horizontal Layer method, the Vertical Slice algorithm evaluates normal and shear forces active in segments of the failure block. The confining force due to the water in the channel is modeled by extending the slip surface vertically through the water and applying a horizontal hydrostatic force on the vertical portion of the slip surface. Figure 64 shows an assumed failure block configuration and its subdivision into slices. The streambank is separated into vertical slices whereby there are an equal number of J slices and layers. Each slice is then subdivided into three subslices to increase the accuracy of the F_s calculations.

The calculation of F_s is a four-step iterative process: (1) vertical forces acting on a slice are summed to determine the normal force acting at the base of a slice, N_j; (2) horizontal forces acting on a slice are summed to determine the interslice

normal force, I_{nj}; (3) the interslice shear force, I_{sj} is computed from I_{nj} using the method of Morgenstern and Price (1965); and (4) horizontal forces are summed over all slices to obtain F_s. During the first iteration, the interslice normal and shear forces are neglected and:

$$N_j = W_j \cos\beta \tag{4.15}$$

where W_j is the weight of the j^{th} slice. This first iteration yields the Ordinary F_s. The interslice normal forces are then determined from:

$$I_{nj} = I_{nj-1} - \left(c'_j L_j + \left(\mu_a - \mu_w\right)_j L_j \tan\phi^b_j - \mu_{a\,j} L_j \tan\phi'_j\right)\frac{\cos\beta}{F_s} + N_j\left(\sin\beta - \frac{\cos\beta\tan\phi'_j}{F_s}\right) \tag{4.16}$$

and, in turn, the interslice shear forces are determined from:

$$I_{sj} = 0.4 I_{nj} \sin\left(\frac{\pi L_j}{\sum L_j}\right) \tag{4.17}$$

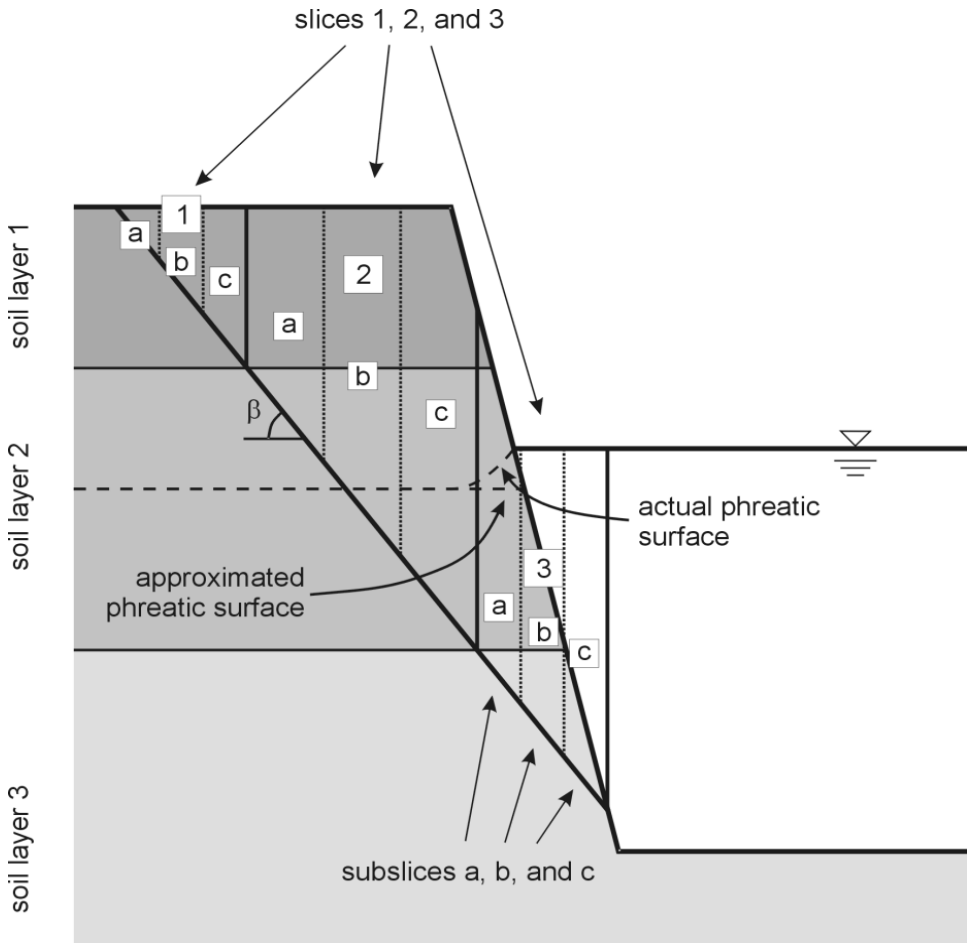

Figure 64. Subdivision of a failure block into slices

After the first iteration, the normal force, N_j equates to:

$$N_j = \frac{W_j + I_{sj-1} - I_{sj} - \sin\beta\left(\dfrac{c'_j L_j + \left(\mu_a - \mu_w\right)_j L_j \tan\phi^b_j - \mu_{aj} L_j \tan\phi'_j}{F_s}\right)}{\cos\beta + \dfrac{\tan\phi'_j \sin\beta}{F_s}} \tag{4.18}$$

for the j^{th} slice out of J slices.

This completes the second iteration. Often, the calculated interslice normal forces are negative (indicating tension) near the top of the failure block. Since soil is unable to withstand large tensile stresses, a tension crack is assumed to form at the last interslice boundary with tension, providing it does not exceed the maximum height of a tension crack. The tension crack depth z_c is usually equated

to the depth at which the active earth pressure is zero (e.g. Lohnes and Handy, 1968):

$$z_c = 2\frac{\sum_{j=1}^{J}\left[\frac{c_j' L_j \tan\left(45+\phi_j'/2\right)}{\gamma_j}\right]}{\sum_{j=1}^{J} L_j} \tag{4.19}$$

where γ = soil bulk unit weight (kN m^{-3}).

Factor of safety is then determined by the balance of forces in horizontal and vertical directions for each subslice and in the horizontal direction for the entire failure block. F_s is given by:

$$F_s = \frac{\cos\beta\sum_{j=1}^{J}\left(c_j' L_j + \left(\mu_a - \mu_w\right)_j L_j \tan\phi_j^b + \left[N_j - \mu_{aj} L_j\right]\tan\phi_j'\right)}{\sin\beta\sum_{j=1}^{J}\left(N_j\right) - P_j} \tag{4.20}$$

where the subscript j represents the j^{th} slice and J = number of slices in the failure block. The model then repeatedly iterates through equations 10 to 12 until the value of F_s converges

4.5.4.3 QUANTIFYING THE HYDRAULIC SCOUR OF THE BANK FACE AND/OR BANK TOE

Whether sediment is entrained by a moving fluid depends on both the properties of the fluid (i.e. its density, viscosity and velocity) and the physical properties of the sediment, such as its size, shape, density and arrangement (Knighton, 1998). A basic distinction exists between the entrainment of non-cohesive sediment (usually coarse silt, sand, gravel and boulders or cobbles) and cohesive sediments, because the entrainment of the latter is complicated by the presence of cohesion (Knighton, 1998). In both cases, most approaches to sediment transport have relied upon the concept of a critical value of a parameter such as either the depth-averaged or near-bed velocity (Hjulström, 1935), unit streampower (Bagnold, 1966; Yang, 1973) or bed shear stress (e.g. Meyer-Peter and Müller, 1948; Laursen, 1958; van Rijn, 1984a; 1984b; Parker, 1990; Wu *et al*., 2000 and many others). In the near-bank zone, the present model utilizes the bed shear stress, τ_o as the independent variable.

Sediment Entrainment and the Shields Curve

Shields (1936) conducted laboratory flume studies examining incipient motion and bed-load transport of non-cohesive, nearly uniform grains. The dimensionless critical shear stress, which appears on the *y*-axis of the Shields diagram (Figure 65), is defined as:

$$\tau^*_c = \frac{\tau_c}{g(\rho_s - \rho)D_{50}} \tag{4.21}$$

where τ_c = critical shear stress (Pa), g = acceleration due to gravity (9.807 m s^{-2}), ρ_s = density of sediment (kg m^{-3}), ρ = density of water (kg m^{-3}) and D_{50} = median diameter of grains in the bed (m). The critical shear stress, τ_c, can be determined from $\tau_c = c_f \rho U^2$, where c_f = a non-dimensional bed roughness coefficient (~0.00416 for sand beds; Hanson and Cook, 1997) and U = flow velocity (m s^{-1}). τ^*_c can be interpreted as the ratio of the average drag force per unit area to the average gravitational force resisting motion per unit area. The critical roughness Reynolds number, which appears on the *x*-axis of the Shields diagram, is defined as:

$$\mathrm{Re}^*_c = \sqrt{\frac{\tau^*_c(\rho_s - \rho)gD_{50}}{\rho}}\,\frac{D_{50}}{\nu} \tag{4.22}$$

where ν = kinematic viscosity of water ($m^2 s^{-1}$).

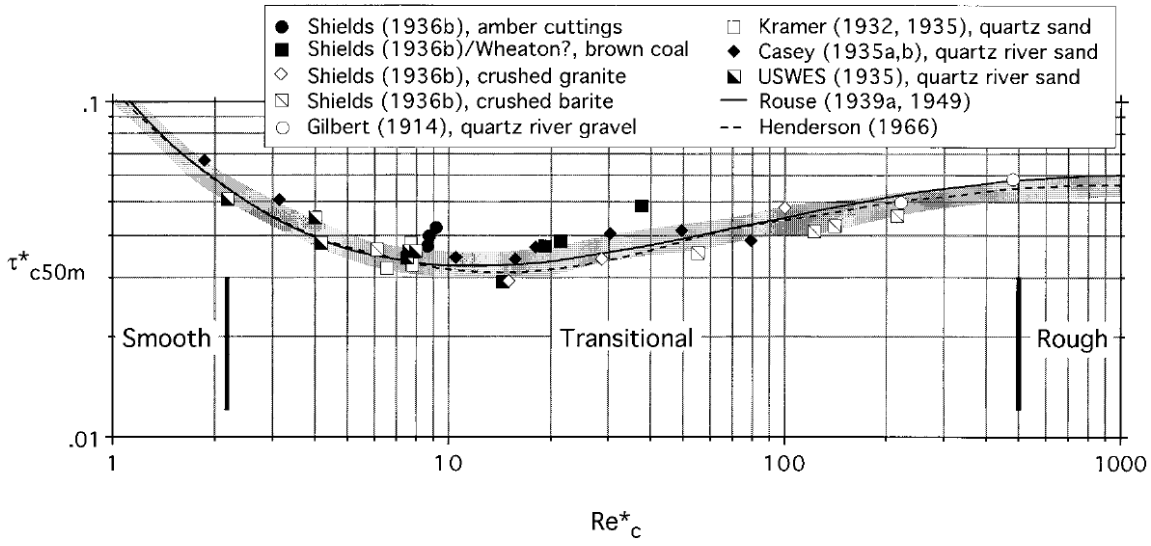

Figure 65. Shields diagram for incipient motion (modified from Buffington, 1999). The *y*-axis is defined by (B13) and the *x*-axis is defined by (B14)

The roughness Reynolds number is defined using the shear velocity, $u_* = \sqrt{\tau_o/\rho}$, as the velocity scale and the particle diameter as the length scale. At the onset of motion, $\tau_o \approx \tau_c$ and equation (4.22) is obtained. Re^*_c can be interpreted as being

proportional to the ratio between the particle size and the thickness of the viscous sublayer, and therefore its value indicates the extent to which particles protrude into the turbulent boundary layer.

The Shields diagram clearly shows that finer particles, those with critical roughness Reynolds numbers less than 10, become progressively harder to erode. These roughness Reynolds numbers correspond to clay grade material that exhibit cohesive forces.

Mechanisms of Cohesive Sediment Erosion

Mechanistically, the detachment and erosion of cohesive (silt- and clay-sized) material by gravity and/or flowing water is controlled by a variety of physical, electrical, and chemical forces. Identification of all of these forces and the role they play in determining detachment, incipient motion, and erodibility, of cohesive materials is incomplete and still relatively poorly understood (Winterwerp and van Kesteren, 2004). Assessing the erosion resistance of cohesive materials by flowing water is complex due to difficulties in characterizing the strength of the electro-chemical bonds that define the resistance of cohesive materials. The many studies that have been conducted on cohesive materials have observed that numerous soil properties influence erosion resistance including antecedent moisture, clay mineralogy and proportion, density, soil structure, organic content, as well as pore and water chemistry (Grissinger, 1982). For example, Arulanandan (1975) described how the erodibility of a soil decreases with increasing salt concentration of the eroding fluid, inducing weakening of inter-particle bonds. Kelly and Gularte (1981) showed that for cohesive sediments, increasing temperature increases erosion rates, particularly at low salinity, while at high salinity, there is less of an effect on erosion. Furthermore, studies of streambank stability in cohesive materials (Casagli *et al*., 1997; Rinaldi and Casagli, 1999; Simon *et al*., 2000) led to the idea that positive and negative pore-water pressures may play an important role in the entrainment and erosion of cohesive streambed particles or aggregates (Simon and Collison, 2001). Negative pore-water pressures increase the shear strength of unsaturated, cohesive materials by providing tension between particles.

Cohesive materials can be eroded in three contrasting ways (Mehta 1991; Figure 4): (1) surface erosion of bed aggregates; (2) mass erosion of the bed; and (3) entrainment of fluid mud (See Figure 66). Partheniades (1965) showed that clay resistance to erosion seemed to be independent of the macroscopic shear strength of the bed, provided that the bed shear stresses did not exceed the macroscopic shear strength of the material. Once the bed shear stress exceeds some critical value, then following Ariathurai and Arulanandan (1978) the rate of erosion, ε, of cohesive materials can be predicted by:

$$\varepsilon = k_d \left(\frac{\tau_o}{\tau_c} - 1 \right)^a$$

$$\varepsilon = 0 \qquad (\text{for } \tau_o \le \tau_c) \qquad (4.23)$$

where ε = erosion rate (m s^{-1}), k_d = erosion rate coefficient (m s^{-1}), τ_o = bed shear stress (Pa), τ_c = critical shear stress (Pa), and a = exponent assumed to equal 1.0. Equation (B15) may also be written as (Partheniades, 1965):

$$\varepsilon = \frac{k_d}{\tau_c}(\tau_o - \tau_c) = k(\tau_o - \tau_c) \qquad (\text{for } \tau_o > \tau_c)$$

$$\varepsilon = 0 \qquad (\text{for } \tau_o \le \tau_c) \qquad (4.24)$$

where k = erodibility coefficient ($m^3 N^{-1} s^{-1}$), representing the volume of material eroded per unit force and per unit time.

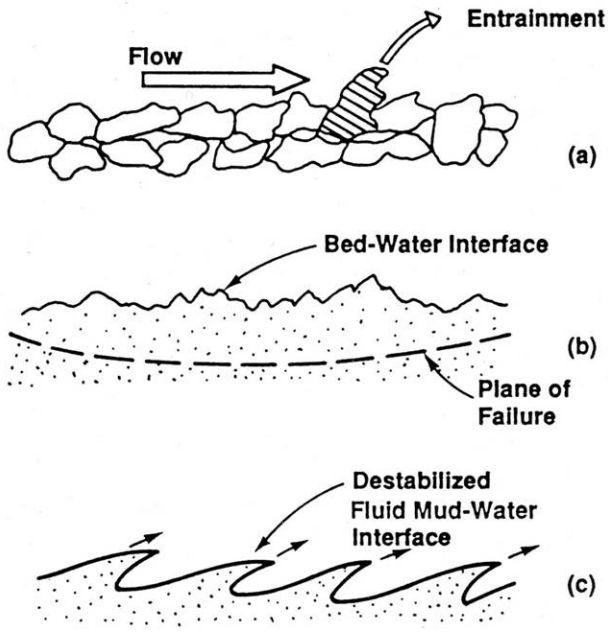

Figure 66. Three modes of cohesive sediment erosion: a) surface erosion of bed aggregates; b) mass erosion of the bed; c) entrainment of fluid mud (from Mehta, 1991, fig.1, p.41)

A submerged jet-test device has been developed by Hanson (1990) to conduct soil erodibility tests *in situ*. This device has been developed based on knowledge of the hydraulic characteristics of a submerged jet and the characteristics of soil material erodibility. Utilizing this device, Hanson and Simon (2001) developed the following relation between τ_c and k for cohesive silts, silt-clays and clays:

$$k = 2 \times 10^{-7} \tau_c^{-0.5} \qquad (4.25)$$

This relation is very similar to observed trends reported by Arulanandan *et al*. (1980) in laboratory flume testing of streambed material samples from across the United States. Jet-testing on bank toes suggests that although the exponent is the same, the coefficient is instead 1×10^{-7}.

Predicting the Distribution of Near-Bank Shear Stress

The magnitude of bank-face, bank-toe and bed erosion and the extent of bank steepening by hydraulic forces are calculated using an algorithm that computes the hydraulic forces acting on either the left or right near-bank zone during a particular flow event. As a two-dimensional numerical model, SRH-2D provides an estimate of the depth-averaged boundary shear stress vector in each cell within the computational mesh but does not provide any information as to how that boundary shear stress is vertically distributed. In the present approach, the boundary shear stress exerted by the flow on each node, *i*, is estimated by dividing the flow area at a cross-section into segments that are affected only by the roughness of the bank or the bed and then further subdividing to determine the flow area affected by the roughness on each node (e.g. Einstein, 1942; Figure 67). The hydraulic radius of a segment, R_i, is the area of the segment, A_i, divided by the wetted perimeter of the segment. The boundary shear stress active at the node *i* may then be estimated as:

$$\tau_{oi} = \tau_o \frac{R_i}{\sum_{i=1}^{i=I} R_i} \tag{4.26}$$

where τ_o = depth-averaged boundary shear stress in the near-bank cell.

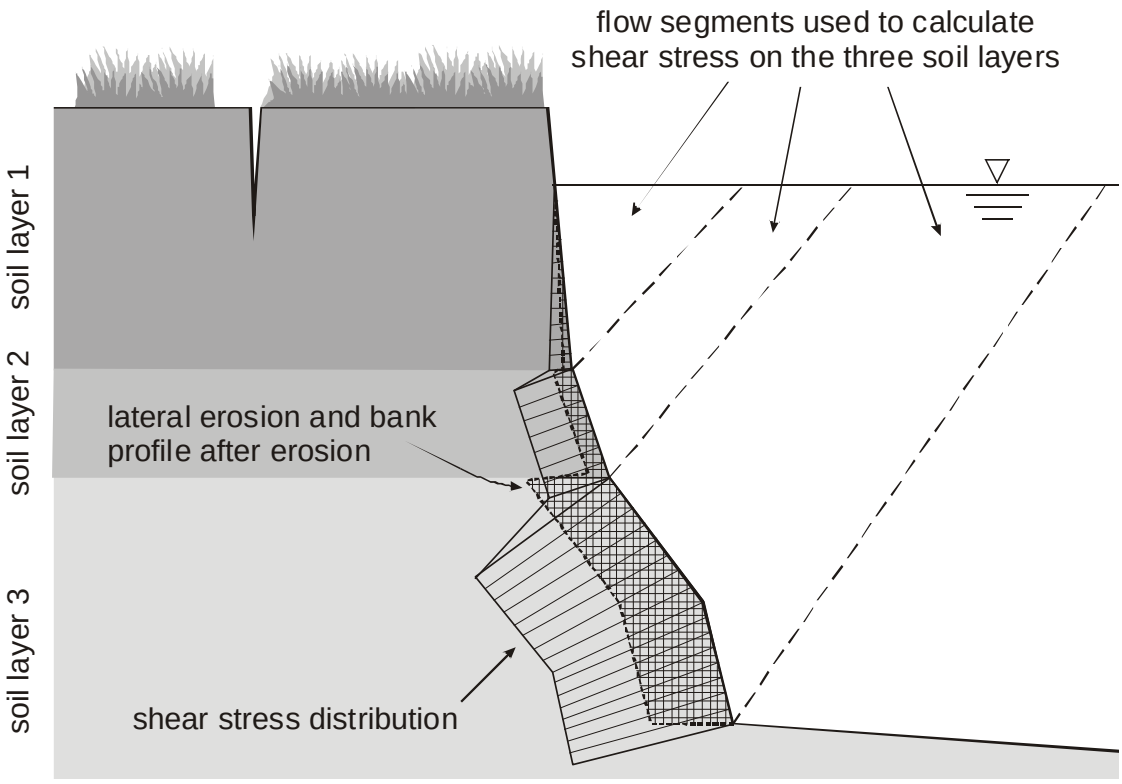

Figure 67. Segmentation of local flow areas and hydraulic radii

Flow resistance in an open channel is a result of viscous and pressure drag over its wetted perimeter. For a vegetated channel, this drag may be conceptually divided into three components: 1) the sum of viscous drag on the ground surface and pressure drag on particles or aggregates small enough to be individually moved by the flow (grain roughness); 2) pressure drag associated with large non-vegetal boundary roughness (form roughness); and 3) drag on vegetal elements (vegetal roughness) (Temple *et al*., 1987). As energy lost to the flow represents work done by a force acting on the moving water, the total boundary shear stress may also be divided into three components:

$$\tau_o = \tau_{og} + \tau_{of} + \tau_{ov} \tag{4.27}$$

where the subscripts *g*, *f* and *v* signify the grain, form and vegetal components of the boundary shear stress, respectively.

If it is assumed that these components may be expressed in terms of a Manning's coefficient for each, and Manning's equation is assumed to apply for each component, equation (4.26) can be rewritten as (Temple, 1980):

$$n^2 = n_g^2 + n_f^2 + n_v^2 \tag{4.28}$$

where n = Manning's roughness coefficient (s $m^{-1/3}$). Grain roughness is estimated for each node on the bank profile using the equation of Strickler (Chow, 1959):

$$n_g = 0.0417 \, (D_{50}{}^{1/6}) \tag{4.29}$$

Combining equations (4.27) and (4.28), the effective boundary shear stress, the component of the boundary shear stress acting on the boundary in the absence of form and vegetal roughness, may be computed as:

$$\tau_g = \tau_o \, (n_g{}^2 / n^2) \tag{4.30}$$

The rate of erosion of bank-face, bank-toe and bed materials can then be calculated using equations (4.24) and (4.30) (Hanson, 1990). During the dynamic simulations described herein, the erosion distance during a time step is computed by integrating the erosion rate within the time step by the time step size:

$$E = \varepsilon \Delta t \tag{4.31}$$

where E = erosion distance (m), and Δt = time step (s).

4.6 Progress of Non-Cohesive Model Development

The non-cohesive bank erosion module is developed first, as the modeling procedure, moving-mesh implementation, and various programmatic changes and implementations are directly extendable to cohesive bank module. The angle-of-repose method is used to compute the retreat of the bank which has been described in the above. The progress of its development is reported below.

The bank erosion module with the non-cohesive bank, as outlined in the above sub-section, was incorporated into SRH-2D. The ALE moving mesh formulation was also developed and tested. A process of debug and testing was carried out. In the following, preliminary verification study is reported with examples.

An experimental bank erosion case carried out by Nagata et al. (2000) was selected to test and verify the numerical model. Although improvements are still needed, preliminary results are reported. Experiments were carried out in a tilting flume with a length of 10 m, width of 1 m, and depth of 0.2 m. The initial meander channel form used for simulation, and the layout of the flume, are shown in Figure 68. The meander channel was set as a sine-generated curve with wavelength of 2 m and 30^o maximum angle from the longitudinal direction. The cross section of the channel is trapezoidal with dimensions shown in Figure 68. Four wavelengths were used in the experiment; but measured data were only in the second from the upstream as impacts from upstream and downstream were small. The numerical model simulated only the first three wavelengths.

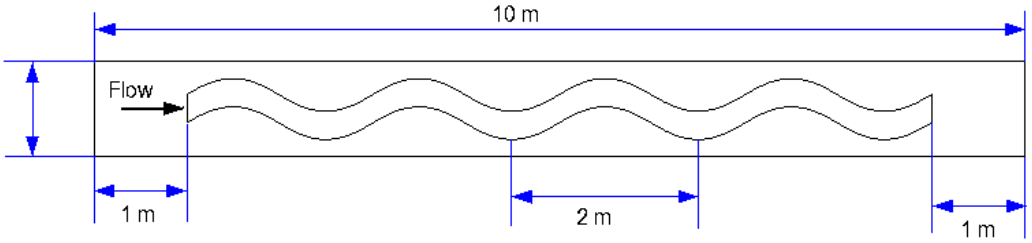

(a) Plan Form

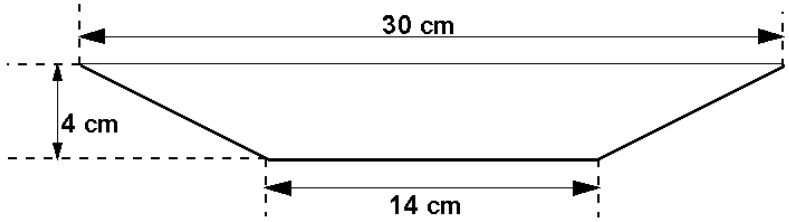

(b) Cross Section

Figure 68. Flume configuration and geometry of the initial meander channel for the case of Nagata et al. (2000)

Run number 1 was modeled first. The case has a flow discharge of 1,980 cm3/s, initial bed slope of 1/300, and initial water depth of 3 cm. Run number 3 was then modeled. This case has a flow of 1,000 cm3/s, initial bed slope of 1/100, and initial water depth of 1.42 cm.

A mesh of 2,684 quadrilateral cells (2829 nodes) was used, consisting of 123 streamwsie points and 23 lateral points, for both run 1 and run 3 (see Figure 69a). For run 3, an additional mesh was used which used the triangular cells within the main channel (see Figure 72a). The second mesh has 10,944 mesh cells with 8,015 mesh nodes.

The bed and bank had the same sediments with fairly uniform sand of a mean diameter of 1.42 mm ($\sqrt{d_{84}/d_{16}} = 1.28$). Sediment was fed at the upstream end of the channel continuously in the experiment. In the numerical modeling, the sediment feed rate was computed based on the sediment transport capacity so that there was not net erosion and deposition at the upstream boundary. For sandy bed, the Engelund-Hansen equation was used for the sediment equation and the Sutherland formula was adopted for the bedload adaptation length. The active layer thickness was 10 times the sediment diameter, as normally the practice. At the beginning, a flow-only simulation was carried out to obtain an initial flow field and it was used as the initial condition for the sediment transport and bank erosion modeling. A uniform Manning's roughness coefficient of 0.016763 was used for the channel based on the standard grain shear stress expression of $n = d^{1/6}/20$, where d is the mean sediment diameter.

Further, bank erosion mode parameters are as follows. The lateral bank tor erosion is based on equation (3) with the critical shear stress computed with the Shields number of 0.027, leading to $\tau_c = 0.62\,Pa$. The erodibility constant was determined to be $k = 2.0e-4\ m/Pa-s$ though calibration.

For Run 1, the model results are shown in Figure 69 and Figure 70. Figure 69 shows the initial mesh at t=0 and the new moved mesh at t=125 minutes, along with the predicted net eroded depth at t=125 minutes. It is seen that bank erosion occurs at the downstream half of the outer bend while bar deposition occurs on the downstream half of the inner bend. Comparison of the bank line retreat in Figure 70 at different times shows that the model predicted the bank retreat reasonably.

Run 2 results are compared in Figure 71 through Figure 73. It is seen that the predicted bank retreat agrees with the measured data well. Also, model results from the two quite different meshes are similar indicating that the errors introduced by the mesh is relatively small and negligible.

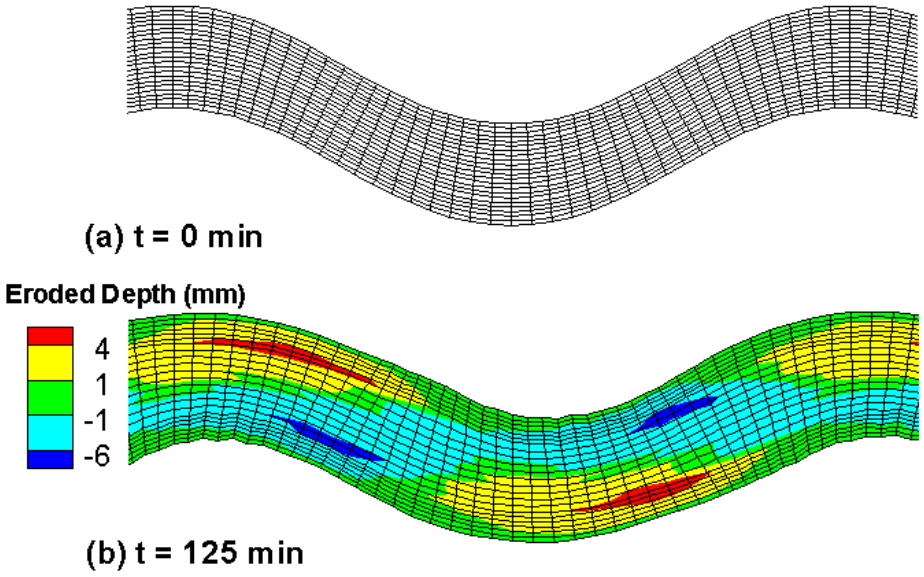

Figure 69. Comparison of meshes at t=0 min and t=125 min, along with the predicted net eroded depth at t=125 min

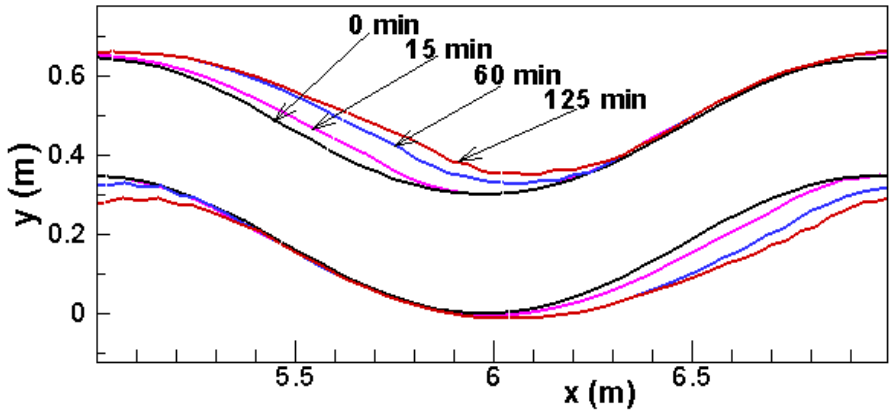

(a) Model Prediction

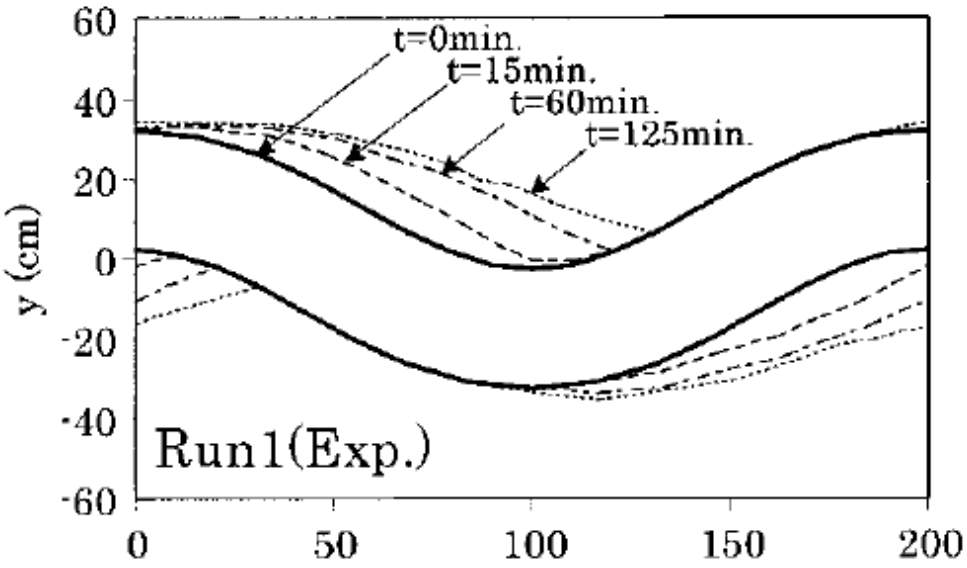

(b) Experimental Data (Source: Nagata et al, 2000)

Figure 70. Comparison of predicted and measured bank retreat at different times for the case of Run 1 of Nagata eta al. (2000).

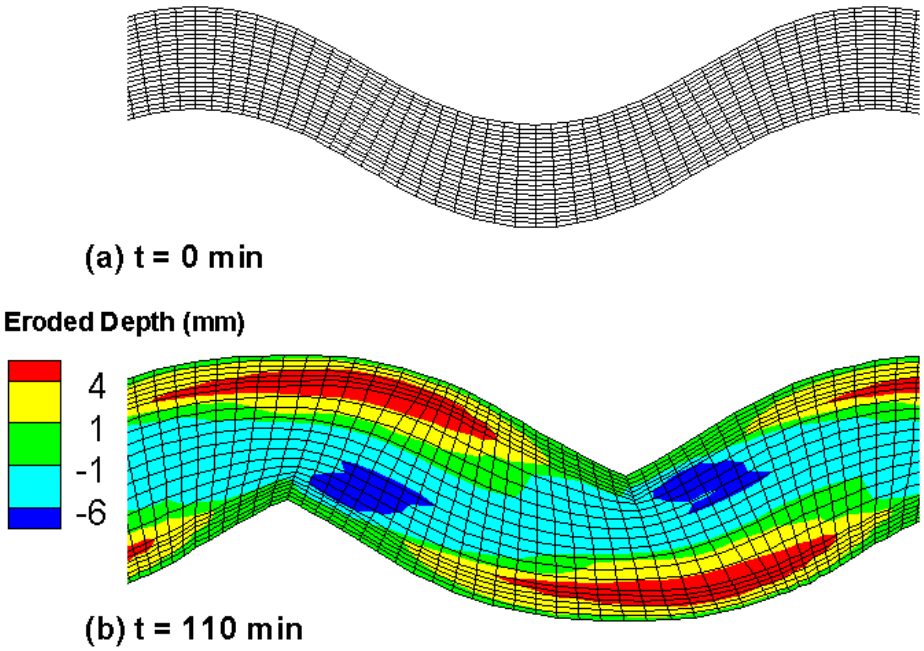

Figure 71. Comparison of quadrilateral meshes at t=0 min and t=110 min, along with the predicted net eroded depth at t=110 min

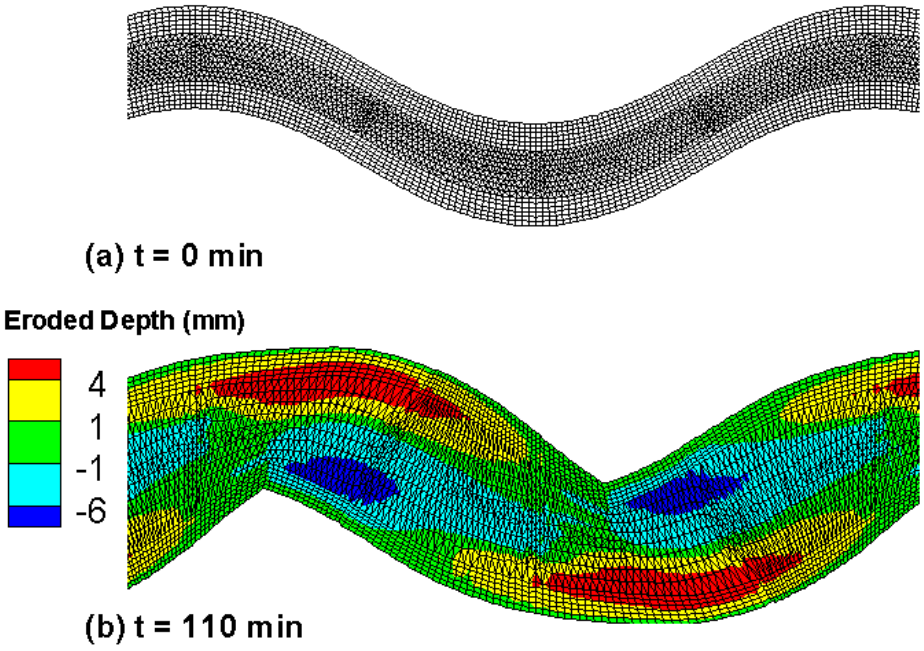

Figure 72. Comparison of triangular meshes at t=0 min and t=110 min, along with the predicted net eroded depth at t=110 min

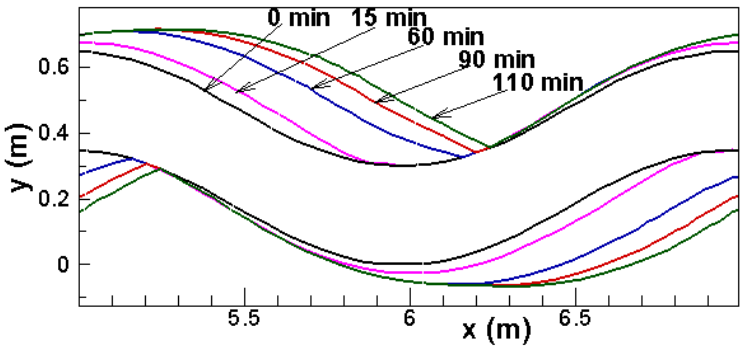

(a) Model prediction with quadrilateral mesh

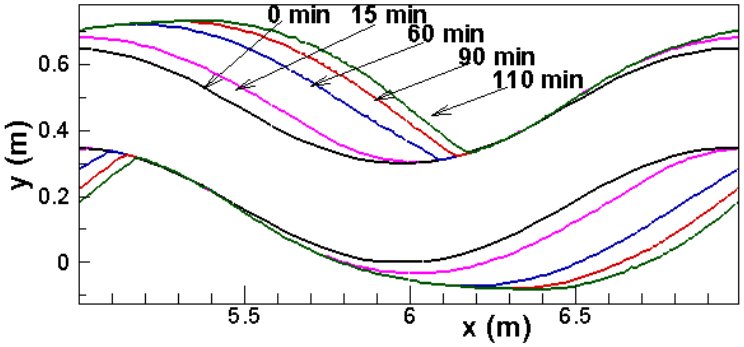

(b) Model prediction with triangular mesh

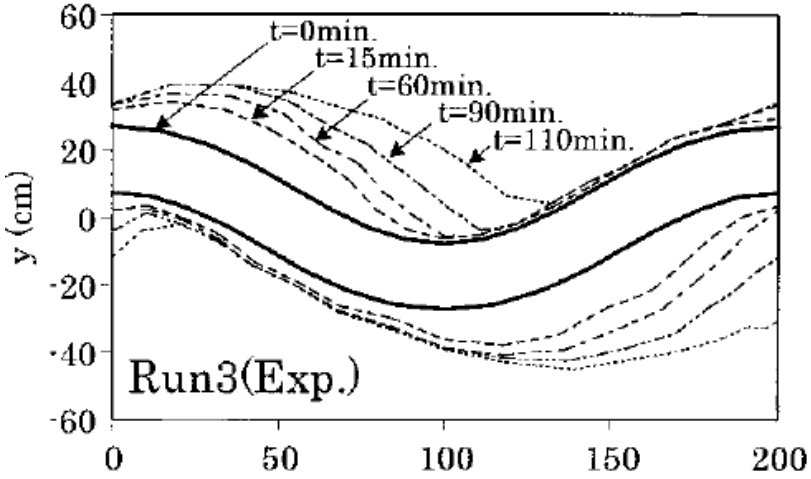

(c) Experimental Data (Source: Nagata et al, 2000)

Figure 73. Comparison of predicted and measured bank retreat at different times for the case of Run 3 of Nagata eta al. (2000)

4.7 Progress of Cohesive Model Development

A separate cohesive bank erosion module is to incorporate a version of BSTEM into SRH-2D. The coupled model, SRH-BSTEM, intends to model bank erosion with multi-layer cohesive banks. Progresses made in this year are summarized below:

- The BSTEM model was originally developed as a spreadsheet tool, written in computer languages other than FORTRAN. NSL/ARS has spent effort to develop a FORTRAN version of the BSTEM model. This version is needed to for incorporation into SRH-2D as SRH-2D was written in FORTRAN.
- Extensive debug and testing have been carried out at NSL/ARS to ensure that the new FORTRAN-based BSTEM works the same way as the original spreadsheet version.
- Work is currently under way to "merge" BSTEM model into SRH-2D.

5 Turbidity Current Modeling – A Progress Report

A literature review was provided and a specific turbidity current modeling approach was recommended in our previous report for modeling turbidity current flows (Lai and Greimann, 2008). This portion of the document is not repeated in this report. The development of a layer-averaged turbidity current model was initiated in 2009 and continued this year in 2010. This chapter will focus on the progress achieved in the model development effort.

In the following, the governing equations of the recommended layer-averaged turbidity current model are presented, along with the theory of the model, and potential limitations. A number of previous 2D layer-averaged numerical methods are reviewed; and the proposed numerical method is then presented. The layer-averaged turbidity current model is under development at present. Preliminary results are presented.

5.1 Background

Layer-averaged turbidity current models were proposed by Lai and Greimann (2008) based on the following observations: (1) Many reservoirs are not narrow so that laterally averaged models are not applicable; (2) Most empirical and analytical models deal with conservative gravity currents, while turbidity currents are often non-conservative due to sediment exchange between sediments in water and bed; and (3) 3D models are still not very practical and mostly at a research stage.

Based on our review (Lai and Greimann, 2008), a 2D layer-averaged turbidity current model was recommended, with the unsteady modeling capability and the sediment transport delta development model. We believe such a model have the best chance to be applicable to and useful for the Shihmen Reservoir, which is of interest to Taiwan for further analysis.

5.2 Plunge Point Determination

Up to five zones may be formed for a general turbidity current, according to Alavian et al. (1992), as illustrated in Figure 74. The initial zone (zone 1) consists of a “plug” type incoming flow which may be analyzed with the conventional open channel flow hydraulics (e.g., Chow, 1959). Overflow would be formed immediately if the incoming flow density is lower than the ambient (or receiving) water. In the study, however, the density of the incoming water is higher than the

ambient, so plunge would occur as depicted in Figure 74. Zone 2 represents the transition where the incoming flow plunges to bed. The location of the plunge point is the result of a balance between the inflow momentum and the baroclinic pressure resulting from the density difference. Beyond the plunge point, a two-layer flow develops. Initially, the current (zone 3) is attached to the bed as an underflow propagating down a slope. If the reservoir is stratified, the underflow may reach a depth in the reservoir where the underflow becomes neutrally buoyant with respect to its immediate surroundings. This neutral zone is the separation zone (zone 4); downstream of the separation zone, an interflow or intrusion (zone 5) is developed which is lifted up from the bed. The separation point is determined by similar parameters of the plunge point.

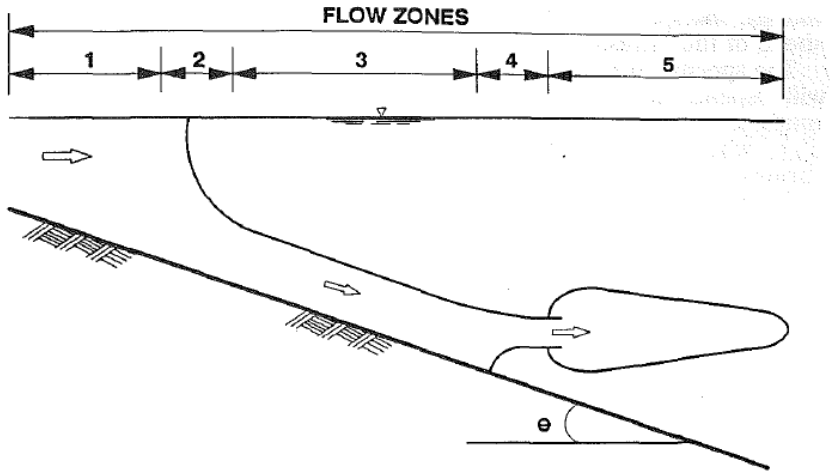

Figure 74. Sketch for a turbidity current flow: zone 1=initial flow; zone 2=plunge; zone 3=under current; zone 4=separation; zone 5=interflow (Source: Alavian et al. 1992)

In this study, it is assumed that the turbidity current will not lift up from the bed. Therefore, only the first three zones are present, without the formation of interflow.

A description of the turbidity current structure under consideration is shown in Figure 75. During a flood, muddy water plunges at a point above the foreset face, resulting in the formation of a bottom turbidity current along the bed. Just beyond the plunge point, the turbidity current may be supercritical in the densimetric Froude sense if the slope of the foreset is steep enough. As the head of the current runs into the dam and reflects back, however, it sets up a quasi-steady flow with an internal hydraulic jump. Downstream of this internal hydraulic jump, a highly Froude-subcritical internal muddy pond with a settling interface can form, with clear water above and muddy water below the interface. With multiple suspended sediments, the interface may represent a finite thickness layer instead of a clear line. Only a line is assumed in our model.

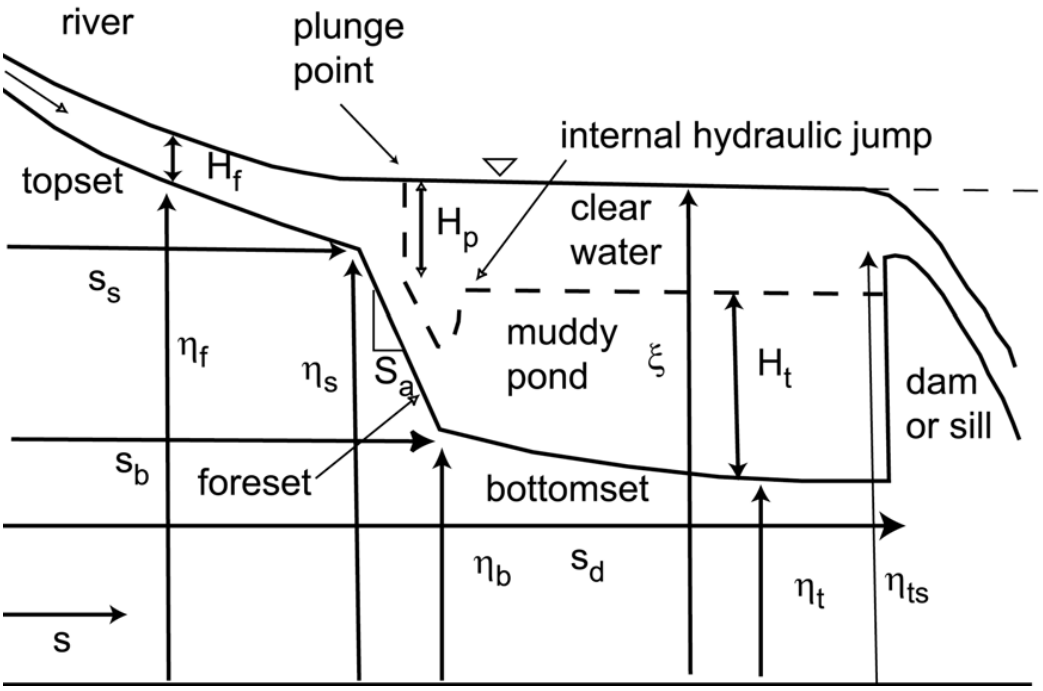

Figure 75. Sketch of turbidity current configuration (Source: Toniolo et al. 2007)

The location of the plunging point needs to be known for modeling purpose. In a narrow reservoir the plunging flow usually forms a line across the width. In a wide reach of reservoir, however, the turbid surface water may extend into the reservoir as an irregular tongue-like current which can shift from one side of the impoundment to the other (see Fleenor, 2001). In theory, the plunge point is determined by a balance between the inflow momentum, the pressure gradient across the interface separating the river and reservoir water, and the resisting shear forces. The location can also be influenced by morphological factors (bed slope, bed friction, cross-sectional area). The plunge point location is highly dynamic; it can move several kilometers in a few hours in response to dynamics flow events (storm event, hydropower operation).

A number of empirical equations have been developed to determine the plunge point. Different authors assume different cross section geometries, resulting in different expressions for the plunge depth equations. Four equations were used by the Reclamation's DCURL model (Simoes, 1999).

In one approach, the water depth at the plunge point was estimated based on the densimetric Froude number at the plunge point as (Morris and Fan 1998):

$$F_p = \frac{V_i}{\sqrt{\frac{\rho_i - \rho_a}{\rho_a} g h_p}} \tag{5.1}$$

where V_i is the depth-averaged velocity of the incoming flow, g is the acceleration due to gravity, h_p is the depth at the plunge point, and ρ_a and ρ_i are the densities of the ambient and the incoming waters, respectively. Both flume tests and field measurements in reservoirs indicate that F_p has a value of about 0.78. Ranges of values have been reported and they are summarized in Table 9 (Morris and Fan 1998).

Table 9. Densimetric Froude number at the plunge point (Morris and Fan 1998)

Author	Lab or Field Data	F_p
Bu et al. 1980	Liujiaxia Reservoir	0.78
Fan, 1991	Guanting Reservoir	0.5 – 0.78
Fan, 1960	Flume tests: 3-19g/l	0.78
Cao et al. 1984	Flume tests: 10-30 g/l	0.55 – 0.75
	100-360 g/l	0.4 – 0.2
Singh and Shan 1971	Saline water	0.3 – 0.8
Farrel and Stephan 1986	Cold water	0.67

Akiyama and Stefan (1986) also provided a comprehensive summary of F_p values from the literature. Channels with constant width and bed slopes ranging from 10^{-3} to 10^{-1} have been found to plunge at a value of F_p near 0.56.

The plunge point estimation was also proposed by others. For example, Singh and Shah (1971) conducted an experimental study of the plunging phenomenon using a tilting flume with salt water flowing into a reservoir filled with tap water. They derived the plunging point equation as follows:

$$F_p = 0.0185 + 1.3\left(\frac{h_p V_i}{\frac{\rho_i - \rho_a}{\rho_a} g}\right) \tag{5.2}$$

Another way to determine the plunging point is to rely on the measured and/or observed data at a specific reservoir, whenever such data are available. Usually, the plunge point is located within the foreset of the reservoir bottom. The convergence of surface flow created by plunging can often cause debris such as logs to accumulate along the plunge line, which may provide a good indication of the plunge point.

5.3 Governing Equations

Upstream of the plunging point, the regular depth-averaged open channel flow models, such as SRH-2D, are applicable. Solutions may be obtained up to the plunge point.

Downstream of the plunging point, undercurrent forms and a new set of layer-averaged 2D equations are derived to compute the undercurrent flow. The governing equations take the following forms, which are an extension of the 1D work by Toniolo et al. (2007):

$$\frac{\partial h}{\partial t}+\frac{\partial hU}{\partial x}+\frac{\partial hV}{\partial y}=(1-\delta)e_w U_t-\delta\omega_m \tag{5.3}$$

$$\frac{\partial hU}{\partial t}+\frac{\partial hUU}{\partial x}+\frac{\partial hVU}{\partial y}=\frac{\partial hT_{xx}}{\partial x}+\frac{\partial hT_{xy}}{\partial y}-(RgC_t)h\frac{\partial Z}{\partial x}-\frac{Rg}{2}h^2\frac{\partial C_t}{\partial x} -(1+r_w)u_*^2-\delta\omega_m U \tag{5.4}$$

$$\frac{\partial hV}{\partial t}+\frac{\partial hUV}{\partial x}+\frac{\partial hVV}{\partial y}=\frac{\partial hT_{xy}}{\partial x}+\frac{\partial hT_{yy}}{\partial y}-(RgC_t)h\frac{\partial Z}{\partial y}-\frac{Rg}{2}h^2\frac{\partial C_t}{\partial y} -(1+r_w)v_*^2-\delta\omega_m V \tag{5.5}$$

$$\frac{\partial hC_k}{\partial t}+\frac{\partial hUC_k}{\partial x}+\frac{\partial hVC_k}{\partial y}=\upsilon_k(p_k E_k-C_{bk}) \tag{5.6}$$

$$(1-\gamma)\frac{\partial z_b}{\partial t}=\sum_k \upsilon_k(C_{bk}-p_k E_k) \tag{5.7}$$

In the above, t = time; x and y = horizontal Cartesian coordinates; h = turbidity current thickness; U and V = layer-averaged current velocities in the x and y directions, respectively; C_k = layer-averaged volumetric concentration of the kth sediment size class; Z is top elevation of the current; and z_b is the bed elevation. A few auxiliary variables include: $U_t=\sqrt{U^2+V^2}$ is total velocity; C_t = total sediment concentration ($C_t=\sum_k C_k$); R is the submerged specific gravity of sediments in the turbidity current ($R=\sum_k R_k C_k/C_t$); and $R_k=(\rho_{sk}-\rho_a)/\rho_a$ (ρ_{sk} is density of the kth sediment size class and ρ_a the density of the ambient water). Other variables and parameters are to be defined next.

Equation (5.3) is the mass conservation equation. The first term on the right hand side is the entrainment from the ambient fluid, and the second term represents detrainment due to settling of sediments. The dimensionless entrainment coefficient (e_w) needs to be determined, as discussed below, δ is the settling parameter that is a function of the Froude number, and ω_m is the average sediment fall velocity. On one scenario, the settling parameter takes the value zero

in a Froude-supercritical turbidity current without a settling interface (supercritical zone upstream of the internal hydraulic jump). On the other extreme, δ takes value one in a highly Froude-subcritical turbidity current (the Froude number is much less than 1) with a clear settling interface (ponded zone). In the highly ponded case, the interface would remain its position in time if the detrained water would be constantly replaced by the upstream inflow. If the detrainment discharge across the interface is less than the inflow discharge of water, however, the interface will move above the lip of the downstream barrier, and both water and sediment will overspill in the form of an exiting turbidity current.

The entrainment coefficient may be computed according to Parker et al. (1986) as:

$$e_w = \frac{0.00153}{0.0204 + Ri} \qquad Ri = \frac{ghRC_t}{U^2 + V^2} \tag{5.8}$$

In the above, g is the acceleration of gravity. It was based on the bulk Richardson number related to the densimetric Froude number ($Ri = 1/Fr^2$). This equation was used by Toniolo et al. (2007), for example. Another equation is according to Parker et al. (1987) as:

$$e_w = \frac{0.075}{\sqrt{1 + 718\,Ri^{2.4}}} \tag{5.9}$$

The equation was used by Bradford and Katopodes (1999), for example. In this study, (5.9) is used.

In the momentum equations (5.4 and 5.5), the extra parameter represented by the r_w takes into account the friction due to the upper fluid layer (or interfacial friction). Parameter r_w is the ratio of upper interface resistance to bed resistance. Bed resistance is determined by the friction velocity components, u_* and v_*, in the *x* and *y* directions, respectively. The shear velocities are computed as:

$$u_*^2 = C_f U\sqrt{U^2 + V^2} \qquad v_*^2 = C_f V\sqrt{U^2 + V^2} \tag{5.10}$$

In the above, C_f is the bed drag coefficient. Often, the drag coefficient may be used to represent the "total" drag combining both the bed and interfacial friction, and it is usually a model calibration parameter. A typical range of values, according to Parker et al. (1987), are from 0.002 to 0.05. The smaller values are associated with relatively larger scale flows, while the larger values are associated primarily with laboratory simulations. We believe an analogy with the shallow

water equation may be made so that $C_f = \frac{gn^2}{h^{1/3}}$. This way, n is the equivalent of the Manning's roughness coefficient and is calibrated to represent the total friction. Of course, the meaning of the Manning's coefficient has to be different but it is cast as a function of the current thickness. However, the form of the Manning's equation is yet to be tested and studied.

It is also noted that the dispersion terms represented by T_{xx}, T_{xy}, and T_{yy} are added to the momentum equations in our study. They may be calculated with the Boussinesq's formulation as:

$$T_{xx} = 2(\upsilon + \upsilon_t)\frac{\partial U}{\partial x} \qquad T_{xx} = 2(\upsilon + \upsilon_t)\frac{\partial U}{\partial x} \qquad T_{xy} = (\upsilon + \upsilon_t)(\frac{\partial U}{\partial y} + \frac{\partial V}{\partial x}) \qquad (5.11)$$

where υ is kinematic viscosity of water and υ_t is dispersive "eddy viscosity". The standard turbulence models used by SRH-2D may be adopted to compute the eddy viscosity.

The sediment concentration equation (5.6) is based on the mass conservation principle. The first term on the right hand side represents the erosion potential from the bed. The volume fraction of the *k*th sediment size class on the bed is represented by p_k, and E_k is the erosion potential for the *k*th sediment size class. The last term represents the deposition potential of the sediment in the current; the parameter C_{bk} is the near-bed concentration of the *k*th sediment. The variable C_{bk} may be related to the depth averaged concentration as $C_{bk} = r_{0k}C_k$ and the determination of the shape factor was discussed by Garcia (1994). In general, r_{0k} should be a function of grain size; but a value close to 2 may be used. A general expression is as follows:

$$r_{0k} = 1.64 + 0.4(\frac{d_k}{d_{gm}})^{1.64} \qquad \ln(d_{gm}) = \frac{\sum C_k \ln(d_k)}{\sum C_k} \qquad (5.12)$$

where d_k is the diameter of sediment size *k*.

Finally, υ_k is the fall velocity of the *k*th sediment size class. Determination of erosional potential was discussed by Bradford and Katopodes (1999). However, use of existing sediment transport capacity formulae, may also be an option. One option is to use the formula by Garcia and Parker (1993), as adopted by Imran et al. (2002), as follows:

$$E_k = \frac{aZ_k^{\,5}}{1+\frac{a}{0.3}Z_k^{\,5}} \qquad Z_k = \alpha_1 \zeta \frac{u_*}{\upsilon_k} R_{pk}^{\,\alpha_2} \left(\frac{d_k}{d_{50}}\right)^{0.2} \qquad R_{pk} = \sqrt{\frac{Rgd_k^3}{\nu^2}} \quad (5.13)$$

In the above, $a = 1.3\times10^{-7}$; $\zeta = 1 - 0.288\sigma$; $(\alpha_1, \alpha_2) = (1, 0.6)$ if $R_{pk} > 2.36$ and $(\alpha_1, \alpha_2) = (0.586, 1.23)$ if $R_{pk} \le 2.36$; σ is the standard deviation (on a phi-scale) of the sediment mixture, characterizing the non-uniformity of the mixture.

The last equation (5.7) represents the bed elevation change due to erosion and deposition processes between the turbidity current and bed materials (γ is the bed porosity).

5.4 Numerical Methods

2D layer-averaged turbidity current numerical models are scarce. One such model was by Imran et al. (1998) who developed a finite-difference scheme to predict channel inception by assuming an antecedent turbid flow thickness to be present in the solution domain. Only a uniform grain size is considered. The flow equations were solved by using the Beam and Warming implicit finite difference scheme, which was described, e.g., by Fennema and Chaudhry (1989), and the sediment equation was solved with an explicit time marching scheme.

Choi (1998; 1999) developed a finite element technique to solve the layer-averaged equations. The finite element method had two aspects: the dissipative algorithm and the front tracking technique. Since the standard Galerkin method yields spurious oscillations when applied to convection-dominated flows, the dissipative-Galerkin technique having a selective dissipation property was used. Also, in order to track the moving front accurately, a deforming grid technique based on the arbitrary Lagrangian-Eulerian approach was employed. The developed numerical procedure was applied to a decelerating-turbidity current generated in the laboratory experiment. Time-dependent profiles for the current thickness and layer-averaged velocity field and volumetric concentration are obtained. The relevant depositional structure by this underflow event was estimated by incorporating the double grid finite element method into the flow algorithm.

Bradford and Katopodes (1999) incorporated the most recent closure relations to produce a turbidity current model that has the ability not only to predict the flow hydrodynamics, but also to simulate the resulting sedimentation and bed evolution. The mathematical model was developed for unsteady, two-dimensional, single-layer, depth-averaged turbid underflows driven by non-uniform, non-cohesive sediment. The numerical solution is obtained by a high resolution, total variation diminishing, finite-volume numerical model, which is known to capture sharp fronts accurately. The monotone upstream scheme for conservation laws was used in conjunction with predictor-corrector time-stepping

to provide a second-order accurate solution. Flux-limiting was implemented to prevent the development of spurious oscillations near discontinuities. The model also possesses the capability to track the evolution and development of an erodible bed, due to sediment entrainment and deposition. This is accomplished by solving a bed-sediment conservation equation at each time step, independent of the hydrodynamic equations, with a predictor-corrector method.

In this study, the equation set described above have extra terms added which incorporate the "detrainment" effect into consideration. Detrainment is the process of "water loss" from the turbidity current and it is effected due to the settling of sediments in the current (Toniolo et al. 2007). Therefore, detrainment terms are proportional to the sediment fall velocity. As a first step, the numerical method developed in this study follows the method of SRH-2D for the regular shallow water equation. Note that the governing equations (B3) to (B7) are similar to the shallow water equations except for the hydrostatic thrust terms. The terms are reduced by a factor of RC_t in the turbidity current equations, which has the effect of reducing the momentum of the flow. The numerical model development is speeded up tremendously due to the availability of SRH-2D model. It is cautioned that the numerical algorithm of SRH-2D is not specifically designed to simulate supercritical flows accurately. Therefore, the applicability of the chosen method to turbidity current flows remains to be tested; and improvements are needed if necessary.

The finite-volume based, segregated numerical method of SRH-2D is adopted which follows the original method of Lai et al. (2003). The governing equations of mass and momentum can be recast in tensor form as:

$$\frac{\partial h}{\partial t} + \nabla \bullet (h\vec{V}) = (1-\delta)e_w U_t - \delta\omega_m \tag{5.14}$$

$$\frac{\partial (h\vec{V})}{\partial t} + \nabla \bullet (h\vec{V}\vec{V}) = -RgC_t h\nabla z + \nabla \bullet \left(h\vec{\vec{T}}\right) - \frac{\vec{\tau}_b}{\rho} + \vec{S} \tag{5.15}$$

where $\vec{V}$ is the velocity vector, $\vec{\vec{T}}$ is the 2nd-order stress tensor, $\vec{\tau}_b$ is the bed shear stress vector, and $\vec{S}$ is the source term vector. The solution domain defined first and is covered with an unstructured mesh and cells may assume the shapes of arbitrary polygons. All dependent variables are stored at the geometric centers of the polygonal cells. The governing equations are integrated over polygonal cells using the Gauss integral. As an illustration, consider a generic convection-diffusion equation that is representative of all governing equations:

$$\frac{\partial h\Phi}{\partial t} + \nabla \bullet (h\vec{V}\Phi) = \nabla \bullet (\Gamma\nabla\Phi) + S_\Phi^* \tag{5.16}$$

Here Φ denotes a dependent variable, a scalar or a component of a vector, Γ is diffusivity coefficient, and S_Φ^* is the source/sink term. Integration over an arbitrarily shaped polygon *P* shown in Figure 76 leads to:

$$\frac{(h_P^{n+1}\Phi_P^{n+1} - h_P^n\Phi_P^n)A}{\Delta t} + \sum_{all-sides}(h_C V_C|\vec{s}|)^{n+1}\Phi_C^{n+1} = \sum_{all-sides}(\Gamma_C^{n+1}\nabla\Phi^{n+1}\bullet\vec{n}|\vec{s}|) + S_\Phi \quad (5.17)$$

In the above, Δt is time step, *A* is cell area, $V_C = \overrightarrow{V_C}\bullet\vec{n}$ is velocity component normal to the polygonal side (e.g., P_1P_2 in Figure 76) and is evaluated at the side center *C*, $\vec{n}$ is unit normal vector of a polygon side, $\vec{s}$ is the polygon side distance vector (e.g., from P_1 to P_2 in Figure 76), and $S_\Phi = S_\Phi^* A$. Subscript *C* indicates a value evaluated at the center of a polygon side and superscript, *n* or *n*+1, denotes the time level. In the remaining discussion, superscript *n*+1 will be dropped for ease of notation. The first-order Euler implicit time discretization is adopted. The remaining task is to obtain appropriate expressions for the convective and diffusive fluxes at each polygon side.

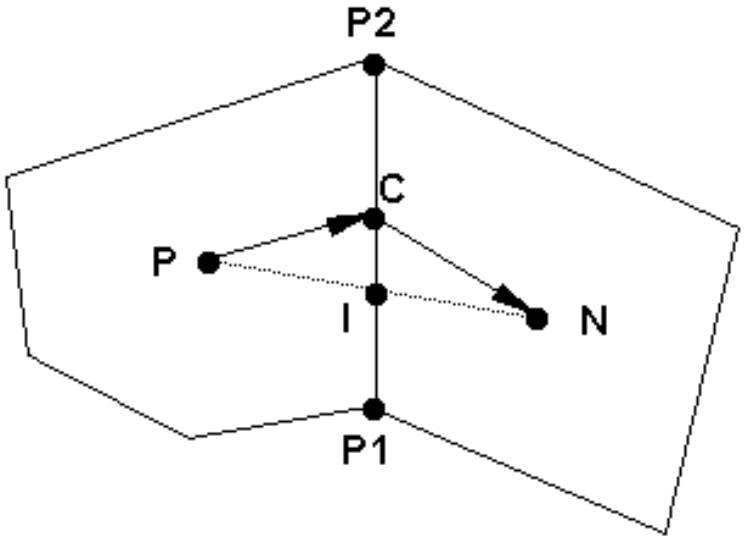

Figure 76. Schematic illustrating a polygon cell *P* along with one of its neighboring polygons *N*

Discretization of the dispersion term, the first on the right hand side of (5.17), is carried out first and the final expression is derived as:

$$\nabla\Phi\bullet\vec{n}\,|\vec{s}| = D_n(\Phi_N - \Phi_P) + D_c(\Phi_{P2} - \Phi_{P1}) \quad (5.18)$$

$$D_n = \frac{|\vec{s}|}{(\vec{r}_1 + \vec{r}_2)\bullet\vec{n}}; \qquad D_c = -\frac{(\vec{r}_1 + \vec{r}_2)\bullet\vec{s}/|\vec{s}|}{(\vec{r}_1 + \vec{r}_2)\bullet\vec{n}} \quad (5.19)$$

In the above, $\vec{r}_1$ is the distance vector from *P* to *C* and $\vec{r}_2$ is from *C* to *N*. The "normal" and "cross" diffusion coefficients, D_n and D_c, at each polygon side involve only geometric variables; they are calculated only once in the beginning of the computation.

Computation of a variable, say *Y*, at the center C of a polygon side invokes interpolations. As shown in Figure 76, the point *I* is defined as the intercept point between line *PN* and line P_1P_2. A second-order interpolation for point *I* may be expressed as

$$Y_I = \frac{\delta_1 Y_N + \delta_2 Y_P}{\delta_1 + \delta_2} \tag{5.20}$$

in which $\delta_1 = \vec{r}_1 \bullet \vec{n}$ and $\delta_2 = \vec{r}_2 \bullet \vec{n}$. Y_I may be used to approximate the value at the side center *C*. This treatment, however, does not guarantee second-order accuracy unless $\vec{r}_1$ and $\vec{r}_2$ are parallel. A truly second-order expression is derived as:

$$Y_C = Y_I - C_{side}(Y_{P2} - Y_{P1}) \tag{5.21}$$

$$C_{side} = \frac{(\delta_1 \vec{r}_2 - \delta_2 \vec{r}_1) \bullet \vec{s}}{(\delta_1 + \delta_2)\left|\vec{s}\right|^2} \tag{5.22}$$

The extra term in the above is similar in form to the cross diffusion term in (5.19).

Φ_C in the convective term of (5.17) needs further discussion. If the second-order central scheme is used directly, spurious oscillations may occur for flows with a high cell Peclet number (Patankar, 1980). Therefore, a damping term is added to the central difference scheme similar to the concept of artificial viscosity. The damped scheme is as follows:

$$\Phi_C = \Phi_C^{CN} + d(\Phi_C^{UP} - \Phi_C^{CN}) \tag{5.23}$$

$$\Phi_C^{UP} = \frac{1}{2}(\Phi_P + \Phi_N) + \frac{1}{2} sign(V_C)(\Phi_P - \Phi_N) \tag{5.24}$$

where Φ_C^{CN} stands for the second-order scheme expressed in (5.21). In the above, *d* defines the amount of damping. Note that *d* is not a calibration parameter and a non-zero *d* makes the convective scheme less than second-order accuracy.

The final discretized equation at mesh cell *P* may be organized as a linear equation:

$$A_P \Phi_P = \sum_{nb} A_{nb} \Phi_{nb} + S_{diff} + S_{conv} + S_\Phi \tag{5.25}$$

where "*nb*" refers to all neighbor cells surrounding cell *P*.

For a non-staggered mesh, a special procedure is used to obtain the polygon side normal velocity that is used to enforce the mass conservation; otherwise the well-known checkerboard instability may appear (Rhie and Chow, 1983). Here the procedure proposed by Rhie and Chow (1983) is adopted, i.e., the normal velocity is obtained by averaging the momentum equation from cell centers to cell sides. A detailed derivation is omitted, and interested readers are referred to the previous work (e.g., Rhie and Chow, 1983; Peric et al., 1988; and Lai et al. 1995). It is sufficient to present only the final form of the equation as follows:

$$V_C = <\vec{V}> \bullet \vec{n} + \left\langle \frac{A}{A_P} \right\rangle < gh\nabla z > \bullet \vec{n} - \left\langle \frac{A}{A_P} \right\rangle gh\nabla z \bullet \vec{n} \tag{5.27}$$

where "< >" stands for the interpolation operation from mesh cell center to side as expressed in (B21). When a vector appears in the interpolation operation, the interpolation is applied to each Cartesian component of the vector.

The velocity-elevation coupling is achieved using a method similar to the SIMPLEC algorithm (Patankar, 1980). In essence, if elevation z^n is known from a previous time step or iteration, an intermediate velocity is obtained first by solving the linearized momentum equation:

$$A_P \vec{V}_P^* = \sum_{nb} A_{nb} \vec{V}_N^* - a\nabla z^n + \vec{S}_V \tag{5.28}$$

where a is a constant. Next, we seek velocity correction $\vec{V}' = \vec{V}^{n+1} - \vec{V}^*$ and elevation correction $z' = z^{n+1} - z^n$ such that both the momentum and the mass conservation equations are satisfied. For the momentum equation, it is

$$A_P \vec{V}_P^{n+1} = \sum_{nb} A_{nb} \vec{V}_N^{n+1} - a\nabla z^{n+1} + \vec{S}_V \tag{5.29}$$

Or, the following correction equation is obtained:

$$A_P \vec{V}_P' = \sum_{nb} A_{nb} \vec{V}_N' - a\nabla z' \tag{5.30}$$

With the SIMPLEC algorithm, the above may be approximated as:

$$\vec{V}_P' = -\frac{a}{A_P - \sum_{nb} A_{nb}} \nabla z' \tag{5.31}$$

Substitution of the above into the mass conservation equation leads to the following elevation correction equation:

$$\frac{z'}{\Delta t}+\nabla\bullet(\vec{V}\,z')=\nabla\bullet\left(\frac{ah}{A_P-\sum_{nb}A_{nb}}\nabla z'\right)-\nabla\bullet\left(h^n\vec{V}^*\right) \tag{5.32}$$

The above elevation correction equation is solved for z', and (5.31) is then used to obtain the velocity correction. A number of iterations are usually needed within each time step if the flow is unsteady; but only one iteration is used for a steady state simulation.

Governing equations are solved in a segregated manner. In a typical iterative solution process, momentum equations are solved first assuming known water surface elevation and eddy viscosity at a previous time step. The newly obtained velocity is used to calculate the normal velocity at cell sides using (5.27). This side velocity will usually not satisfy the continuity equation. Therefore, the elevation correction equation (5.32) is solved to obtain a new elevation, and subsequently a new velocity with (5.31). Other scalar equations, such as turbulence, are solved after the elevation correction equation. This completes one iteration of the solution cycle. The above iterative process may be repeated within one time step until a preset residual criterion for each equation is met. The solution would then advance to the next time step. In this study, the residual of a governing equation is defined as the sum of absolute residuals at all mesh cells. The implicit solver requires the solution of non-symmetric sparse matrix linear equations (5.28) and (5.32). In this study, the standard conjugate gradient solver with ILU preconditioning is used (Lai, 2000).

5.5 Preliminary Case Study Results

Numerical model test studies are divided into three parts in the following: test of unsteady flow modeling capability; test of a simple case for identification of a numerical problem with turbidity current modeling, and test cases and comparison with flume experiments.

5.5.1 Unsteady Modeling with SRH-2D

It is realized that unsteady, time-accurate flow modeling is needed to solve the governing equations of turbidity currents. So far, the numerical scheme of SRH-2D model has been extensively tested, verified, and validated with a wide range of flume and field cases with constant discharge only (steady-state solutions). There is no systematic test and verification of SRH-2D's capability to model the unsteady time-accurate flows with a time series hydrograph. Therefore, such tests are conducted during this study, and results are reported.

Flooding and dam-break simulations are particularly relevant with regard to the unsteady time-accurate modeling; and they present challenges to any numerical models. Therefore, dam break flows are selected for the purpose. These flows are difficult to model as they are highly unsteady with complex flow features such as the occurrence of moving hydraulic jumps. Modeling procedure is briefly described, key parameters are discussed, and sample case studies are presented to demonstrate the accuracy of SRH-2D.

Steady-state flow modeling with SRH-2D is relatively straightforward and simple to carry out. The only key modeling parameter is the time step which is mainly used to ensure stability. For time-accurate unsteady modeling, stability is still determined by the time step; but the time step is also related to the time accuracy. In addition, a number of other modeling parameters may be needed to ensure solution accuracy and they are discussed below.

For a time-accurate unsteady modeling, the following procedure is recommended:

- Initial Condition: The initial condition needs to be determined first. It may be set up using one of three ways: (1) ZONAL method; (2) DRY bed method; or (3) RST method. "ZONAL" method is to use SMS to divide the entire mesh into different zones represented by SMS material types. Within each zone, users may specify a constant water surface elevation or a constant water depth. "DRY" bed is to let the entire mesh to have zero water depth. With the RST method, a steady state solution with a constant flow discharge is obtained first. This solution, stored in the restart (or hot-start) file, _RST.dat, is then used as the initial condition for a time-accurate unsteady modeling.
- Initial Time Step: An initial time step is estimated first. At present, we have not developed a guideline on how to estimate it. As a general rule, a time step of 0.1 to 1.0 second may be used for field cases; and smaller time step may be needed for flume cases. With time-accurate unsteady modeling, a small time step may be needed to obtain the needed solution accuracy; and we found that the time step restriction was less due to the numerical stability.
- Relaxation Parameter: A relaxation parameter, named RELAX_H, is used by SRH-2D to control the solution stability. This parameter, ranging from 0.1 to 0.9, can only be set up using the _DIP.dat file. The recommended value RELAX_H=0.8 to 0.9 for unsteady time-accurate modeling. If stability becomes an issue for rare cases, reduction of time step is preferred. In rare cases, RELAX_H may have to be reduced to as low as 0.2, if instability occurs and a reduction of time step does not help. A baseline solution should be obtained first with the initial time step and an appropriate RELAX-H parameter.
- Finally, a time-step sensitivity study is recommended. One or two smaller time steps should be used, while keeping other parameters unchanged, and

the solutions should be compared. The "final" solution is the one whose results do not change noticeably if the time step is reduced further. A good strategy is to reduce the time step at least by half.

Two extra parameters may be used in conjunction with the modeling of unsteady flows: DAMP and NITER (both may be set up in the _DIP.dat file). DAMP is used to activate the second-order numerical scheme. DAMP ranges from 0.1 to 1.0. A typical value of DAMP=0.35 is recommended. Smaller DAMP is closer to a "purely" 2nd-order central difference scheme which may leads to oscillatory results due to lack of damping. NITER is the number of iterations within each time step. A default setting of NITER=3 is used by SRH-2D. Occasionally, higher number may be used, e.g., NITER=5, particularly when smaller RELAX_H (e.g., below 0.4) has to be used. Higher number of NITER will increase the computing time though.

In the following, two time-accurate unsteady solution cases are presented. They demonstrate how SRH-2D may be used to compute the dam/levee break flows and good solutions may be obtained. In general, we found that (1) the water front computation is less difficult and not sensitive to model parameters; (2) the traveling hydraulic jump is harder to predict and it is sensitive to a number of model parameters; and (3) laboratory flume cases are more sensitive to model parameters than field cases.

Case 1: One-Dimensional Dam Break Flow over a Straight Channel

This case is selected from the dam-break flume experiment conducted by the U.S. Army Corps of Engineers Waterways Experimental Station (USACE, 1960, 1961). The rectangular flume has a length of 400 ft, a width of 4 ft, and a slope of 0.5%. Initially, water is stored upstream of the dam located at 200 ft into the flume and the water surface elevation is leveled with the upstream of the flume (x=0). The flume downstream of the dam is dry. At time zero, the dam is suddenly removed to simulate an instantaneous breach and the water stored upstream starts to move downstream.

The simulation uses a mesh consisting of 102 uniform cells in the flow direction and 3 lateral cells (a total of 306 cells). The upstream boundary is assigned as a "WALL" boundary condition type, the downstream boundary is a free out-fall boundary with "EXIT-EX" type, and two side boundaries are set up as "SYMMETRY" to model the 1D nature of the flow. The Manning's roughness coefficient is 0.009 $s/m^{1/3}$. This value was recommended by the USACE report (USACE, 1960); the same value was also used by Wang and Bowles (2006) and Savant et al. (2010) in their numerical modeling of the case. The initial condition at time zero is as follows: zero velocity everywhere, constant water surface elevation upstream of the dam, and dry bed downstream of the dam. In addition, the following parameters are used (assigned using _DIP file): dtnew=0.1, niter=5, relax_h=0.9, and damp=0.35.

The simulated SRH-2D results are compared with the measured data in Figure 77 and Figure 78. Overall, SRH-2D obtained good solutions that matched measured data well.

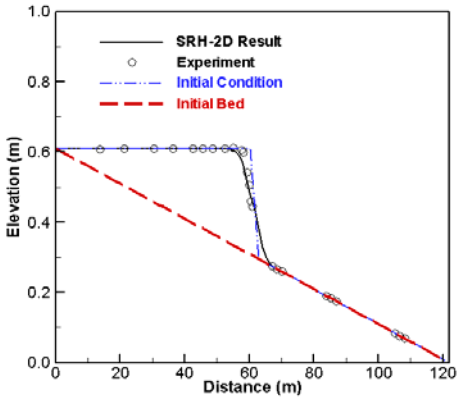

(a) Time = 2s

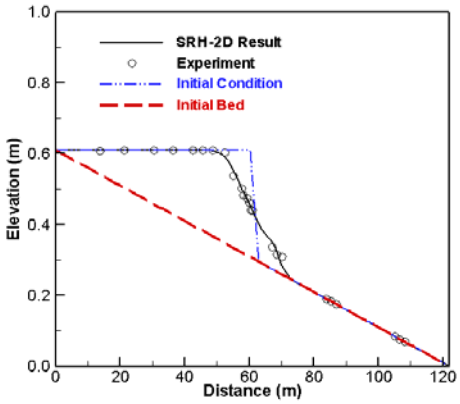

(b) Time = 5s

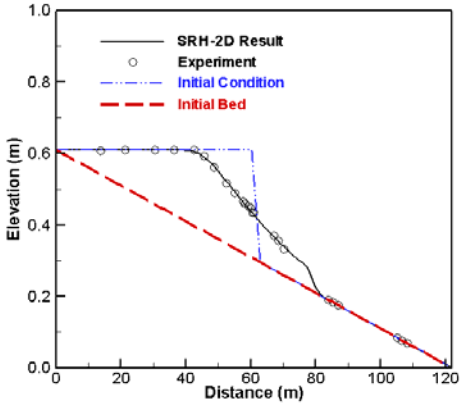

(c) Time = 10s

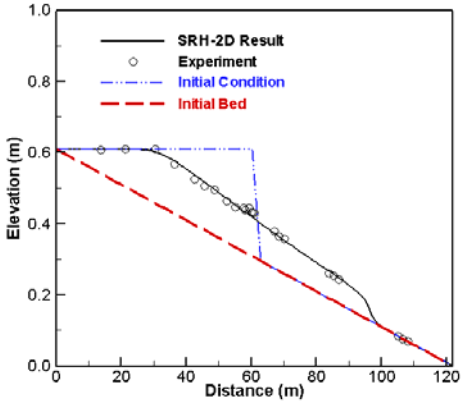

(d) Time = 20 s

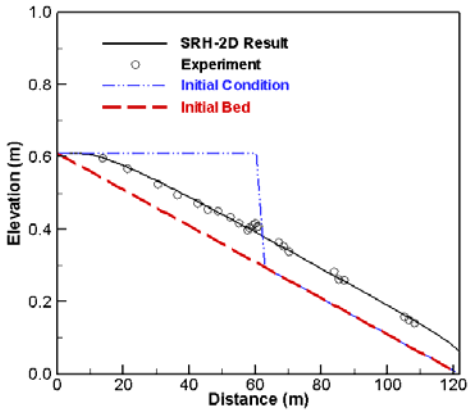

(e) Time = 40 s

Figure 77. Comparison of predicted and measured water surface elevation at different times after dam-break for the 1D case

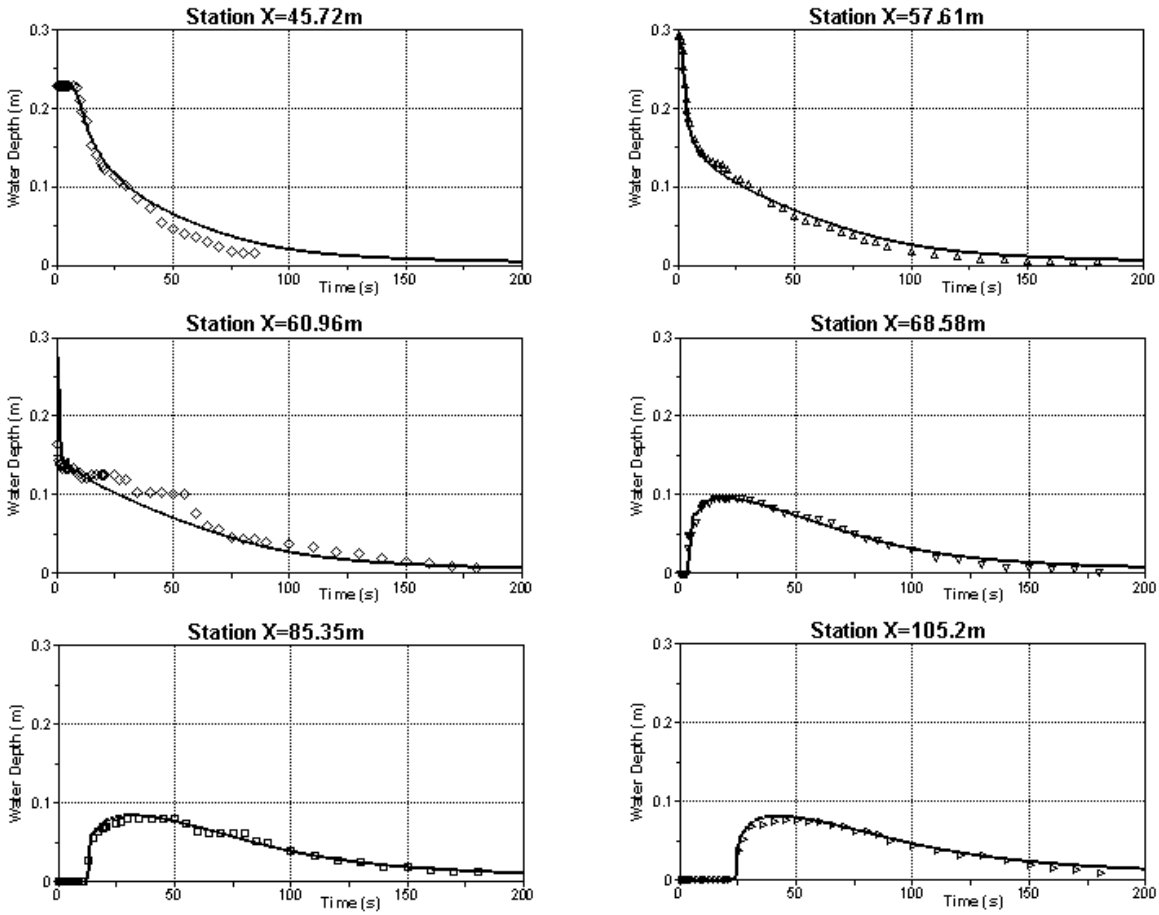

Figure 78. Comparison of predicted and measured water depth variation with time at the selected measurement stations for the 1D dam-break case

Case 2: Two-Dimensional Dam-Break Flow over Two Channels with 45° Angle

The next selected test case is a benchmark test problem proposed by the European Union CADAM (Concerted Action on Dam-Break Modeling) project (Morris, 2000). Numerical modeling has been carried out by many researchers (e.g., Brufau and Garcia-Navarro, 2000; Zhou et al. 2004; Savant et al. 2010). The plane view of the test case geometry is shown in Figure 79. The case consists of a square-shaped upstream reservoir and a 45° bend channel. The flow is essentially two dimensional in nature with two special dam break features: the damping effect of the corner and the upstream moving of the hydraulic jump (formed by the reflection at the corner).

The drainage channel is made of 4.25m and 4.15m long and 0.495m wide rectilinear reaches connected at 45° angle by an element. The channel is flat without slope. The reservoir has a length of 2.44m and a width of 2.39; the

reservoir is 0.33m below that of the channel, forming a vertical step at the entrance to the channel. The initial water depth in the reservoir is 0.58m but the depth in the channel is 0.01m. All boundaries are solid non-slip walls except the exit if the downstream channel. The exit is a free-fall boundary and the "EXIT-EX" boundary type is used by SRH-2D. However, when the flow at the exit is below subcritical, the "EXIT-EX" boundary produced unrealistic upstream-traveling waves. One way to implement the free-fall condition is to add a small section at the end of the channel with a steep enough bed to produce a supercritical flow. In this study, an extra 2 ft (0.615 m) section is added with a 1^o bed slope (1.63%). The energy loss of the flow is complex for the test case as it comes from several sources: bed roughness, side wall roughness of the channel, and contraction loss from the reservoir to the channel (see discussion by Zhou et al., 2004). Study of Zhou et al. (2004) showed that the upstream traveling of the hydraulic jump is sensitive to the contraction loss The CADAM workshop recommended the use of the Manning's roughness coefficient of 0.0095 for the bed and 0.0195 for the channel side wall. In this study, the head loss due to the contraction is added by setting the small section (length of 0.15 ft or 0.046 m) of the channel downstream of the dam to a Manning's coefficient of 0.06 (instead of the value of 0.095). The side wall roughness is incorporated through the approach presented by Lai and Greimann (2010) in which an effective roughness height is used. The effective roughness height (δ) of the side wall is estimated to be 2.34 mm, which corresponds to a Manning's coefficient (n) of 0.0195 if $n = \delta^{1/6}/18.7$ is assumed.

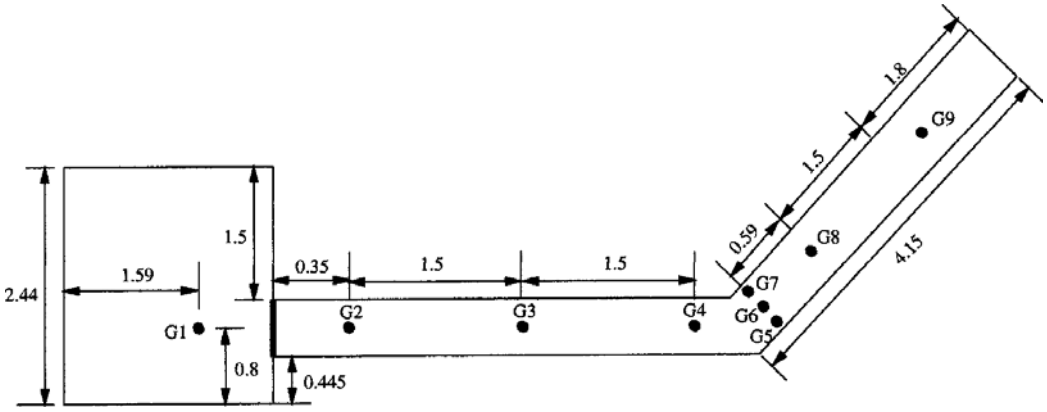

Figure 79. Plane view of the 2D dam-break case

A quadrilateral mesh is generated with 11,500 cells, which has a similar mesh resolution to other studies (e.g., Savant et al. 2010). A very small time step of 0.03 second is needed to obtain the time-independent solutions. Other simulation parameters include the following: NITER=5; RELAX_P=0.9; DAMP=0.25; and A_TURB=0.2.

Comparison of the model results with the measured data are made at nine gage points shown in Figure 79. The water surface elevation in time was measured at all stations; and comparisons are shown in Figure 80. Overall, SRH-2D obtained

reasonably good results in comparison with the measured data. The major mismatch is the prediction of the water depth at the gage station G2 (the nearest station to the dam). This mismatch is not unique to SRH-2D model and has been reported, to a certain degree, by most numerical models.

Parametric study showed that the movement of water front may be modeled well by the numerical model; but the modeling of the upstream traveling hydraulic jump caused by the corner is more difficult to capture, which has been a problem for other numerical models. We believe higher order numerical schemes alone are not sufficient to capture all details. The predicted hydraulic jump is sensitive to a number of parameters such as the contract loss, side wall roughness, and the amount of turbulence, all of which are difficult to represent in a numerical model.

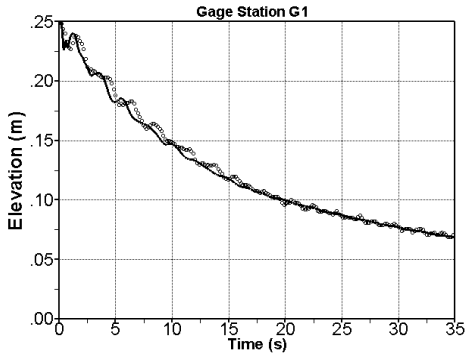

(a) Station G1

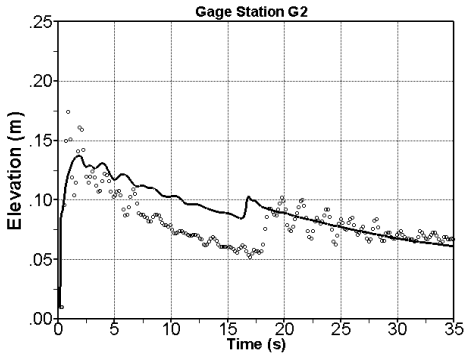

(b) Station G2

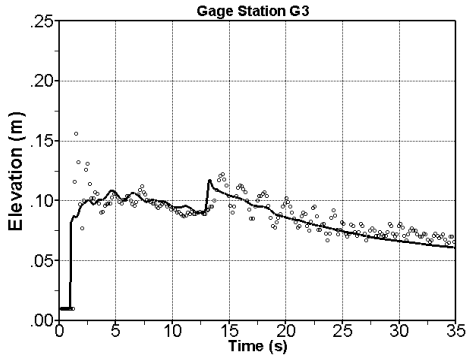

(c) Station G3

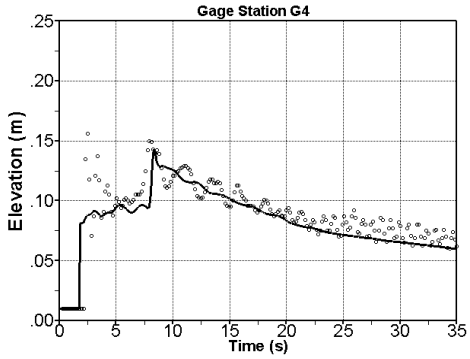

(d) Station G4

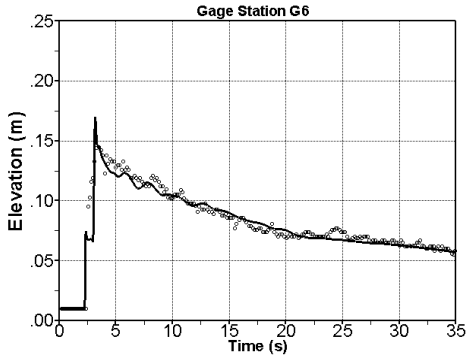

(e) Station G6

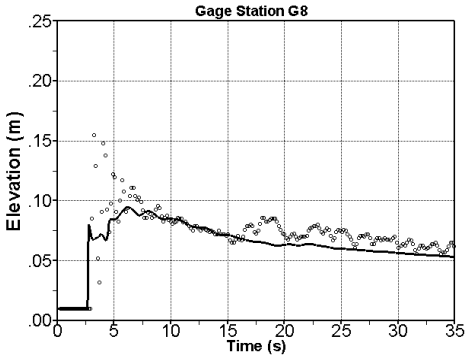

(f) Station G8

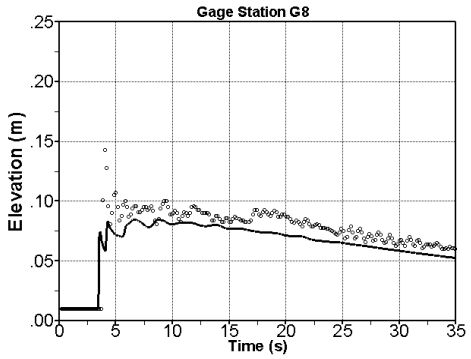

(g) Station G9

Figure 80. Comparison of predicted and measured water depth history at seven gage stations (see Figure 79 for the locations of all stations)

5.5.2 A Numerical Issue Associated with the Turbidity Current Numerical Method

A simple 1D test case was created for debugging and testing purpose to model the turbidity current. Particularly, this case is used to illustrate a numerical issue associated with the density current modeling with numerical methods.

A turbidity current with a thickness (water depth) of 0.03 m and sediment concentration of 0.03 enters a rectangular 1D channel with length of 12 m, width of 1 m, and speed of 0.1 m/s (Figure 81). A mesh with 100 cells longitudinally and 3 cells laterally is used for the modeling. The head (or front) of the current will propagate through the solution domain and it represents a "shock-like" discontinuity. In the test, the turbidity current is "conservative" in that the erosion and deposition terms in the sediment concentration equation are set to be zero.

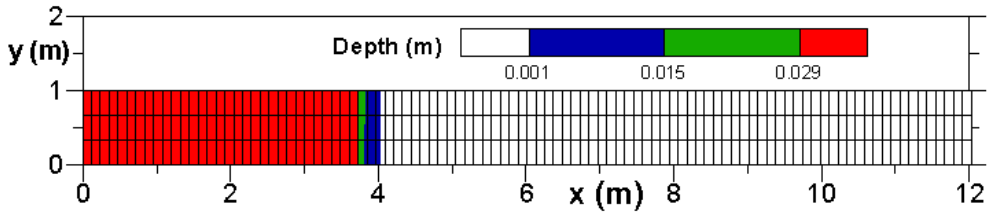

Figure 81. The mesh for the 1D case and the predicted water depth and front propagation at time = 36 s

The predicted water depth and sediment concentration with and without the entrainment are shown in Figure 82 and Figure 83. Notice that an "anomaly" of the predicted water depth appears in the head area of the current for both cases: an over-shoot (or over-prediction) of the depth at the head. This occurs whether there is entrainment or not. The anomaly is caused by the faster "smearing" of the sediment concentration in the head region, not due to entrainment. During the study, efforts have been spent to "correct" this problem with various higher-order schemes; but only limited success has been achieved at present. This issue will be a continued research effort in the next year study. We came across a recent study by Groenenberg (2007), who found the same anomaly with his sophisticated high-order TVD schemes. So it confirmed that this may be a "universal" problem for many numerical methods. In the study of Groenenberg (2007), an extrapolation method was applied to the concentration to "force" reduction of the smearing in ceoncentration. This "fix" was not ideal, in our opinion, but it could be an option worthy of trying in the future. Other ways to overcome the difficulty continue to be sought in the future.

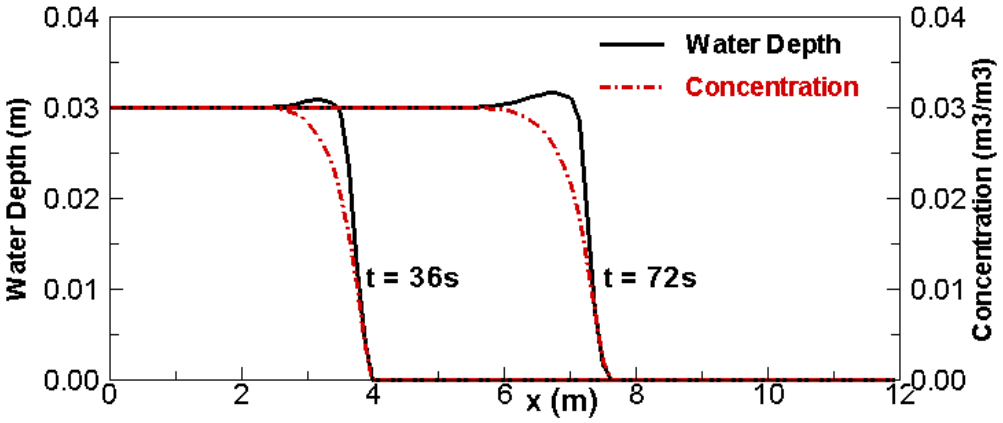

Figure 82. Predicted water depth and sediment concentration at two times for the 1D conservative turbidity current without the entrainment term

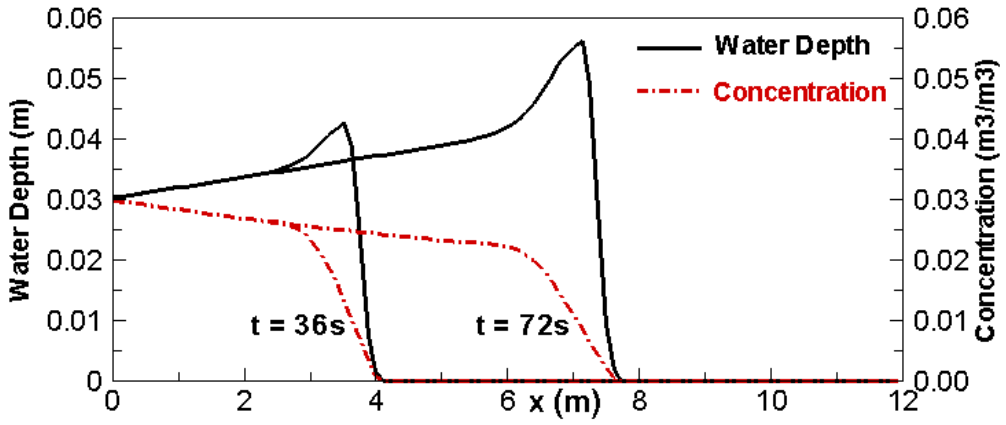

Figure 83. Predicted water depth and sediment concentration at two times for the 1D conservative turbidity current with the entrainment term

5.5.3 Simulation of Turbidity Currents in the Laboratory Setting

In this section, we proceed to the testing and verification studies. Despite the anomaly mentioned above, it is found that the impact to results is limited to the head region of a turbidity current; even the propagation speed of the head is not influenced much by the current numerical method.

A serious of experiments were carried out by Luthi (1980a, 1980b, 1981) to investigate the behavior of non-channelized turbidity currents and deposits. The experimental setting emulates flows near river mouths where water and sediments flow into reservoirs, lakes, or oceans. In the experiment, a thoroughly mixed suspension of freshwater and solid particles was discharged into a basin through an entry gate which had a width of 30 cm and a height of 5 cm. The basin was 10 m long, 6 m wide, and 1 m deep. It was filled with clear water to the top edge of the entry gate. A ramp, with 9 m long, 5 m wide and a constant inclination of 2.3º or 5º, was placed in the basin as the bed for the development of the current. Therefore, water depth is 5 cm at the entry gate. The discharge in all experiments was kept constant at 3.5 l/s. Also, during an experiment, a relay-controlled drainage system was used to maintain the water level in the basin constant. This prevented the generation of a counter-current in the upper layer above the turbidity current.

In the first set of experiments, chalk powder, with a mean grain diameter of approximately 3 μm (maximum size of 10 μm), was used as the sediment. This resulted in quasi-steady flows without deposition. Measured contour plots were available showing the propagation of the front in time through the basin. Also at selected points, flow velocity and sediment concentration were measured in time.

In the second set of experiments, quartz silt was used with an almost lognormal size distribution. Mean grain size was 4.76 Φ (37 μm) with a standard deviation

of 0.52 Φ. These represented rapidly waning flows with quick loss of sediments and deposition. Measured data included deposit thickness, mean grain size, standard deviation, and skewness of the deposit. A description of observed sedimentary structures was also provided. Figure 84 displays a deposit photo for one such experiment. The current entry is in the upper left corner. Characteristic features of the deposit include an area of non-deposition near the entry gate, bounded on both sides by levee-like ridges, ripples on the surface of the deposit, and the lobe-like shape of the deposit. Also, just downstream of the area of non-deposition, the deposit quickly attains its maximum thickness, which gradually decreases away from the entry gate.

Figure 84. Photo of deposit from a turbidity current experiment with quartz silt (source: Luthi, 1980b)

Conservative Turbidity Current

A conservative, quasi-steady, turbidity current run case is selected for testing and verification in this study, in which very fine chalk powder was used.

The current has an initial depth of 5 cm, corresponding to the height of the entry gate, a cross-sectional area of the entry gate of 0.015 m^2, and a flow discharge of 3.5 l/s. The current flow has an initial velocity of 0.233 m/s and an initial sediment concentration of 0.788%. The diameter of the grain size is chosen to be 7.5 μm so that the reported settling velocity of 0.004 cm/s of the chalk powder may be obtained. The density of the powder is assumed to be 2650 kg/m3. Also,

the drag coefficient, C_f, is important and may be treated as a calibration parameter. In this study, C_f =0.045 is used.

A mesh with a size of 180 cells longitudinally and 100 cells laterally is used; so each cell is a square with side length of 5 cm. A time step of 0.1 s is used in order to obtain time-independent results.

The simulated results at 100 seconds are shown in Figure 85, Figure 86, and Figure 87. Comparison of the predicted current front propagation in time with the measured data is shown in Figure 88.

In Figure 88, the location of the front of the turbidity current is represented by contours, drawn at 10 s intervals. The distance between the contours stabilizes after approximately 30 s, at which point the flow velocity is near-constant indicating a quasi-steady flow. This is expected as the incoming current has a constant depth, discharge, and sediment concentration and the under flow does not interact with the bed due to the easily suspended chalk powder used.

Notice the following:

- The “anomaly” in water depth near the head region still exists, but it does not exist in the velocity;
- The predicted sediment concentration has large “smearing’ which is the cause for the anomaly; and
- The predicted front propagation pattern agrees with the measured data reasonably well except that the predicted speed is slightly faster than the measured value. Increase of the resistance drag coefficient will match the computed speed with the measured data accurately; but it is not carried out. The reason is that the turbidity current results are preliminary and further model development is needed to fix the “anomaly” problem discussed above.

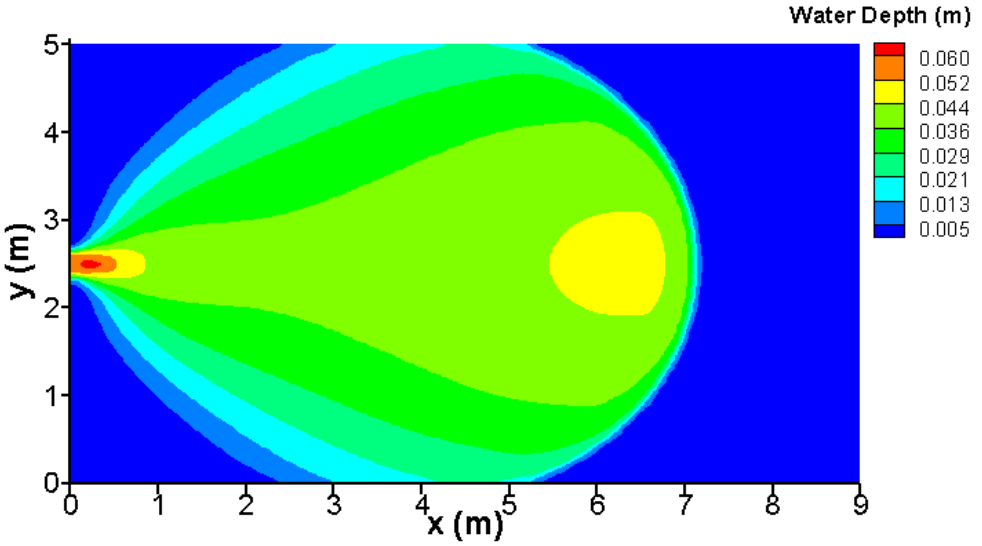

Figure 85. Predicted turbidity current thickness (water depth) at 100 seconds for the Luthi case 1

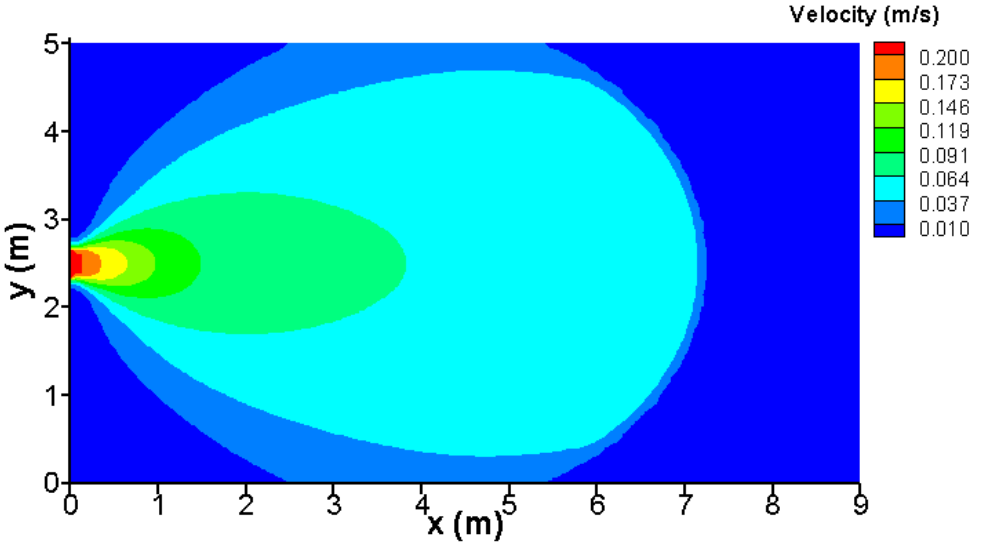

Figure 86. Predicted current velocity at 100 seconds for the Luthi case 1

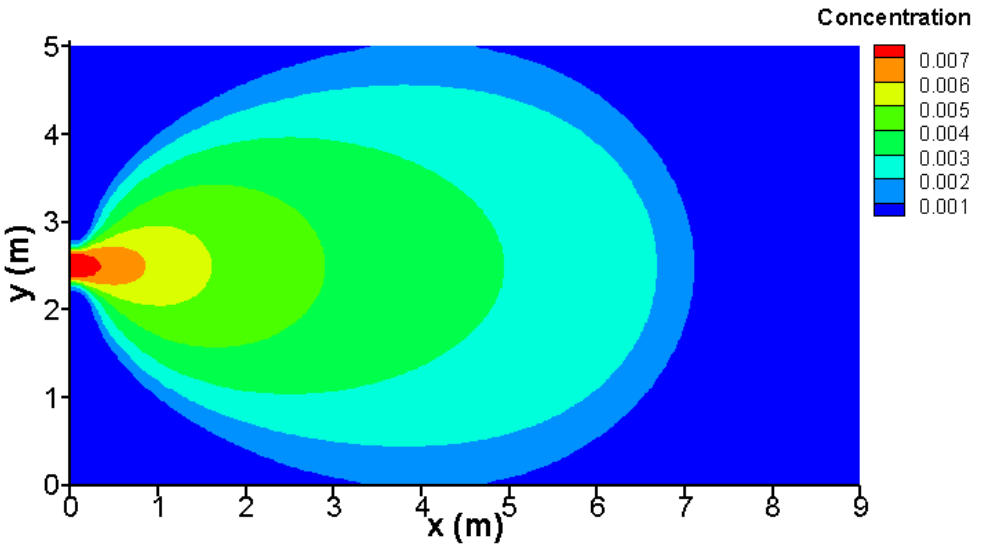

Figure 87. Predicted turbidity current sediment concentration at 100 seconds for the Luthi case 1

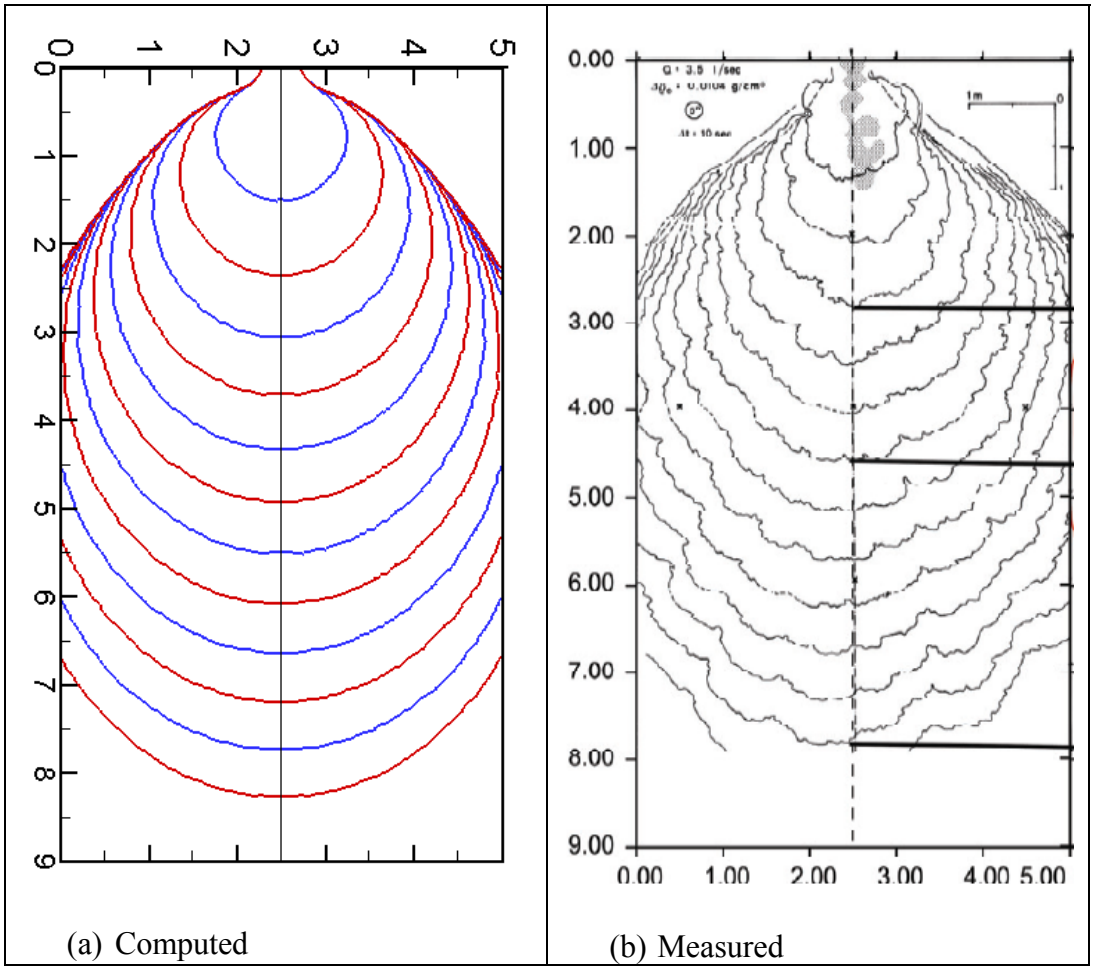

(a) Computed (b) Measured

Figure 88. Comparison of simulated front locations with the measured data for the conservative, quasi-steady turbidity current; each contour represents 10 seconds apart from 10 s to 120 s

Non-Conservative Waning Turbidity Current

The next test case corresponds to the second set of experiments in which a non-conservative waning turbidity current was generated by using the quartz silt as the sediment particles. The mean grain size was $4.76\,\Phi$ (37 μm) with a standard deviation of $0.52\,\Phi$. The size distribution nearly follows the lognormal distribution. Three size classes are used to represent the sediments: 53.2 μm with a probability of 0.278, 37.1 μm with a probability of 0.444, and 21.1 μm with a probability of 0.278. Other initial conditions and model parameters are the same as the conservative turbidity current case discussed in the above.

Preliminary results are shown in Figure 89 through Figure 91 and comparison of deposit thickness with the measured data is shown in Figure 92. . It is seen that the model captures the essential features of the waning turbidity current, although

many details are yet to be matched with refined models. More test and study are planned for this case next year.

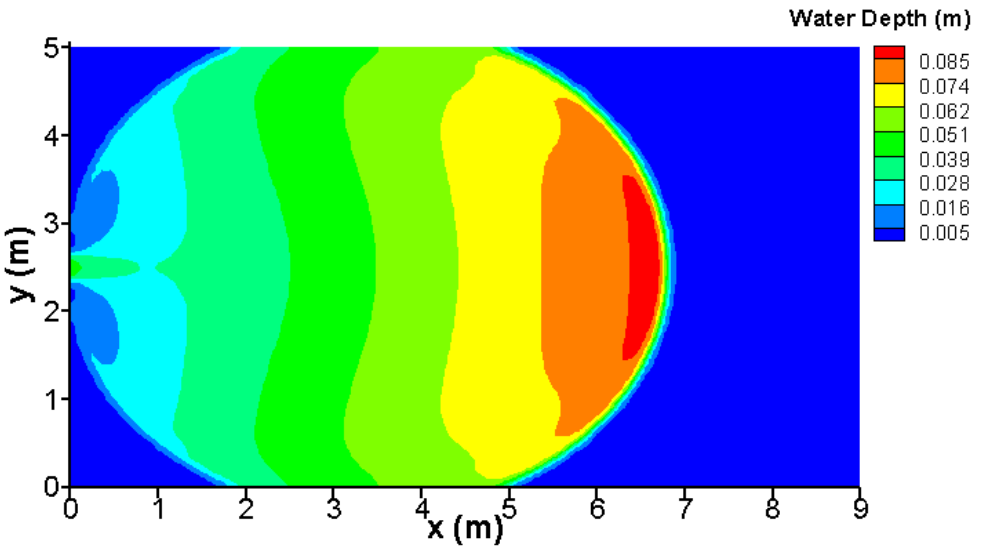

Figure 89. Predicted turbidity current thickness (water depth) at 70 seconds for the waning turbidity current case

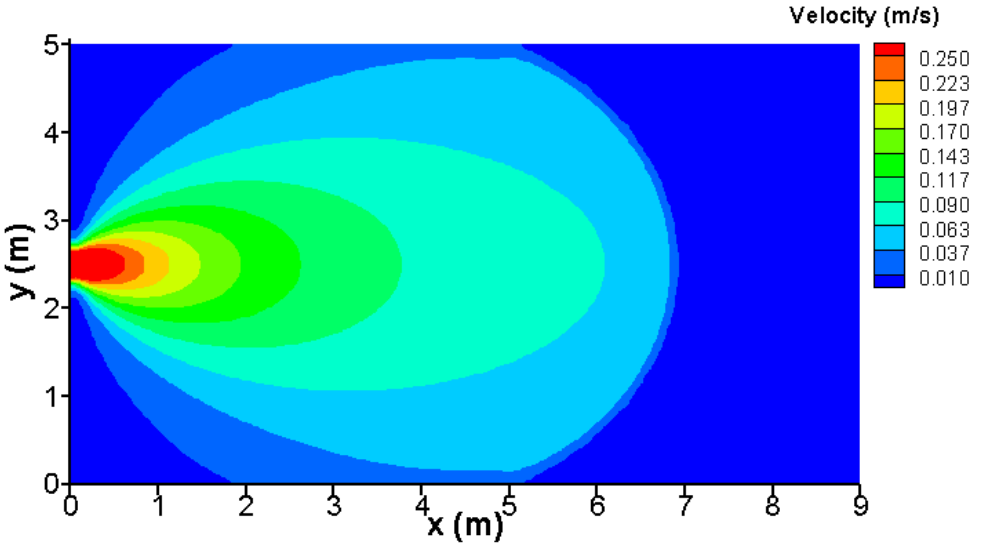

Figure 90. Predicted current velocity at 70 seconds for the waning turbidity current case

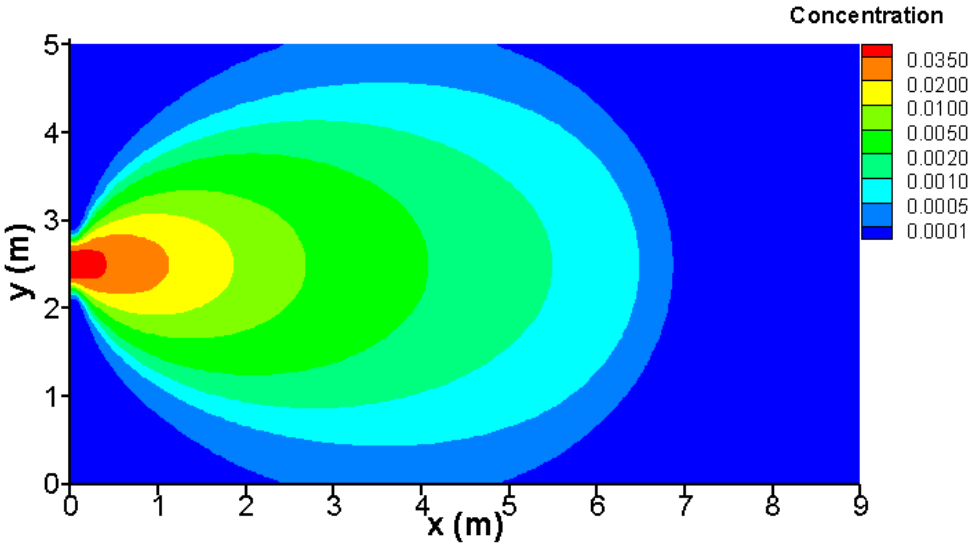

Figure 91. Predicted turbidity current sediment concentration at 70 seconds for the waning turbidity current case

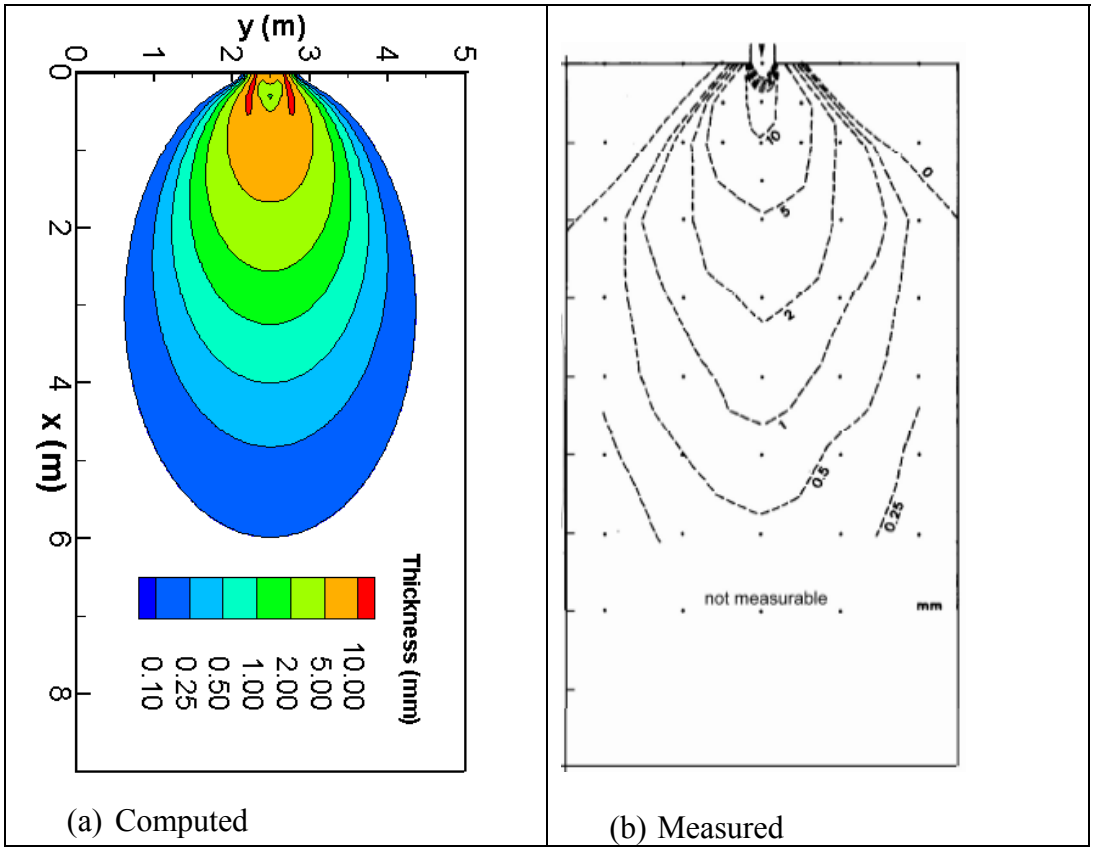

Figure 92. Comparison of computed and measured deposit thickness for the non-conservative waning turbidity current flow at t = 120 seconds.

5.6 Potential Model Limitations

A few potential limitations of the proposed layer-averaged model under development in this study are discussed below.

A major limitation is related to the assumption that depth-averaging is valid for representation of the turbidity current. The assumption was found to be generally accurate by Parker et al. (1987), and particularly so for supercritical flows (Garcia, 1994). In theory, a bottom turbidity current develops downstream of the plunge point, and will reach the dam. If it is not vented, or is vented slowly, the head of the current runs up against the face of the dam and forms a backward-migrating bore (Bell, 1942). This bore eventually stabilizes in the form of an internal hydraulic jump, downstream of which an internal muddy pond forms. The turbidity current within the pond is subcritical. If the Froude number is sufficiently less than 1, the pond is deep and a fairly sharp horizontal interface would form, with muddy water below and ambient water above. Under such circumstance, the layer-averaged formulation works. Otherwise the layer-averaged equation is applicable only for the period before the current reaches the dam.

Initial development of the model in this study further assumes that the reservoir is quiescent and unstratified except for the turbidity current itself. If the ambient water is also moving, a multi-layer model may need to be developed; for such a case, the theory developed by Hogg et al. (2005) may be referred to.

Strictly speaking, the formulation is valid only if $C_t << 1.0$. Therefore, the validity of the model for dense current is yet to be tested.

6 References

Akiyama, J., and H.G. Stefan, H.G. (1986). “Prediction of turbidity currents in reservoirs and coastal regions.” Proc. Third Symp. River Sedimentation, University of Mississippi, 1295-1305.

Alavian, V., Jirka, G.H., Denton, R.A., Johnson, M.C., Stefan, H.G. (1992). “Turbidity currents entering lakes and reservoirs,” J. Hydraulic Engineering, 118(11), 1464-1489.

Annandale, G.W. (1999). "Estimation of Bridge Pier Scour Using the Erodibility Index Method" in Stream Stability and Scour at Highway Bridges, ASCE Compendium of Water Resources Engineering Conferences 1991-1998, edited by Richardson and Lagasse, pp 83-97, Reston, VA.

Annandale, G.W., (2006). Scour Technology, Mechanics and Engineering Practice. McGraw Hill, New York.

Ariathurai, R., and Arulanandan, K., 1978. Erosion rates of cohesive soils. Journal of the Hydraulics Division, ASCE, 104(HY2), 279-283.

Arulanandan, K., 1975. Fundamental aspects of erosion of cohesive soils. Journal of the Hydraulics Division, ASCE, 101(HY5), 635-639.

Arulanandan, K., Gillogley, E., and Tully, R., 1980, Development of a quantitative method to predict critical shear stress and rate of erosion of natural undisturbed cohesive soils, Technical Report GL-80-5. U.S. Army Engineers Waterways Experiment Station: Vicksburg, MS.

ASCE Task Committee (1998). River width adjustment. I. Process and mechanism, J. Hydraul. Eng., ASCE, vol.9, 881-902.

Bagnold, R.A. 1966. An approach to the sediment transport problem from general physics. U.S. Geological Survey Professional Paper 422-I. US Government Printing Office: Washington, DC.

Banglapedia, (2005). River bank erosion.

http://banglapedia.search.com.bd/HT/R_0211.htm , Sept, 2005.

Bell, H. S. (1942). “Stratified flow in reservoirs and its use in preventing silting.” Miscellaneous Publication 491, U.S. Department of Agriculture, Washington, D.C.

Bradford, S.F., and Katopodes, N.D. (1999). “Hydrodynamics of turbidity underflows. I: Formulation and numerical analysis.” J. Hydraulic Engineering, 125(10), 1006-1015.

Brufau, P. and Garcia-Navarro, P. (2000). “Two-dimensional dam break flow simulation.” Int. J. Numer. Meth. Fluids, 33, 35-57.

BSTEM, (2009). "BSTEM Manual," the content can be found from at the website: http://www.ars.usda.gov/SP2UserFiles/Place/64080510/XLS/BSTEM-5.0.xls

Buffington, J.F., 1999. The legend of A. F. Shields. Journal of Hydraulic Engineering, ASCE, 125(4), 376-387.

Buffington, J.M, and D.R. Montgomery (1997). "A systematic Analysis of Eight Decades of Incipient Motion Studies, with special Reference to Gravel-Bedded Rivers," Water Resources Research, Vol. 33, No. 8, pp. 1993-2029.

Carson, M.A., and Kirkby, M.J., 1972. Hillslope Form and Process. Cambridge University Press: Cambridge, UK.

Casagli, N., Curini, A., Gargini, A., Rinaldi, M. and Simon, A., 1997. Effects of pore pressure on the stability of streambanks: Preliminary results from the Sieve River, Italy, In: S.S.Y. Wang, E.J. Langendoen, and F.D. Shields Jr. (eds.), Management of Landscapes Disturbed by Channel Incision. University of Mississippi: University; pp.243-248.

Cassagli, N., Rinaldi, M., Gargini, A., Curina, A. (1999) Pore water pressure and streambank stability: results from a monitoring site on the Sieve River, Italy. Earth Surface Processes and Landforms 24: 1095–1114.

Chang, H. H., and Hill, J. C. (1976). Computer modeling of erodible flood channels and deltas." J. Hydr. Div. 102_10_, 1461–1477.

Chang, H.H. (1979). Minimum stream power and river channel patterns. J. Hydrol. 41, 301–327.

Chang, H.C. (1988). Fluvial Processes in River Engineering, John Wiley & Sons, Inc.

Chen, D., and Duan, J.G. (2006). "Modeling width adjustment in meandering channels," J. Hydrology, 321, 59-76.

Chen, D., and Duan, J.G. (2008). Case study: two-dimensional model simulation of channel migration processes in west Jordan River, Utah. J. Hydraulic Engineering, 134(3).

Choi, S.-U. (1998). "Layer-averaged modeling of turbidity currents with a dissipative-Galerkin finite element method, Part I: Formulation and application example." J. Hydraulic Res., 36(3), 339-362.

Choi, S.-U. (1999). "Layer-averaged modeling of two-dimensional turbidity currents with a dissipative-Galerkin finite-element method, Part II: Sensitivity analysis and experimental verification." J. Hydraul. Res., 37(2), 257–271.

Chow, V.T. (1959). Open Channel Hydraulics. 1st Ed., McGraw-Hill Book Co., New York, N.Y.

Crosato, A. (1989). Meander migration prediction, Excerpta, GNI, 4. Libreria Progetto, Volume 4, published by GNI, Gruppo Nazionale Idraulica, Padova. pp.169-198.

Dapporto, S., Rinaldi, M., Casagli, N., Vannocci, P. (2003). Mechanisms of riverbank failure along the Arno River, Central Italy. Earth Surface Process and Landforms 28: 1303–1323.

Darby, S.E, Thorne, C.R. (1996). Stability analysis for steep, eroding, cohesive riverbanks. Journal of Hydraulic Engineering 122: 443–454.

Darby, S.E., Alabyan, A.M, Van de Wiel, M.J. (2002). Numerical simulation of bank erosion and channel migration in meandering rivers. Water Resources Research 38: 1163–83.

Darby, S.E., Spyropoulos, M., Bressloff, Rinaldi, M. 2004: Fluvial bank erosion in meanders: a CFD modelling approach. Pp. 268–273 in Proceedings 5th International Symposium on Ecohydraulics, Madrid, Spain 12-17 September 2004, International Association of Hydraulic Engineering and Research.

Darby, S.E., Rinaldi, M., and Dapporto, S. (2007). Coupled simulations of fluvial erosion and mass wasting for cohesive river banks, J. Geophys. Res., 112, F03022, doi:10.1029/2006JF000722.

Dickinson, W.T., Rudra, R.P., Wall, G.J. (1989). Nomographs and software for field and bank erosion. Journal of Soil and Water Conservation 44: 596–600.

Duan, G., Wang, S.S.Y., Jia, Y., (2001). The applications of the enhanced CCHE2D model to study the alluvial channel migration processes. J. Hydraul. Res., IAHR 39, 469–480.

Duan, J. G., and Julien, P.Y., (2005). Numerical simulation of the inception of channel meandering, Earth Surf. Process. Landforms, 30, 1093–1110. DOI: 10.1002/esp.1264

Dunne, T., and Leopold, L.B. (1978). Water in environmental planning. W.H. Freeman, San Francisco. 818 pp.

Eaton, B.C., Church, M., Millar, R.G., (2004). Rational regime model of alluvial channel morphology and response. Earth Surf. Proc. Land. 29, 511–529.

Einstein, H.A., 1942. Formulas for the transportation of bed load. Transactions of the ASCE, 107, 561-597.

Engelund, F., and Hansen, E. (1972). *A monograph on sediment transport in alluvial streams*, Teknish Forlag, Technical Press, Copenhagen, Denmark.

Environment Agency, (1999). Waterway bank protection: a guide to erosion assessment and management. R and D Publication 11, Environment Agency, 235 pp.

Federal Interagency Stream Restoration Working Group 2001: Stream Corridor Restoration: Principles, Processes and Practices. Federal Interagency Stream Restoration Working Group. GPO Item No. 0120-A; SuDocs No. A 57.6/2:EN3/PT.653.

Fennema, R.J., and Chaudhry, M.H. (1989). "Implicit methods for two-dimensional unsteady free-surface flows," J. Hyd. Res. 27(3), 321-332.

Ferguson, R.I. (1973). Channel pattern and sediment type. Area 5, 38-41.

Fleenor, W.E. (2001). Effects and Control of Plunging Inflows on Reservoir Hydrodynamics and Downstream Releases, Ph.D. Thesis, Civil and Environmental Engineering, Univ. of California, Davis.

Fredlund, D.G., and Rahardjo, H., 1993. Soil Mechanics of Unsaturated Soils. John Wiley and Sons, Inc.: New York.

Fredlund, D.G., Morgenstern, N.R., and Widger, R.A., 1978. The shear strength of unsaturated soils. Canadian Geotechnical Journal, 15, 313-321.

Garcia, M., and Parker, G. (1993). "Experiments on the entrainment of sediment into suspension by a dense bottom current." J. Geophys. Res., 98(C3), 4793–4807.

Garcia, M. H. (1994). "Depositional turbidity currents laden with poorly sorted sediment." J. Hydr. Engrg., ASCE, 120(11), 1240–1263.

Glover, R.E., Florey, Q.L., (1951). Stable channel profiles, vol. 235. US Bureau of Reclamation, Denver, CO.

Greimann, B.P., and Vandeberg, M., (2008). Predicting Rock Scour, Technical Report SRH-2008-01, Technical Service Center, Bureau of Reclamation, Denver, CO.

Grissinger, E.H., 1982. Bank erosion of cohesive materials, In: R.D. Hey, J.C. Bathurst, and C.R. Thorne (eds.), Gravel-bed Rivers. John Wiley & Sons Ltd.: Chichester, UK; pp.273-287.

Hanson, G.J., 1990, Surface erodibility of earthen channels at high stress, Part II - Developing an in situ testing device, Transactions of the American Society of Agricultural Engineers, 33(1), 132-137.

Hanson, G.J., and Cook, K.R., 1997. Development of excess shear stress parameters for circular jet testing, American Society of Agricultural Engineers Paper No. 97-2227. American Society of Agricultural Engineers: St. Joseph.

Hanson, G.J., and Simon, A., 2001. Erodibility of cohesive streambeds in the loess area of the midwestern USA, Hydrological Processes, 15(1), 23-38.

Hasegawa, K., (1981). Bank–erosion discharge based on a nonequilibrium theory. Proc. JSCE, Tokyo, 316, 37–50 (in Japanese).

Hey, R.D. and Thorne, C.R. (1986). Stable channels with mobile gravel beds. J. Hydraul. Eng. Div., ASCE 112, 671-689.

Hjulström, F., 1935. The morphological activity of rivers as illustrated by River Fyris. Bulletin of the Geological Institute, University of Uppsala, 25(3), 221-527.

Hogg, A.J., Hallworth, M.A., and Hupperrt, H.E. (2005). "On gravity currents driven by constant fluxes of saline and particle-laden fluid in the presence of a uniform flow," J. Fluid Mech. Vol.539, 349-385.

Hooke, J.M., 1980. Magnitude and distribution of rates of river bank erosion. Earth Surf. Proc. Land. 5, 143–157.

Howard, A., S.R. Raine, and G. Titmarsh, (1998). The contribution of stream bank erosion to sediment loads in Gowrie Creek, Toowoomba. ASSI National Soils Conference, Brisbane, volume 2004, pp.491-493.

(http://www.usq.edu.au/users/raine/index_files/ASSSI98_Howard_etal.pdf).

Huang, H.Q., Nanson, G.C., (2000). Hydraulic geometry and maximum flow efficiency as products of the principle of least action. Earth Surf. Proc. Land. 25, 1–16.

Huang, J., and Greimann, B.P., (2008). *User's Manual for SRH-1D 2.1 (Sedimentation and River Hydraulics – One Dimension Version 2.1),* Bureau of Reclamation, Technical Service Center (www.usbr.gov/pmts/sediment).

Ikeda, S., Parker, G., Sawai, K., (1981). Bend theory of river meanders. Part I. Linear development. J. Fluid Mech. 112, 363–377.

Ikeda, S., Parker, G., Kimura, Y., (1988). Stable width and depth of straight gravel rivers with heterogeneous bed materials. Water Resour. Res. 24 (5), 713–722.

Ikeda, S., Izumi, N., (1990). Width and depth of self-formed straight gravel rivers with bank vegetation. Water Resour. Res. 26 (10), 2353–2364.

Imran, J., Parker, G., and Katopodes, N.D. (1998). "A numerical model of channel inception on submarine fans." J. Geophys. Res., 103(C1), 1219-1238.

Imran, J., Parker, G., and Harff, P. (2002). "Experiments on incipient channelization of submarine fans," J. Hydraulic Research, 40(1), 21-32.

Johannesson, H., Parker, G., (1989). Velocity redistribution in meandering rivers. J. Hydraul. Eng. 115 (8), 1019–1039.

Kellerhals, R., and Church, M. (1989). The morphology of large rivers: characterization and management. In: D.P. Dodge (ed.), Proceedings of International Large River Symposium, Special Publication 106, Canadian Journal of Fisheries and Aquatic Sciences, pp.31-48.

Kelly, W.E., and Gularte, R.C., 1981. Erosion resistance of cohesive soils. Journal of the Hydraulics Division, ASCE, 107, 1211-1223.

Kirkby, M.J. (1977). Maximum sediment efficiency as a criterion for alluvial channels. In: Gregory, K.J. (Ed.), River Channel Changes. Wiley, Chichester, pp. 429–442.

Knighton, A.D. (1998), Fluvial Forms and Processes: A New Perspective. Arnold, London, UK. 383 pp.

Kovacs, A., Parker, G., (1994). A new vectorial bedload formulation and its application to the time evolution of straight river channels. J. Fluid Mech. 267, 153–183

Kronvang, B., R. Grant and A.L. Laubel, (1997). Sediment and phosphorus export from a lowland catchment: Quantification of sources. Water Air and Soil Pollution, 99 (1-4), 465-476.

López, R. and Barragán, J. (2008). "Equivalent Roughness of Gravel-Bed Rivers," *Journal of Hydraulic Engineering*, ASCE, 134(6):847-851.

Lai, Y.G., and Przekwas, A.J. (1994). "A Finite-Volume Method for Fluid Flow Simulations with Moving Boundaries," Computational Fluid Dynamics, vol.2, 19-40.

Lai, Y.G., So, R.M.C., and Przekwas, A.J. (1995). "Turbulent transonic flow simulation using a pressure-based method," Int. J. Engineering Sciences, 33(4), 469-483.

Lai, Y.G. (2000). "Unstructured grid arbitrarily shaped element method for fluid flow simulation," AIAA Journal, 38 (12), 2246-2252.

Lai, Y.G., Weber, L.J., and Patel, V.C. (2003). "Non-hydrostatic three-dimensional method for hydraulic flow simulation - Part I: formulation and verification," J. Hydraul. Eng., ASCE, 129(3), 196-205.

Lai, Y.G. (2008). *SRH-2D Theory and User's Manual version 2.0,* Technical Service Center, Bureau of Reclamation, Denver, CO.

Lai, Y.G., Greimann, B.P. (2008). Rock erosion modeling on selected alluvila rivers in Taiwan," Technical Report SRH-2008-08, Technical Service Center, Bureau of Reclamation, Denver, CO.

Lai, Y.G., and Greimann, B.P. (2009). "Rock Erosion Modeling for Rivers in Taiwan and Progress Report of Bank Erosion and Turbidity Current Modeling," Technical Report Number SRH-2009-40, Technical Service Center, Bureau of Reclamation.

Lai, Y. G. and Greimann, B.P. (2010). "Predicting contraction scour with a two-dimensional depth averaged model." Journal of Hydraulic Research, 48(3), 383-387.

Lane, E.W., (1955). Design of stable channels. Trans. ASCE 120, 1234–1260.

Langbein, W.B., Leopold, L.B., (1966). River meanders: theory of minimum variance, Professional Paper 422-H. US Geological Survey.

Langendoen, E.J., and Simon, A., 2008. Modeling the evolution of incised streams. II: Streambank erosion. Journal of Hydraulic Engineering, ASCE, 134(7), 905-915.

Laursen, E.M., 1958. The total sediment load of streams. Journal of the Hydraulics Division, ASCE, 84, 1530-1–1530-36.

Larsen, E.W., (1995). Mechanics and modeling of river meander migration. PhD Dissertation, University of California, Berkeley, CA.

Leopold, L.B. and Maddock, T. (1953). The hydraulic geometry of stream channels and some physiographic implications, Professional Paper, 252, US Geological Survey. 57. pp.

Lohnes, R.A., and Handy, R.L., 1968. Slope angles in friable loess. Journal of Geology, 76(3), 247-258.

Luthi, S. M. (1980a). "Some new aspects of two-dimensional turbidity currents." Sedimentology 28: 97–105.

Luthi, S. M. (1980b). "Die eigenschaften nichtkanalisierte trubestrome: eine experimentelle untersuchung." Eclogae Geologicae Helvetiae 73(3): 881-904.

Luthi, S. M. (1981). "Experiments on non-channelized turbidity currents and their deposits." Marine Geology 40: M59-M68.

Merritt, W.S., Letcher, R.A., Jakeman, A.J. (2003). A review of erosion and sediment transport models. Environmental Modeling and Software 18: 761–799.

Mehta, A.J., 1991. Review notes on cohesive sediment erosion. In: N.C. Kraus, K.J. Gingerich, and D.L. Kriebel, (eds.), Coastal sediment '91, Proceedings of Specialty Conference on Quantitative Approaches to Coastal Sediment Processes, ASCE; pp.40-53.

Meyer-Peter, E., and Müller, R., 1948. Formulas for bed-load transport. In: 2nd Meeting of the International Association for Hydraulic Structures Research, 7-9 June, 1948, Stockholm, 39-64.

Millar, R.G., Quick, M.C., (1993). Effect of bank stability on geometry of gravel rivers. J. Hydraul. Eng., ASCE 119 (12), 1343–1363.

Millar, R.G., Quick, M.C., (1998). Stable width and depth of gravel bed rivers with cohesive banks. J. Hydraul. Eng. 124 (10), 1005–1013.

Montgomery, D.R. and Gran, K.B. (2001). Downstream variations in the width of bedrock channels. Water Resour. Res. 37(6). 1841-1846.

Morgenstern, N.R., and Price, V.R., 1965. The analysis of the stability of general slip surfaces. Geotechnique, 15, 79-93.

Morris, G., and Fan, J. (1998). Reservoir sedimentation handbook, McGraw-Hill Publishing Company.

Morris, M. (2000). "CADAM: Concerted action on dambreak modeling – Final report." Rep. No. SR 571, HR Wallingford.

Mosselman, E. (1992). Mathematical modeling of morphological processes in rivers with erodible cohesive banks, Communications on Hydraulic and Geotechnical Engineering, 92. Delft University of Technology, Delft.

Mosselman, E., (1998). Morphological modeling of rivers with erodible banks. Hydrol. Process. 12, 1357–1370.

Nagata, N., Hosoda, T., Muramoto, Y., (2000). Numerical analysis of river channel processes with bank erosion. J. Hydraul. Eng. 126(4), 243–252.

Nanson, G.C., Hickin, E.J., (1983). Channel migration and incision on the Beatton River. J. Hydraul. Eng. 109, 227–327.

Odgaard, A.J., (1989). River meander model. I. Development. J. Hydraul. Eng. 115 (11), 1433–1450.

Olsen, N.R.B., (2003). Three-dimensional CFD modeling of selfforming meandering channel. J. Hydraul. Eng. 129 (5), 366–372.

Osman, M.A., Thorne, C.R. (1988). Riverbank stability analysis: I. Theory. ASCE Journal of Hydraulic engineering 114(2): 134–150.

Ott, R.A. (2000). Factors affecting stream bank and river bank stanbility, with an emphasis on vegetation influences, An Annotated Bibliography, available at: http://forestry.alaska.gov/pdfs/2BankStabilityfinal.pdf

Parker, G., (1978). Self-formed straight rivers with equilibrium banks and mobile bed. Part 2. The gravel river. J. Fluid Mech. 89 (1), 127–146.

Parker, G., (1983). Theory of meander bend deformation. In: Elliott, C.M. (Ed.), River Meandering Proceedings of ASCE River'83 Conference, ASCE, pp. 722–731.

Parker, G., 1990. Surface-based bedload transport relation for gravel rivers. Journal of Hydraulic Research, 28(4), 417-436.

Parker, G., Sawai, K., Ikeda, S., (1982). Bend theory of river meanders. Part II. Nonlinear deformation of finite-amplitude bends. J. Fluid Mech. 115, 303–314.

Parker, G., Andrew, E.D., 1986. On the time development of meander bends. J. Fluid Mech. 162, 139–156.

Parker, G., Fukushima, Y., and Pantin, H. M. (1986). "Self-accelerating turbidity currents." Journal of Fluid Mechanics 171, 145-181.

Parker, G., Garcia, M., Fukushima, Y., and Yu, W. (1987). "Experiments on turbidity currents over an erodible bed." J. Hydr. Res., 25(1), 123–147.

Partheniades, E., 1965. Erosion and deposition of cohesive soils. Journal of the Hydraulics Division, ASCE, 91(HY1), 105-139.

Patankar, S.V. (1980). Numerical Heat Transfer and Fluid Flow, McGraw-Hill, New York.

Peric, M., Kessler, R., and Scheuerer, G. (1988). "Comparison of finite volume numerical methods with staggered and collocated grids." Computers in Fluids, 16(4), 389-403.

Pollen, N.; Simon, A. (2005). Estimating the mechanical effects of riparian vegetation on stream bank stability using a fibre bundle model. Water Resources Research 41:

Prosser, I., Rustomji, P., Young, B, Moran, C., Hughes, A. (2001). Constructing river basin sediment budgets for the national land and water resources audit. CSIRO Land and Water Technical Report Number 15/01, CSIRO Land and Water, Canberra.

Rhie, C.M., and Chow, W.L. (1983). "Numerical study of the turbulent flow past an airfoil with trailing edge separation," AIAA Journal, 21(11), 1526-1532.

Rinaldi, M., Casagli, N. (1999). Stability of streambanks formed in partially saturated soils and effects of negative pore water pressures: the Sieve River (Italy). Geomorphology 26(4): 253–277.

Rosgen, D.L. (1996). Applied River Morphology, Wildland Hydrology Inc. Pagosa Springs, Colorado.

Rosgen, D.L. (2001). A practical method of computing streambank erosion rate. Proceedings of the Seventh Federal Interagency Sedimentation Conference, March 25-29, 2001, Reno, Nevada, Vol. 2: 9-15.

Savant G, Berger C., McAlpin, T.O., and Tate, J.N. (2010). "A finite element dam and levee break model." World Environmental and Water Resources Congress, Providence, RI, May 17-20, 2010.

Schumm, S.A. and Lichty, R., (1963). Channel widening and flood plain construction along the Cimarron River in south-western Kansas. U.S. Geological Survey professional paper 352D: 71-88.

Schumm, S.A. (1968). River adjustment to altered hydrologic regime – Murumbidgee River and Paleochannels, Australia, Professional Paper No.598. US Geological Survey. 65 pp.

Shields, A. (1936). Application of similarity principles and turbulence research to bed-load movement. W.P. Ott, and J.C. van Uchelen (translators), Hydrodynamics Laboratory Publication 167. USDA Soil Conservation Service Cooperative Laboratory, California Institute of Technology: Pasadena, CA.

Simoes, F.J.M. (1999). *User's Manual for DCURL – a model for routing density currents in reservoirs and lakes*, Technical Service Center, Bureau of Reclamation, Denver, Colorado.

Simon, A, Wolf, W.J., Molinas, A. (1991). Mass wasting algorithms in an alluvial channel model. Proceedings 5th Federal Interagency Sedimentation Conference, Las Vegas, Nevada, Vol. 2: 8-22–8-29.

Simon, A., (1992). Energy, time, and channel evolution in catastrophically disturbed fluvial systems. Phillips, J.D. and W.H.Renwick (eds). Geomorphic Systems: Geomorphology, 1:345 – 372.

Simon, A., M. Rinaldi, and G. Hadish, (1996). Channel evolution in the loess area of the Midwestern United States. Sixth Federal Interagency Sedimentation Conference, Las Vegas, pp III-86 to III-93.

Simon, A., and Curini, A., 1998. Pore pressure and bank stability: The influence of matric suction, In: S.R. Abt, J. Young-Pezeshk and C.C. Watson, (eds.), Water Resources Engineering '98, ASCE: Reston; pp.358-363.

Simon, A., Curini, A. Darby, S.E., Langendoen, E.J. (1999). Streambank mechanics and the role of bank and near-bank processes in incised channels. Pp. 123–152 in Incised River Channels, S.E Darby and A. Simon (Eds), John Wiley and Sons Ltd, Chichester, England.

Simon, A., Curini, A., Darby, S.E., Langendoen, E.J. (2000). Bank and near-bank processes in an incised channel, Geomorphology, 35(3-4): 193–217.

Simon, A.; Collison, A.J.C. (2001). Pore-water pressure effects on the detachment of cohesive streambeds: seepage forces and matric suction. Earth Surface Processes and Landforms 26(13): 1421–1442.

Simon, A., Collison, A.J.C., and Layzell, A. (2003). Incorporating Bank-Toe Erosion by Hydraulic Shear into the ARS Bank-Stability Model: Missouri River, Eastern Montana, World Water & Environmental Resources Congress 2003.

Simon, A., M. Doyle, M. Kondolf, F.D. Shields Jr., B. Rhoads, and M. McPhillips (2007). Critical evaluation of how the Rosgen classification and associated " Natural Channel Design" mothods fail to integrate and quantify fluvial processes and channel response. Journal of the American Water Resources Association, 43(5), 1117-1131.

Simons, D.B., Li, R.M. (1982). Bank erosion on regulated rivers. Pp. 717–754 in Hey, R.D.; Bathurst, J.C.; Thorne, C.R. (Eds) Gravel-bed Rivers, John Wiley and Sons Ltd, Chichester, England.

Singh, B., and Shah, C.R. (1971). "Plunging phenomenon of density currents in reservoirs," La Houille Blanche, 26 (1), 341-352.

StØlum, H.H., (1998). Planform geometry and dynamics of meandering rivers. GSA Bull. 110 (11), 1485–1498.

Sun, T., Meakin, P., JØssang, T., Schwarz, K., (1996). A simulation model for meandering rivers. Water Resour. Res. 32, 2937–2954.

Sun, T., Meakin, P., JØssang, T., (2001a). Meander migration and the lateral tilting of floodplains. Water Resour. Res. 37 (5), 1485–1502.

Sun, T., Meakin, P., JØssang, T., (2001b). A computer model for meandering rivers with multiple bed load sediment sizes. I. Theory. Water Resour. Res. 37 (8), 2227–2241.

Temple, D.M., 1980. Tractive force design of vegetated channels. Transactions of the American Society of Agricultural Engineers, 23(4), 884-890.

Temple, D.M., Robinson, K.M., Ahring, R.M., and Davis, A.G., 1987. Stability Design of Grass-Lined Open Channels. USDA ARS Agriculture Handbook Number 667. US Government Printing Office: Washington, DC.

Thakur, T. R. and A. E. Scheidegger, (1970). A chain model of river meander. Journal of Hydrology, Vol. 12, pp. 25-47.

Thorne, C.R., 1982, Processes and mechanisms of river bank erosion. In: R.D. Hey, J.C. Bathurst and C.R. Thorne, (eds.), Gravel-Bed Rivers. John Wiley & Sons Ltd.: Chichester, UK, pp. 227-271.

Thorne, C.R. (1998). Stream Reconnaissance Handbook. John Wiley and Sons Ltd, Chichester, England, 133 pp.

Thorne, C.R., and Tovey, N.K. (1981). Stability of composite river banks. Earth Surface Processes and Landforms 6: 469–484.

Thorne, C.R., Abt, S.R. (1993). Analysis of riverbank stability due to toe scour and lateral erosion. Earth surface Processes and Landforms 18: 835–843.

Thorne, C.R., Murphey, J.B., and Little, W.C., 1981. Bank stability and bank material properties in the bluffline streams of Northwest Mississippi, Stream Channel Stability, Appendix D, Section 32 Program, Work Unit 7, U. S. Army Corps of Engineers, Vicksburg District: Vicksburg, Mississippi.

Toniolo, H., Parker, G., and Voller, V. (2007). "Role of ponded turbidity currents in reservoir trap efficiency," J. Hydraulic Engineering, 133(6), 579-595.

USACE, U.S. Army Corp of Engineers, Waterways Experiment Station (1960). "Floods resulting from suddenly breached dams: Conditions of minimum resistance." Paper: 2-237, report 1.

USACE, U.S. Army Corp. of Engineers, Waterways Experiment Station (1961). "Floods resulting from suddenly breached dams: Conditions of maximum resistance." Paper: 2-274, report 2.

van Rijn, L.C., 1984a. Sediment transport, Part I: Bed Load Transport. Journal of Hydraulic Engineering, ASCE, 110(10), 1431-1456.

van Rijn, L.C., 1984b. Sediment transport, Part II: Suspended Load Transport. Journal of Hydraulic Engineering, ASCE, 110(11), 1613-1641.

Vigilar, G.G., Diplas, P., (1997). Stable channels with mobile bed: formulation and numerical solution. J. Hydraul. Eng. 123 (3), 189–199.

Walling, D.E., P.N. Owens, and G.J.L. Leeks, (1999). Fingerprinting suspended sediment sources in the catchment of the River Ouse, Yorkshire, UK. Hydrol. Proc., 13(7), 955-975.

Wang, Z. and Bowles, D.S. (2006). "Three-dimensional non-cohesive earthen dam breach model. Part 1: Theory and methodology." Advances in Water Resources 29, 1528-1545.

Watson, A.J. and Marden, M. (2004). Live root-wood tensile strengths of some common New Zealand indigenous and plantation tree species. New Zealand Journal of Forestry Science 34(3): 344–353.

Watson, A.J. and L.R. Basher, (2006). Stream bank erosion: a review of processes of bank failure, measurement and assessment techniques, and modeling approaches, Landcare ICM Report No. 2005-2006/01, Landcare Research, Lincoln, Private Bag 6, Nelson, NEW ZEALAND.

Wilcox, P.R. and Crowe, J.C. (2003). Surface-Based Transport Model for Mixed-Size Sediment. Journal of Hydraulic Engineering, 129: 120-128.

Wilkin, D.C. and S.J. Hebel, (1982). Erosion, redeposition, and delivery of sediment to Midwestern streams. Water Resour. Res. 18(4), 1278-1282.

Williams, G.P., (1978). Hydraulic geometry of river cross sections—theory of minimum variance, Professional Paper, No.1029. US Geological Survey. 47 pp.

White, W.R., Bettess, R., Paris, E., (1982). Analytical approach to river regime. J. Hydraul. Div. 108, 1179–1193.

Winterwerp, J.C., and van Kesteren, W.G.M., 2004. Introduction to the physics of cohesive sediment dynamics in the marine environment. Elsevier: Amsterdam.

WRA (Water Resources Agency in Taiwan), (2008a). "Proposed engineering schemes for river stability control and energy dissipation for downstream of the Chichi Weir (集集攔河堰下游河道穩定及水流消能治理工法佈置方案)," in Chinese, 4th River Division (經濟部水利署第四河川局).

WRA (Water Resources Agency in Taiwan), (2008b). "Implement and Application Study of NCCHE's River Migration Models," in Chinese.

Wu, W, Wang, S.S.Y., and Jia, Y., 2000. Nonuniform sediment transport in alluvial rivers. Journal of Hydraulic Research, 38(6), 427-434.

Yang, C.T., 1973. Incipient motion and sediment transport. Journal of the Hydraulics Division, ASCE, 99(HY10), 1679-1704.

Yang, C.T. (1976). Minimum unit stream power and fluvial hydraulics. J. Hydraul. Div. 102, 769–784.

Yang, C.T., and Simões, F.J.M. (2000). *User's manual for GSTARS 2.1 (Generalized Stream Tube model for Alluvial River Simulation version 2.1)*. U.S. Bureau of Reclamation, Technical Service Center, Denver, Colorado.

Zhou, J.G., Causon, D.M., Mingham, C.G., and Ingram, D.M. (2004). "Numerical prediction of dam-break flows in general geometries with complex bed topography." J. Hydraulic Engr, ASCE, 130(4), 332-340.